This electronic thesis or dissertation has been downloaded from Explore Bristol Research, http://research-information.bristol.ac.uk

Author:
Field, Lorraine Patricia

Title:
The magnetic evolution of Dabbahu Volcano and the 2010 eruption of Erta Ale, Afar, Ethiopia

General rights
The copyright of this thesis rests with the author, unless otherwise identified in the body of the thesis, and no quotation from it or information derived from it may be published without proper acknowledgement. It is permitted to use and duplicate this work only for personal and non-commercial research, study or criticism/review. You must obtain prior written consent from the author for any other use. It is not permitted to supply the whole or part of this thesis to any other person or to post the same on any website or other online location without the prior written consent of the author.

Take down policy
Some pages of this thesis may have been removed for copyright restrictions prior to it having been deposited in Explore Bristol Research. However, if you have discovered material within the thesis that you believe is unlawful e.g. breaches copyright, (either yours or that of a third party) or any other law, including but not limited to those relating to patent, trademark, confidentiality, data protection, obscenity, defamation, libel, then please contact: open-access@bristol.ac.uk and include the following information in your message:

- Your contact details
- Bibliographic details for the item, including a URL
- An outline of the nature of the complaint

On receipt of your message the Open Access team will immediately investigate your claim, make an initial judgement of the validity of the claim, and withdraw the item in question from public view.

The Magmatic Evolution of Dabbahu Volcano and the 2010 eruption of Erta Ale, Afar, Ethiopia

Lorraine Field

School of Earth Sciences

University of Bristol

Thesis submitted in accordance with the requirements of the
degree of Doctor of Philosophy in the Faculty of Science

July 2011 40, 760 words

Abstract

The development of magmatism during the transition from continental rifting to sea-floor spreading remains poorly understood as most rifted margins are now inactive and buried beneath thick sediments. Dabbahu and the basaltic Erta Ale volcanoes situated within the actively rifting Afar region of northern Ethiopia, offer a unique opportunity to address this problem.

The nature of rhyolitic volcanism, the sub-volcanic system, and their relationship to basaltic magmas involved in dyking events is investigated at Dabbahu volcano and forms the main subject of this study. The evolution of the volcano is constrained through 9 new $^{40}Ar/^{39}Ar$ dates and geochemical analysis of 93 samples, supplemented by a new geological map. Dabbahu has been active for over 65,000 years, erupting basalts through to evolved pantellerites. Modelling shows the evolved magmas were derived through protracted (>80%) fractional crystallisation. A shallow magma storage region (1-5 km) is confirmed through melt inclusion analysis, and further constrained with seismic and InSAR data. However, it is proposed that this region is a temporary site of pre-eruptive storage for evolved products and the site of differentiation lies at depth within the crust (14-20 km). Field evidence indicates that magmas were not erupted in fractionation sequence and mixing between cogenetic magmas is recorded on all scales. The input of new magma may have been a key eruption trigger at Dabbahu throughout its history, as was the case in the most recent 2005 eruption at the Da'Ure vent following dyke injection.

Erta Ale is a basaltic shield within the most northerly magmatic segment of the same name, and contains one of the world's longest lived lava lakes. An overview of the events of the November 2010 eruption in this remote area has been constructed through a combination of ground observation and remote sensing. Analysis of zero age lavas provides new insights into this unique volcano.

Acknowledgements

This Ph.D could not have been completed without the help of many people, given in many different ways, but to whom I am indebted. My supervisors, Jon Blundy and David Pyle for their input of ideas and patience reading endless manuscripts: Jon Blundy for allowing me to realise a dream and witness a volcanic eruption. To members of the Afar Consortium, particularly Elias Lewi for always smiling; without his help in sorting endless paperwork, and his continuous support at all times, we would never have made it into the field. My sincere thanks to Julie Rowland for sitting up with me all night in Digdigga to coax me back to health. To field assistants: Elias Abebe, Mulugeta Channe, Mohammed Adem, Yaragal Yenealem; and our police officers from the Semera Police Department who were continually bemused and amused by us. To Osman Tajuddin, the best field assistant one could hope for, and who became a friend; who saved our lives on the summit of Dabbahu, and then tragically lost his own life in 2010: you will always be remembered. To Derek Keir, for being a terrific person to share an eruption with – may the memories last the years. For technical assistance I will always be indebted to Andy Calvert for teaching me the value of good sample preparation at the USGS, Nick Marsh and Rob Kelly at Leicester (XRF), Richard Hinton and John Craven at Edinburgh (SIMS), Stuart Marsh at Bristol (EMPA & SEM). To Vicky Smith, Ian Bastow and Penny Widdison, for believing in me. To the occupants of G9, and room ‘M’; especially Joe Pickles, Pete Holland, Emma Humphries, Emma Kiddle and Janine Kavanagh for keeping me sane, and Kate Saunders for endless coffees. To Mell Freeman, Lyn Holt, Barbara Perks and Emma Teakle for periodically dragging me away from work, and patiently listening to my witterings.

Finally to Paul, and Mum and Dad, without whose support and encouragement this would not have been possible.

This research has been sponsored by:

The Natural Environmental Research Council as tied studentship grant (NE/F007604/1), part of the larger Consortium grant, “How does the Earth's crust grow at divergent plate boundaries? A unique opportunity in Afar, Ethiopia”, (NE/E005284/1).

Declaration

I declare that the work presented in this thesis was carried out in accordance with the Regulations of the University of Bristol. The work is original, except where indicated by special reference in the text, and no part of the dissertation has been submitted for any other academic award. Chapters 3, 4 and 5 are based on manuscripts which are currently being reviewed for publication and which have been written in co-operation with other researchers. Any views expressed in the dissertation are those of the author.

Lorraine Field July 2011

Table of contents

Table of contents cont.

Appendices CD-ROM

Appendix 1	Sample summary	(Microsoft Word 2010)
Appendix 2	Dabbahu data	(Microsoft Excel 2010)
Appendix 3	Erta Ale data	(Microsoft Excel 2010)
Appendix 4	Photographs of rock samples	
Appendix 5	Erta Ale video	

List of figures

List of figures cont.

List of tables

Thesis introduction

Chapter

1

Overview

The Earth's surface is continually re-shaped through continental rifting processes, ultimately rupturing the tectonic plates to form new ocean basins (e.g. Grove 1986; Yirgu et al. 2006; Ebinger et al. 2010). Both rifting and seafloor spreading involve the closely linked processes of mechanical extension and magmatism; most large scale continental rifts develop a pre-rift large igneous province (Pik et al. 1998; Rogers 2006). At one extreme, continental rifts are characterised by relatively broad zones of extension with typically silicic dominated bimodal volcanism and large silicic volcanoes developing on the rift floor; at the other extreme, oceanic volcanism at fast spreading oceanic centres is dominated by narrow zones of basaltic magma intrusion and eruption (Mutter and Karson 1992). Eruption occurs at volcanic centres and cones, or through intrusion of sheeted dykes along oceanic ridges reaching the surface and causing fissural eruptions. However, discrete rifting episodes can rarely be observed, and it is often only the end result which can be studied i.e. the oceanic basin and rifted continental margins on either side (e.g. Rogers 2006).

The East African rift system provides a unique opportunity to investigate rifting. Extension along the active rift currently encompasses all stages of passive margin development; from juvenile continental rifting to incipient sea-floor spreading. The rift extends > 3000 km from Mozambique in the south, through to Ethiopia, Djibouti and the Afar depression in the north. The Ethiopian rift forms the third arm of the Red Sea – Gulf of Aden triple junction within the complex Afar region. This Afar volcanic province is the classic location to study the role of magma during continental break up, and transition to oceanic basin.

The Ethiopian rift system is one of the few locations worldwide where active continental break-up can be observed (e.g. Hayward and Ebinger 1996). The current phase of rifting began in September 2005 with a major 60 km basaltic dyke intrusion and a small rhyolitic eruption, believed to be the first such eruption in ~ 150 years (fig. 1.1); prior to this episode, just seven of Africa's volcanoes had erupted in historical times (Ayele et al. 2007).

The Afar region forms a triangular low-lying region (-120 – 500 m elevation) where the Red Sea, the Gulf of Aden and the East African Rift meet (fig. 1.2), bordered by the Ethiopian plateau to the west (~2000 - 3000m), the Somali plateau to the southeast, and the Danakil block to the northeast. As early as 1970, it was suggested that the entire Red Sea trough was formed by the removal of Arabia away from the African and Somalian plates (McKenzie et al. 1970).

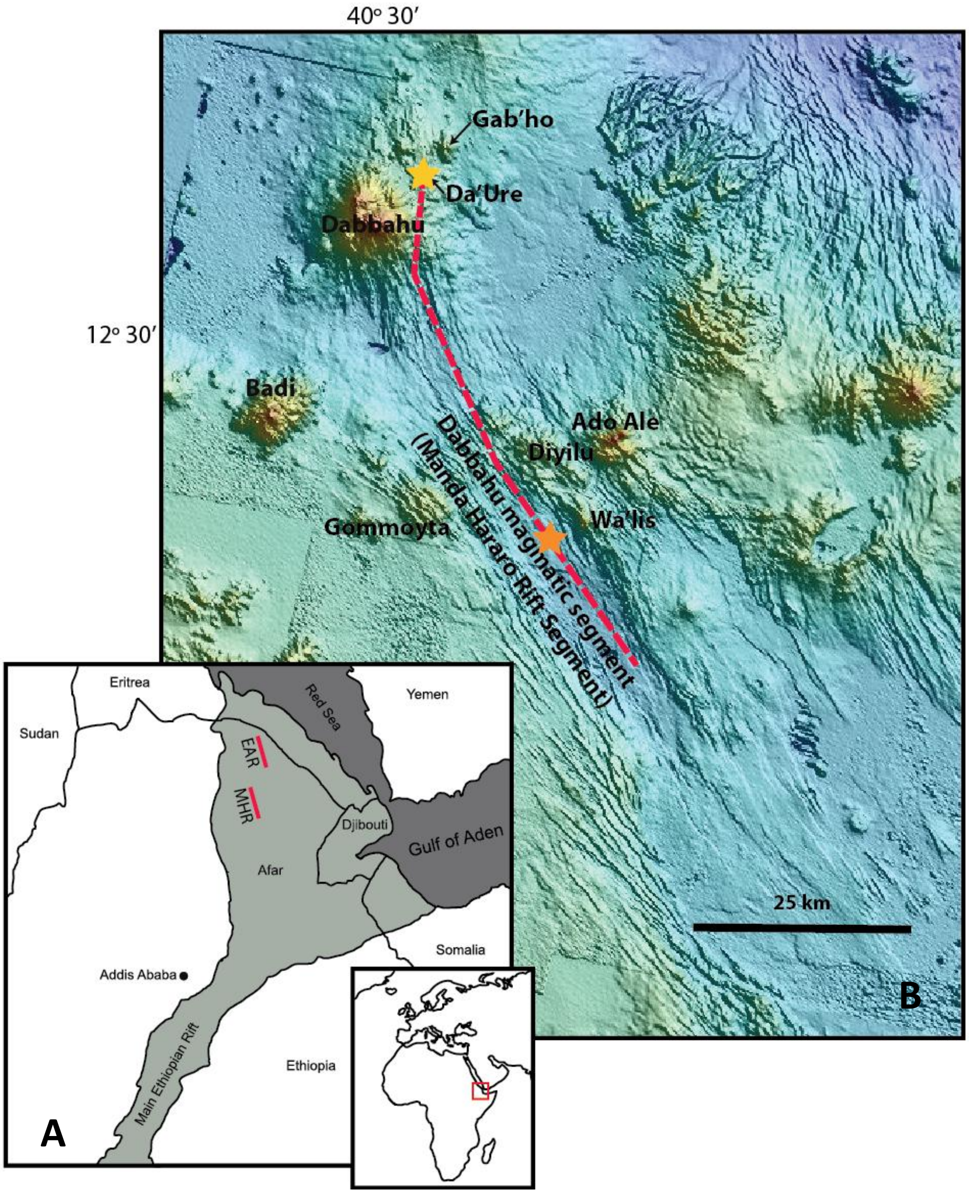

Figure 1.1. *A) Location map of the Manda Hararo and Erta Ale rift segments within the Afar region. B) False colour SPOT image of the Manda Hararo rift segment showing the location of Dabbahu volcano (SPOT image courtesy of S. Hautot). Red dashed line – indication of September 2005 dyke emplacement, yellow star indicates the Da'Ure vent eruption. Orange star indicates the location of the 2007 and 2009 fissure eruptions. Ado Ale, Gommoyta, Dryilu and Wa'lis are also known as the Ado Ale volcanic complex.*

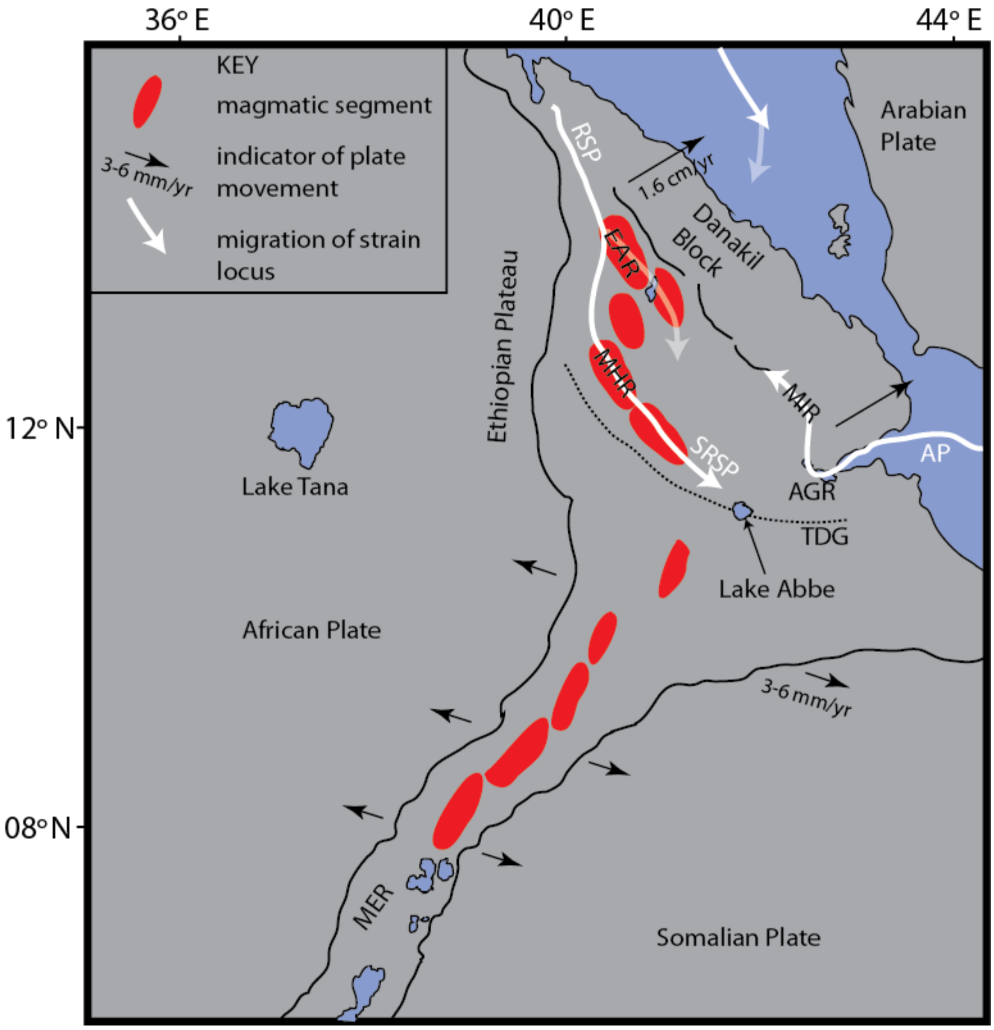

Figure 1.2. *Regional setting of Afar, and model reflecting current rifting and shift of the strain locus in Afar. EAR – Erta Ale Rift, MER – Main Ethiopian Rift, MHR – Manda Hararo Rift, MIR- Manda Inakir Rift, AGR – Asal-Ghoubbet Rift, TDG – Tendaho-Goba'ad Discontinuity, RSP – migration of strain of the Red Sea rift, SRSP – migration of strain of the Southern Red Sea rift, AP – migration of strain of the Gulf of Aden rift.*

The separation rotation angles and pole can be obtained by fitting together the coast lines (McKenzie et al. 1970).

Volcanism dates from ~45 Ma in Southern Ethiopia (George et al. 1998), but the main eruptive period began with the eruption of flood basalts in Afar between 29 and 31 Ma (Hofmann et al. 1997), roughly coeval with the initiation of NE-directed extension in the southern Red Sea and Gulf of Aden (Wolfenden et al. 2005). The main rifting began at ~35 Ma in the Gulf of Aden (d'Acremont et al. 2005), ~28 Ma in the Red Sea (Wolfenden et al. 2005) and at 15 - 18 Ma in the southern and central Main Ethiopian Rift (MER), where the locus of strain shifted northwards (Wolfenden et al. 2004). The triple junction formed when the MER reached the Red Sea rift at ~11 Ma (Wolfenden et al. 2004); some 20 million years after the emplacement of the flood basalts and the initial onset of rifting. The actual triple junction is believed to be currently located near Lake Abbe, in a complex zone on the Ethiopian / Djibouti border (Mohr 1972; Tesfaye et al. 2003). In the Gulf of Aden the rifting has progressed to oceanic spreading (e.g Manighetti et al. 1997), and the Red Sea rift has opened southwards to 14 ^{o}N (Prodehl et al. 1997), where it is believed to have moved on land thus isolating the Danakil microplate (fig. 1.2). The Danakil microplate is an area of continental material isolated between the oceanic rift to the northeast and a subaerial rift zone to the southwest within the Afar depression (Rowland et al. 2007). It has been proposed that the rifting in the region may have been initiated by an upwelling of hot mantle material beneath Africa, which is supported by geochemical signatures in the Ethiopian plateau flood basalts suggesting deep mantle involvement (Pik et al. 1999). However, there is continued debate regarding the nature of the plume i.e. whether there is just one, two or a modified plume with several small plumes rising from the main body (e.g. Davies 1998; Ebinger and Sleep 1998; George et al. 1998). The Arabian plate is currently moving away from Africa at a rate of 16 mm yr^{-1}, and across the northern sector of the MER, recent studies suggest that there is 3-6 mm yr^{-1} of movement between the Somalia and African plates (fig.1.2), (Chu and Gordon 1998; 1999).

The Afar is a region undergoing transition to an embryonic ocean (Makris and Ginzburg 1987), and the crust is thinning as it is being extended. Current studies show that the crust thins from ~26 km in the south to <14 km in the north, and is bounded by ~40 km thick crust beneath the Ethiopian and Somali plateaux (Hammond et al. 2011.). Crust beneath the Manda-Hararo / Dabbahu volcanic segments is ~20-22 km (Hammond et al. 2011.). The overall deformation in the area shows a number of first order morphological similarities to slow spreading oceanic ridges e.g. large extension fractures and open normal faults with tilted hanging-walls (Hayward and Ebinger 1996). The region exhibits nascent sea-floor spreading (Ebinger and Hayward 1996); not yet oceanic crust, but thinned and attenuated continental crust (Makris and Ginzburg 1987; Ebinger and Hayward 1996). Recent controlled source and receiver function work has found evidence for lower crustal high velocity layers, interpreted as highly intruded crust (e.g. Maguire et al. 2006; Cornwell et al. 2010).

The locus of strain has shifted southwards from the Red Sea rift to sub-aerial northern Afar, in a series of successive, discrete rift jumps; most of the volcanic and tectonic activity in Afar is due to the mechanical interaction of this on-land continued opening of the Red Sea rift (Acocella et al. 2008). As the rift localised at ~3 Ma, magmatism and faulting in Afar became focused along ~60 km long segments (Hayward and Ebinger 1996) which are zones of fissural flows, aligned basaltic scoria cones, volcanoes, shallow seismicity and positive gravity anomalies, collapsed grabens, and domino tilted blocks (Barberi and Varet 1977; Hayward and Ebinger 1996; Acocella 2010; Beutel et al. 2010; Ebinger et al. 2010). These magmatic segments are the locus of magma intrusion and formation of new crust. The individual rift segments are similar in size, morphology, structure and spacing to those observed along an oceanic boundary (e.g. Hayward and Ebinger 1996). To the north, the segments of Erta Ale and Tat'Ale are characterised by axial volcanic ridges of transitional alkali / tholeiitic composition (Barberi et al. 1972). Southward continuation of the rift steps across to the western Alayta segment, and then to the Manda-Hararo rift zone which comprises the active northern Dabbahu magmatic segment and the currently tectonically inactive southern Hararo segment (Rowland et al. 2007). The Manda-Hararo rift is characterised by a central depression ~35 km wide, in contrast to the elevated topography of the northern segments. The Dabbahu segment is punctuated by the volcanoes of the Ado' Ale complex and in the north, Dabbahu (fig.1.1) (Lahitte et al. 2003).

Many studies on Ethiopian rift magmatism have been carried out on a regional scale (e.g. Hart et al. 1989; Trua et al. 1999; Ayalew et al. 2006) and detailed studies on individual volcanoes are more infrequent (Peccerillo et al. 2003; Wiart and Oppenheimer 2005). The volcanoes in southern and central Afar are central silicic volcanoes which emerge from the floor of Stratoid Series; a thick stratiform sequence of basaltic lava flows resulting from widespread fissural activity; the principle volcanic formation in the Afar (Barberi and Varet 1977). Silicic central volcanoes (SCVs) differ from volcanoes observed in northern Afar, where differentiated series erupted as large shield volcanoes e.g. Erta Ale and Tat'Ale (Lahitte et al. 2003), and the reasons behind their formation and the north-south differences are not yet fully understood. Recent studies have suggested that the eruption of

SCVs occur prior to the emplacement of a propagating rift zone which then appears to be 'captured' by the volcanoes, as the migration of rift segments is favoured by the weaker zones created by the volcanoes and their associated crustal magma reservoirs (van Wyk de Vries and Merle 1996; Lahitte et al. 2003). Ebinger et al (2008) suggest that volcanoes such as Dabbahu are located at the tip of the rift segments due to the offset of the one segment to another e.g. the Alayta segment is offset to the east of the Dabbahu segment. This places the tip of the Dabbahu segment against colder, thicker lithosphere, inhibiting lateral propagation of dykes, allowing the magma to pond in crustal reservoirs. However initiated, it has been suggested these volcanoes are gradually dismantled due to tectonic deformation as rifting progresses (e.g. Lahitte et al. 2003; Wiart and Oppenheimer 2005).

The Manda-Hararo rift segment is the current locus of magmatism as demonstrated by the prevalence of dyking events along the axial zone which have been observed since 2005 (Hamling et al. 2009). This ongoing magmatic activity is thus occurring on the easternmost edge of the thinnest crust (Makris and Ginzburg 1987; Hammond et al. in prep.), which may be explained by the rotation of the Red Sea rift from a north-south orientation to the present north-west / south-east direction, caused by the migration north-eastwards of the triple junction: ~160 km northeast in 10 Myr (Tesfaye et al. 2003).

On the 9th September 2005 a seismo-volcanic crisis began, which continued until mid-October of the same year, and involved > 400 earthquakes, 210 with a magnitude Mw ≥ 3.6 and 15 Mw ≥ 5, and a small rhyolitic eruption at the Da'Ure vent (fig. 1.2), just to the north-west of Dabbahu (Wright et al. 2006; Ayele et al. 2007; Ayele et al. 2009). Deformation associated with the event has been modelled as due to the injection of a basalt dyke, ~10 km deep, with up to 8 m of opening along a distance of ~60 km – the largest dyke opening event ever measured, and the first such event in the modern age of satellite geodetic methods (Wright et al. 2006). The basaltic dyke is likely to have thermally reactivated an existing shallow silicic magma chamber at Da'Ure causing the small eruption of ash, and extrusion of a small rhyolitic pumice dome (Ayele et al. 2007).

This event highlighted the unparalleled setting in which continental break-up and its relation to volcanism can be studied in detail, and reactivated interest in what is traditionally considered an inhospitable and inaccessible location. As suggested by Ayele et al (2007), the interests of both safeguarding the population and advancing science, converge in the Afar region.

Aims of this study

Following the September 2005 volcano-seismic crisis in Afar, a NERC urgency grant was awarded to allow an initial rapid response and assessment of the crisis. Following the initial assessment, the NERC funded Afar Rift Consortium was conceived; a collaboration of 5 universities from the UK, and partners from the British Geological Survey, Addis Ababa, the USA, France and New Zealand, bringing together expertise across different disciplines.

The overarching aims of the Consortium project are to investigate active magmatism and tectonics in the Afar region of northern Ethiopia, and track the creation, migration, evolution and emplacement of magma from the asthenosphere to the crust. To achieve this, the Afar Consortium has taken a multidisciplinary approach involving seismicity, remote sensing, InSAR, structural, gravity, magnetotellurics, GPS, petrology and geochemisty teams.

As part of the petrological and geochemical studies, the overall aim of this project is to further understand the nature of magmatic processes in an active continental rift environment by studying the Dabbahu volcano at the northern end of the currently active Manda-Hararo rift segment, near the western margin of the Afar depression (12^{o} 39’39.24” N, 40^{o} 28’45.10” E). Despite some detailed work during the CNR – CNRS campaigns of the late 1960s and early 1970s, Dabbahu volcano is still something of an enigma, and cannot be clearly categorised. Lahitte et al., (2003) describe it in the context of both an SCV and as one of the northern basaltic shield volcanoes, Barberi et al., (1974) described it as a basaltic shield volcano with silicic products , Yirgu et al., (2006) as a strato-cone. The September 2005 eruption at the Da’ Ure vent occurred just north of the Dabbahu edifice (fig.1.1b), and InSAR studies show that the dyke injection was partially supplied by magma from the Gab’ho and Dabbahu volcanic centres (Wright et al. 2006), indicating that Dabbahu is still an active centre.

The volcano was last studied in detail ~30 years ago (Barberi et al. 1974; Bizouard et al. 1980), and no modern petrological, radiometric or geochemical work has been done on these rocks. The objectives of this study are to obtain absolute ages and constrain the age –

stratigraphic framework, the relationships between the erupted units of Dabbahu, and its relationship to the rift segment; to constrain the volatile content and storage conditions of the rhyolite magmas; and to obtain mineral analyses to further understand the evolution of this volcano. Various techniques were utilised to fulfil these objectives, such as Secondary Ion Mass Spectrometry (SIMS), Electron Microprobe Analysis (EMPA), ^{40}Ar-^{39}Ar dating, remote sensing and aerial photography.

The Erta Ale magmatic segment (fig.1.1a) comprises six volcanic centres (fig. 1.3), from north to south: Gada Ale, Alu-Dalafilla, Borale Ale, Erta Ale, Hayli Gubbi and Ale Bagu, the latter being located off the axis of the main chain (Barberi and Varet 1970).

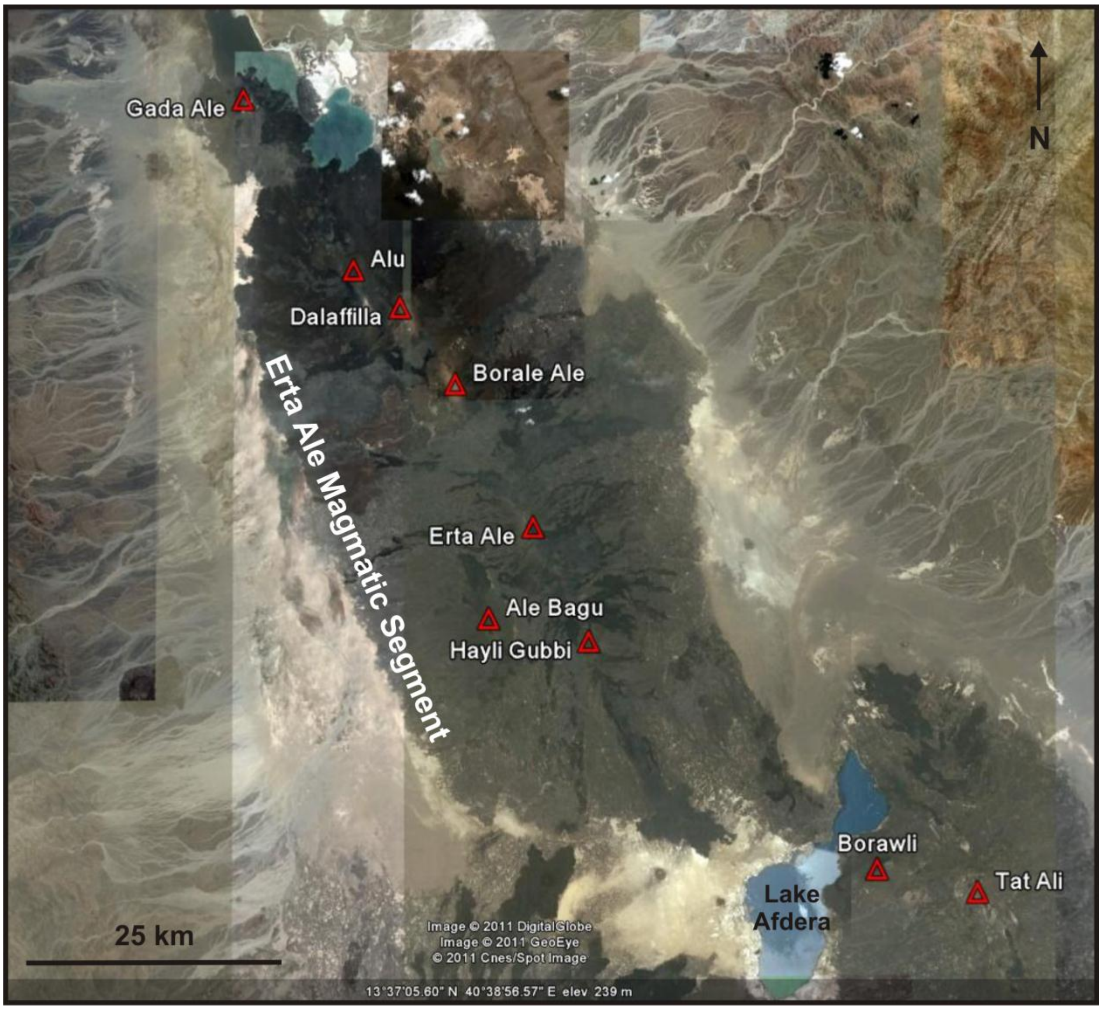

Figure 1.3. *Map of the Erta Ale magmatic segment indicating the volcanic centres. Erta Ale volcano is located in the centre of the segment.*

The Erta Ale volcano is a basaltic shield, and is well known due to its long lived lava lake (e.g. Barberi and Varet 1970; Barberi et al. 1973). The inaccessibility and the volcano's proximity to the Ethiopian / Eritrean border has resulted in limited scientific study; the first systematic study of the segment was carried out as part of the CNR-CNRS campaigns in the late 1960s. The sub-magmatic system is still poorly constrained and understood. In November 2010 the arrival of the field team as part of the bi-annual seismometer servicing run, fortuitously coincided with an eruption and overflow of the south pit lava lake. This allowed us the opportunity to determine if satellite data can be interpreted to correlate to on the ground observations, which would allow remote monitoring of this volcano in future. The overflows into the main caldera allowed a unique opportunity to sample zero age lavas. For the first time pristine melt inclusions hosted in euhedral olivines were located in samples from Erta Ale, and their analysis has enabled further insight into the magmatic system at Erta Ale. This study from the most northern and mature magmatic segment allows us to make comparisons between the northern Erta Ale volcanic system and the Dabbahu volcano.

Thesis overview

This thesis is largely based on the analysis of samples collected during three field campaigns; two at Dabbahu and one at Erta Ale. Both Dabbahu field campaigns were organised by, and were the responsibility of the author, and involved expedition planning including the calculation and acquisition of field provisions e.g. water, budget planning, first aid training for expedition members etc. Due to security issues, just seven days were spent on the volcano itself. The expedition planning also involved an additional two trips to the Semera and Teru authorities some months before the expeditions themselves, to facilitate the permissioning process.

Chapter 2 provides details of the methodologies used for each of the analytical processes. The processes described are: whole rock X-ray fluorescence, scanning electron microscopy, electron microprobe analysis, secondary ion-mass spectrometry, Fourier transform infrared spectrometry, argon-argon geochronology and point counting.

Chapter 3 provides an introduction to Dabbahu volcano itself, and the history of work to date. Details of the field campaigns and sampling strategy from this study are documented. Stratigraphic relationships and ^{40}Ar-^{39}Ar dating provide a context for the volcano summarised in a new geological map, based on field evidence and remote sensing. A full geochemical description of the rock types of Dabbahu determined from X-ray fluorescence analysis of major and trace elements is provided, together with detailed analysis of the mineralogy of the sampled lava flows. The evolution through the rock types is explored, and determination of intrinsic parameters of temperature and oxygen fugacity and their implications is discussed. These results are compared to other analysis from the Manda Hararo rift segment, together with some recent experimental results. This chapter forms the basis of a paper in review with the Geological Society of America.

Chapter 4 describes the pre-eruptive volatile content of the Dabbahu peralkaline rocks, and estimates of physical constraints for the magma storage region given (temperature, pressure, depth), with a comparison to the seismic and InSAR data gathered by members of the consortium. The results and discussion form the basis for a paper in review with the Bulletin of Volcanology.

Chapter 5 details the November 2010 eruption of Erta Ale. On the ground observations have been used to interpret SEVERI satellite images in collaboration with Talfan Barney at Cambridge, and together this approach has allowed us to reconstruct the entire eruptive period. Zero-age samples have been analysed using the same processes used for the Dabbahu samples, including volatile analysis of melt inclusions, leading to new insights into this unique volcano. These data have formed the basis for a manuscript which has been submitted to Earth and Planetary Science Letters.

Chapter 6 draws together the main results and conclusions from each of the preceding chapters and identifies the key contributions of the thesis. This chapter also suggests areas of further investigation at Dabbahu.

Methodology

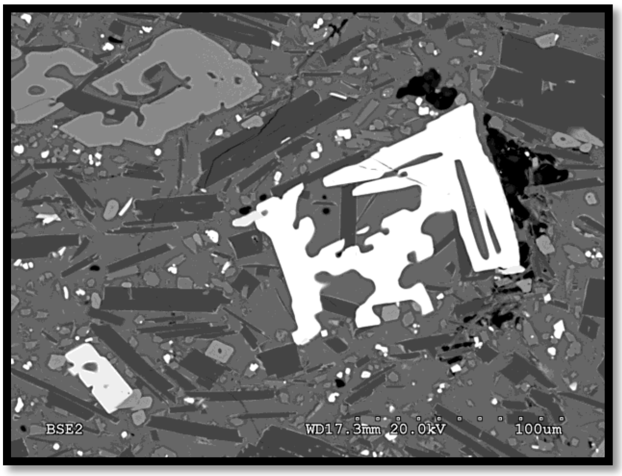

Chapter

2

Introduction

Various techniques were used in this study to analyse the Dabbahu and Erta Ale samples. This chapter describes the procedures used for sample preparation, analysis and data processing. Samples were analysed using the following methods: whole-rock X-ray fluorescence, scanning electron microscopy (SEM), electron microprobe analysis (EMPA), secondary ion mass spectrometry (SIMS), Fourier Transform Infrared Spectrometry (FTIR) and ^{40}Ar-^{39}Ar geochronology. Great care was taken with sample preparation to reduce contamination and ensure the data acquired was of the best quality.

Whole-rock X-Ray Fluorescence

Sample preparation

Rock samples were prepared for analysis by removing any weathered material using a rock splitter. The fresh sample was manually crushed on an acetone-cleaned steel plate to minimise contamination, until the average clast size 2-3 mm. This was then milled to a fine powder using a Retsch Agate Planetary Ball Mill. Approximately 50 g of powdered material was produced for each sample.

Fusion beads

Glass fusion beads were prepared for major element analysis (Leake et al. 1969) using approximately 10 g of powdered sample that had dried for 12 hrs at 110 ^{o}C to remove low temperature absorbed volatiles. Loss on Ignition (LOI) was determined in a two-step procedure due to the alkaline nature of the samples. Alkaline samples have a low melting temperature, and the usual method of heating in one step at 950^{o}C can cause the sample to melt to a glass bead, thus preventing use of the ignited powder. In this case, samples were ignited in two stages initially at 750 ^{o}C, and then 950 ^{o}C. The weight of the crucible (W1) and the weight of the crucible plus sample before ignition (W2) were recorded and the samples ignited for 1.5 hrs at 750 ^{o}C. Following ignition, the samples were allowed to cool to room temperature in a desiccator and reweighed (W3). Ignited sample (0.6 g) was removed to make the fusion bead, and the LOI process was repeated at 950 ^{o}C on the remainder of the sample.

The percentage weight loss (LOI) for each stage can then be determined using the following simple formula:

$LOI = 100*(W2 - W3)/(W2 - W1)$

The total LOI from both stages can be calculated as follows:

LOI = (LOI@750 ^{o}C) + (LOI@950 ^{o}C)

To make the fusion beads, the sample powder was mixed with a flux of 80:20 Li metaborate: Li tetraborate, heated on a gas burner and agitated to ensure good mixing. When sufficiently homogenised the liquid was cast, cooled, labelled and stored ready for analysis.

Powder pellets

Powder pellets, made from ~10 grams of powdered sample, were prepared for trace element analysis. The rock powder was mixed with Moviol 88 binding solution, placed into a 32 mm diameter die and compressed in a hydraulic press at a pressure of 10 tons per square inch. The resulting pellet was left to dry for ~12 hrs before being labelled and stored ready for analysis.

Analysis

Whole rock major and trace elements were determined for 93 samples from Dabbahu and 3 from Erta Ale using a PANalytical Axios-Advanced XRF spectrometer at the University of Leicester, equipped with a 4Kw Rhodium anode end window super sharp ceramic technology X-Ray tube. In addition to the 10 standards analysed as part of each run, a total of nine 'blind' analyses were made of known standards (JR1, JR2, JG2 and BHV02), together with 4 'blind' duplicate samples per run, to ensure consistency and quality of data (table 2.1). The samples were analysed for the following major elements: SiO_2, TiO_2, Al_2O_3, Fe_2O_3, MnO, MgO, CaO, Na_2O, K_2O, P_2O_5 and SO_3. Trace elements analysed were: Rb, Sr, Y, Zr, Nb, Mo, Pb, U, Th, Ga, Zn, Cu, Ni, Co, Cr, V, Sc, Ba, La, Ce, Nd and Cs.

Data processing

Standards were verified against the preferred or certified values reported in the literature. Data was then reviewed and major element data with totals outside of 100 ±2% were rejected. Uncertainties for both major and trace elements were determined by taking the counting statistical error (CSE) and applying this as a percentage to the actual wt% or ppm value. Error values were < 0.025% for major elements and generally < 1 ppm for trace elements. Anhydrous normalised values were calculated for all data.

	JR1 run 1	**JR1 run 2**	**Preferred values**
SiO_2	76.29	75.36	73.52-76.8
TiO_2	0.11	0.11	0.10-0.12
Al_2O_3	12.85	12.86	12.53-13.17
Fe_2O_3t	0.9	0.88	0.74-0.92
MnO	0.1	0.1	0.09-0.16
MgO	0.04	b.d.	0.07-0.24
CaO	0.66	0.63	0.69-0.76
Na_2O	3.96	4.1	3.89-4.37
K_2O	4.07	4.47	4.26-4.87
P_2O_5	0.02	0.01	0.02-0.03

Table 2.1. *Example of 'blind' standard JR1 (Wada Toge rhyolite obsidian) major element determinations together with the reference values (Ando 1984). Fe_2O_3t refers to Fe_2O_3 as total iron.*

Melt inclusions and glasses

Sample preparation

Grain mounts were prepared for melt inclusion (MI) analysis to concentrate the number of MI available for analysis. Rock samples were coarsely crushed using an acetone-cleaned steel plate, and pestle and mortar to minimise contamination. Material was dry sieved to extract a target fraction split (coarser than 50 µm and finer than the largest crystals in each sample (usually <1 mm)). The samples were washed, with a final rinse in distilled water, and dried for 24 hrs at ~ 80^{o}C to remove dust particles. Anorthoclase, clinopyroxene (cpx) and olivines were hand-picked under a binocular microscope. Petrographic observation ensured all the feldspar grains mounted contained melt inclusions. In dark host minerals (e.g. Fe-augite) this was not possible as the dark colouration concealed them. These minerals were therefore mounted en masse to maximise the opportunity of locating MI. Crystals were then mounted in metal ring holders on double-sided tape and a glass slide. Once mounted the metal ring was half filled with EpoFix© cold-cure resin after thorough mixing followed by agitation in a hypersonic bath for 5 minutes to remove bubbles. Mounts were removed from the tape and glass slide after 24 hrs and left to cold cure for 2 weeks prior to polishing. Polishing was carried out using 200, 400, 800 and 1200 carbide grit papers and 6, 3 and 1 µm diamond polishing pads until a smooth surface, free of any scratches was achieved. Variability in surface topography will affect the accuracy and precision of any analysis (Lifshin and Gauvin 2001).

Analysis

Exposed grains were examined and mapped using a Hitachi S-3500N scanning electron microscope (SEM) at the University of Bristol. Only MI that did not have a link to the outside of the crystal (via a melt channel or crack) or obvious post-entrapment crystallisation, were selected for analysis. Samples are usually coated with a conducting thin carbon coat prior to SEM analysis, however, the initial investigation of the MI was carried out using uncoated samples under variable pressure mode to minimise surface contamination of carbon, which could have compromised subsequent CO_2 analysis. MI were then analysed for volatile phases and trace elements using a SIMS at the University of Edinburgh, before being carbon coated for major element analysis using the Electron Microprobe at the University of Bristol.

Scanning Electron Microscopy

The SEM was used for identification, mapping and imaging of grain mounts and polished thin sections. Grain mounts were initially imaged uncoated to minimise potential carbon contamination. This required the SEM to be run under variable pressure mode at 50 MPa and 15 kV. A low beam current measured by proxy, (~15 nA) producing <2000 cps on the EDS detector, was used to prevent any risk of damage to glass.

Imaging was carried out in backscatter mode. For mapping, the working distance was set at the maximum of 50 mm, and for imaging individual crystals, at 21 mm. Thin sections and grain mounts (following SIMS analysis), were carbon coated. Analysis was then performed under high vacuum. For major element mapping of MI, the system was run at maximum beam current (producing 40,000 cps) which caused permanent damage to glass; this technique was limited to one MI.

Electron Microprobe Analysis

Sample preparation

Polished thin sections were made of all samples collected. EMPA concentrated on crystal-bearing lava flow samples as the majority of explosively erupted material (pumices) are aphyric or contain rare, small crystals. 68 thin sections were coated with 15-20 nm layer of carbon prior to initial analysis using a Hitachi S-3500N scanning electron microscope (SEM) at the University of Bristol. Suitable crystals for analysis were identified and imaged. EMPA was carried out following SIMS analysis of grain mounts; the gold coat (for SIMS analysis) was removed using a lint-free cloth with de-ionised water, and was replaced with a 15-20 nm thick carbon coat.

Analysis

EMPA was carried out on phases large enough to accommodate the EMP beam (>15 µm for glass and feldspars, >10 µm for mafics), which resulted in phases not being analysed in some samples. The aim was to analyse a minimum of 6 crystals of each mineral phase per thin section. Analysis of grain mounts to determine major elements in glasses (matrix and MI) and host crystals was carried out after SIMS analysis. For MI, the EMPA points were set around each SIMS point (up to 4, depending on the size of the MI). The major element compositions were determined using a CAMECA SX-100 electron microprobe with five wavelength dispersive spectrometers at the University of Bristol. A combination of crystals [(Thallium acid phthalate (TAP), Pentaerythritol (PET), Lithium fluoride (LIF), and a pseudo-crystal comprising alternating layers of silica and tungsten (PCO)] were utilised in each set up, with three set-ups in total: one for glass and feldspar, a second for mafic crystals, and a third for fluorine and chlorine in glasses.

A 15 kV accelerating voltage, 4 nA beam current and defocused 10 µm beam were used for matrix glasses, feldspars, fluorine and chlorine analyses; and 20 kV accelerating voltage, 10 nA beam current and a focused beam (1 µm) for mafic elements. Six primary calibration points per element were measured on peak for 10 seconds as per the setup in table 2.2. The instrument was calibrated using a suite of well characterised mineral standards at the start of each session (maximum period of each session was 48 hrs) to optimise operating conditions prior to analysis.

Prior to calibrating for fluorine, an FKα test was carried out on TAP and PCO to determine if a) fluorine was present in sufficient quantity to be detected, and b) to determine peak offsets and the most appropriate crystal. Fluorine detection can suffer from phosphorous peak interference on PCO and iron peak interference on TAP. MgF_2 was used for calibration with a 15 kV accelerating voltage, 10µm beam, a 2 second dwell time at each point in the scan during a total run time of 45 minutes. The results showed that insufficient counts would be yielded on TAP, thus resulting in an unrealistic counting time (fig. 2.1). Using PCO, sufficient yield would be gained on a count time of 100 cps, and Fe and F peaks could be sufficiently separated using background positions of -800 and +1000 from the peak position.

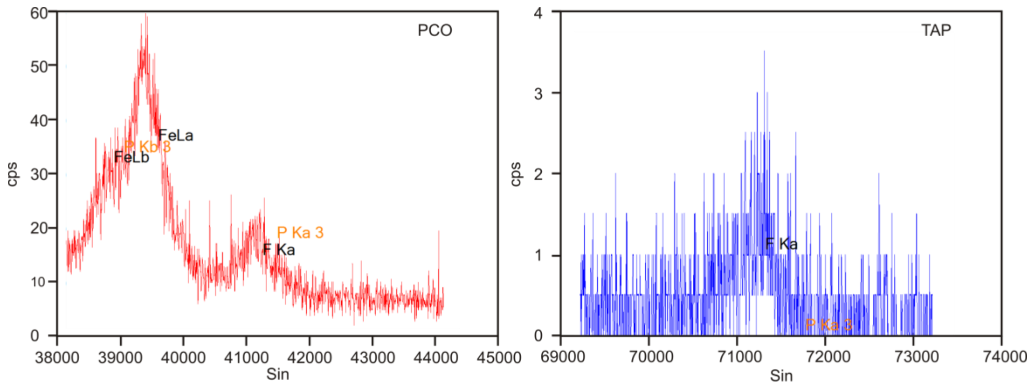

Figure 2.1. *Wavelength spectra from FKα test on Dabbahu glass. TAP yields insufficient counts to be practical. PCO shows interference of FeLα peak which can be eliminated using background positions (peak offset) of -800 and +1000 from the peak position.*

Secondary standards were run each day to monitor the instrument. Secondary standards used include KN18 (rhyolite glass, SW Naisasha Kenya (Nielsen and Sigurdsson 1981)), KK1 (Kakanui Kaersutite, New Zealand (Reay et al. 1989)), Amelia Albite (Rutherford no 2 mine, Amelia Court House, Amelia County, Virginia (Waldbaum 1966)), BCR2 (Basaltic glass, Columbia River (Wilson 1997)). A typical example of the precision and accuracy of the EMPA data is shown in table 2.2.

	BCR2	BCR2	BCR2	BCR2	BCR2	BCR2	mean	STDEV	2SD	% 2SD precision	% diff accuracy	Ref values	±
SiO_2	54.45	54.71	54.27	54.89	54.9	54.89	54.69	0.27	0.54	0.98	1.08	54.1	0.8
TiO_2	2.19	2.28	2.27	2.32	2.23	2.32	2.27	0.05	0.1	4.3	0.33	2.26	0.05
Al_2O_3	13.4	13.55	13.44	13.41	13.51	13.41	13.45	0.06	0.12	0.92	-0.35	13.5	0.2
FeO	12.61	12.65	12.55	12.53	12.67	12.53	12.59	0.06	0.13	1.01	1.47	12.42	0.2
MgO	3.57	3.49	3.56	3.5	3.66	3.5	3.55	0.07	0.13	3.72	-1.17	3.59	0.05
CaO	7.25	7.3	7.18	7.22	7.34	7.22	7.25	0.06	0.12	1.71	1.85	7.12	0.11
Na_2O	3.08	2.89	3.06	3.09	2.92	3.09	3.02	0.09	0.18	5.94	-4.4	3.16	0.11
K_2O	1.79	1.79	1.77	1.79	1.79	1.79	1.79	0.01	0.02	0.92	-0.1	1.79	0.05

Table 2.2. *Precision and accuracy of basaltic glass BCR2 reference standard for a typical run of secondary standards, where accuracy is a measure of how close a measurement may be to the reference value, and precision a measure of statistical repeatability. Major elements with values > 1 wt% are shown. Calculation of %2SD (precision) = (2SD / mean)*100; % difference (accuracy) = ((mean - reference value) / reference value)*100. Reference values from Wilson (1997).*

A fixed-order was used for all element set-ups. Na and Si were always analysed first on separate spectrometers to reduce the effects of alkali migration (Humphreys et al. 2006). Count times were optimised for each element and varied from 10 to 100 seconds per element to acquire statistically significant counts (refer to example set-ups in table 2.3). Data were corrected for x-ray absorption, secondary fluorescence, electron backscattering and the electron stopping power of the sample using the reiterative 'PAP' (ϕ-ρ-z) correction procedure (Pouchou and Pichoir 1984; Pouchou and Pichoir 1991). Oxygen was calculated by stoichiometry, and weight percent oxide totals are reported.

Kα X-ray intensity maps for phosphorous, Ca and Fe were obtained in two stages. The first mapped P and Fe with a 256 x 256 pixel image with a dwell time of 100 ms per pixel. A second run at higher resolution used dwell times of 200 ms per pixel and a 512 x 512 pixel image, imaging P and Ca. For both runs, a beam current of 400 nA, an accelerating voltage of 20 kV and beam diameter of 1 µm was used. Phosphorous was mapped on four of the five spectrometers in both cases, and the end images were combined.

Data processing

The detection limit data are reported by element in ppm. These were converted to oxide wt% and measured values which fell below this minimum limit were marked as below detection (b.d.). The chemical formula was calculated for each mineral using the methods of Deer, Howie and Zussman (1992). Clinopyroxene were classified according to Morimoto (1989), amphibole according to Leake (1997), Fe-Ti oxides using ILMAT (Lepage 2003). The amount of ferrous and ferric iron was calculated according to Schumacher (1991) for all cpx; Fe-Ti oxides were calculated using the method of Carmichael (Carmichael 1967). The chemical formula calculations for each mineral were evaluated by comparing the cations and cations per site to the ideal stoichiometry. For example, the ideal stoichiometry of feldspar is Si+Al+Ti+Fe = 4 cations, Ca+Na+K = 1 cation. If the calculated value was outside of the ideal formula value by ±0.05, the data was rejected. Uncertainty is calculated from the standard deviation as given by the EMP software, based upon count statistics. The count statistics of the standards is comparable to those of the unknowns.

Table 2.3 (overleaf). *Example set ups for rhyolite glass and MI, fluorine and chlorine in a selection of MI and glasses, and Erta'Ale mafic minerals. BG = background count time, TAP - Thallium acid phthalate, PET - Pentaerythritol, LIF - Lithium fluoride, and PCO - a pseudo-crystal comprising alternating layers of silica and tungsten, 'L' before the crystal e.g. LPET, denotes a large crystal.*

Rhyolite glasses and feldspars

Oxide	Internal calibration standard	Counting time		Background positions	Crystal	Spectrometer
		BG (±)	Peak			
SiO_2	Amelia Albite	10	20	-700 +800	TAP	4
TiO_2	Ilmenite	10	20	±800	LLIF	5
Al_2O_3	Eifel Sanidine	10	20	±500	TAP	4
FeOt	Ilmenite	15	30	±1000	LLIF	5
MnO	Mn metal	15	30	±800	LLIF	5
MgO	St John's Olivine	30	60	±1000	TAP	2
CaO	Wollastonite	10	20	-800 +700	LPET	3
Na_2O	Amelia Albite	5	10	±800	TAP	2
K_2O	Eifel Sanidine	5	10	-800 +700	LPET	1
P_2O_5	Durango Apatite	15	30	±800	LPET	1
SO_3	$BaSO_4$	15	30	±500	LPET	1
Zr	KIM5 zircon	15	30	±800	LPET	3
Cl	KCl_CL028	15	30	±500	LPET	3

Fluorine in MI and glasses

Oxide	Internal calibration standard	Counting time		Background positions	Crystal	Spectrometer
		BG (±)	Peak			
SiO_2	Amelia Albite	5	10	-700 +800	TAP	4
TiO_2	Ilmenite	15	30	±800	LLIF	5
Al_2O_3	Eifel Sanidine	5	10	±500	TAP	4
FeOt	Ilmenite	15	30	±1000	LLIF	5
MnO	Mn metal	15	30	±800	LLIF	5
MgO	St John's Olivine	30	60	±1000	TAP	4
CaO	Wollastonite	10	20	-800 +700	LPET	3
Na_2O	Amelia Albite	5	10	±800	TAP	4
K_2O	Eifel Sanidine	5	10	-800 +700	LPET	1
P_2O_5	Durango Apatite	20	40	±800	LPET	1
SO_3	$BaSO_4$	20	40	±500	LPET	1
Zr	KIM5 zircon	20	40	±800	LPET	3
Cl	KCl_CL028	20	40	±500	LPET	3
F	MgF_2	50	100	-800 +1000	PCO	2

Mafic Minerals

Oxide	Internal calibration standard	Counting time		Background positions	Crystal	Spectrometer
		BG (±)	Peak			
SiO_2	Amelia Albite	10	20	-700 +800	TAP	4
TiO_2	Ilmenite	20	40	±800	LLIF	3
Al_2O_3	Eifel Sanidine	15	30	±800	TAP	4
FeOt	Ilmenite	15	30	±1000	LLIF	5
MnO	Mn metal	20	40	±800	LLIF	5
MgO	St John’s Olivine	15	30	-800 +1000	TAP	2
CaO	Wollastonite	15	30	-800 +700	LPET	1
Na_2O	Amelia Albite	5	10	±800	TAP	2
K_2O	Eifel Sanidine	15	30	-800 +700	LPET	1
Ni	Ni_Ni009	25	50	±1000	LLIF	5
Cr_2O_3	Cr_2O_3_ Cr016	25	50	±800	LPET	3
P_2O_5	Durango Apatite	30	60	±800	LPET	1

Secondary Ion Mass Spectrometry

Sample preparation

Grain mounts were prepared and mapped as described above. The selected mounts were polished with 0.3 µm alumina for 20 seconds, cleaned in the hypersonic bath, and a 20 nm gold coat applied. Samples were then loaded into the airlock 24 hrs prior to analysis to allow the vacuum to pump down to ~10^{-7} Torr, before being transferred into the main chamber.

Analysis

Dabbahu samples

71 melt inclusions (59 in feldspar, 9 in cpx, 3 in olivine), 12 obsidian matrix glasses and 8 pumice matrix glasses from Dabbahu were analysed by secondary ion mass spectrometry (SIMS) for dissolved volatiles H_2O and CO_2, and selected trace elements, using a CAMECA ims-4f ion microprobe at the NERC facility, University of Edinburgh. The analyses were performed at 5 nA, 10 kV (nominal) O- beam with a 15 µm spot, 4.5 kV with a 75 eV offset to minimise molecular ion transmission. Secondary ions were collected in two runs on exactly the same spot: the ‘heavy elements’ consisting of ^{25}Mg/2+, ^{26}Mg+, ^{30}Si+ , ^{42}Ca+, ^{44}Ca+, ^{45}Sc+, ^{47}Ti+, ^{85}Rb+, ^{88}Sr+, ^{89}Y+, ^{90}Zr+, ^{93}Nb+, ^{138}Ba+, ^{139}La+, ^{14oC}e+, ^{141}Pr+, ^{143}Nd+,

^{149}Sm+, ^{151}Eu+, ^{154}Gd+, ^{156}Gd+, ^{157}Gd+, ^{159}Tb+, ^{161}Dy+, ^{165}Ho+, ^{171}Yb+, ^{178}Hf+, ^{181}Ta+, ^{232}Th+, ^{238}U+, comprised run 1, and were analysed for 8 cycles; and the light elements consisting of ^{1}H+, ^{7}Li+, ^{9}Be+, ^{11}B+, ^{12}C+, ^{19}F+ , ^{30}Si+, ^{35}Cl+ comprised run 2, and were analysed for 5 cycles. Samples were pre-sputtered using a 50 µm beam for 2 minutes to remove any surface contamination. Ion yields were calibrated using NIST 610 glass. Additional standards of known element content, including NIST-28, NIST-610, RB-480, SISS-51, together with a rhyolite glass from Dabbahu as a monitor of background consistency, were analysed at the start and end of each day. A working curve was constructed of the known H_2O and CO_2 contents versus $^{1}H/^{30}Si$ and $^{12}C/^{30}Si$ respectively each morning and evening to check the set up (fig. 2.2)

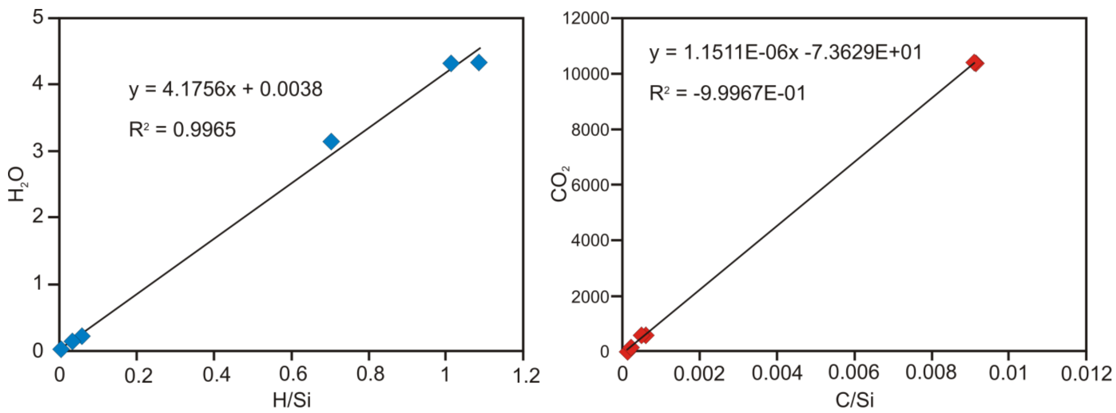

***Figure 2.2** Example working curves from the morning of July 23rd 2008 for H_2O and CO_2 (Dabbahu calibration).*

Erta Ale samples

A one day access grant was secured to analyse volatiles (H_2O and CO_2) in basaltic MI hosted in euhedral olivines from Erta Ale lavas. As these glasses are Mg rich, the set up was slightly different from that used to analyse the Dabbahu samples. Both H_2O and CO_2 analyses were determined on exactly the same spot in each MI.

Eleven spot analyses from five separate melt inclusions were made, analysing for CO_2, H_2O and a number of trace elements on the secondary ion mass spectrometer (SIMS) at the University of Edinburgh with a 10kV (nominal) O- primary beam and 4500 eV positive secondary ions with an offset applied to reduce transmission of molecular ions. To enhance relief, grain mounts were polished with 0.3 µm alumina for 30 seconds prior to gold coating. CO_2 ($^{12}C^{+}$) was determined first at moderate mass resolution (~1600) to separate

$^{24}Mg^{2+}$ from ^{12}C. A 5nA primary beam, with a 15 µm focused spot was used, with 50 eV offset. 25 and 250 µm lenses were activated to give a 60 µm image field with field aperture no.2 providing a ~15-20 µm restricted central area for analysis. Entrance slits were set at ~110 (entrance), and 112 (exit). A 2 minute pre-splutter with a 15 µm raster removed surface contamination prior to using a stable spot beam for analysis. For subsequent H_2O and trace element determinations a 5 nA primary beam with 75 eV offset and 30 second pre-splutter, was focused in the same location as the CO_2 analysis. Secondary ions of $^{1}H^{+}$, $^{7}Li^{+}$, $^{9}Be^{+}$, $^{11}B^{+}$, $^{12}C^{+}$, $^{25}Mg^{2+}$, $^{26}Mg^{+}$, $^{30}Si^{+}$, $^{42}Ca^{+}$, $^{44}Ca^{+}$, $^{45}Sc^{+}$, $^{47}Ti^{+}$, $^{88}Sr^{+}$, $^{89}Y^{+}$, $^{90}Zr^{+}$, $^{93}Nb^{+}$, $^{138}Ba^{+}$, $^{139}La^{+}$, $^{140}Ce^{+}$, $^{141}Pr^{+}$, $^{143}Nd^{+}$, $^{149}Sm^{+}$, $^{151}Eu^{+}$, $^{154}Gd^{+}$, $^{156}Gd^{+}$, $^{157}Gd^{+}$, $^{159}Tb^{+}$, $^{161}Dy^{+}$, $^{165}Ho^{+}$, $^{166}Er^{+}$, $^{169}Tm^{+}$, $^{171}Yb^{+}$, $^{178}Hf^{+}$, $^{181}Ta^{+}$, $^{232}Th^{+}$, $^{238}U^{+}$ were collected at low mass resolution, with a 25 micron image field and field aperture no.2 providing ~ 10 micron area of analysis. Calibration and secondary standards included a range of glasses of pre-determined H_2O and CO_2 values, the basaltic glasses (1, 2 and 6) of Shishkina et al., (2010), BCR2g, TPA, TPF, SRM610, and CFD. A working curve was determined for known H_2O and CO_2 contents versus $^{1}H/^{30}Si$ and $^{12}C/^{30}Si$ for each run, prior to determining the volatile values of the unknowns, to monitor any drift. An olivine from EA003 was used as a monitor of background consistency.

Data processing

Raw data was initially processed through the local SIMS conversion programme, JCION6. For the Dabbahu samples, the last five cycles of the heavy elements (run 1) were accepted, together with all cycles of the light elements (run 2). For Erta Ale twenty cycles of the analysis were performed for CO_2, with the first 10 being discarded ensuring only the stabilised yields in the last 10 cycles were used whereas for H_2O all cycles were accepted.

Processing of the data involved calculating the actual H_2O or CO_2 by calculating the average background from standards data for the week and removing this from the H/Si and C/Si values, and propagating the associated errors. CO_2 has an additional step of peak-stripping. Taking CO_2 as the example, the data processing was carried out as follows: CO_2 in the rhyolites was initially processed by correcting ^{12}C counts for the $^{24}Mg^{2+}$ isobaric interference by peak-stripping using $^{25}Mg^{2+}$ at mass 12.5 (Blundy and Cashman 2008). By using the ratio of ^{25}Mg to ^{24}Mg, the amount of ^{24}Mg to be subtracted from the ^{12}C count can be determined. The value for the ratio is 7.900 but it has been determined from over 20 years of analysis that at Edinburgh, due to instrumental reasons, the ratio to be applied is 8.223. Therefore to obtain a C/Si ratio corrected for ^{24}Mg, the following equation (a) was applied:

a)

$$\frac{C}{Si} = \left(\frac{^{12}C}{^{30}Si}\right) - 8.223 * \left(\frac{^{25}Mg}{^{30}Si}\right)$$

The C/Si value was calculated for both the standards and the unknown samples. To obtain the value of CO_2 the background counts need to be removed from the C/Si value. The background count was calculated from the average of all NIST28 values obtained from the week; NIST28 contains no CO_2, and therefore is an ideal measure of any background CO_2). The final CO_2 value for the unknowns was calculated by equation (b). The value for the slope of the working curve (*M*), was calculated by regression of the standards data (the *y* range being CO_2 and *x* range being C/SI) in EXCEL©.

b)

$$CO_2 = M\left[\left(\frac{^{12}C}{^{30}Si}\right)_{sample} - \left(\frac{^{12}C}{^{30}Si}\right)_{bkg}\right]$$

The error for each value was calculated by propagating through using equation (c), where σ is the error e.g. σM^2 is the error on the slope (*M*):

c)

$$= \sqrt{\left[\left(\frac{C}{Si}\right)_{sam} - \left(\frac{C}{Si}\right)_{bkg}\right]^2 \sigma M^2 + M^2\left[\sigma\left(\frac{C}{Si_{sam}}\right)^2 + M^2\,\sigma\left(\frac{C}{Si_{bkg}}\right)^2\right]}$$

Uncertainties in element abundance, determined from normal error propagation are typically <±0.03 wt% for H_2O, and <±40 ppm for CO_2 for Dabbahu samples, and <±0.003 wt% for H_2O and <±5 ppm for CO_2, for the Erta Ale samples.

Trace element concentrations were normalised to EMPA SiO_2 content of the same melt inclusion. Titanium values from SIMS were compared to the Ti values obtained through EMPA, and analyses outside of the 95% confidence interval were rejected.

Fourier Transform Infrared Spectroscopy

Fourier Transform Infrared Sepctroscopy (FTIR) was carried out by Richard Brooker at the University of Bristol. Mid-IR spectra for H_2O in three matrix glasses for Dabbahu samples, and in matrix glasses and melt inclusions for Erta Ale samples were obtained using a Nicolet Nexus 670 FTIR spectrometer with an IR PLAN microscope attachment, Glowbar source, KBr beamsplitter and MCT detector (512 scans at 8cm-1 resolution). Double polished plates of around 80-380 µm thickness for prepared for Dabbahu samples and samples were sectioned perpendicular to any flow banding to examine any variation associated with this feature. Erta Ale samples were prepared at ~50 µm thickness which allowed an 80 µm beam to pass through the melt inclusions (or the matrix glass) uninterrupted. Spectra were compared to a volatile-free basalt to estimate peak heights. All plates were measured with a Mitutoyo Digital Micrometer to ± 1µm. Absorption peak heights at 3550 cm-1 were converted to concentrations using the beer Lambert equation and extinction coefficients of 56 L/mol.cm (Newman et al., 1986) for Dabbahu samples with an assumed density of 2350 g/l (corrected to low pressure from Tamic et al. 2001). for the Erta Ale samples, 63 L/mol.cm was used for water at 3550 cm-1 and 375 L/mol.cm for one of the carbonate doublet peaks at 1375 cm-1 (from Dixon et al. (1988) and Fine & Stolper (1986) respectively). For the matrix glass, the CO_2 peak is not visible suggesting it is below the detection limit of about 50 ppm for this sample thickness.

^{40}Ar-^{39}Ar Geochronology

Sample preparation

^{40}Ar-^{39}Ar ages were only obtained for samples from Dabbahu. Samples were collected during the field campaign of 2007. Samples were reviewed for suitability to application of the ^{40}Ar/^{39}Ar dating technique based on minimum alteration, vesicularity and amounts of interstitial glass (<5%). Following analysis of the thin sections, many Dabbahu samples had to be rejected as unsuitable for this technique as they contained too high a percentage of glass, or fines. 10 suitable and representative samples were chosen from across Dabbahu (Chapter 3, fig. 3.5). Three of these samples were basaltic trachy andesites (BTA), two were peralkaline comenditic rhyolites and four were pantelleritic rhyolites (refer to Chapter 3 p40 for comendite and pantellerite definition). Groundmass separate was used in the BTA samples, and anorthoclase phenocryst separates were prepared for the comendites and pantellerites. Obsidian samples were chosen according to the size (ideally >3 mm), and freshness of the anorthoclase phenocrysts. Phenocrysts which were inclusion-fee were preferentially chosen.

Contamination is a critical factor in this process, and therefore great care was taken with regards to the cleanliness of all equipment and work surfaces throughout the process. Preparation was carried out both at the University of Bristol and the USGS facilities at Menlo Park. Samples were manually crushed to fine gravel using a hammer and steel plate. Samples were dry sieved throughout using a stack of sieves to ensure the target size fraction was retrieved. All equipment was thoroughly cleaned between samples to reduce risk of contamination. The target fraction was then repeatedly cleaned in an ultrasonic bath (water, solvent and finally de-ionised water) which commonly improves radiogenic yield and minimises argon recoil by removing glass and any clay fraction which trap atmospheric argon, and cryptocrystalline groundmass. The samples were then dried at ~70°C and re-sieved to remove any remaining fines released by the ultrasonic processing. Fine feldspar can cause problems during the irradiation as reactor-induced ^{39}Ar moves ~0.1 µm (Villa, 1997), and if it is liberated from its crystal or moves to a more retentive phase, the radiogenic ^{40}Ar is no longer correlated with the ^{39}Ar. A magnetic separator was used to concentrate the 50-90% most magnetic portion. Finally around 150-200 mg was prepared for irradiation by hand-picking contaminants out of the split. Glass was removed from the anorthoclase separates using HF acid at Menlo Park. Irradiation of the samples was performed at the USGS TRIGA reactor in Denver, Colorado (Dalrymple et al. 1989).

The analysis and data processing was carried out using the method of Calvert and Lanphere (2006) at the facilities of USGS by Andy Calvert. Calibration was carried out using TCR-2 (Taylor Creek Rhyolite - sanidine 85G003 USGS reference standard, 27.92 Ma (Duffield and Dalrymple 1990)) reference standard (co-irradiated for neutron fluence). Data was assessed in light of field relations, and one age (sample 10) was rejected as unfeasible. The sample contains phenocrysts which are xenocrystic and therefore give an age older than the emplacement of the lava flow. Figure 2.3 shows an example of the results for sample 054 which has an indicated mean weighted plateau age of 30.1 ± 0.4 ka.

Point counting

Sixty-eight samples from Dabbahu and three from Erta Ale were point counted using a Pelcon automatic point counter to ascertain what percentage of the deposits were phenocrysts. On average 1500 points were counted for each sample using polished thin sections. These estimations are within ± 2.5% (2σ estimated) using the method of Van der Plas and Tobi (1965). Similar limits are found using the 95% 2-sided confidence level of Howarth (1998; average upper and lower limits <1.5% for Dabbahu, and <3.5% for Erta Ale, see appendices A2.10 and A3.4). However, due to the paucity of crystals the uncertainty in estimations may be larger than these estimates.

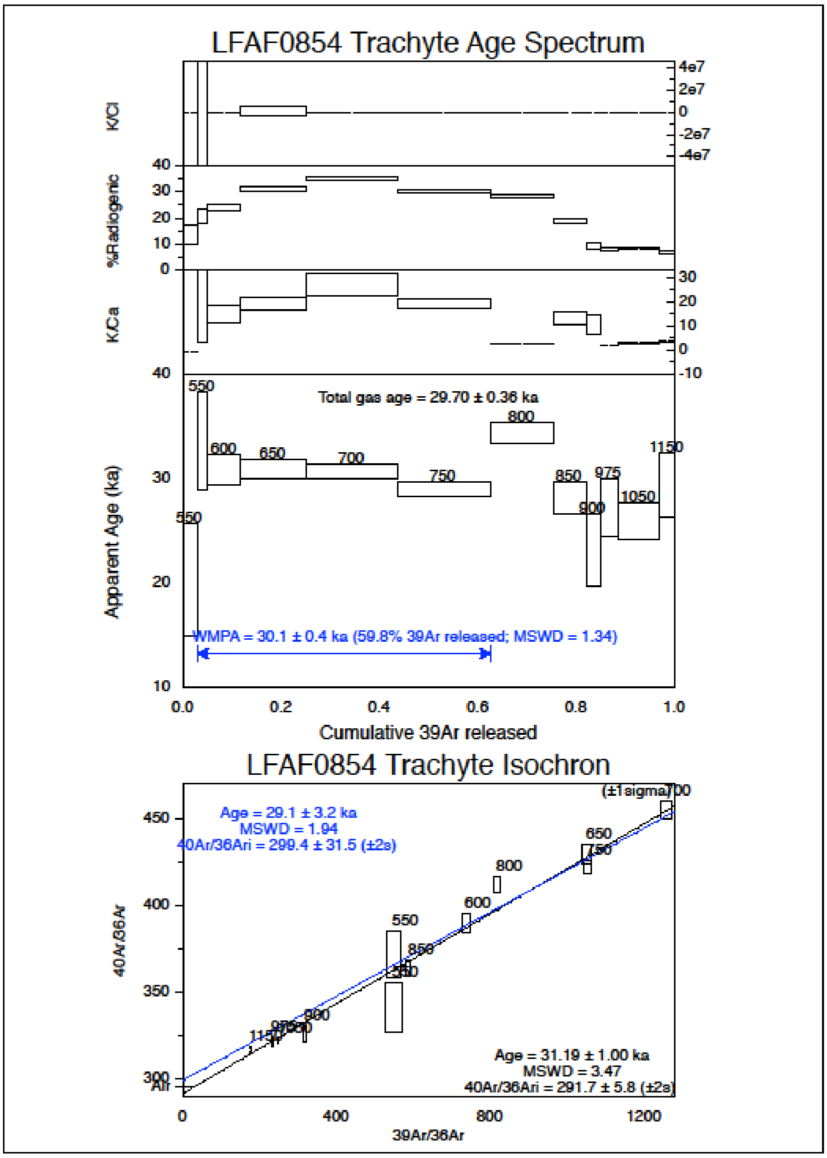

Figure 2.3 showing the ^{40}*Ar-*^{39}*Ar data for sample 054. MSWD = Mean Square Weighted Deviation, WMPA = Weighted Mean Plateau Age. The isochron shows two ages. The black date and black isochron line include all steps, the blue date and line include only a subset as shown in the age spectrum. In this example the blue Weighted Mean Plateau Age is the preferred age as this reflects a well-defined plateau.*

The magmatic evolution of Dabbahu

Chapter

3

Author Contribution

This chapter forms the basis for a manuscript in review with the Geological Society of America Bulletin:

Field, L., Blundy, J., Calvert, A., and Yirgu, G., 2011 “The magmatic history of Dabbahu”. GSA. *In review*.

Enlightening discussion with J. Blundy provided direction and greatly improved the manuscript. L. Field was the lead author and contributed all work unless otherwise stated, including sample preparation. Determination of $^{40}Ar/^{39}Ar$ geochronology was carried out by A. Calvert, who also provided a review of the manuscript. G. Yirgu assisted with logistics and in the field in Ethiopia.

Abstract

Dabbahu is a composite volcano at the north end of the active Manda-Hararo segment of the Afar Rift in northern Ethiopia. We present 93 new whole rock major and trace element data, mineral analysis from 65 samples and 9 new $^{40}Ar/^{39}Ar$ dates for rocks ranging in composition from mildly alkaline basalt through trachyandesite to peralkaline rhyolite (comendite and pantellerite) erupted from Dabbahu. These data, supplemented by a new geological map are used to provide insights to the evolution of the volcano. We show that Dabbahu has been active for over 60,000 yrs, but a hiatus occurred between the eruption of comendite (29 ka) and pantellerite (~8 ka) lavas. Continuous variations in whole rock chemistry, mineral compositions and calculated eruption temperatures support earlier findings (Barberi et al. 1974) that the magmas were derived through protracted (~90%) fractional crystallisation from a basaltic parent. Geochemistry and modelling indicates recently erupted basalts from the Manda-Hararo rift constitute plausible parent compositions. Field evidence indicates that magmas were not erupted in fractionation sequence and some mixing occurred between more and less evolved compositions. We propose that the site of differentiation lies at depth within the crust, rather than in a shallow sub-volcanic magma chamber. Shallow magma reservoirs are likely to have provided only a means of temporary pre-eruptive magma storage and are the locus of mixing events. Input of new magma batches into these reservoirs may be a key eruption trigger at Dabbahu.

Introduction

Since 2005, the Dabbahu Magmatic Segment (DMS) which forms the northern part of the Manda Hararo rift segment has been subject to considerable scientific scrutiny using a combination of ground-based and satellite geodesy, potential field measurements, seismology, and petrology. Over this time period a series of rifting events has led to the emplacement of 13 basaltic dykes with a total width of 5-8 m (Hamling et al. 2009; Hamling et al. 2010). Three eruptions have occurred in this region since 2005: a rhyolitic ash eruption following the 2005 dyking event at Da'Ure on the northern flanks of Dabbahu (Wright et al. 2006), and two basaltic fissure eruptions in the DMS approximately 30 km south of Dabbahu (Ferguson et al. 2010).

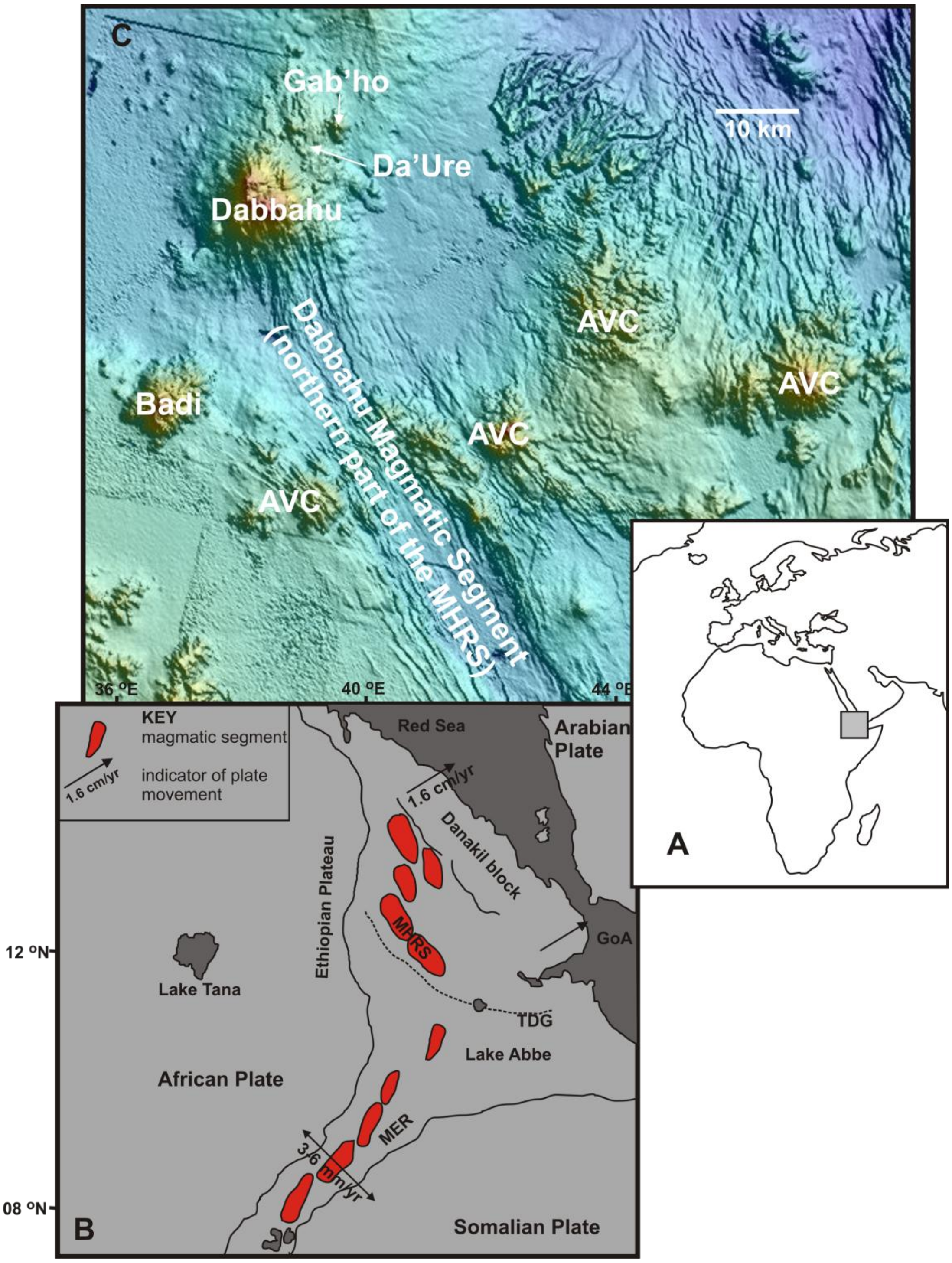

Figure 3.1. *A) Location of study area in the Afar region of Ethiopia, B) sketchmap showing the regional setting of Afar after Rowland et al 2007. Plate movement rates from Chu and Gordon 1998, 1999. MER – Main Ethiopian Rift, MHRS – Manda Hararo Rift Segment, TDG – Tendaho-Goba'ad Discontinuity, GoA - Gulf of Aden, C) detail of the Dabbahu Magmatic Segment (northern end of the Manda Hararo Rift Segment), AVC – Ado Ale Volcanic Complex.*

The Afar rift is punctuated by a series of composite volcanoes whose eruption products range from basalt to rhyolite via a range of intermediate magma types. Although the exact relationship of these volcanic centres to the main rift-related basaltic magmatism remains unclear, there is general consensus that intra-crustal differentiation of rift basalts played a key role in generating the evolved magmas. Here we focus on one of the composite volcanoes, Dabbahu, associated with the Manda-Hararo Rift Segment (MHRS), using a combination of geochemistry, radiometric dating and petrology to constrain the processes and timing of differentiation in order to place the magmatism in the wider context of rift-related activity.

Geological Setting

Dabbahu is a quaternary volcano situated at the northern end of the MHRS (12^{o} 39’39.24” N, 40^{o} 28’45.10” E), (fig. 3.1c). The MHRS is characterised by a 35 km wide central depression punctuated by silicic edifices (Lahitte et al. 2003). The northern part of the MHRS is known as the DMS which is an area ~ 60 km long and ~15 km wide. This trends SSE-NNW from a dissected central silicic complex known as the Ado’Ale Volcanic Complex (AVC) (fig. 3.1c) to Dabbahu (Rowland et al. 2007). Dabbahu was first sketch-mapped by Brinckmann and Kuersten (1970) from aerial photographs, and subsequently by Barberi et al.,(1974). Variously known also as Boina, Boyna or Moyna, Barberi et al. (1974; 1974) describe Dabbahu as a ~1400 m high volcanic edifice, rising from a base of fissural basalts. It is cited as an example of a full fractional crystallisation suite from mildly alkaline basalts to mildly peralkaline rhyolites, erupted from a central volcano above a shallow magma chamber (Barberi et al. 1974; Barberi et al. 1974; Bizouard et al. 1980). Since the pioneering work of the CNR-CNRS campaigns (Barberi et al. 1974; Barberi et al. 1974; Bizouard et al. 1980), no further analysis has been carried out, due in no small part to the remoteness and inaccessibility of the area. Interest in this area was invigorated in 2005 when a small rhyolitic ash eruption and extrusion of a small pumice dome from the Da’Ure vent (fig. 3.2) on the northern flanks of Dabbahu (12^{o} 39’00.58” N, 40^{o} 31’10.43” E) coincided with the largest dyke opening event ever measured (Ayele et al. 2007). Modelled as a basaltic dyke injection ~10 km deep, it was shown that up to 8 m of opening along a distance of ~60 km occurred. This event probably triggered the Da’Ure eruption by interaction of basaltic magma with a shallow silicic reservoir (Wright et al. 2006).

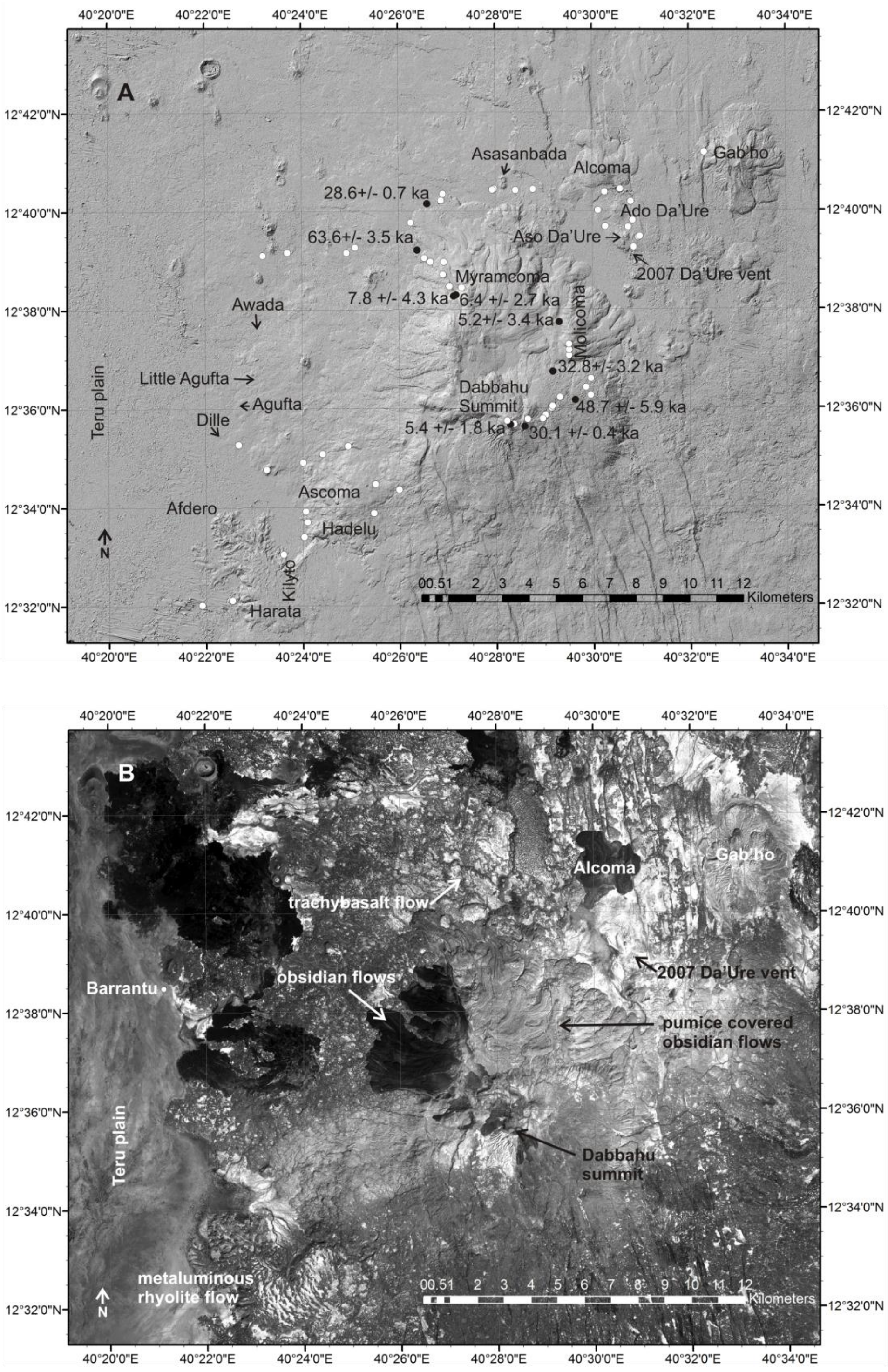

Figure 3.2. *A) Sampling localities. White circles indicate locations of samples at Dabbahu, black circles indicate samples dated by* $^{40}Ar/^{39}Ar$*. Some of the local place-names are also indicated. Hillshade image based on SPOT DEM courtesy of Sophie Hautot. B) SPOT image showing key textures such as the distinctive obsidian flows on the northern flanks of Dabbahu, and the prominent metaluminous rhyolite flow to the SW.*

Sampling and analytical techniques

Fieldwork and sampling were carried out during field campaigns in 2008 and 2009. Dabbahu is remote and difficult to access, so the emphasis was on identifying and sampling as many lava flows as possible. In total 95 samples were collected and analysed (fig. 3.2a, table 3.1). The fieldwork was supported by the Natural Environmental Research Council Airborne Research and Survey Facility (NERC ARSF) aerial photographs obtained using a Leica RCD105 39 megapixel digital camera as part of a LiDAR acquisition. These data were used to obtain information on inaccessible areas, together with digital elevation model analysis in ArcGIS®.

Whole rock major and trace elements were analysed by X-ray fluorescence (XRF) using a PANalytical Axios-Advanced XRF spectrometer at Leicester University for 93 samples, details are given in Chapter 2.

Analysed rocks included lava flows, obsidians and pumices. As the pumices are mostly aphyric, or contain rare, very small crystals, microanalysis was concentrated on crystal-bearing lava flow samples. Techniques applied to these samples include XRF, SEM, EMPA, SIMS, Ar-Ar geochronology and point counting. Techniques are detailed in Chapter 2.

Compositional Overview

In terms of the total alkalis – silica diagram (Le Maitre 2002), Dabbahu has a complete sequence of rock types from basalt through to rhyolite (fig. 3.3). Silica content (anhydrous basis) ranges between 45.6 wt% SiO_2 (sample 101a, a basaltic scoria cone) and 74.0 wt% SiO_2 (sample 071, a comenditic obsidian).

The basalts are transitional in character, closely following the alkaline – subalkaline divide of Irvine and Baragar (1971). They are more alkaline than the light rare earth element (LREE)-depleted samples of the MHRS (Barrat et al. 2003). There are apparent slight compositional gaps between 56 and 59 wt% SiO_2, and between 64 and 69 wt% SiO_2. The peralkalinity of the rhyolites and trachytes were calculated (molar $(Na_2O+K_2O)/Al_2O_3$ >1, (NK/A)) (e.g. Macdonald and Bailey 1973; Macdonald 1975), and the rhyolites further

Table 3.1 *overleaf. Locations of analysed samples with rock type.*

Location of samples

Name	Lat	Long	Rock type	sub-division	Type
LF AF 08 03	12° 39 04.8' N	40° 25 29.2' E	rhyolite	pantellerite	pumice
LF AF 08 05	12° 38 39.1' N	40° 26 24.4' E	BTA[1]	shoshonite	lava flow
LF AF 08 06	12° 38 34.6' N	40° 26 30.2' E	BTA	mugearite	lava flow
LF AF 08 07A	12° 38 29.2' N	40° 26 34.4' E	rhyolite	pantellerite	lava flow
LF AF 08 07B	12° 38 29.2' N	40° 26 34.4' E	rhyolite	pantellerite	lava flow
LF AF 08 07C	12° 38 29.2' N	40° 26 34.4' E	rhyolite	pantellerite	lava flow
LF AF 08 07D	12° 38 29.2' N	40° 26 34.4' E	rhyolite	pantellerite	lava flow
LF AF 08 08	12° 38 25.2' N	40° 26 36.0' E	rhyolite	pantellerite	lava flow
LF AF 08 09	12° 38 24.8' N	40° 26 36.4' E	rhyolite	pantellerite	lava flow
LF AF 08 10	12° 38 26.6' N	40° 26 41.1' E	rhyolite	pantellerite	lava flow
LF AF 08 11	12° 38 56.6' N	40° 26 43.5' E	rhyolite	comendite	lava flow
LF AF 08 12	12° 38 54.7' N	40° 26 55.3' E	rhyolite	pantellerite	pumice
LF AF 08 13	12° 38 54.7' N	40° 26 55.3' E	rhyolite	pantellerite	lava flow
LF AF 08 13B	12° 38 54.7' N	40° 26 55.3' E	rhyolite	pantellerite	lava flow
LF AF 08 14	12° 38 52.3' N	40° 27 04.1' E	rhyolite	pantellerite	lava flow
LF AF 08 15	12° 38 52.3' N	40° 27 04.1' E	rhyolite	pantellerite	lava flow
LF AF 08 16	12° 38 39.3' N	40° 27 19.7' E	rhyolite	pantellerite	lava flow
LF AF 08 17	12° 38 28.3' N	40° 27 26.1' E	rhyolite	pantellerite	lava flow
LF AF 08 18	12° 38 20.9' N	40° 27 35.8' E	rhyolite	pantellerite	pumice
LF AF 08 19	12° 38 20.9' N	40° 27 35.8' E	rhyolite	pantellerite	lava flow
LF AF 08 20A	12° 38 23.03' N	40° 27 38.15' E	rhyolite	pantellerite	pumice
LF AF 08 20B	12° 38 23.03' N	40° 27 38.15' E	rhyolite	pantellerite	pumice
LF AF 08 20C	12° 38 23.03' N	40° 27 38.15' E	rhyolite	pantellerite	pumice
LF AF 08 20D	12° 38 23.03' N	40° 27 38.15' E	rhyolite	pantellerite	pumice
LF AF 08 21	12° 38 23.03' N	40° 27 38.15' E	rhyolite	pantellerite	lava flow
LF AF 08 22	12° 38 54.3' N	40° 27 19.3' E	rhyolite	pantellerite	injurated ash
LF AF 08 23	12° 39 43.5' N	40° 26 30.2' E	rhyolite	pantellerite	lava flow
LF AF 08 24	12° 40 04.8' N	40° 26 50.6' E	rhyolite	pantellerite	pumice
LF AF 08 25	12° 40 04.8' N	40° 26 50.6' E	BTA	mugearite	lava flow
LF AF 08 26	12° 40 11.8' N	40° 27 04.9' E	rhyolite	metaluminous	lava flow
LF AF 08 27	12° 40 16.1' N	40° 27 10.9' E	rhyolite	pantellerite	pumice
LF AF 08 28	12° 40 16.0' N	40° 28 16.4' E	TB[2]	hawaiite	lava flow
LF AF 08 29	12° 40 16.0' N	40° 28 16.4' E	rhyolite	comendite	lava flow
LF AF 08 30	12° 40 13.3' N	40° 28 44.1' E	TB	hawaiite	lava flow
LF AF 08 31	12° 40 17.8' N	40° 28 17.7' E	BTA	mugearite	scoria
LF AF 08 32A	12° 40 16.3' N	40° 29 14.1' E	trachyte		pumice
LF AF 08 32B	12° 40 16.3' N	40° 29 14.1' E	rhyolite	comendite	pumice
LF AF 08 33A	12° 39 47.1' N	40° 30 24.4' E	rhyolite	comendite	lava flow
LF AF 08 33B	12° 39 47.1' N	40° 30 24.4' E	rhyolite	comendite	lava flow
LF AF 08 34	12° 39 30.3' N	40° 30 36.2' E	rhyolite	comendite	lava flow
LF AF 08 36	12° 38 58.5' N	40° 31 10.0' E	rhyolite	comendite	pumice
LF AF 08 37	12° 39 21.7' N	40° 31 08.1' E	rhyolite	comendite	lava flow
LF AF 08 38	12° 39 21.7' N	40° 31 08.1' E	rhyolite	comendite	pumice
LF AF 08 39A	12° 39 39.3' N	40° 31 02.0' E	rhyolite	comendite	pumice
LF AF 08 39B	12° 39 39.3' N	40° 31 02.0' E	rhyolite	comendite	pumice
LF AF 08 39C	12° 39 39.3' N	40° 31 02.0' E	rhyolite	comendite	pumice
LF AF 08 39G	12° 39 39.3' N	40° 31 02.0' E	rhyolite	comendite	pumice
LF AF 08 40	12° 39 38.0' N	40° 31 01.2' E	Gabbro		lava flow
LF AF 08 41	12° 40 06.2' N	40° 31 01.9' E	rhyolite	comendite	lava flow
LF AF 08 42	12° 40 16.6' N	40° 30 55.1' E	rhyolite	comendite	lava flow
LF AF 08 43	12° 40 16.8' N	40° 30 38.5' E	rhyolite	comendite	lava flow
LF AF 08 44	12° 39 00.3' N	40° 25 22.3' E	Basalt	transitional	lava flow
LF AF 08 45	12° 38 52.2' N	40° 23 57.9' E	Basalt	transitional	lava flow
LF AF 08 46	12° 38 48.5' N	40° 23 22.5' E	BTA	mugearite	lava flow
LF AF 08 47A	12° 36 09.8' N	40° 29 53.8' E	BTA	shoshonite	lava flow
LF AF 08 47B	12° 36 09.8' N	40° 29 53.8' E	BTA	mugearite	lava flow
LF AF 08 48	12° 35 57.6' N	40° 29 34.4' E	trachyte		lava flow
LF AF 08 49	12° 35 59.2' N	40° 29 35.3' E	rhyolite	comendite	lava flow

Location of samples

Name	Lat	Long	Rock type	sub-division	Type
LF AF 08 50	12° 36 14.3' N	40° 29 36.3' E	BTA	mugearite	lava flow
LF AF 08 51	12° 35 50.9' N	40° 29 28.6' E	rhyolite	pantellerite	lava flow
LF AF 08 52	12° 35 46.3' N	40° 29 25.0' E	rhyolite	pantellerite	lava flow
LF AF 08 53	12° 35 42.99' N	40° 29 06.25' E	rhyolite	pantellerite	lava flow
LF AF 08 54	12° 35 34.9' N	40° 29 02.7' E	rhyolite	comendite	lava flow
LF AF 08 55	12° 35 38.1' N	40° 28 52.9' E	rhyolite	pantellerite	lava flow
LF AF 08 56	12° 35 38.1' N	40° 28 52.9' E	rhyolite	pantellerite	pumice
LF AF 08 57	12° 35 38.9' N	40° 28 47.3' E	rhyolite	pantellerite	lava flow
LF AF 08 58	12° 36 31.5' N	40° 29 55.9' E	rhyolite	pantellerite	pumice
LF AF 08 59	12° 36 36.7' N	40° 29 58.2' E	BTA	shoshonite	lava flow
LF AF 08 60	12° 36 47.9' N	40° 29 54.3' E	rhyolite	pantellerite	lava flow
LF AF 08 61	12° 36 55.3' N	40° 29 57.0' E	rhyolite	pantellerite	lava flow
LF AF 08 62	12° 37 01.9' N	40° 29 56.1' E	rhyolite	pantellerite	pumice
LF AF 08 63	12° 37 01.9' N	40° 29 56.1' E	rhyolite	pantellerite	lava flow
LF AF 08 64	12° 36 43.7' N	40° 29 37.5' E	BTA	mugearite	lava flow
LF AF 08 65	12° 36 22.5' N	40° 29 59.8' E	BTA	mugearite	lava flow
LF AF 08 66	12° 31 41.4' N	40° 22 08.5' E	TA[3]	benmoreite	lava flow
LF AF 08 67A	12° 31' 55.9 N	40° 22' 43.8 E	rhyolite	metaluminous	lava flow
LF AF 08 67B	12° 31' 55.9 N	40° 22' 43.8 E	rhyolite	metaluminous	lava flow
LF AF 08 67C	12° 31' 55.9 N	40° 22' 43.8 E	rhyolite	metaluminous	lava flow
LF AF 08 71	12° 41' 00.6 N	40° 32' 40.8 E	rhyolite	comendite	lava flow
LF AF 08 91	12° 38' 23.3 N	40° 27' 38.15 E	rhyolite	pantellerite	bomb
LF AF 08 92	12° 36' 36.73 N	40° 29' 58.22 E	rhyolite	pantellerite	bomb
LF AF 08 93	12° 38' 23.3 N	40° 27' 38.15 E	rhyolite	pantellerite	bomb
LFAF09 100	12° 34' 42.9 N	40° 22' 39.2 E	TA	benmoreite	lava flow
LFAF09 101A	12° 34' 34.2 N	40° 23' 32.7 E	Basalt	transitional	scoria
LFAF09 101B	12° 34' 34.2 N	40° 23' 32.7 E	rhyolite	pantellerite	pumice
LFAF09 102	12° 34' 40.0 N	40° 23' 59.5 E	TA	benmoreite	lava flow
LFAF09 103	12° 34' 46.1 N	40° 24' 11.4 E	Basalt	transitional	lava flow
LFAF09 104A	12° 34' 50.0 N	40° 24' 37.8 E	rhyolite	pantellerite	pumice
LFAF09 106	12° 34' 15.8 N	40° 25' 51.1 E	TA	benmoreite	lava flow
LFAF09 107A	12° 34' 13.2 N	40° 26' 21.9 E	trachyte		lava flow
LFAF09 107B	12° 34' 13.2 N	40° 26' 21.9 E	trachyte		lava flow
LFAF09 108A	12° 33' 36.1 N	40° 25' 47.9 E	TA	benmoreite	lava flow
LFAF09 108B	12° 33' 36.1 N	40° 25' 47.9 E	TA	benmoreite	lava flow
LFAF09 109a	12° 33' 42.1 N	40° 24' 12.8 E	trachyte		lava flow
LFAF09 110b	12° 33' 42.1 N	40° 24' 12.8 E	trachyte		lava flow
LFAF09 110	12° 33' 33.0 N	40° 24' 15.2 E	TA	latite	lava flow
LFAF09 111a	12° 33' 17.5 N	40° 24' 20.5 E	rhyolite	metaluminous	lava flow
LFAF09 111b	12° 33' 17.5 N	40° 24' 20.5 E	rhyolite	metaluminous	lava flow
LFAF09 112	12° 33' 00.2 N	40° 23' 59.0 E	rhyolite	metaluminous	lava flow

[1] *BTA - basaltic trachy andesite*

[2] *TB - trachy basalt*

[3] *TA - trachy andesite*

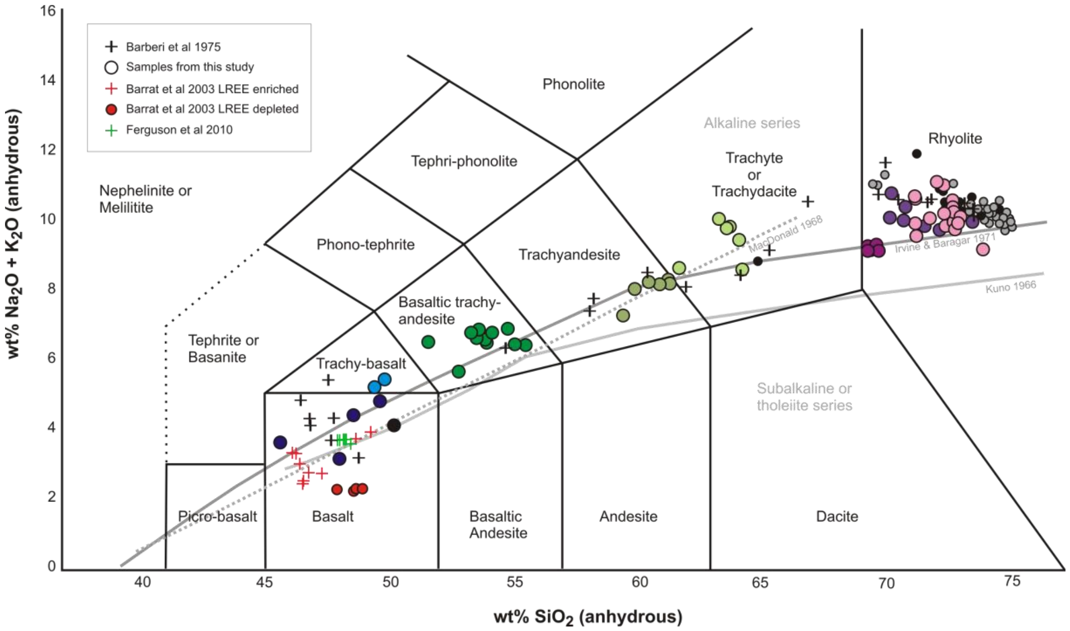

Figure 3.3. *Total alkalies-silica diagram (Le Maitre 2002). Dabbahu samples range from basalts through to peralkaline rhyolites (anhydrous normalised). Coloured circles – whole rock samples (colour used to highlight the different rock types. Rhyolites sub-divided into magenta – metaluminous rhyolite, purple – comendite, pink – pantellerite), and black circles – matrix glasses both from this study, grey circles – melt inclusion glasses, Field et al, 2011 (in review), black crosses - samples from Barberi et al (1975), green crosses – samples from eruptions in the Dabbahu segment (2007 and 2009) – Ferguson et al (2010), red crosses (LREE enriched) and circles (LREE depleted) samples from the Manda Hararo rift segment - Barrat et al (2003).*

classified into metaluminous, comenditic and pantelleritic using the criteria of Macdonald (1975; fig. 3.4).

Whole rock analyses are plotted with their matrix glass analysis; three pairs of whole rock / glass analysis cross the divide between pantellerite and comendite. 57 whole rock samples have N/KA >1, with 20 > 1.5. The highest N/KA of 1.68 (sample 022), comes from a sample of indurated volcanic ash and the peralkalinity may have been affected through heating of the ash layer by subsequent eruptions. The major element data of the peralkaline rocks were assessed for post eruptive alkali loss (e.g. through weathering) using the molar $FeO+K_2O/Al_2O_3$ (FK/Al) criteria of White et al. (2003). All samples fell inside the 95% confidence lines and therefore the samples are deemed not to have suffered any significant alkali loss.

Figure 3.5 overleaf*. New geological map of Dabbahu based on field sampling and NERC ARSF aerial photographs*

BLANK FOR GEOLOGICAL MAP

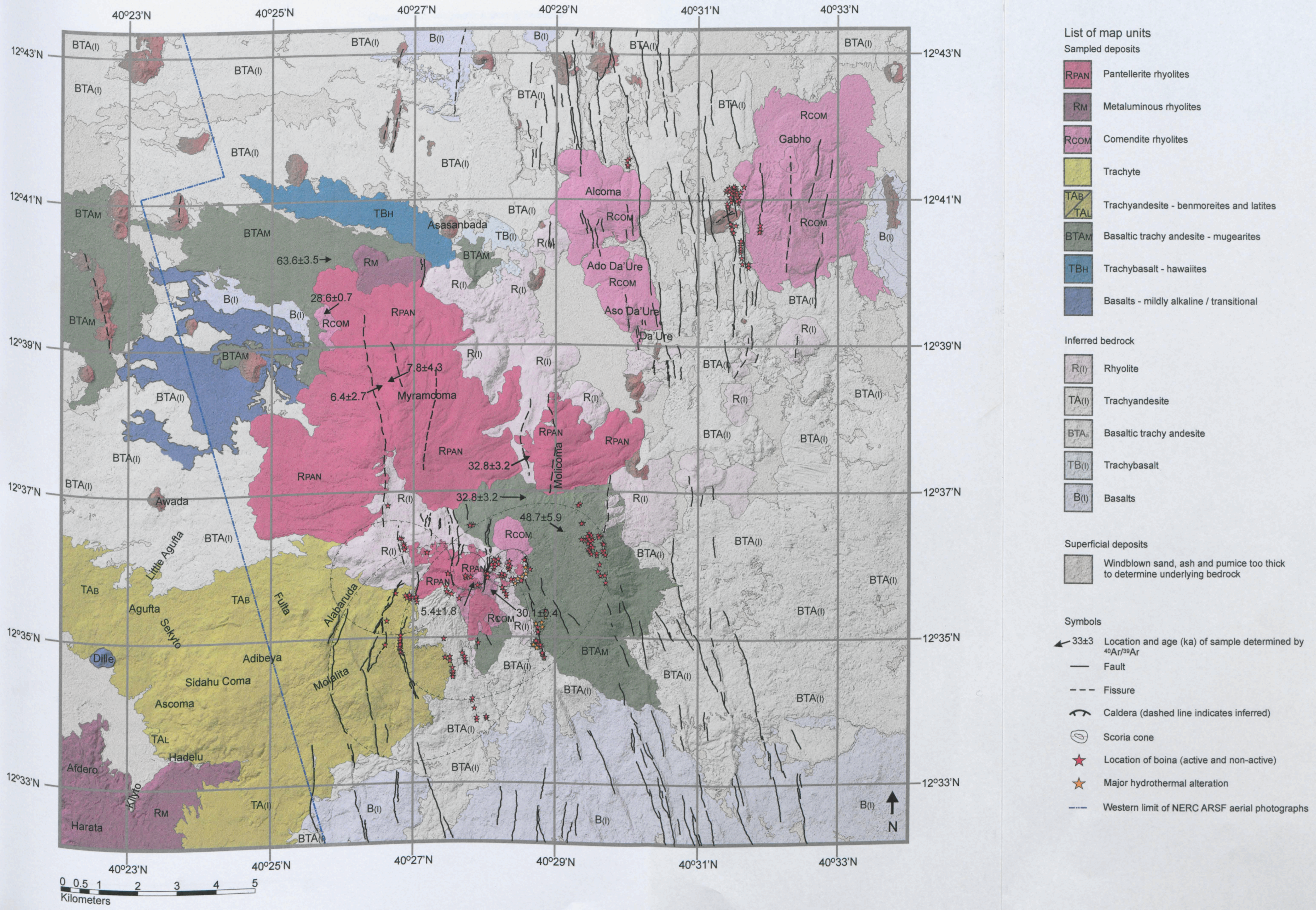
40°23'N
40°25'N
40°27'N
40°29'N
40°31'N
40°33'N
12°43'N
12°41'N
12°39'N
12°37'N
12°35'N
12°33'N
Gabho
Alcoma
Ado Da'Ure
Aso Da'Ure
Da'Ure
Asasanbada
Myramcoma
Molicoma
Awada
Little Agufta
Agufta
Sekyto
Fulta
Alabaruda
Dille
Adibeya
Sidahu Coma
Ascoma
Molalita
Hadelu
Afdero
Kilyto
Harata
63.6±3.5
28.6±0.7
7.8±4.3
6.4±2.7
32.8±3.2
32.8±3.2
48.7±5.9
5.4±1.8
30.1±0.4
N
0 0.5 1 2 3 4 5
Kilometers
List of map units
Sampled deposits
RPAN Pantellerite rhyolites
RM Metaluminous rhyolites
RCOM Comendite rhyolites
Trachyte
TAB/TAL Trachyandesite - benmoreites and latites
BTAM Basaltic trachy andesite - mugearites
TBH Trachybasalt - hawaiites
Basalts - mildly alkaline / transitional
Inferred bedrock
R(I) Rhyolite
TA(I) Trachyandesite
BTA Basaltic trachy andesite
TB(I) Trachybasalt
B(I) Basalts
Superficial deposits
Windblown sand, ash and pumice too thick to determine underlying bedrock
Symbols
33±3 Location and age (ka) of sample determined by $^{40}Ar/^{39}Ar$
Fault
Fissure
Caldera (dashed line indicates inferred)
Scoria cone
Location of boina (active and non-active)
Major hydrothermal alteration
Western limit of NERC ARSF aerial photographs

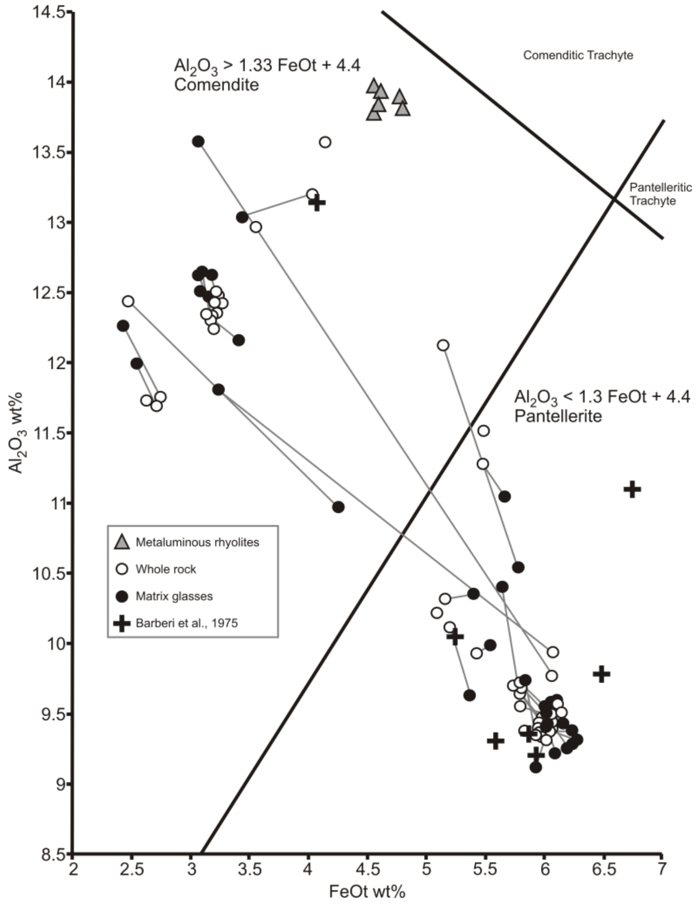

Figure 3.4. *Peralkaline/comendite diagram based on MacDonald (1974). FeO* is calculated as total Fe. Tie lines join whole rock with corresponding matrix glass analysis where available. Circles – samples from this study, crosses represent data from Barberi et al (1975). Metaluminous rhyolites are plotted for reference (triangles).*

Field Relationships

The sampled units (fig. 3.2a, tables 3.1 and 3.2) provide new insights into the eruptive history of Dabbahu. The samples, together with NERC ARSF aerial photographs, have been used to create a new geological map of Dabbahu (fig. 3.5), which illustrates the field relationships. Typical terrain is shown in figure 3.6. An interpretation has been made of non-sampled units, which ideally require confirmation through further fieldwork. Demonstrably the rock units were not emplaced in a strict order of increasing SiO_2 content as previously suggested (Barberi et al. 1974). For example, trachytes have only been found stratigraphically beneath basaltic trachyandesite units, and early metaluminous rhyolites underlie intermediate units (figs. 3.6a and 3.7). A summary of each of the principal rock units is given below.

Figure 3.6. *Typical terrain A) view of the metaluminous rhyolite flow to the SW of Dabbahu. Flow is up to ~100 m high, B) obsidian flows on the northern side of Dabbahu, C) polygonal surface of a trachyandesite (walking pole ~1 m long), D) Flow texture in an obsidian flow (pen for scale), E) basalt exposed in an ephemeral river bed, NW Dabbahu, F) small crater east of the summit partially infilled with obsidian flows. This crater is hydrothermally active and contains many boina (fumeroles used to condense water by the Afari), G) layers of pumice, ash, lithic fragments and obsidian bombs in an eroded canyon north of Aso Da'Ure (walking pole ~1 m high).*

Representative XRF major and trace element analysis

TAS definition[1]	**Gabbro**	**Basalt**	**basalt**	**trachy basalt**	**trachy basalt**	**BTA**	**BTA**	**BTA**	**Trachyandesite**	**Trachyandesite**	**Trachyandesite**	**trachyte**	**trachyte**
Sub-division		**transitional**	**transitional**	**hawaiite**	**hawaiite**	**shoshonite**	**mugearite**	**mugearite**	**benmoreite**	**benmoreite**	**benmoreite**		
Area	*Canyon S of Ado Da'Ure*	*NW Dabbahu*	*NW Dabbahu*	*N Dabbahu*	*N Dabbahu*	*N Dabbahu*	*N Dabbahu*	*N Dabbahu*	*SW Dabbahu*	*SW Dabbahu*	*SW Dabbahu*	*N Dabbahu*	*River bed nr Dabbahu summit*
Identifier	*Lithic*	*lava flow*	*lava flow*	*lava flow*	*lava flow*	*lava flow*	*lava flow*	*lava flow*	*lava flow*	*lava flow*	*lava flow*	*pumice*	*lava flow*
Sample	**LFAF08 040**	**LFAF08 044**	**LFAF08 045**	**LFAF08 028**	**LFAF08 030**	**LFAF08 005**	**LFAF08 006**	**LFAF08 025**	**LFAF08 066**	**LFAF09 100**	**LFAF09 106**	**LFAF08 032a**	**LFAF08 048**
SiO_2	49.54	47.45	48.69	49.40	49.67	55.20	54.61	54.87	59.86	58.73	60.61	63.43	64.41
TiO_2	2.13	1.86	3.39	3.61	3.50	2.33	2.04	2.41	1.67	1.62	1.34	0.71	0.78
Al_2O_3	16.70	14.94	14.95	13.45	13.36	14.95	15.97	13.81	14.54	13.95	14.23	14.30	15.27
$Fe_2O_{3(T)}$	10.71	10.65	14.39	14.91	14.71	10.65	10.04	12.38	8.49	8.45	8.64	8.31	7.80
MnO	0.17	0.18	0.23	0.27	0.29	0.22	0.22	0.31	0.23	0.24	0.25	0.32	0.21
MgO	5.42	8.48	4.74	4.51	4.31	3.00	2.80	2.78	1.74	1.47	1.18	0.44	0.34
CaO	9.70	11.39	9.06	7.79	7.51	6.10	6.36	5.47	3.75	4.40	3.63	2.56	2.15
Na_2O	2.98	2.50	3.44	3.89	3.99	4.14	4.27	4.89	5.06	4.96	5.09	5.68	5.59
K_2O	1.03	0.58	0.96	1.29	1.39	2.21	2.09	1.97	3.08	2.90	3.02	2.79	4.30
P_2O_5	0.26	0.21	0.41	0.82	0.86	0.53	0.65	1.17	0.48	0.80	0.43	0.13	0.15
SO_3	0.01	0.56	0.02	0.09	0.17	0.13	0.04	0.06	0.08	0.55	0.30	0.04	0.02
LOI	1.83	0.93	0.88	0.14	0.22	1.04	2.10	0.17	1.02	1.61	0.85	1.85	0.68
Total	100.49	99.74	101.14	100.17	99.98	100.48	101.18	100.29	100.00	99.66	99.58	100.57	101.72
NK/A	*0.36*	*0.32*	*0.45*	*0.58*	*0.60*	*0.61*	*0.58*	*0.74*	*0.80*	*0.81*	*0.82*	*0.87*	*0.91*
Rb	28	48	23	30	35	55	51	51	76	16	77	72	120
Sr	402	437	403	428	435	357	431	416	304	396	322	153	197
Y	30	69	40	50	53	62	55	72	74	45	72	92	79
Zr	188	400	228	273	284	473	382	453	635	236	683	616	973
Nb	30	71	37	51	53	70	67	78	93	36	93	85	142
Mo	2	4	3	3	3	4	4	4	5	2	4	4	6
Pb	4	5	3	4	4	6	5	5	6	3	9	9	10
Th	4	5	3	3	5	7	6	7	8	3	10	9	18
U	2	2	b.d.	1	2	1	2	2	2	1	3	2	3
Ga	20	24	22	23	25	23	22	25	25	23	28	27	32
Zn	72	129	103	114	122	116	107	128	125	117	128	141	132
Cu	77	8	51	24	25	29	17	13	4	46	b.d.	8	5
Ni	35	b.d.	9	2	b.d.	3	3	b.d.	b.d.	13	b.d.	2	b.d.
Co	34	21	40	35	35	21	19	22	10	47	9	6	4
Cr	77	8	10	b.d.	b.d.	4	3	9	b.d.	25	b.d.	b.d.	b.d.
V	279	100	445	330	311	178	135	108	62	372	16	12	9
Sc	27	26	36	30	29	22	19	23	12	47	16	15	8
Ba	308	757	311	470	542	600	611	730	763	303	841	1046	1053
La	24	59	25	37	37	52	53	62	66	28	65	70	93
Ce	55	133	69	92	90	122	120	142	148	66	147	152	219
Nd	28	71	35	50	48	59	59	72	72	39	69	75	89
Cs	b.d.	3	b.d.	6	2	b.d.	3	4	2	b.d.	b.d.	b.d.	b.d.

[1] TAS definition - based on anhydrous norm basis

*[2] Error is calculated from the counting statistic error ε = value * (cps/100)*

XRF analysis carried out at Leicester University

b.d. is 'below detection'

Table 3.2 *Representative XRF analyses for major and trace elements*

Representative XRF major and trace element analysis

TAS definition[1]	trachyte	rhyolite	rhyolite	rhyolite	rhyolite	rhyolite	rhyolite	rhyolite	rhyolite	rhyolite	typical
Sub-division		**comendite**	**comendite**	**comendite**	**comendite**	**metaluminous**	**metaluminous**	**pantellerite**	**pantellerite**	**pantellerite**	**error (±)[2]**
Area	*SW Dabbahu*	*N Dabbahu*	*N Dabbahu*	*Dabbahu summit*	*Gab'ho*	*N Dabbahu*	*Kilyto SW Dabbahu*	*N Dabbahu*	*Dabbahu Summit*	*Molicoma*	
Identifier	*lava flow*	*lava flow*	*lava flow*	*lava flow*	*lava flow*	*lava flow*	*lava flow*	*lava flow*	*lava flow*	*lava flow*	
Sample	**LFAF09 109a**	**LFAF08 011**	**LFAF08 029**	**LFAF08 054**	**LFAF08 071**	**LFAF08 026**	**LFAF09 112**	**LFAF08 007C**	**LFAF08 055**	**LFAF08 061**	
SiO_2	63.12	70.06	70.00	70.49	74.03	68.84	68.47	72.49	72.75	73.26	*2.25E-02*
TiO_2	0.87	0.34	0.40	0.33	0.16	0.43	0.45	0.37	0.36	0.32	*5.43E-06*
Al_2O_3	15.48	13.75	12.10	13.55	12.37	13.83	13.67	9.40	9.32	10.11	*1.61E-03*
$Fe_2O_{3(T)}$	6.28	4.67	5.69	4.60	2.74	5.00	5.27	6.59	6.60	5.76	*1.31E-04*
MnO	0.22	0.15	0.18	0.14	0.08	0.14	0.15	0.21	0.21	0.18	*1.53E-06*
MgO	0.74	b.d.	b.d.	b.d.	b.d.	b.d.	0.18	b.d.	b.d.	b.d.	*4.11E-07*
CaO	2.35	0.95	0.67	0.70	0.33	1.54	1.68	0.29	0.27	0.27	*1.54E-05*
Na_2O	6.06	5.75	6.20	5.59	5.16	4.89	4.81	6.08	5.99	5.77	*5.57E-04*
K_2O	3.64	4.25	4.48	4.33	4.61	4.27	4.18	4.37	4.25	4.27	*2.07E-04*
P_2O_5	0.20	0.02	0.02	0.01	0.00	0.04	0.06	0.01	0.01	0.01	*5.73E-08*
SO_3	0.21	0.02	0.07	0.01	b.d.	b.d.	0.02	0.03	b.d.	b.d.	*2.20E-07*
LOI	0.96	1.28	0.60	0.66	0.64	0.63	0.18	0.42	0.16	0.67	
Total	100.13	101.15	100.39	100.35	100.10	99.63	99.10	100.25	99.92	100.49	
NK/A	*0.90*	*1.02*	*1.24*	*1.02*	*1.09*	*0.92*	*0.91*	*1.57*	*1.55*	*1.40*	
Rb	88	110	131	107	162	111	106	162	163	161	*0.198*
Sr	238	50	17	35	3	28	151	3	3	4	*0.034*
Y	70	103	126	113	143	116	94	164	165	156	*0.159*
Zr	653	928	1041	1007	845	986	796	1300	1304	1284	*0.491*
Nb	93	136	157	146	127	145	99	206	206	191	*0.117*
Mo	4	3	8	3	7	3	5	9	10	10	*0.010*
Pb	9	10	13	13	16	12	12	17	17	17	*0.061*
Th	10	13	15	15	20	15	12	20	20	20	*0.061*
U	3	1	4	2	5	3	3	5	5	5	*0.015*
Ga	26	30	33	32	27	32	26	34	35	32	*0.179*
Zn	111	155	216	159	144	181	115	271	273	250	*0.511*
Cu	2	5	b.d.	b.d.	b.d.	b.d.	2	6	2	b.d.	*0.022*
Ni	b.d.	b.d.	2	b.d.	b.d.	b.d.	b.d.	2	b.d.	b.d.	*0.008*
Co	7	4	2	3	b.d.	3	3	4	3	1	*0.011*
Cr	b.d.	b.d.	2	b.d.	b.d.	b.d.	b.d.	b.d.	b.d.	b.d.	*0.003*
V	10	6	5	1	b.d.	2	10	b.d.	1	b.d.	*0.014*
Sc	9	2	2	2	1	1	6	1	b.d.	b.d.	*0.011*
Ba	954	971	421	763	48	843	999	3	6	43	*0.722*
La	67	101	114	112	103	109	85	143	147	139	*0.395*
Ce	145	219	243	209	220	231	191	311	311	301	*0.642*
Nd	68	94	110	104	99	104	89	143	138	136	*0.331*
Cs	2	b.d.	4	b.d.	5	3	2	8	10	10	*0.026*

[1] TAS definition - based on anhydrous norm basis

*[2] Error is calculated from the counting statistic error ε = value * (cps/100)*

XRF analysis carried out at Leicester University

b.d. is 'below detection'

Table 3.2 cont. *Representative XRF analyses for major and trace elements*

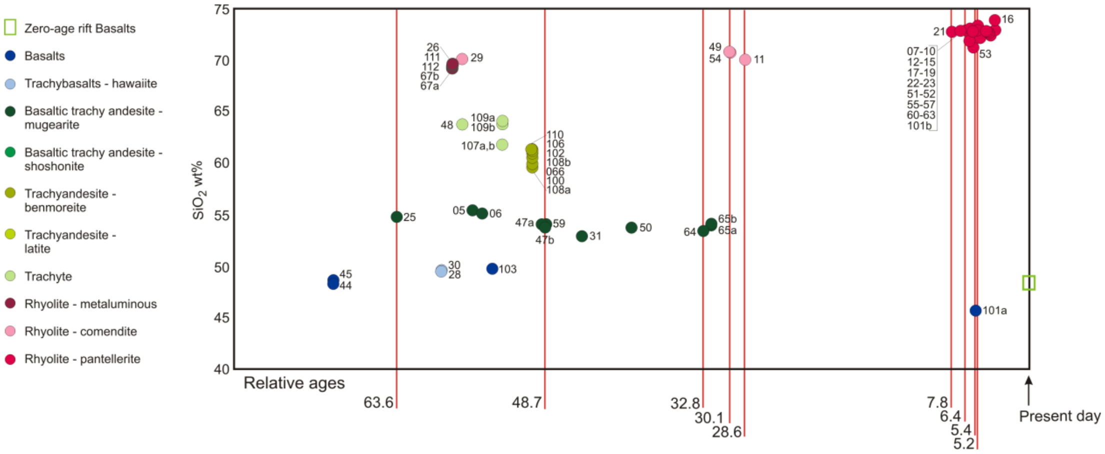

Figure 3.7. *Estimate of relative ages v SiO_2 (wt%) content (anhydrous normalised basis), based on field relations for Dabbahu (excludes most pumices, and other centres e.g. Gab'ho)). Absolute $^{40}Ar/^{39}Ar$ ages are indicated. Zero-age rift basalts from Ferguson et al. (2010).*

Basalts

Sampled Dabbahu basalts are limited to two basalt flows, a dyke, a lithic fragment and a scoria cone called Dille. Two of the basalt flows are exposed in ephemeral river beds; one is located in the extensive drainage system NW of the edifice where basalt is exposed beneath thin basaltic trachyandesite flows (fig. 3.6e), the other was emplaced below the trachyandesite flows to the SW of the edifice, close to Dille. The scoria cone itself, is interbedded with thin layers of pantellerite pumice indicating that its formation was coeval with the eruption of the pantellerites. A complex of 5 basaltic dykes rise above the surrounding lava plain to the NW of the Dabbahu edifice. A coarse grained lithic was found in a 10 m deep eroded canyon through layers of explosive material (pumices, bombs and lithics), between Ado Da'Ure and Aso Da'Ure (fig. 3.6g). The main Dabbahu basalts are located to the south of the edifice summit, which is the northern extremity of the Manda Hararo rift zone, where geologically recent flows can be seen to have erupted over older basalts.

Trachybasalts

A striking, low-lying (<5 m high) SE-NW flow is visible from aerial photographs and satellite images (figs. 3.2b, 3.5), just north of the Dabbahu edifice which is the only sampled trachybasalt flow. The composition is sodic hawaiite. The source vent of this flow cannot be determined as it is now covered by Dabbahu rhyolites. At the base of the flow, a comenditic obsidian is located; magma mingling between the two rock types is visible on a macro to a micro scale (fig. 3.10).

Basaltic Trachyandesites

Basaltic trachyandesite lavas are one of the most extensive rock units at Dabbahu. Sampled basaltic trachyandesites are located around to the NW of the Dabbahu edifice and on the eastern side of the edifice itself. They underlie most of the other rock types except the basalts. The basaltic trachyandesite flows may have completely covered the edifice prior to eruption of the later peralkaline units. The eruption source for the basaltic trachyandesite lavas is not clear due to the covering by later units; however a small caldera ~0.75 km diameter is partially exposed east of the summit and has since been partially infilled with peralkaline products (fig. 3.6f). The basaltic trachyandesite lavas form the rim of this caldera suggesting this was one of the source vents. The scoria cones to the NW of Dabbahu have also erupted basaltic trachyandesite products. Potassic basaltic trachyandesite products (shoshonites) have been found stratigraphically below the sodic basaltic trachyandesite products (mugearites) in each case.

Trachyandesites

Trachyandesites are located to the SW of Dabbahu and have flowed over and around a large metaluminous rhyolite flow. It is difficult to define the exact extent of this series of flows from the aerial photographs due to the extensive pumice cover in this area. All flows are of sodic benmoreite, except one sample which is defined as potassic latite. This was collected from the base of the flow front and the age relationship is unclear with regards to the other trachyandesite flows. These flows are typically hummocky, up to ~ 4 m high, with polygonal cooling joints (fig. 3.6c).

Trachytes

Trachytes are limited in extent at Dabbahu and the only surface level trachyte is a weathered trachyte dome located at the edge of the Dabbahu flows in the SW, just south of Dille. The remaining two trachytes sampled are located in ephemeral stream beds beneath surface flows of basaltic trachyandesite. Trachytic pumice was located beneath comendite pumices to the north of Dabbahu.

Rhyolites

Rhyolites are located roughly within a band spanning SW – NE across Dabbau (fig. 3.5) and comprise metaluminous and peralkaline rhyolitic obsidians. On the Dabbahu edifice itself, rhyolites dominate the summit region and the northern section. Metaluminous rhyolites have been sampled in the north and south west of Dabbahu. The prominent flow to the south-west is up to ~100 m high with distinct semi-circular flow ridges visible from the NERC ARSF aerial photographs. From these photographs the flow front can be seen to divide into several small, sinuous branches giving a tendril-like appearance (fig. 3.2 and 3.6a). This flow was previously interpreted as intermediate composition by Barberi et al. (1974); it shares similar morphological features to intermediate flows in the N and NW, in particular the tendril nature of its flow front. A key difference is the substantial height of this flow (~100 m). The rhyolite is one of the most weathered samples present at Dabbahu, and from field evidence, one of the oldest of the Dabbahu edifice. It underlies the trachyandesite flows which surround it and cover its source. To the north, another equally weathered flow is located, which is ~30 m high but with rounded flow fronts. This flow pre-dates the later pantelleritic obsidian flows which it underlies. A number of unsampled flows to the north-east, observed in aerial photographs, closely resemble both of the sampled flows and these could also prove to be metaluminous. The remaining metaluminous sample is a dyke located in an ephemeral river bed, overlain by sedimentary flood deposits, just north of the prominent SW flow. The dyke has a bulk composition very similar to this major flow, and is likely coeval.

The domes to the north of Dabbahu (Alcoma, Gab’ho, the Da’Ure group) are all comenditic obsidians covered with various thicknesses of pumice. Comendites are also located on the summit of Dabbahu, and one flow is found in the NNW of Dabbahu. However, only one comendite from Dabbahu itself is obsidian. Field evidence shows these flows are older than the pantellerite flows, are more weathered, had a higher viscosity and formed rounded flow fronts. It is likely that comendite flows are largely responsible for the topography underlying the pantellerites at the summit.

The pantellerite flows cap the northern half of the Dabbahu edifice and are distinctive due to their sinuous nature (figs. 3.2b, 3.6b). The northern flows were erupted from a series of N-S fissure systems. Just to the south of this system, the summit pantellerites have been erupted from a small caldera (~0.15 km, 12°35'41.27N, 40°28'44.62E), which sits within an inferred larger caldera (~0.8 x ~1 km). The obsidians have flowed over this second caldera's rim. There are also small obsidian flows partially infilling a small, partially exposed caldera (~0.75 km diameter) to the east of the summit (fig. 3.6f). The flows to the east are heavily pumice-covered and thus pre-date those to the west. Flow banding is often observed within the obsidian flows (fig. 3.6d).

Pumice

It has been suggested that pyroclastic products are scarce at central volcanoes (Lahitte et al. 2003). However, pyroclastic material in the form of airfall pumice is extensive at Dabbahu with up to ~10 m of pumice covering underlying flows, and extensive pumice outwash rafts in the plains to the SW of Dabbahu. Over 20 samples of pumice and a scoria sample were collected. Colour varies from grey through buff to green in the pumices, and dark brown-black in the trachytic pumice and scoria. The pumices comprise layers (2 cm to 1 m) of angular to sub-angular clasts (0.5 – 10 cms). The pumice layers are reasonably well sorted. Some reworking of pumices can be seen where clasts have been rounded, in particular in the outwash plains to the NW, but the majority still appear to be in situ with limited reworking. Pumice is largely aphyric, or contains rare microphenocrysts which may be due to volatile stratification (Caricchi et al. 2011). One trachytic pumice layer was located below comendite pumice to the north of Dabbahu. Comendite pumice covers Ado Da'Ure, Aso Da'Ure, Gab'ho and the area to the NE of Dabbahu (fig. 3.2). A canyon has formed through drainage erosion between Ado Da'Ure and Aso Da'Ure and ~10 m of pumice layers and obsidian bombs can be seen (fig. 3.6g). Layers are often interspersed with thin (<0.5 cms) layers of obsidian lithics. Pantellerite pumice is found to the NE, covering the pantellerite obsidian flows in up to ~8 m of pumice. The basaltic trachyandesite and trachyandesite flows to the S and E are also covered in pantellerite pumices. The basaltic scoria cone of Dille contains thin layers of pantellerite pumice within its structure showing its emplacement was coeval with the pantellerite eruptions of

Dabbahu. Immediately west of Dabbahu summit is an extensively pumice covered slope which has been cut by deep erosion gullies.

Eruption styles

Small calderas were identified on and near the summit of Dabbahu. One is ringed by basaltic trachyandesite and partially infilled with rhyolites and hydrothermally altered material. This caldera is one of the key areas for "boina" (fumaroles adapted by the Afar pastoralists to condense drinking water). A second is surrounded by pantellerite obsidians. Fault systems and other structures are suggestive of four potential underlying caldera structures which may have been infilled by subsequent lava flows. However, these structures can only be inferred (fig. 3.5). The majority of pantellerites have been erupted from fissure systems which are orientated roughly N-S in line with the general direction of faulting on Dabbahu and elsewhere in this region (fig. 3.2b).

^{40}Ar/^{39}Ar Geochronology

The only previously published dates for Dabbahu used fission track or K-Ar dating methods, two of which were from the same sample (Barberi et al. 1974). Five samples are designated 'Boina' and two as 'Boina centre'. The exact locations of the samples have not been published. However, the samples are all obsidian, which limits their localities to the summit and the northern half of Dabbahu, and these are the youngest rocks. No radiogenic Ar was detected in three of Barberi et al's., (1974) samples (D211, D221 and D229), so a maximum age value was calculated assuming a radiogenic Ar content equal to 10% of the total ^{40}Ar. The range of dates obtained, are 0.01 Ma (fission track) to 1.15 Ma (K/Ar – maximum age value). The authors themselves note that the values obtained are extremely high, and it is the fission track ages of 44,000 and 10,500 which are quoted as dates for obsidian emplacement at Dabbahu (e.g.Barberi et al. 1974; Woolley 2001).

Nine new ^{40}Ar/^{39}Ar dates were obtained for Dabbahu samples (fig. 3.2a, table 3.3). The basaltic trachyandesites are the oldest samples dated, with a sample just north of the main edifice (sample 025) yielding a maximum age of 63.6 ±3.5 ka. This sample yielded a U-shaped spectrum suggesting either a mixed population of crystals, or excess argon, and therefore the weighted mean of the youngest steps is favoured as a maximum age for this sample. This sample overlies the original basalts from Dabbahu (figs. 3.2a & 3.5), suggesting that Dabbahu began to evolve prior to ~64 ka. The peralkaline rhyolites were dated by anorthoclase separates which potentially provide an age slightly older than that of eruption (Esser et al. 2004). The oldest dated comendite rhyolite, which overlies basaltic trachyandesite lavas to the E of the summit overlaps within error with the youngest dated basaltic trachyandesite, suggesting that the comenditic eruptions may have commenced close to the waning of basaltic trachyandesite eruptions, or soon after they had ceased.

This is supported by the field evidence as the peralkaline rhyolites overlie all other rock units. The pantellerite obsidians are all younger than 7.8 ±4.3 ka. The obsidians that are not pumice-covered were erupted after the pumice-covered Molicoma obsidians.

Preferred ^{40}Ar/^{39}Ar dates

Sample	Rock type[1]	Method[2]	Age[3]	error
LFAF08 025	BTA	separate	63.6	±3.5 ka
LFAF08 047	BTA	grndms	48.7	±5.9 ka
LFAF08 064	BTA	grndms	32.8	±3.2 ka
LFAF08 054	comendite	grndms	30.1	±0.4 ka
LFAF08 011	comendite	grndms	28.6	±0.7 ka
LFAF08 021	pantellerite	separate	7.8	±4.3 ka
LFAF08 019	pantellerite	separate	6.4	±2.7 ka
LFAF08 055	pantellerite	separate	5.4	±1.8 ka
LFAF08 063	pantellerite	separate	5.2	±3.4 ka

[1] *As determined by XRF. BTA - basaltic trachy andesite. Comendite and pantellerites are obsidians.*

[2] *method - groundmass or anorthoclase separates*

[3] *preferred weighted mean plateau age*

Table 3.3 *^{40}Ar/^{39}Ar geochronology*

However, the age errors on these samples overlap, and relative ages rely on field evidence (fig. 3.7). These anorthoclase-bearing samples are young and were problematic to date. Low temperature gas fraction produced excess ^{36}Ar and ^{39}Ar making the age young, whereas late gas fractions were enriched in residual ^{40}Ar, yielding old apparent ages.

The dates obtained as part of this study are significantly younger than those obtained by Barberi et al (1972). Taking into consideration the new dates, field relationships and stratigraphy of units, Dabbahu must have begun to erupt some time prior to the oldest date obtained by us (i.e. >64 ka) and has remained active to the present day (fig. 3.7).

Petrography

The Dabbahu samples are weakly to highly porphyritic (0-47% by volume phenocrysts) with an average phenocryst content of 7% overall (fig. 3.8). The basalt samples are reasonably porphyritic (10 – 47% by volume), containing phenocrysts up to 4mm diameter. Plagioclase dominates the assemblage of plagioclase + cpx + olivine ± magnetite ± apatite, which is set in holocrystalline groundmass, containing the same minerals. The exception is a sample from the Dille scoria cone, which is weakly micro-porphyritic (2%). One basalt sample has distinct euhedral olivines (~2 mm) with prominent Fe-rich rims (fig. 3.9a). Sample 040 shows dis-equilibrium, particularly in olivine crystals which show extensive alteration to iddingsite.

The trachybasalt samples have a low percentage of phenocrysts (2-5 % by volume). Their phenocryst assemblage comprises alkali feldspar+plagioclase+cpx+olivine+magnetite. Phenocrysts are up to 2 mm in size. Both samples have a crystalline groundmass, and both show signs of disequilibrium with embayed and rimmed phenocrysts; e.g. ribbon corona ~60μm wide surround the plagioclase (fig. 3.9b). Glassy blebs are visible in the matrix in thin section.

There is variation across the basaltic trachyandesite samples with regards to texture; some are consistently vesicular whilst others are hypocrystalline with low vesicularity. They are weakly to highly porphyritic (0.8-17% by volume) within a fine grained groundmass. The assemblage is plagioclase + olivine + magnetite ± cpx ± ilmenite ± apatite ± rare alkali fsp, with minor FeS found in the groundmass of two samples. A higher proportion of samples in this rock type contain ilmenite than any other rock type. Crystals largely occur in glomerocrysts which are up to ~4 mm across, and contain numerous inclusions of apatite and Fe-Ti oxides. Skeletal crystals of olivine and Fe-Ti oxides are also numerous (fig. 3.9c). Several of these samples have been subjected to some mixing, particularly noticeable in some samples where there are distinctive groundmass textures; separate patches of coarse and fine grained groundmass with a sharp divide between.

Trachyandesite samples have 6-22% volume phenocrysts and an assemblage of plagioclase + cpx + olivine + magnetite ± ilmenite ± apatite ± rare alkali fsp. FeS is found in the groundmass of more than 50% of trachyandesite samples. Plagioclase (~1 mm) have distinct rims which are more Na rich than the cores.

The trachyte lavas are similar to trachyandesite samples with regards to volume % phenocrysts (6-18%) of plagioclase + cpx + olivine + magnetite ± apatite ± alkali fsp ± rare ilmenite, however the trachyte pumice has <1% phenocrysts, comprising just plagioclase.

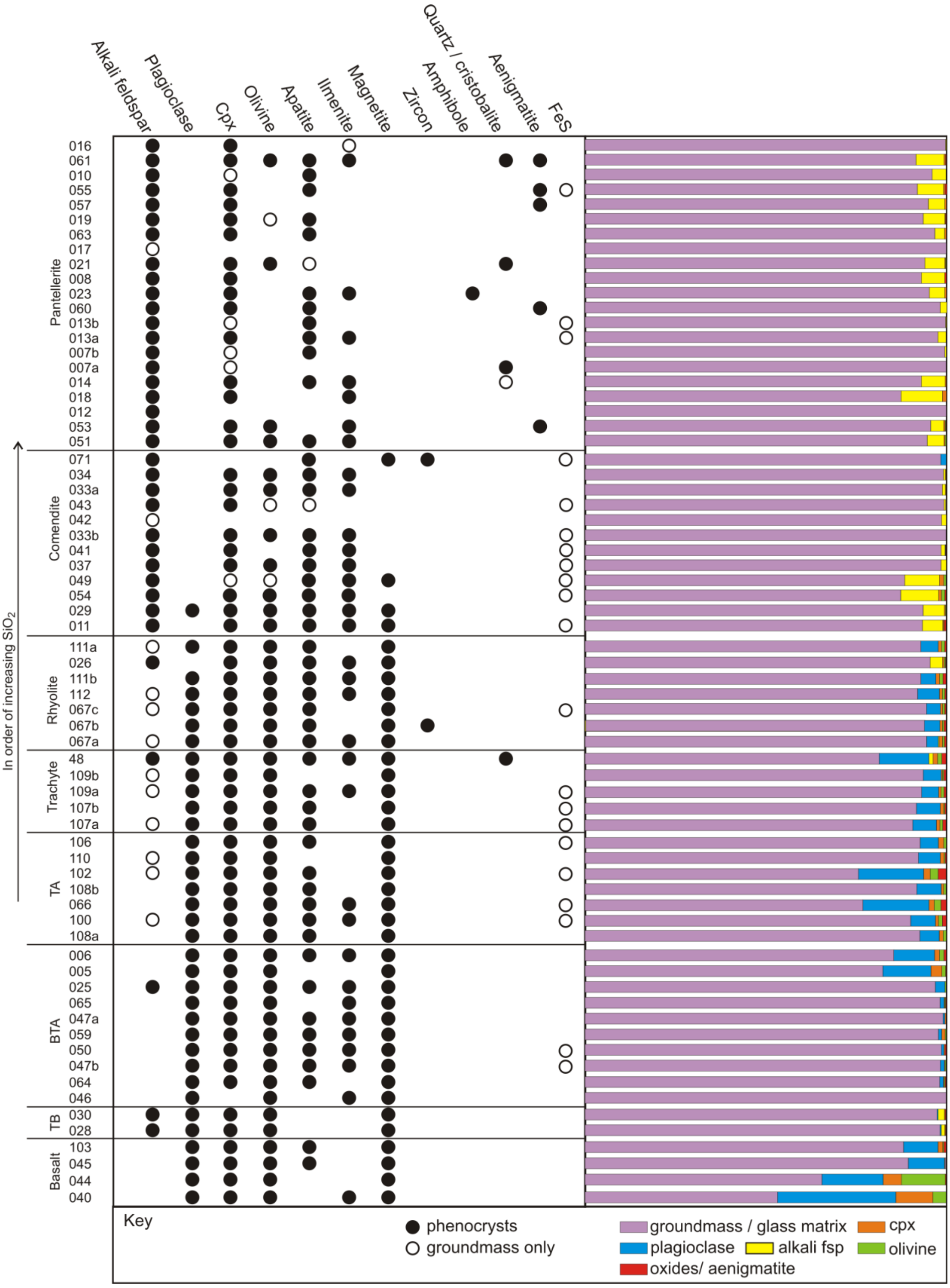

Figure 3.8. *Summary of mineralogy from analysed phenocryst bearing samples. A) Plot represents samples in which mineralogy have been analysed (aphyric samples and some pumices omitted). Black circles denote inclusions or groundmass only. B) Bar chart showing proportion of phenocrysts present in each sample. Average phenocryst content of porphyritic samples <7 modal % . Groundmass or matrix glass is the dominant component of the Dabbahu samples.*

Cpx is often radially intergrown with plagioclase. Cristobalite crystals (~400 µm) are found in one sample (fig. 3.9d). Groundmass is glassy, often with quench textures. Changes across the groundmass textures can be seen in all trachyte thin sections from coarse to fine grained. All the trachytes have dis-equilibrium textures in the phenocrysts, such as cpx, which have undergone dissolution prior to being overgrown by thin Fe-rich rims (fig. 3.9e). Magnetite occasionally shows exsolution textures.

The metaluminous rhyolites have a consistent volume of phenocrysts (5-8%) which sit in glassy groundmass dominated by feldspar crystallites. The phenocryst assemblage is cpx + olivine + magnetite + apatite ± alkali fsp ± ilmenite. Rare euhedral zircons (~20 µm) were located in one sample. Apatite is numerous, in some cases forming clusters around phenocryst rims. Many of the oxides show exsolution textures indicative of slow cooling. Olivines have undergone some alteration to Fe-rich iddingsite. Plagioclase phenocrysts are often euhedral, but other phenocrysts are rounded and embayed.

Comendites are highly variable in their texture; some are aphyric, whereas porphyritic examples contain up to 12% phenocrysts. Porphyritic examples are dominated by alkali feldspar, ± cpx ± olivine ± apatite ± ilmenite ± magnetite, in a glass matrix. Plagioclase is only found in one sample (029), and these are small crystals (200 µm) located within trachybasalt blebs (fig. 3.10e). FeS is found as groundmass or inclusions in two thirds of samples. An obsidian from Gabho, contains numerous euhedral zircons > 40 µm in diameter (fig. 3.9f). Some comendites show signs of mixing, particularly sample 029 where mixing is manifest on all scales (fig. 3.10).

Pantellerites have an average phenocryst content by volume of <2%, with a range of 1-11% in the porphyritic samples. Pumices are generally aphyric with minor microlites or very rare phenocrysts. The pantellerites are dominated by alkali feldspar with subordinate cpx. The assemblage is alkali feldspar ± cpx ± apatite ± ilmenite ± fayalite ± aenigmatite. The most porphyritic pantellerite contains euhedral quartz (~600 µm), and quartz-feldspar granophyric textured intergrowths (<1 mm). Three other samples contain secondary cristobalite, and three samples contain FeS. Only one amphibole crystal (~400 µm), was found in the Dabbahu samples (fig. 3.9g). The pantellerites are all glassy and often very vesicular. Flow banding is common, caused by high concentration of microlites and / or vesicles. Alkali feldspar and cpx crystals are generally euhedral, although some show rounding suggestive of reheating and resorption. Aenigmatites are found as phenocrysts (up to 400 µm) in five samples (fig. 3.9h), and comprise up to 10% of the total phenocryst content.

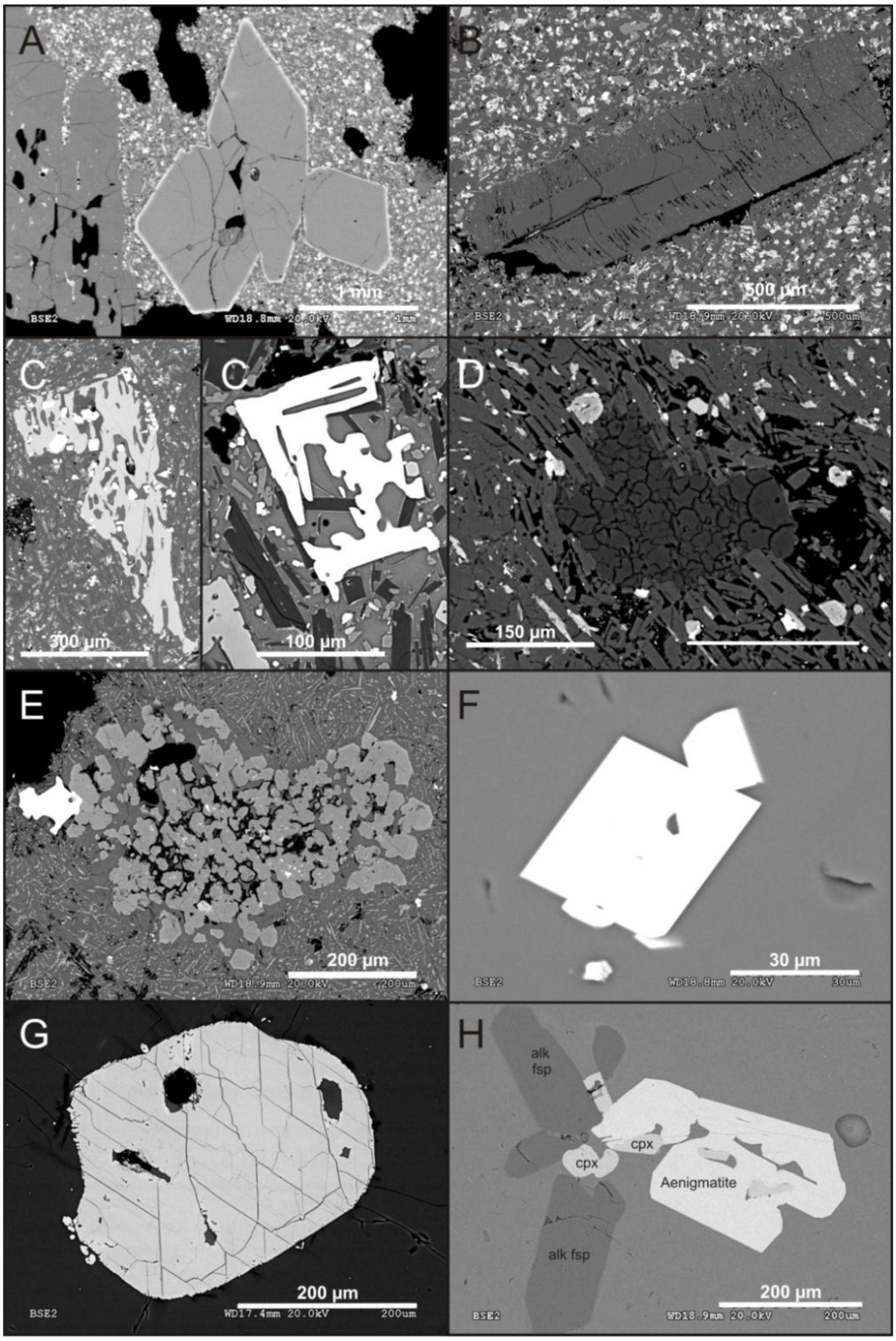

Figure 3.9. *Backscatter images of representative textures found in the Dabbahu Rocks. A) sample 44, basalt, Fe-rich rimmed olivines in fine grained groundmass (cores* Fo_{83-76}*, rims* Fo_{80-57}*), B) sample 28, trachybasalt, ribbon-rimmed feldspar (core* An_1Or_{35}*, rim* $An_{11}Or_{25}$*), C) samples 25 and 46, basaltic trachyandesites, skeletal olivine (*Fo_{47}*, left) and magnetite (right), D) sample 048, trachyte, cristobalite crystal, E) sample 106, trachyandesite, sponge textured cpx, F) sample 071, comendite, euhedral zircon, G) sample 023, pantellerite, amphibole xenocryst – this is the only amphibole crystal found in the Dabbahu samples, H) sample 055, pantellerite, aenigmatite phenocryst with alkali feldspar and cpx.*

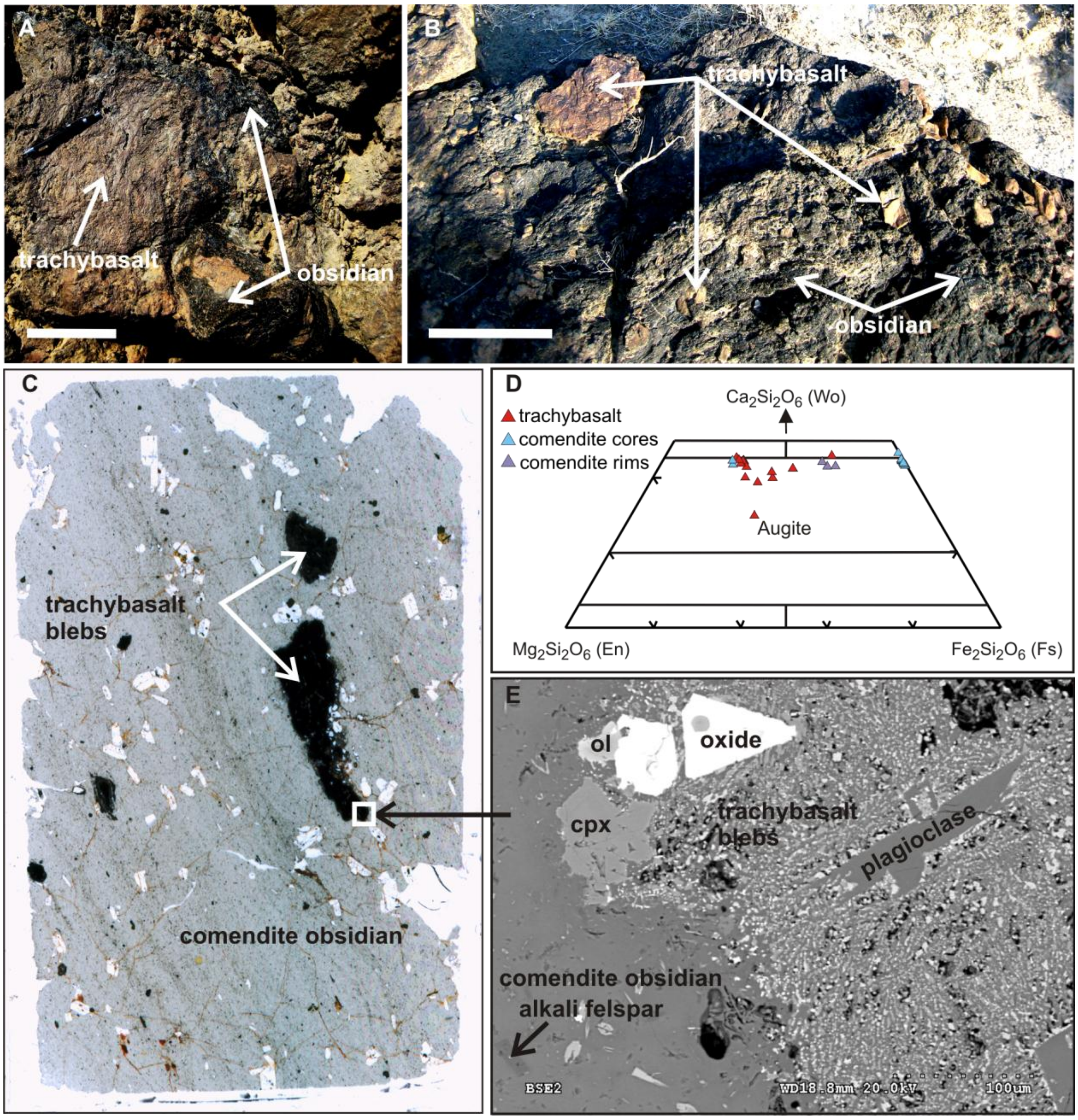

Figure 3.10. *An example of magma mingling at Dabbahu (sample 029). A and B photographs of the outcrop. A) Glassy comendite can be seen mingled with the trachybasalt, B) obsidian surrounds clasts of trachybasalt. White scale bars indicate ~15 cms and ~50 cms respectively. C) A scan of the thin section shows blebs of trachybasatic material which have been incorporated. D) Cpx compositions show correlation between samples 028 and 029, and the rims from 029 sit between two groups of core compositons. E) An BSE image of the thin section shows the crystalline groundmass of the trachybasalt bleb contrasting with the glass of the comendite obsidian.*

Geochemistry

Major and trace elements

Major element whole rock data are given in table 3.2, and selected data are plotted in Harker diagrams in figure 3.11. New data are augmented by the published data of Barberi et al. (1974) from Dabbahu, and rift basalts from Ferguson et al. (2010) and Barrat et al. (2003). Some elements show smoothly curved variation in concentration with SiO_2, e.g. CaO (fig. 3.11d) and MgO (fig. 3.11b) due to changing composition of the major phenocryst phases. Others show classic fractionation trends with increasing SiO_2, due to abrupt changes in phenocryst assemblage. For example, P_2O_5 (fig. 3.11g) shows a sharply defined inflexion due to apatite saturation at ~55 wt% SiO_2 while the inflexion in Al_2O_3 at ~60 wt% SiO_2 marks the onset of plagioclase as a major phenocryst phase (fig.3.11c). The inflexions in Na_2O and K_2O reflect the disappearance of plagioclase from rhyolites and the dominance of alkali feldspar as a phenocryst phase. Early saturation in ilmenite + magnetite leads to the very sharp peak observed in TiO_2 and, less clearly, Fe_2O_3. In the case of P_2O_5 there is minor scatter beneath the peak, suggesting the possibility of some mixing (Marshall and Sparks 1984) in basaltic trachyandesite samples. Al_2O_3, TiO_2 and Fe_2O_3 trends show a marked bifurcation at ~70 wt% SiO_2 (fig. 3.11a, c and e) into the Fe- and Ti-rich, Al-poor pantellerites and Fe- and Ti-poor, Al-rich comendites. Fe enrichment and Al depletion is characteristic of pantellerite rocks (Noble 1968). Melt inclusion and groundmass glasses extend the trends to SiO_2 contents of almost 80 wt%, primarily along the pantellerite array.

The basaltic end of the Dabbahu whole-rock trend is defined by four analyses from this study and a further seven from Barberi et al., (1974). They range from 4 to 10 wt% MgO, with Mg# up to 47, and variable TiO_2, from 2 to 4 wt%. This compositional range is embraced by the LREE-enriched basalts of the Manda Hararo Rift (Barrat et al. 2003) indicating that some rift basalts have compositions consistent with parents to the overall Dabbahu fractionation sequence. Chemical variation within these basalts likely reflects a combination of variable degrees of mantle melting, followed by fractionation within the crust. It is noticeable that the LREE-depleted samples of Barrat et al., (2003) do not match any samples from Dabbahu, particularly in their low TiO_2 and K_2O. The Barrat et al., (2003) samples are the most southerly, located approximately 85 km south of Dabbahu, with the LREE depleted samples mainly located on the western margin of the fissural basalts. The 2007 and 2009 eruptions in the Dabbahu magmatic rift segment (approximately 30 km

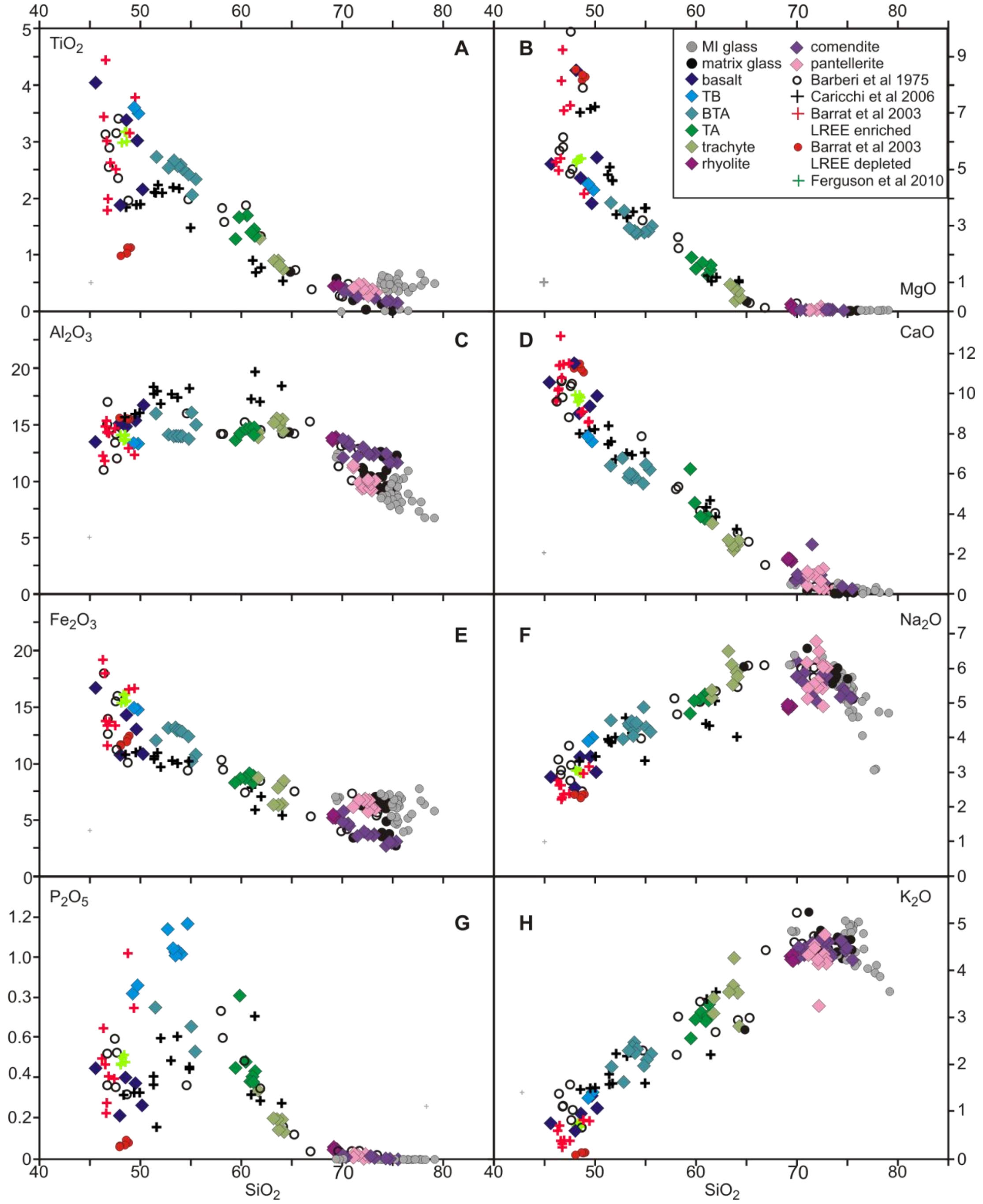

***Figure 3.11**. Selected major element v SiO$_2$ Harker diagrams for Dabbahu, together with samples from Barberi et al (1975), experimental results from Caricchi et al (2006), Manda Hararo basalts from Barrat et al (2003), and 2007 and 2009 rift basalts from Ferguson et al (2010).*

south of Dabbahu) fit closely with the Dabbahu basalts and trachybasalts (Ferguson et al. 2010), again suggesting a close link between rift basalts and parental magmas to Dabbahu.

We also show in figure 3.11 the experimentally-determined liquid lines of descent for a rift basalt with 4 wt% initial H_2O from Caricchi et al. (2006). These data largely mimic the

Dabbahu whole-rock trends, although saturation in plagioclase is delayed in the experiments (i.e. they extend to higher Al_2O_3), presumably due to elevated H_2O contents relative to natural rocks. There is a lack of marked TiO_2 and Fe_2O_3 enrichment in the experimental liquids compared to the natural rocks which may be due to lower TiO_2 and Fe_2O_3 in the experimental starting compositions; a possible reflection of differences in oxidation states; low crystallisation of Fe-Ti oxides (ilmenite) in the experiments (<3 modal % in the fractional crystallisation experiments only). The overall similarity between experimental fractionation trends and the whole rocks supports the notion that Dabbahu records a fractionation sequence from parental basalt under crustal conditions.

For rocks suites that show protracted differentiation, SiO_2 has limited utility as an index of fractionation. At high SiO_2 the rate of change of SiO_2 with fractionation is considerably less than at lower SiO_2, giving a misleading impression of the extent of fractionation when viewed purely as Harker diagrams. Preferable to SiO_2 is a trace element that remains entirely incompatible throughout differentiation and which has been measured with adequate precision in all of the studied rocks. At Dabbahu Zr fulfils this purpose. Zircon saturation is typically delayed in alkaline rocks because of its high solubility. Thus Zr concentrations at Dabbahu increase from ~100 in basalts to over 1000 in rhyolites. Moreover, Zr is readily and precisely analysed by XRF. We additionally have Zr data for a large number of inclusions and matrix glasses analysed by SIMS, for the purposes of extending the dataset to the most extreme end of the differentiation trend.

Figure 3.12 shows a range of trace elements plotted against Zr in a logarithmic plot, in order to capture the full differentiation trend. These plots illustrate clearly the continuous differentiation sequence recorded at Dabbahu. Fractionation vectors for individual minerals are linear on such plots; their direction reflects the relative mineral-melt partition cofficients (D's) for the elements of interest, while their length denotes the absolute value of the D's. Thus P_2O_5 shows an abrupt inflexion at ~500 ppm Zr due to the saturation of apatite (fig. 3.12a), as previously noted in figure 3.10. A similarly abrupt inflexion in Ba marks the appearance of alkali feldspar as a major phenocryst phase (fig. 3.12d). A less abruptly curved trend for Ti reflects the increasing importance of ilmenite (fig. 3.12c). Vanadium and Sc reflect the importance of both magnetite and cpx through the sequence from basalt through to comendite and pantellerite respectively (figs. 3.12e and f). Sr also shows a relatively smooth variation (fig. 3.12e) due to the progressive change in feldspar composition from anorthite to albite to anorthoclase, and the corresponding increase in D_{Sr} (Blundy & Wood, 1991).

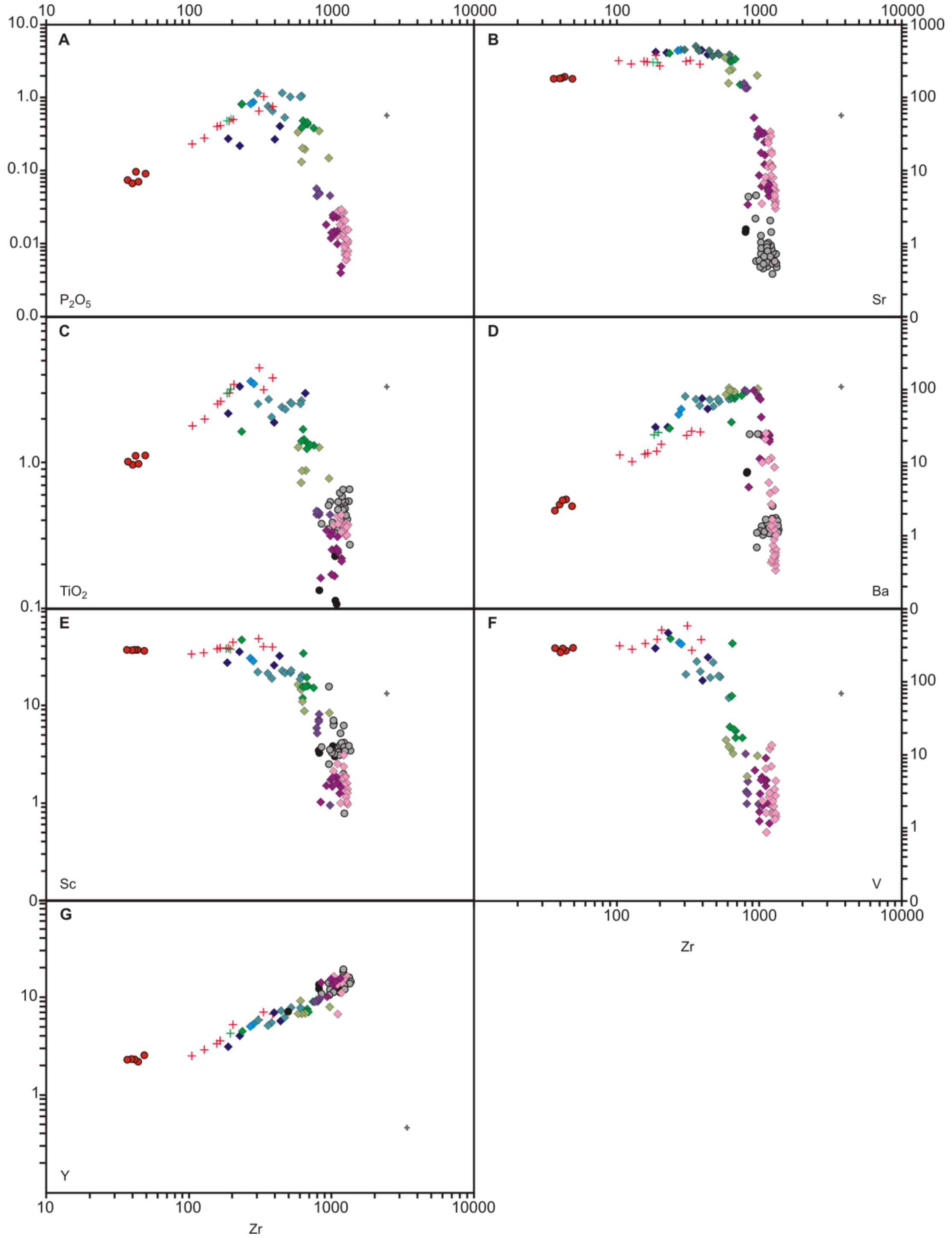

***Figure 3.12**. Trace element variation diagrams plotted against Zr as a proxy for melt fraction. Note the continuous variation from basalt to pantellerite and the large variation in compatible elements. The correlation of Y with Zr testifies to the absence of amphibole as a controlling mineral phase. Key as for figure 3.7.*

In contrast, Y shows a positive trend, reflecting the lack of amphibole crystallisation at Dabbahu (fig. 3.12g). The Manda Hararo basalts of Ferguson et al., (2010) lie at the low-Zr extrapolation of the Dabbahu rocks, as do the LREE enriched samples of Barrat et al., (2003). The LREE-depleted samples of Barrat et al.(2003) are no longer discrepant to the overall Dabbahu trend, but displaced to markedly lower Zr. The trend from low to high LREE basalts is controlled by mantle processes, wheras the trend from the enriched basalts to higher Zr is controlled by crustal processes (fractional crystallisation and mixing). The overall increase in Zr from the most Zr-poor LREE-enriched rift basalt of Barrat et al. (2003) to the most evolved rhyolites is from 105 to 1308, consistent with overall fractionation of 92% by weight.

Mineralogy

Low phenocryst content is a characteristic of the Dabbahu samples; many pumices and peralkaline rhyolites are aphyric. The mineralogy of the porphyritic samples is summarised in figure 3.8. Feldspars are the dominant phase, with plagioclase dominating at the mafic end, and alkali feldspar dominating in the rhyolites. Plagioclase and alkali feldspar coexist in intermediate rocks. The mafic minerals cpx and olivine are present almost across the entire composition range. Ilmenite and magnetite coexist in intermediate rocks only, with more evolved samples characterised by ilmenite alone. Quartz is surprisingly rare; it is found as a phenocryst in just one rhyolite (sample 061). Hydrous minerals are conspicuously lacking at Dabbahu; just one amphibole xenocryst was located in all samples studied.

In order to view the evolving mineral chemistry across such a wide range of rock types we show all mineral compositions on charts similar to figure 3.8, with samples arranged in order of increasing SiO_2 along the vertical axis. We distinguish texturally between phenocryst cores and rims, and microlites or groundmass crystals. To facilitate comparison between the different mineral plots we have left blank lines for samples which either lack a given mineral phase or for which analyses were not obtained.

Feldspar

Feldspar occurs in almost every sample either as a phenocryst, or in the groundmass (fig. 3.8, 3.13). It is the most common mineral comprising up to 100% of the total phenocrysts in any one sample. Representative analyses are given in table 3.4. The feldspars cover a

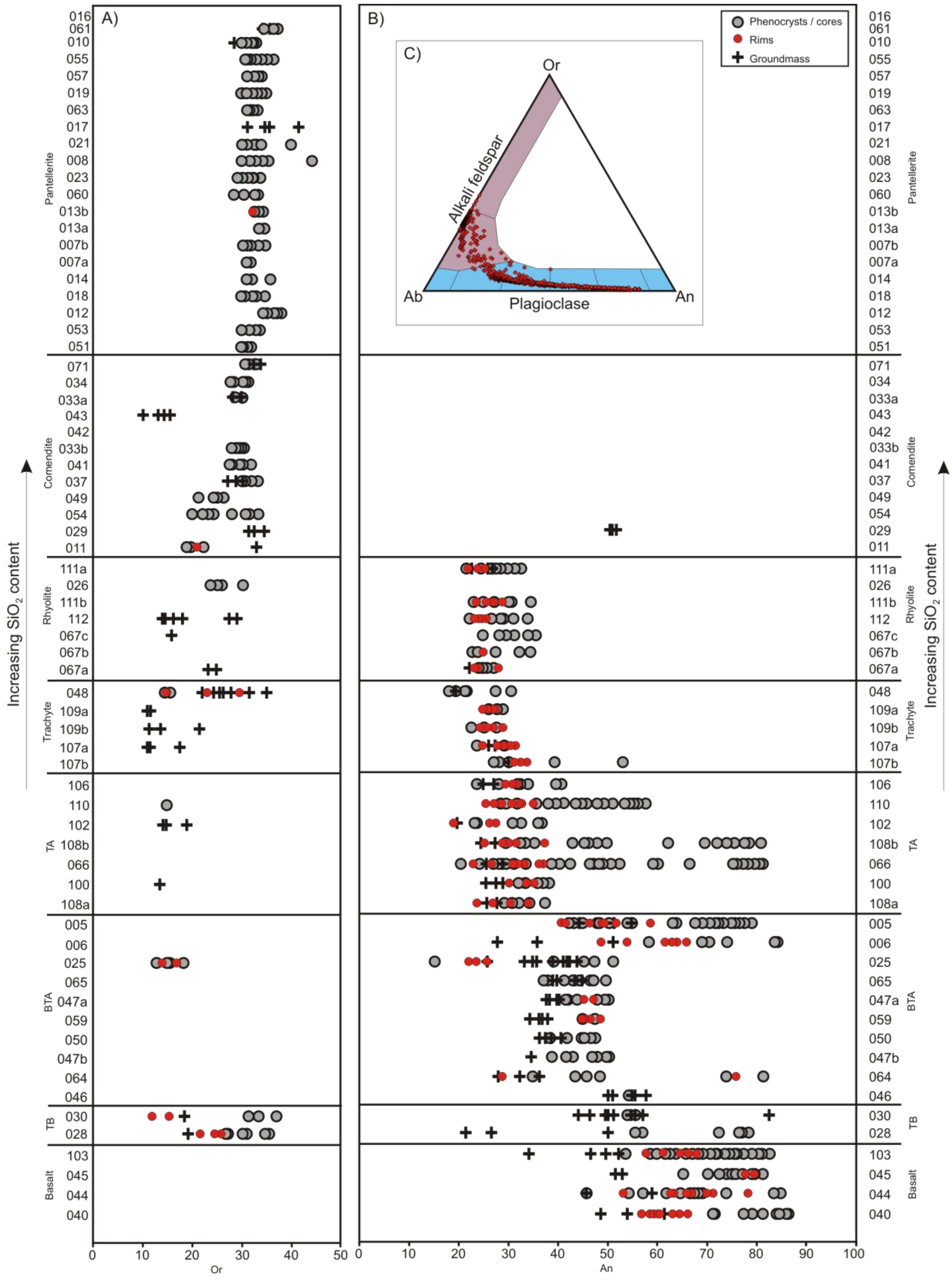

***Figure 3.13**. Feldspar compositions according to rock type. A) alkali feldspars, B) plagioclase feldspars C) ternary diagram of all Dabbahu feldspars showing the range of compositions. Sample list as for figure 3.9. Blank lines denote no feldspar in that sample or no analysis of this phase.*

Representative EMPA analyses of Feldspar

Alkali Feldspar

TAS definition of whole rock		TB[1]	BTA[2]	TA[3]	Trachyte	Comendite	Rhyolite	Pantellerite	
	Sample	028	025	110	048	011	026	057	
	Crystal	1	5	1	1	4	4	1	*Typical error*
	Identifier	core	core	core	core	core	core	core	*1 σ*
wt % oxide	SiO_2	66.75	65.30	61.92	64.32	65.69	66.26	67.87	*0.14*
	TiO_2	b.d.	b.d.	0.49	b.d.	b.d.	b.d.	b.d.	*0.01*
	Al_2O_3	19.05	20.26	21.50	21.27	20.04	19.77	18.65	*0.10*
	$FeO_{(T)}$	0.46	0.25	1.74	0.14	0.24	0.25	0.71	*0.03*
	MnO	b.d.	b.d.	b.d.	b.d.	b.d.	b.d.	b.d.	*0.02*
	MgO	b.d.	b.d.	0.12	b.d.	b.d.	b.d.	b.d.	*0.00*
	CaO	0.19	1.15	4.95	1.87	1.04	0.52	b.d.	*0.01*
	Na_2O	7.50	8.84	6.51	7.77	9.08	8.80	8.38	*0.14*
	K_2O	6.23	2.71	2.37	3.93	3.47	4.27	5.78	*0.07*
	Total	100.17	98.51	99.60	99.29	99.54	99.87	101.39	
No of cations	**Si**	2.98	2.93	2.79	2.88	2.93	2.95	3.00	
(8 oxygens)	**Ti**	0.00	0.00	0.02	0.00	0.00	0.00	0.00	
	Al	1.00	1.07	1.14	1.12	1.05	1.04	0.97	
	Fe	0.02	0.01	0.07	0.01	0.01	0.01	0.03	
	Mn	0.00	0.00	0.00	0.00	0.00	0.00	0.00	
	Mg	0.00	0.00	0.01	0.00	0.00	0.00	0.00	
	Ca	0.01	0.06	0.24	0.09	0.05	0.02	0.00	
	Na	0.65	0.77	0.57	0.68	0.79	0.76	0.72	
	K	0.36	0.16	0.14	0.22	0.20	0.24	0.33	
	CATSUM	5.02	4.99	4.97	5.00	5.03	5.03	5.04	
End Members	**An**	0.88	5.62	25.29	9.07	4.80	2.42	0.00	
	Ab	64.09	78.53	60.25	68.23	76.08	73.94	68.78	
	Or	35.04	15.85	14.45	22.71	19.12	23.63	31.22	

Plagioclase

TAS definition of whole rock		basalt	TB[1]	BTA[2]	TA[3]	Trachyte	Rhyolite	
	Sample	040	028	005	066	107a	112	
	Crystal	1	2	2	2	3	3	*Typical error*
	Identifier	core	core	core	core	core	core	*1 σ*
wt % oxide	SiO_2	47.11	53.50	50.24	59.24	61.43	62.99	*0.18*
	TiO_2	b.d.	0.18	b.d.	b.d.	b.d.	b.d.	*0.03*
	Al_2O_3	33.28	28.21	30.61	25.01	24.41	23.41	*0.32*
	$FeO_{(T)}$	0.48	0.99	0.74	0.42	0.45	0.27	*0.30*
	MnO	b.d.	b.d.	b.d.	b.d.	b.d.	b.d.	*0.03*
	MgO	0.13	0.13	0.16	0.06	b.d.	b.d.	*0.01*
	CaO	16.87	11.60	14.35	7.05	6.03	4.73	*0.08*
	Na_2O	2.01	4.65	3.22	7.25	7.68	8.26	*0.15*
	K_2O	0.18	0.27	0.19	0.84	0.79	1.24	*0.02*
	Total	100.07	99.53	99.52	99.86	100.80	100.88	
No of cations	**Si**	2.17	2.44	2.31	2.66	2.72	2.78	
(8 oxygens)	**Ti**	0.00	0.01	0.00	0.00	0.00	0.00	
	Al	1.81	1.52	1.66	1.32	1.27	1.22	
	Fe	0.02	0.04	0.03	0.02	0.02	0.01	
	Mn	0.00	0.00	0.00	0.00	0.00	0.00	
	Mg	0.01	0.01	0.01	0.00	0.00	0.00	
	Ca	0.83	0.57	0.71	0.34	0.29	0.22	
	Na	0.18	0.41	0.29	0.63	0.66	0.71	
	K	0.01	0.02	0.01	0.05	0.04	0.07	
	CATSUM	5.02	5.01	5.01	5.02	5.00	5.00	
End Members	**An**	81.41	57.03	70.37	33.29	28.90	22.35	
	Ab	17.56	41.40	28.53	61.96	66.58	70.68	
	Or	1.03	1.57	1.10	4.75	4.52	6.97	

[1] TB - trachybasalt

[2] BTA - basaltic trachyandesite

[3] TA - trachyandesite

b.d. - below detection

EMPA analyses carried out at University of Bristol

Table 3.4. *Representative EMPA data for Dabbahu feldspar*

considerable range of compositions when viewed as a whole, from bytownite through to sanidine, defining a smooth continuation variation across the feldspar ternary (fig. 3.13c). Plagioclase compositions are equally represented from bytownite through to oligoclase. Groundmass generally has a lower anorthite (An) content than the phenocrysts. Overall, there is a general decrease in An content with increasing SiO_2. This trend is most pronounced if one looks at the most An-poor plagioclases in each sample, which decreases from ~An_{50} in the basalts to An_{20} in the rhyolites. The plagioclase are generally unzoned, but some plagioclase show abrupt zoning suggestive of a sudden change in crystallisation environment. Both normal and reverse zoned phenocrysts occur. For most samples the overall range in An content is limited to about 15 mol%, although several samples of trachyandesite and basaltic trachyandesite have plagioclase populations with very wide ranges in An. The samples with the greatest total range of feldspars are the trachybasalt samples (028 and 030) which range from bytownite to anorthoclase; e.g. sample 28 has alkali feldspar cores ($An_{0.5}$, Ab_{69}, Or_{30}), plagioclase cores (An_{78}, Ab_{22}, Or_0) and groundmass with compositions in between, suggestive of magma mixing. This sample shows mixing on all scales with a comendite (sample 029), and the thin section contains glassy blebs with a fine grained quenched matrix, in contrast to the coarser groundmass of the main matrix.

Alkali feldspar composition is typically more restricted, particularly in the rhyolites. From the onset of alkali feldspar appearance as a major phenocryst phase the Or content increases from 10 to 32 mol%. The average composition through the entire range of rhyolites is around Or_{30} Ab_{68}. This is consistent with the view of Thompson and Mackenzie (1967) who suggested that pantellerites lie within a 'low temperature zone' which has its origin in the 'thermal valley' of the granite system. The limited compositional range found within anorthoclase phenocrysts from peralkaline samples was proposed as further evidence of this.

Minor elements vary little throughout the feldspars with very low values; MgO and FeO tend to be below detection in alkali feldspars, but in plagioclase, MgO is generally below 0.2 wt% while FeO varies up to 1 wt%.

Olivine

Representative olivine analyses are given in table 3.5. Olivine is present within all rock types, as phenocrysts or groundmass. From basalts to comendite, the composition (calculated on a ternary basis) shows a decrease in forsterite (Fo) from Fo_{83} to nearly pure

EMPA analyses of olivines

	TAS definition of whole rock	**Basalt**	**TB[1]**	**BTA[2]**	**TA[3]**	**Trachyte**	**Rhyolite**	**Comendite**	**Pantellerite**	***Typical error***
	Sample no	**40**	**28**	**5**	**66**	**109b**	**26**	**11**	**53**	***1 σ***
	Crystal no	**2**	**3**	**1**	**2**	**6**	**6**	**4**	**3**	
	Identifier	core	core	rim	core	core	core	core	core	
wt%	**SiO_2**	37.77	39.05	35.60	33.31	32.89	29.11	29.45	29.12	*0.19*
	TiO_2	0.03	b.d.	0.06	0.05	0.03	b.d.	b.d.	b.d.	*0.01*
	Al_2O_3	b.d.	b.d.	b.d.	0.08	b.d.	b.d.	b.d.	b.d.	*0.03*
	$FeO_{(T)}$	25.41	17.60	37.36	45.17	50.15	66.22	66.00	66.51	*0.16*
	MnO	0.39	0.28	0.75	1.70	2.15	3.49	3.49	4.08	*0.01*
	MgO	36.93	42.87	26.61	19.34	16.00	0.35	0.54	0.06	*0.32*
	CaO	0.36	0.30	0.29	0.55	0.33	0.59	0.64	0.51	*0.03*
	Na_2O	b.d.	b.d.	b.d.	b.d.	b.d.	b.d.	b.d.	b.d.	*0.06*
	Total	100.90	100.09	100.67	100.21	101.55	99.76	100.12	100.27	
	Si	0.99	0.99	0.99	0.98	0.98	0.99	0.99	0.99	
	Ti	0.00	0.00	0.00	0.00	0.00	0.00	0.00	0.00	
	Al	0.00	0.00	0.00	0.01	0.00	0.00	0.00	0.00	
	Fe	0.56	0.37	0.87	1.12	1.25	1.88	1.86	1.89	
	Mn	0.01	0.01	0.02	0.04	0.05	0.10	0.10	0.12	
	Mg	1.44	1.63	1.11	0.85	0.71	0.02	0.03	0.00	
	Ca	0.01	0.01	0.01	0.02	0.01	0.02	0.02	0.02	
	Na	0.00	0.00	0.00	0.00	0.00	0.00	0.00	0.00	
	CATSUM	*3.01*	*3.01*	*3.00*	*3.02*	*3.02*	*3.01*	*3.01*	*3.01*	
	Mg#	72	81	56	43	36	1	1	0	
End member calculations	**Forsterite**	72	81	55	42	35	1	1	0	
	Fayalite	28	19	44	56	62	94	94	94	
	Tephroite	0	0	1	2	3	5	5	6	

[1] *TB - trachybasalt*

[2] *BTA - basaltic trachyandesite*

[3] *TA - trachyandesite*

b.d. - below detection

EMPA analyses carried out at University of Bristol

Table 3.5. *Representative EMPA data for Dabbahu olivines.*

end-member fayalite (Fa$_{96}$), with MgO contents below detection. Fo content is shown in figure 3.14. There is a marked drop in Fo of ~20 mol% content between trachytes and rhyolites. A wide range of olivine compositions can be found within some samples of basalt and basaltic trachyandesite. A basalt (sample 044), for example, contains euhedral olivines of composition Fo$_{83-76}$, with distinctive rims of Fo$_{80-57}$ (fig. 3.9a). Where olivines are rimmed, the rim composition is either a lower Fo content than the cores, as for sample 044, or the rim compositions are contained within the range of phenocryst core compositions e.g sample 25 (basaltic trachyandesite; rim compositions Fo$_{40-20}$, and core compositions of Fo$_{48-04}$). This behaviour is suggestive of magma mixing between more and less evolved end-members, producing hybrids with intermediate compositions, or in some cases, may be caused by entrainment of xenocrysts, or incorporation of antecrysts from the previous increment of crystallisation.

Tephroite (Tp) contents increase systematically with decreasing Fo (fig. 3.14). In the rhyolite samples the tephroite component can be significant (average Tp$_5$); the largest Tp component (Tp_4 – Tp_{14}) is found in a comendite sample. This is higher than olivines from the Olkaria (Kenya) peralkaline magmas which have $Tp_{\sim 0.3}$ (Marshall et al. 2009) and Pantelleria

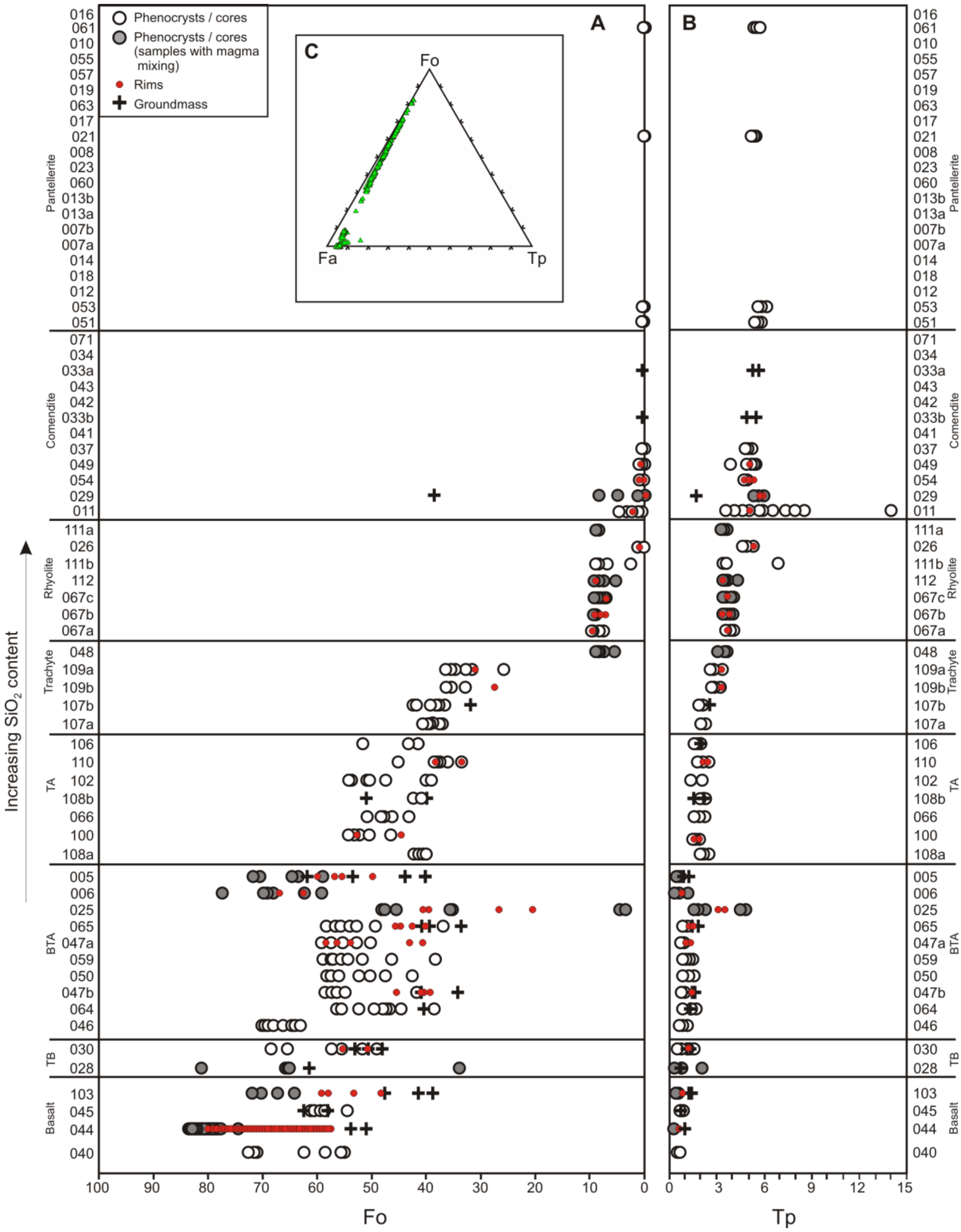

***Figure 3.14**. Forsterite (A) and Tephroite (B) end member range in olivines according to SiO_2 content within rock type (calculated on a ternary basis with Fa). C) Ternary end member diagram. Grey circles indicate samples which show evidence of magma mixing on a macro or micro scale. Sample list as for figure 3.9. Blank lines denote no olivine in that sample, or no analysis of this phase.*

which have up to Tp_7 (White et al. 2009). Calcium is consistently low; always below 2 wt% and typically <1 wt%. Inclusions are found within the olivines, particularly apatite and Fe-Ti oxides and quenched melt inclusions, which are common in the basaltic trachyandesite, trachyandesite and trachyte samples. In the rhyolites, metaluminous and comendite samples contain greater numbers of apatite and oxide inclusions in larger crystals (<1.5 mm) than their pantellerite counterparts (<200 µm).

Clinopyroxene

Clinopyroxenes (cpx) are found within all rock types and compositionally range from Mg-rich augites and diopsides, to Fe-rich augites (fig. 3.15, table 3.6). Five aegerine-augites were identified from 3 peralkaline samples, co-existing with augites. Compositions show a steady decrease in Mg number (100*Mg/(Mg+Fe) from 85 in the basalts through to zero in the comendites (fig. 3.15). 336 cpx analyses from pantellerite rhyolite samples show very limited differences in composition (Mg_{5-0}). The majority of basaltic trachyandesite, trachyandesite and trachyte samples also show a generally restricted composition ~Mg_{75-50}. However, some samples show a large range of compositions such as sample 025 (basaltic trachyandesite) which almost spans the entire range shown by all Dabbahu samples (Mg_{72-4}), and the metaluminous rhyolite cpx which range from Mg_{62-3}. Again, this is suggestive of a component of magma mixing in these samples.

Phenocrysts are diverse in appearance; they can occasionally be zoned, and appear as euhedral crystals, as radial intergrowths with plagioclase, as glomerocrysts, or as sponge textured crystals which have been partially reabsorbed due to dis-equilibrium, and then overgrown with distinct Fe rich rims (fig. 3.9e). The change in Mg# in the latter case is from Mg_{72} in the core to Mg_{50} in the rims. Two distinct populations of cpx cores are found in a comendite sample (029); those which are close to diopside composition and those which are ferrohedenbergite (fig. 3.10d). The rims around the ferrohedenbergite crystals sit between the two core populations in composition indicating this sample has been subjected to magma mixing just prior to eruption.

Minor elements show some variation overall e.g. MnO varies from 4 wt% in one basaltic crystal down to zero in the peralkaline crystals, however the majority contain <1.6 wt% MnO. TiO_2 and Al_2O_3 also show a decrease in content from basalt to the peralkalines, ~4 to zero and 6 to zero respectively, although as per MnO, the bulk of the samples are <1.5 and <3 wt% respectively.

Representative EMPA analyses of Clinopyroxene

TAS definition of whole rock		Basalt	TB[1]	BTA[2]	TA[3]	Trachyte	Rhyolite	Comendite	Pantellerite	*Typical error*
	Sample	**40**	**28**	**5**	**100**	**48**	**112**	**11**	**51**	***1 σ***
	Crystal	**3**	**8**	**6**	**3**	**5**	**1**	**3**	**5**	
	Identifier	**core**	**core**	**core**	**core**	**core**	**core**	**core**	**core**	
	SiO_2	50.63	48.51	51.94	52.98	48.79	49.03	47.76	48.10	*0.01*
	TiO_2	1.22	1.63	0.90	0.33	0.70	0.57	0.42	0.41	*0.06*
	Al_2O_3	2.49	2.21	1.72	0.53	0.78	1.23	0.46	0.19	*0.01*
	$FeO_{(T)}$	8.73	18.21	10.86	12.47	25.41	21.83	29.10	30.66	*0.17*
	MnO	0.21	1.07	0.43	0.68	0.87	0.89	1.34	1.48	*0.04*
	MgO	14.90	8.77	14.56	14.10	3.78	6.59	0.92	0.13	*0.01*
	CaO	21.14	18.95	19.67	18.57	19.47	19.77	19.86	18.74	*0.09*
	Na_2O	0.30	0.49	0.39	0.31	0.24	0.31	0.48	0.95	*0.06*
	K_2O	b.d.	b.d.	b.d.	b.d.	b.d.	b.d.	b.d.	b.d.	*0.01*
	Cr_2O_3	0.12	b.d.	b.d.	b.d.	b.d.	b.d.	b.d.	b.d.	*0.02*
	Total	99.73	99.83	100.47	99.97	100.03	100.22	100.35	100.65	
CATIONS	**Si**	1.88	1.89	1.93	1.99	1.97	1.93	1.96	1.97	
	Ti	0.03	0.05	0.03	0.01	0.02	0.02	0.01	0.01	
	Al	0.11	0.10	0.08	0.02	0.04	0.06	0.02	0.01	
	Fe	0.27	0.59	0.34	0.39	0.86	0.72	1.00	1.05	
	Mn	0.01	0.04	0.01	0.02	0.03	0.03	0.05	0.05	
	Mg	0.83	0.51	0.81	0.79	0.23	0.39	0.06	0.01	
	Ca	0.84	0.79	0.78	0.75	0.84	0.83	0.87	0.82	
	Na	0.02	0.04	0.03	0.02	0.02	0.02	0.04	0.08	
	K	0.00	0.00	0.00	0.00	0.00	0.00	0.00	0.00	
	Cr	0.00	0.00	0.00	0.00	0.00	0.00	0.00	0.00	
	CATSUM	4.00	4.00	4.00	4.00	4.00	4.00	4.00	4.00	
Recalculated Fe[4]	**Fe^{3+}**	0.07	0.06	0.04	0.00	0.00	0.07	0.08	0.10	
	Fe^{2+}	0.20	0.53	0.30	0.39	0.85	0.65	0.92	0.95	
End member calculations	**(Mg) En**	42.59	26.89	41.85	40.94	11.79	19.94	2.91	0.42	
	(Fe) Fs	14.00	31.32	17.51	20.31	44.51	37.06	51.80	55.86	
	(Ca) Wo	43.41	41.78	40.64	38.75	43.70	43.00	45.30	43.72	
	Jd	1.40	2.53	1.87	2.31	1.74	1.24	1.13	0.81	
	Ae	0.84	1.33	1.03	0.00	0.19	1.27	2.87	6.99	
	Q	97.76	96.14	97.10	97.69	98.07	97.50	95.99	92.19	

[1] *TB - trachybasalt*

[2] *BTA - basaltic trachyandesite*

[3] *TA - trachyandesite*

[4] *Recalculated Fe** - calculated using the method of Schumacher (1997)*

b.d. - below detection

EMPA analyses carried out at University of Bristol

Table 3.6. *Representative EMPA data for Dabbahu clinopyroxene.*

Na_2O in contrast shows an increase in the range in each sample with increasing SiO_2; an aegirine augite contains 6 wt%. The higher values are limited to the peralkaline rocks; the bulk of the crystals contain < 1 wt%. The FeO_t content ranges from 5 to 34 wt%. The calculated Fe^{3+} content, estimated from stoichiometry using the method of Schumacher (1991), shows that up to 43% of the FeO_t is Fe^{3+}, although one crystal has a high proportion of 71 wt%.

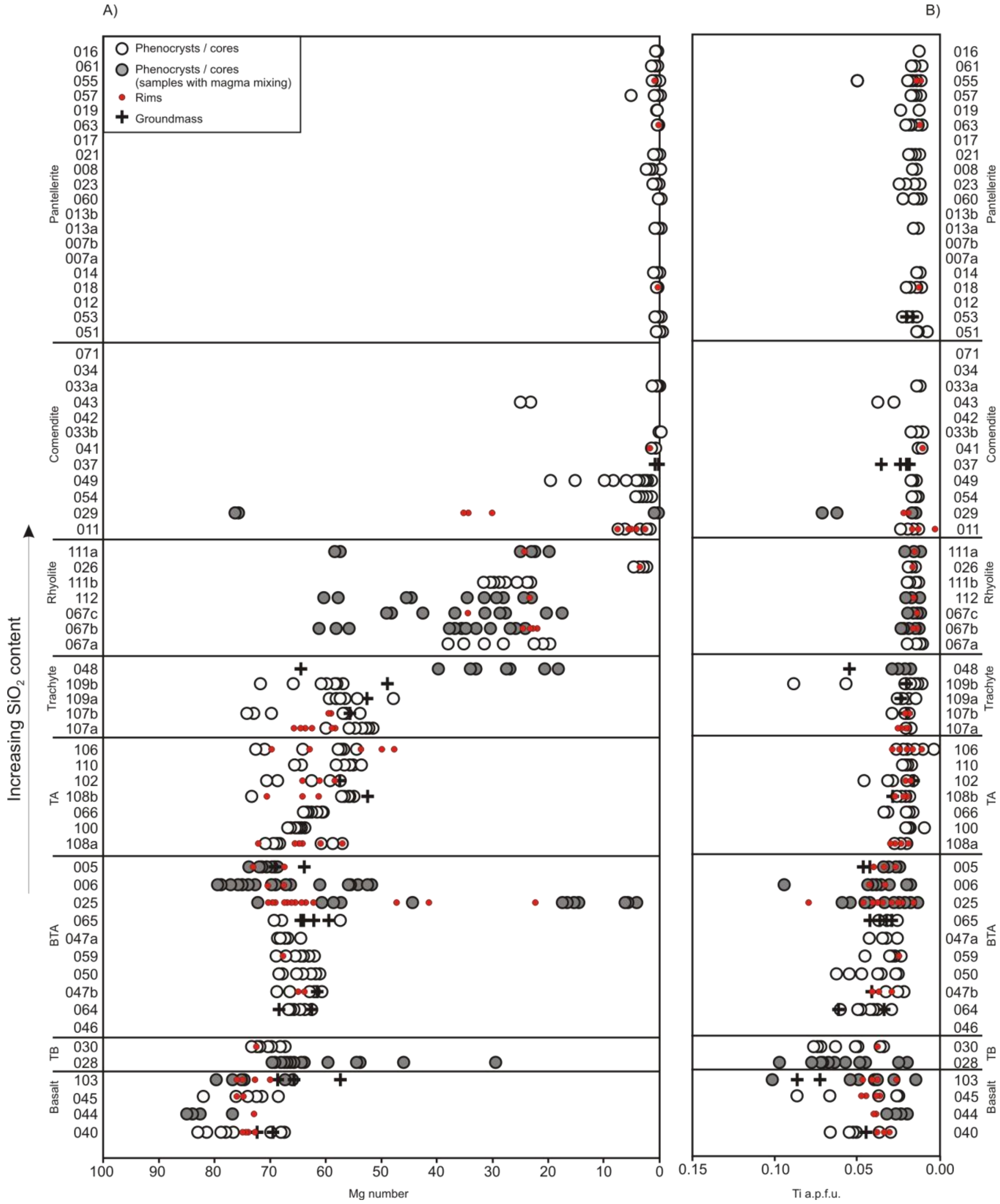

Figure 3.15. *Variation in clinopyroxene compositions according to rock type A) Mg-number. B) Ti atoms per formula unit. TB – Trachy Basaslt, BTA – Basaltic Trachy Andesite, TA – Trachy Andesite. Grey circles indicate potentially mixed samples. Sample list as for figure 3.9. Blank lines denote no cpx in that sample, or no analysis of this phase.*

Fe-Ti oxides

Ilmenite and titanomagnetite are found in all rock types except the trachybasalts which contain magnetite only, and the pantellerites which only contain ilmenite (fig. 3.8). Co-existing pairs are rare. Analyses are given in table 3.7. The ulvöspinel component in the cores of titanomagnetite phenocrysts ranges from 21-82 mol% calculated using ILMAT (Lepage 2003), with the Fe^{2+} and Fe^{3+} recalculation method of Carmichael (1967). Bizouard et al. (1980) suggested that there was a progressive decrease of Ti content in magnetite across the rock types reflected by a decrease in the ulvöspinel content, which in turn reflected an increase in the $Fe^{3+}/(Fe^{3+}+Fe^{2+})$ ratio of the liquid due to temperature decrease. However, although we have found that there is variation in the range of TiO_2 overall (0.2 – 28 wt%, median 22 wt%), there is no progressive decrease observed according to rock type. The ilmenite component in ilmenite phenocrysts ranges from 50-99 mol%, although all but two crystals are within the range 80-99 mol% (median 96 mol%). With regards to peralkalinity, magnetite is only found in the comendites (NK/A=1.02 - 1.24), whereas ilmenite is found in both comendites and pantellerites (pantellerites NK/A=1.32 - 1.55). This in part accounts for the trend of comendites to lower bulk Fe contents than pantellerites. This in turn may be indicating slightly more reducing conditions in the pantellerites which appears to favour ilmenite formation (e.g. Toplis and Carroll 1995; White et al. 2005).

Aenigmatite

In alkaline lavas, aenigmatite commonly occurs as a constituent of the groundmass, and more rarely as phenocrysts; one such occurrence is Fantale, Ethiopia (Gibson 1970). At Dabbahu, aenigmatites are found as phenocrysts up to 350 µm in length, in 5 peralkaline rhyolite samples (fig. 3.9h) in which the NK/A ranges from 1.32 – 1.55; 1.55 is the highest NK/A observed in a porphyritic rock from Dabbahu. The aenigmatites have a restricted compositional range; FeO 41-43 wt%, TiO_2 8.2 – 9.5 wt% (table 3.8) and cluster at the aenigmatite end of the aenigmatite-wilkinsonite solid solution (Grew et al. 2008). Experimental data and analysis at Pantelleria, have indicated that aenigmatite is stable at temperatures below 900 ^{o}C (dry) and low oxygen fugacity (at or below FMQ) (Kunzmann 1999; White et al. 2005). Recent experiments by Di Carlo et al., (2010) have further constrained aenigmatite stability showing that aenigmatite requires NK/A >1.2, pressures >100MPa and >2.8 wt% H_2O_{melt}.

Representative EMPA analyses Magnetite

TAS definition of whole rock	basalt	TB[1]	BTA[2]	TA[3]	trachyte	comendite	rhyolite	*Typical error*
Sample	044	030	006	100	107b	049	067c	*1 σ*
Crystal	1	2	4	3	3	1	3	
SiO_2	b.d.	b.d.	b.d.	b.d.	0.10	0.07	0.11	*0.02*
TiO_2	15.64	20.70	19.48	22.22	23.17	25.52	21.02	*0.15*
Al_2O_3	15.80	3.11	2.87	1.84	1.65	0.33	0.80	*0.01*
$FeO_{(T)}$	48.43	70.41	71.98	69.85	71.58	70.74	73.85	*0.57*
MnO	0.29	0.71	0.64	1.02	0.91	1.44	1.02	*0.03*
MgO	10.99	2.37	2.95	2.18	1.57	b.d.	0.15	*0.01*
CaO	b.d.	0.05	b.d.	b.d.	0.02	b.d.	b.d.	*0.01*
Na_2O	b.d.	b.d.	b.d.	b.d.	b.d.	b.d.	b.d.	
K_2O	b.d.	b.d.	b.d.	b.d.	b.d.	b.d.	b.d.	
Cr_2O_3	5.99	0.10	b.d.	b.d.	b.d.	b.d.	b.d.	*0.02*
ZnO	b.d.	b.d.	0.09	0.10	0.13	0.34	0.27	*0.02*
NiO	0.12	b.d.	b.d.	b.d.	b.d.	b.d.	b.d.	*0.01*
Sum:	97.26	97.47	98.02	97.22	99.13	98.45	97.22	
Recalculated Iron[4]								
Fe_2O_3 wt. %	19.41	26.62	30.30	24.74	23.98	19.39	27.23	
FeO wt. %	30.96	46.46	44.72	47.59	50.01	53.30	49.35	
Total:	99.20	100.13	101.05	99.78	101.54	100.39	99.94	
Cation prop.[5]								
Si	0.00	0.00	0.00	0.00	0.00	0.00	0.00	
Ti	0.38	0.57	0.53	0.62	0.63	0.72	0.59	
Al	0.61	0.13	0.12	0.08	0.07	0.01	0.04	
Fe^{+3}	0.47	0.73	0.82	0.69	0.66	0.54	0.77	
Fe^{+2}	0.84	1.41	1.35	1.47	1.52	1.67	1.55	
Mn	0.01	0.02	0.02	0.03	0.03	0.05	0.03	
Mg	0.53	0.13	0.16	0.12	0.08	0.00	0.01	
Ca	0.00	0.00	0.00	0.00	0.00	0.00	0.00	
Na	0.00	0.00	0.00	0.00	0.00	0.00	0.00	
K	0.00	0.00	0.00	0.00	0.00	0.00	0.00	
Cr	0.15	0.00	0.00	0.00	0.00	0.00	0.00	
Zn	0.00	0.00	0.00	0.00	0.00	0.01	0.01	
Ni	0.00	0.00	0.00	0.00	0.00	0.00	0.00	
CATSUM	3.00	3.00	3.00	3.00	3.00	3.00	3.00	
Mol % Usp								
Carmichael (1967)	38%	57%	53%	62%	64%	72%	60%	
Anderson (1968)	24%	56%	51%	60%	63%	72%	60%	
Lindsley & Spencer (1982)	51%	60%	55%	64%	66%	74%	61%	
Stormer (1983)	72%	62%	57%	64%	67%	72%	61%	

Ilmenite

TAS definition of whole rock	basalt	BTA[2]	TA[3]	trachyte	comendite	pantellerite	rhyolite	*Typical error*
Sample	040	065	100	109a	029	014	067a	*1 σ*
Crystal	2	1	6	2	1	2	2	
SiO_2	0.07	b.d.	b.d.	b.d.	b.d.	0.40	b.d.	*0.05*
TiO_2	50.26	46.34	45.82	49.62	51.63	50.47	49.20	*0.44*
Al_2O_3	0.08	0.20	0.21	0.09	b.d.	0.05	0.06	*0.01*
$FeO_{(T)}$	47.23	46.01	45.90	46.94	46.53	47.37	47.79	*0.87*
MnO	0.64	0.77	1.01	1.86	1.92	2.03	1.49	*0.04*
MgO	1.45	2.20	2.88	1.58	b.d.	b.d.	0.41	*0.01*
CaO	0.26	0.00	0.00	0.10	b.d.	b.d.	0.15	*0.07*
Na_2O	b.d.	b.d.	b.d.	b.d.	b.d.	b.d.	b.d.	
K_2O	b.d.	b.d.	b.d.	b.d.	b.d.	0.06	b.d.	*0.01*
Cr_2O_3	b.d.	b.d.	b.d.	b.d.	b.d.	b.d.	b.d.	
ZnO	b.d.	b.d.	b.d.	0.06	b.d.	b.d.	b.d.	*0.02*
NiO	b.d.	b.d.	b.d.	b.d.	b.d.	b.d.	b.d.	
Sum:	99.99	95.51	95.81	100.25	100.08	100.38	99.10	
Recalculated Iron[4]								
Fe_2O_3 wt. %	6.11	10.03	12.05	7.98	2.24	3.94	6.62	
FeO wt. %	41.73	36.99	35.06	39.76	44.51	43.82	41.84	
Total:	100.61	96.52	97.02	101.05	100.30	100.77	99.77	
Cation prop.[5]								
Si	0.00	0.00	0.00	0.00	0.00	0.01	0.00	
Ti	0.94	0.90	0.88	0.92	0.98	0.95	0.94	
Al	0.00	0.01	0.01	0.00	0.00	0.00	0.00	
Fe^{+3}	0.11	0.19	0.23	0.15	0.04	0.07	0.13	
Fe^{+2}	0.87	0.80	0.75	0.82	0.94	0.92	0.88	
Mn	0.01	0.02	0.02	0.04	0.04	0.04	0.03	
Mg	0.05	0.08	0.11	0.06	0.00	0.00	0.02	
Ca	0.01	0.00	0.00	0.00	0.00	0.00	0.00	
Na	0.00	0.00	0.00	0.00	0.00	0.00	0.00	
K	0.00	0.00	0.00	0.00	0.00	0.00	0.00	
Cr	0.00	0.00	0.00	0.00	0.00	0.00	0.00	
Zn	0.00	0.00	0.00	0.00	0.00	0.00	0.00	
Ni	0.00	0.00	0.00	0.00	0.00	0.00	0.00	
CATSUM	2.00	2.00	2.00	2.00	2.00	2.00	2.00	
Mol% ilmenite								
Carmichael (1967)	94%	90%	88%	92%	98%	96%	94%	
Anderson (1968)	94%	89%	87%	92%	98%	96%	94%	
Lindsley & Spencer (1982)	94%	90%	88%	92%	98%	96%	94%	
Stormer (1983)	94%	90%	88%	92%	98%	96%	94%	

[1] TB - trachybasalt

[2] BTA - basaltic trachyandesite

[3] TA - trachyandesite

[4] Recalculated iron and total (ulvospinel basis) method of Carmichael (1967)

[5] Cation proportion calculated from Carmichael (1967)

b.d. - below detection

EMPA analyses carried out at University of Bristol

Table 3.7. *Representative EMPA of Fe-Ti Oxides.*

Minor Phases

Amphibole is rare in the Dabbahu rocks. A single phenocryst (300 μm in length) was indentified in pantellerite sample 023 (fig. 3.8g); sample analysis is given in table 3.8. The amphibole is a sodic-amphibole (arfvedsonite), which is commonly associated with alkali granites. Textural evidence suggests the phenocryst is xenocrystic. Very little experimental work has been carried out on the stability of arfvedsonite, but Ernst (1962), suggests arvedsonite is stable in temperatures up to 712 °C at 200 MPa P_{fluid} and low oxygen fugacity (iron-wütstite buffer). Plausibly the amphibole was entrained from plutonic equivalents of the pantellerites at shallow depth.

Representative EMPA analyses of Aenigmatites

Sample no	**53**	**55**	**55**	**57**	**57**	**60**	**61**	***Typical error***
Crystal no	**1**	**5**	**21**	**2**	**3**	**1**	**1**	***1 σ***
SiO_2	41.35	39.84	40.11	40.56	40.53	41.41	40.27	*0.18*
TiO_2	9.31	8.86	9.23	9.21	9.25	8.16	8.99	*0.05*
Al_2O_3	0.24	1.02	0.83	0.58	0.60	0.34	0.84	*0.01*
$FeO_{(T)}$	41.92	42.17	41.53	41.90	41.27	42.14	42.10	*0.21*
MnO	1.31	1.27	1.27	1.20	1.21	1.16	1.11	*0.05*
MgO	b.d.	b.d.	b.d.	b.d.	b.d.	b.d.	0.05	*0.01*
CaO	0.18	0.94	0.73	0.54	0.62	0.24	0.81	*0.01*
Na_2O	7.07	6.56	6.79	6.69	6.80	7.04	6.69	*0.11*
K_2O	b.d.	b.d.	b.d.	b.d.	b.d.	b.d.	b.d.	
Total	101.39	100.67	100.50	100.68	100.28	100.50	100.95	
cations (basis of 20 oxygen)								
Si	5.87	5.70	5.74	5.81	5.81	5.91	5.75	
Ti	0.99	0.95	0.99	0.99	1.00	0.88	0.96	
Al	0.04	0.17	0.14	0.10	0.10	0.06	0.14	
Fe	4.97	5.05	4.97	5.02	4.95	5.03	5.02	
Mn	0.16	0.15	0.15	0.15	0.15	0.14	0.13	
Mg	0.00	0.00	0.00	0.00	0.00	0.00	0.01	
Ca	0.03	0.14	0.11	0.08	0.09	0.04	0.12	
Na	1.94	1.82	1.89	1.86	1.89	1.95	1.85	
K	0.00	0.00	0.00	0.00	0.00	0.00	0.00	
CATSUM	14.00	14.00	14.00	14.00	14.00	14.00	14.00	
Recalculated Fe*								
Fe^{3+}	0.19	0.33	0.27	0.16	0.16	0.32	0.29	
Fe^{2+}	4.79	4.72	4.70	4.86	4.79	4.71	4.74	

b.d. - below detection

Recalculated Fe - calculated using the method of Schumacher (1997)*

*Classification** - calculated from Leake et al (1997)*

EMPA analyses carried out at University of Bristol

EMPA analyses of Amphibole

Sample no	**23**	***Typical error***
Crystal no	**1**	***1 σ***
SiO_2	49.51	*0.13*
TiO_2	1.12	*0.01*
Al_2O_3	0.47	*0.01*
$FeO_{(T)}$	36.60	*0.17*
MnO	1.00	*0.03*
MgO	b.d.	
CaO	2.47	*0.03*
Na_2O	6.97	*0.19*
K_2O	1.39	*0.02*
Total	99.53	
Recalculated Fe*		
FeO	*34.55*	
Fe_2O_3	*1.56*	
Total	*99.04*	
cation (basis of 23 oxygen and minimum Fe3+)		
Si	7.90	
Ti	0.13	
Al	0.09	
Fe^{2+}	4.60	
Fe^{3+}	0.28	
Mn	0.14	
Mg	0.00	
Ca	0.42	
Na	2.16	
K	0.28	
CATSUM	16	
Classification**		Arvedsonite

Table 3.8. *Representative EMPA data for Dabbahu aenigmatites and amphibole.*

Apatite is a common constituent of the more silica rich rocks. It is absent from all basalts and trachybasalts except a single sample (103) where apatite inclusions are found in cpx. Apatite appears with more frequency in the basaltic trachyandesites through to rhyolites. Apatite is found as discrete microphenocrysts, but more frequently as inclusions in olivines, cpx, FeTi oxides and plagioclase, particularly within the trachytes and metaluminous rhyolites where the phenocrysts contain a very high number of inclusions. This textural evidence suggests early saturation of apatite, consistent with the observed P_2O_5-SiO_2 trends (Figs. 11g and 12a). Comendites contain far fewer apatites than the metaluminous rhyolites, and these are often zoned. Apatites are even less frequent in the pantellerites although they are found in almost every crystal-bearing sample. They are generally small (<20 µm), although occasionally reach 100 µm in length.

Zircons were found in only two samples; rare zircons in a metaluminous rhyolite (sample 067b), and numerous zircons in a mildly peralkaline comendite (PI = 1.09) from Gab'ho (sample 071). The zircons occur as euhedral microphenocrysts <40 µm in length (fig. 3.9f). Cathodoluminesence analysis reveals concentric zoning and inherited cores. Zircons occur as single microphenocrysts, but more frequently in clusters and occasionally associated with alkali feldspar.

Quartz does not appear as a phenocryst in any Dabbahu sample, except, a peralkaline rhyolite (sample 061), where it is a relatively frequent component (2.9 modal%). This tiny obsidian flow (~100 m x 3 m), is the most crystal-rich of the obsidians with 11 modal % phenocrysts. The quartz phenocrysts are euhedral and up to 500 µm in length. This sample also contains quartz-feldspar overgrowth rims and granophyric intergrowths around feldspars, and quartz-feldspar spherules. Some pantellerites contain rare, anhedral crystals of cristobalite (fig. 3.9d) generally <100 µm. One pantellerite (sample 007a) contains a spherule of crystal-rich material <100 µm diameter, which includes quartz micro-crystals. Melt inclusion analyses (Field et al. 2011) from four Dabbahu samples fall outside of quartz stability fields defined in Scaillet and MacDonald (2001) at the calculated pressure-temperature conditions, which support the absence of quartz phenocrysts.

Intensive Parameters

Temperature

Pre-eruption temperatures were calculated utilising the available mineral compositions; both single and multiple mineral methods and mineral/glass (liquid) thermometers detailed below. Peralkaline rocks, in particular, contain limited phenocrysts, and are usually lacking in the mineral assemblages suitable for thermobarometry analysis. However, by calculating temperatures via several methodologies, it has been possible to build a comprehensive picture of pre-eruption temperatures across all rock types (table 3.9, fig. 3.16).

Fe-Ti Oxides

Co-existing Fe-Ti oxides are limited in the Dabbahu samples; usually one of the oxides will dominate with just one or two crystals of the other being located, and touching Fe-Ti oxide pairs are even more rare. The programme ILMAT (Lepage 2003) was used to calculate the FeO/Fe_2O_3 ratio with the method of Carmichael (1967), and check stoichiometry. Each ilmenite was then checked against each magnetite analysis in the same sample for Mg/Mn equilibrium using the method of Bacon and Hirschmann (1988). Data which failed this test were excluded. Due to the rarity of oxide pairs, individual analysis were used rather than the common practice of averaging the oxides from a sample, as this would introduce uncertainty as to whether all ilmenites were in equilibrium with all magnetites, and would also hide any significant trends or temporal evolution within an individual sample (Blundy and Cashman 2008). Each equilibrium pair was then processed using the method of Ghiorso and Evans (2008) to determine temperature.

Fourteen samples yielded temperatures from Fe-Ti oxides, five of which were rhyolites, the rest being intermediates (table 3.9). The basalts and trachybasalts contained magnetite only, or contained oxides which were deemed to be out of equilibrium. The rhyolites largely contained ilmenite without magnetite. Temperatures range from 716-997 ^{o}C in the rhyolites, and 919-1168 ^{o}C in the intermediates. Bizouard et al. (1980) obtained three temperatures from intermediate samples using Fe-Ti oxides: 930, 990 and 1010 ^{o}C (these samples were originally described as alkali rhyolites). However, recalculating these temperatures using the same methods as for our samples, showed only one sample to have oxides in equilibrium, yielding a temperature of 992 ^{o}C, reduced from the 1010 ^{o}C obtained by Bizouard et al (1980).

The 992 ^{o}C is in line with temperatures gained from the current study for intermediate rocks. When plotted on a simple sample v temperature plot, a trachyandesite (sample 100) shows two distinct temperature groupings of 920 - 924 ^{o}C and 1063-1110 ^{o}C suggestive of magma mixing immediately prior to eruption. Two other samples (066 and 111b) hint at a similar scenario, but are not conclusive.

			Thermometry summary						**Oxygen fugacity**			
			Fe/Ti oxides[1]	**Fsp/liquid[2,3]**		**Ol/Liquid[4]**	**QUILF95[5]**	**CPX/Liquid[6]**	**log $f O_2$ Δ FMQ[7] Ghiorso and Evans 2008**		**log $f O_2$ Δ FMQ[5] QUILF95**	
Sample	**Rock type[8]**	**mol NK/A**		**Plag**	**Alk fsp**				**max**	**min**	**max**	**min**
				SEE ±36 ° C	*SEE ±23 ° C*	*SEE ±44 ° C*		*SEE ±45 ° C*	*stdev ±0.18*			
40	*basalt*	*0.36*						1012-1151				
44	*basalt*	*0.32*						1171-1205				
45	*basalt*	*0.45*						1078				
103	*basalt*	*0.46*				1113-1117		1066-1132				
5	*BTA*	*0.61*						1003-1048				
6	*BTA*	*0.58*	952-1040					994-1064	-0.06	-0.11		
25	*BTA*	*0.74*	919-1043					894-1094	-0.32	-0.37		
47a	*BTA*	*0.67*	1001-1045					1005-1039	-0.79	-0.82		
47b	*BTA*	*0.69*						996-1042				
50	*BTA*	*0.71*	1031-1099					1004-1067	-0.37	-0.39		
59	*BTA*	*0.67*	1042-1168	848-858					-0.48	-0.99		
64	*BTA*	*0.7*						1017-1074				
65	*BTA*	*0.7*	1100-1122					1010-1079	-0.41	-0.44		
28	*TB*	*0.58*						1047-1132				
30	*TB*	*0.6*						1047-1114				
66	*TA*	*0.8*	924-1135						-0.28	-0.94		
100	*TA*	*0.81*	920-1110					992-1017	-0.13	-0.99		
108a	*TA*	*0.77*										
108b	*TA*	*0.79*		963-974				992-1033				
48	*trachyte*	*0.91*										
102	*trachyte*	*0.8*						930-989				
106	*trachyte*	*0.82*		968-983				936-983				
110	*trachyte*	*0.84*										
107a	*trachyte*	*0.84*										
107b	*trachyte*	*0.87*						959				
109a	*trachyte*	*0.9*	983					1008	-0.94			
109b	*trachyte*	*0.95*						899-999				
112	*rhyolite*	*0.91*	844				829-848		-1.89		-1.23	-1.28
111a	*rhyolite*	*0.91*		885-887			803-1043				-0.10	-0.91
26	*rhyolite*	*0.92*					752-844				-0.64	-1.30
67a	*rhyolite*	*0.92*	896-965	1066-1080					0	-1.44		
67b	*rhyolite*	*0.92*		879-883								
67c	*rhyolite*	*0.92*		885-891								
111b	*rhyolite*	*0.93*	866-997	961-966			847-883		-1.19	-1.71	-0.75	-1.00
11	*comendite*	*1.02*	813-1209				635-884		0.49	-0.74	0.07	-1.33
54	*comendite*	*1.02*					707-827				0.12	-0.92
71	*comendite*	*1.09*			798-801							
49	*comendite*	*1.1*	716-815		824-830		777-830		-2.7	-3.6	-1.51	-2.03
34	*comendite*	*1.11*			689-692							
33a	*comendite*	*1.11*			687-690							
33b	*comendite*	*1.13*										
43	*comendite*	*1.14*			689-692							
41	*comendite*	*1.17*			780-787							
37	*comendite*	*1.18*			690-698							
29	*comendite*	*1.24*		903-917	818-827		766-823				-0.60	-2.30
53	*pantellerite*	*1.32*			709-714		750-836				-1.73	-2.55
51	*pantellerite*	*1.33*			856-860		742-771				-0.39	-1.37
12	*pantellerite*	*1.4*			879-886							
61	*pantellerite*	*1.4*			764-769		727-761				-0.27	-0.63
13	*pantellerite*	*1.43*			885-887							
13b	*pantellerite*	*1.43*			696-698							
10	*pantellerite*	*1.45*			690-696							
19	*pantellerite*	*1.47*			697-704							
21	*pantellerite*	*1.5*			691-705							
17	*pantellerite*	*1.51*			686-701							
18	*pantellerite*	*1.51*			786-794							
23	*pantellerite*	*1.52*			697-703							
57	*pantellerite*	*1.52*			697-701							
007b	*pantellerite*	*1.52*			760-767							
63	*pantellerite*	*1.54*			780-782							
8	*pantellerite*	*1.55*			742-766							
14	*pantellerite*	*1.55*			755-762							
55	*pantellerite*	*1.55*			697-704							
60	*pantellerite*	*1.55*			692-701							

[1] *Fe / Ti oxide thermometer – Ghiorso and Evans 2008*

[2] *Plagioclase / liquid thermometer – Putirka 2008, equation 24a*

[3] *Alkali feldspar / liquid thermometer – Putirka 2008, equation 24b*

[4] *Olivine/liquid thermometer - Putirka 2008*

[5] *QUILF95 - Andersen et al 1993*

[6] *Cpx / liquid thermometer – Putirka 2008, equation 33.*

[7] *Oxygen fugacity - Ghiorso and Evans 2008*

[8] *Rock type as determined by TAS. BTA - basaltic trachyandesite, TB - trachybasalt, TA - trachyandesite*

Table 3.9. *Table of temperature ranges for each sample derived by a variety of thermometers.*

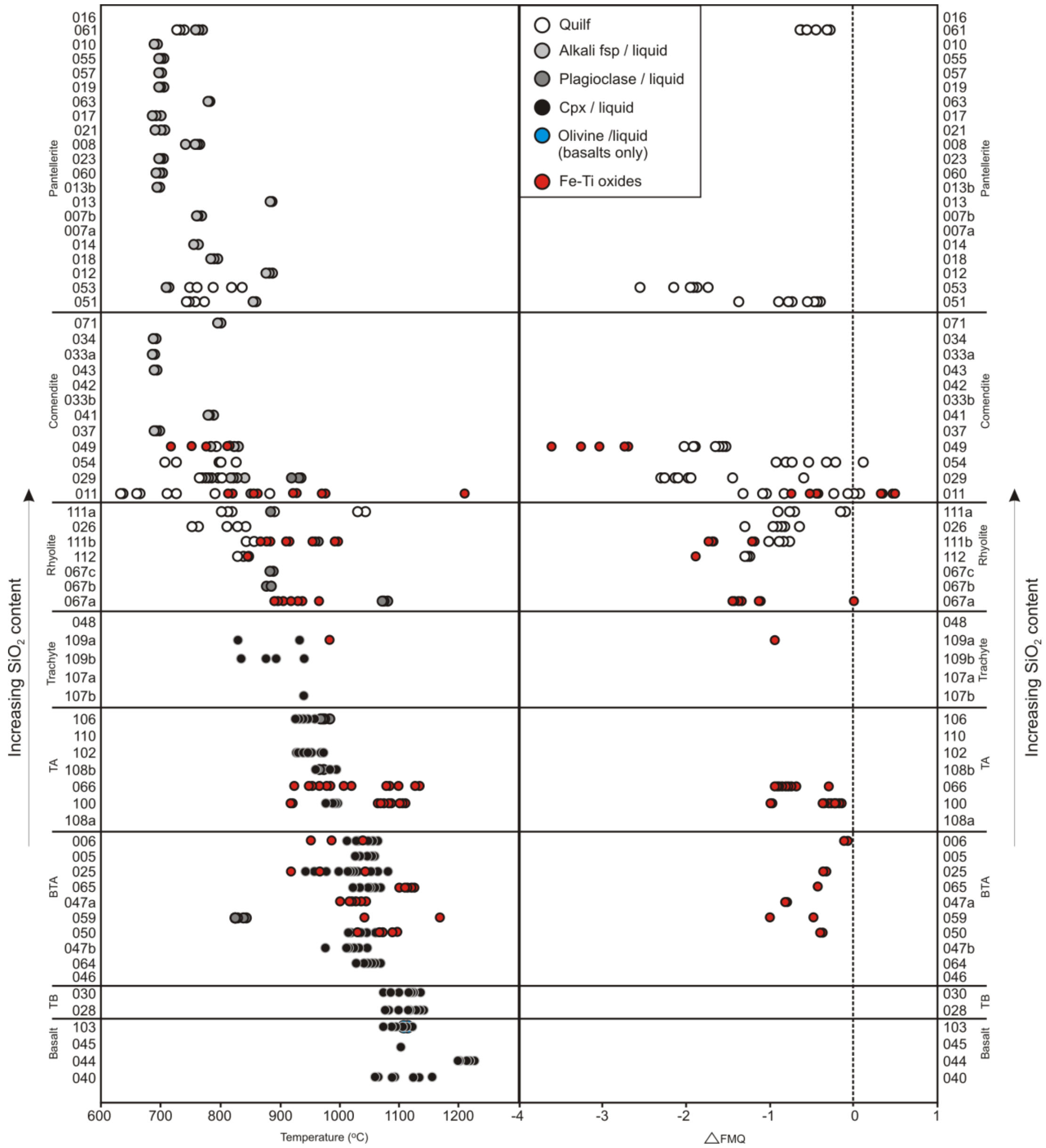

Figure 3.16 *– Summary of calculated temperatures and oxygen fugacities, expressed as log units relative to the fayalite-quartz-magnetite buffer (delta FMQ). The methods used for temperature calculations were: Fe-Ti oxides, Ghiorso and Evans (2008), feldspar / liquid and cpx / liquid, Putirka (2008), QUILF, Andersen et al (1993), olivine / liquid, Putirka (2008). Oxygen fugacity was calculated using the methods of Ghiorso and Evans (2008) and QUILF, Andersen et al (1993).*

Feldspar

Feldspar is the main phenocryst phase in the rhyolites of Dabbahu. As the majority of rhyolites are obsidians, the 'liquid' composition can be obtained from analysing the alkali feldspar and coexisting glass. Plagioclase-liquid thermometry was also used for nine samples. EMPA data from matrix glasses and feldspars (alkali feldspar and plagioclase) were used to calculate the temperature using the method of Putirka (2008). Two feldspar thermometry was not utilised as the feldspars were rejected as texturally unsuitable e.g. plagioclase phenocrysts and alkali feldspar groundmass.

Alkali feldspar-liquid

Temperatures were obtained from twenty seven rhyolite samples using the alkali feldspar / liquid thermometer (table 3.9). The total range of calculated temperatures is 686-887 ^{o}C with an SEE ±23 ^{o}C. In all but four samples, the range of temperatures is very small, <10 ^{o}C.

Plagioclase-liquid

Five rhyolites, three intermediate and a comendite sample yielded temperatures using the plagioclase –liquid thermometer. The calculated temperature range for rhyolites is higher than given by the alkali feldspar/liquid thermometer at 848-1080 ^{o}C with an SEE ±36 ^{o}C; individual samples have ranges spanning <14 ^{o}C. The range within the intermediate samples (848-983 ^{o}C) is lower than the rhyolite range.

Clinopyroxene

Clinopyroxene phenocrysts are found throughout the Dabbahu samples, however it is often difficult to analyse the 'liquid' phase, and therefore the (phenocryst-poor) whole-rock composition has been utilised as representative of a nominal liquid. Cpx thermometry is sensitive to pressure which can be calculated from cpx composition together with a liquid composition by solving P-T equations simultaneously. The cpx and coexisting 'liquid' were checked for equilibrium by using predicted and observed values for cpx components (e.g.DiHd, EnFs etc.) and any data shown not to be in equilibrium were rejected (Putirka 2008). This method was used in preference to Fe-Mg exchange as it has been shown that it can provide a more robust test than the Fe-Mg exchange (Putirka 2008). Moreover, Dabbahu cpx are generally very low in Mg. Thermometry employed the Jd-DiHd exchange thermometer (Putirka 2008). Twenty one samples yielded temperatures using the cpx-liquid thermometer with a total range of 894–1205 ^{o}C, SEE ±45 ^{o}C (table 3.9). Temperatures were derived from cpx from all rock types except rhyolites. The most primitive of all the samples, basalt 044, yielded the highest temperature range of 1171-1205 °C. Where temperatures were derived from both Fe-Ti oxides and cpx-liquid for the same samples, these are generally complementary e.g. in sample 47a Fe-Ti oxides give a temperature range of 1001-1045 °C and cpx-liquid a range of 1005-1039 °C.

Olivine

Olivine / liquid thermometry was used to calculate temperatures for the basalts. As for cpx, whole rock has been utilised as representative of a nominal liquid. The phenocrysts were checked for equilibrium with the whole rock using the method of Roeder (1974). Only two phenocrysts from sample 103 passed the equilibrium test (K_D (Fe-Mg)$^{ol\text{-}liq}$ =0.30±0.03). The calculated temperatures (1113 and 1117 °C, SEE ±53 °C) show a close correlation to the calculated cpx - liquid temperatures.

QUILF

Due to the paucity of mineral pair assemblages for thermometry in peralkaline rocks, QUILF equilibria (Frost 1991; Frost and Lindsley 1992) have been used with some success to constrain equilibrium temperatures and oxygen fugacities using a combination of ilmenite and or magnetite, fayalite olivine, augite and quartz (e.g. White et al. 2005; Ren et al. 2006). The program QUILF95 v6.42 (Andersen et al. 1993) was used to evaluate equilibrium and calculate T and fO_2 in peralkaline comendites and pantellerites. Approximately 6 sets of randomly selected mineral data were processed for each sample to gauge the potential range of temperatures and fO_2. Some metaluminous rhyolites were also calculated in order to provide a comparison to other methods. Where two oxides were present, only oxides which had passed the Bacon and Hirschman (1988) test for equilibrium were input. If none had passed, only ilmenite data were used. SiO_2 activity was set at 1 in the case of sample 061 due to the presence of quartz phenocrysts. Inputs were allowed to 'float' until equilibrium was attained (i.e. set as a trial value). Calculated values are close to trial values suggesting equilibrium, or close to equilibrium conditions between the minerals (Ren et al. 2006). In sample 112, olivine was excluded from some of the QUILF calculations in order to find an optimised solution. This suggests not all the olivines are in equilibrium with ilmenite+magnetite+clinopyroxene, and therefore some may be xenocrysts. The temperatures calculated correspond well to published QUILF temperatures for similar rocks. However, these temperatures are generally lower than temperatures calculated by other methods. For example, the metaluminous rhyolite temperatures are slightly lower than those calculated by Fe-Ti oxides, and generally lower than plagioclase-liquid and cpx methods. The temperature range for each sample can be large e.g. rhyolite 111a has a calculated range of 240 °C, due to the range in mineral composition.

The comendites show both small (53 °C) and large (249 °C) temperature ranges for a given sample. The calculated temperatures are again generally lower than those calculated by other means, except for sample 049 which gives a good match to the Fe-Ti and alkali fsp-liquid calculated temperatures. Temperatures for three pantellerites were calculated with ranges ≤86 °C for each sample.

Summary

The temperatures are broadly consistent with differentiation from basalts (~1100 °C) to rhyolites (~700 °C; fig. 3.16). The oxides have yielded higher temperatures than the feldspars, which is consistent with the oxides crystallising prior to the feldspars. Fe-Ti oxides have been shown to re-equilibriate rapidly in response to changes in temperature and /or fO_2 (e.g. Venezky and Rutherford 1999), so the temperatures represent pre-eruptive temperatures and not necessarily crystallisation temperatures. Although temperature generally decreases with increasing SiO_2 (fig. 3.16), some samples show indications of two groups of temperatures, particularly trachyandesite sample 100, which shows two distinct groupings separated by a temperature gap of ~150 °C. This supports the hypothesis of magma mixing just prior to eruption where insufficient time passed to allow the oxides to re-equilibriate to the new conditions, thus preserving the original temperature signature of the two melts involved.

Where oxide and feldspar methods have been applied to the same samples, in some cases there is a marked difference. For example, in sample 059 (a basaltic trachyandesite) oxides yielded 1042-1168 °C and the plagioclases 848-858 °C. This sample shows distinct blebs of more glassy material in thin section, so some magma mixing probably occurred prior to eruption on timescales insufficient to allow full re-equilibrium of mineral compositions.

The alkali feldspar-liquid temperatures derived for the peralkaline rhyolites were <895 °C and <887 °C for the metaluminous rhyolites. The upper limit is slightly higher, or at the high end of the published temperature estimates for peralkaline rocks. Olkaria obsidians NK/A = 1.01 – 1.55, 660-740 °C (Marshall et al. 2009); Eburru complex NK/A = 1.11 - 2.2, trachytes 709 - 793 °C and pantellerites 668 - 708 °C (Ren et al. 2006); Pantelleria Green Tuff NK/A =

1.07 – 1.97, 703 - 944 ^{o}C (White et al. 2009). It is possible that this is related to the relatively mild peralkalinity of the Dabbahu samples or differing H_2O contents. The Dabbahu samples do not have the same mineral assemblage e.g. quartz is an essential phenocryst in the quoted examples but very rare, or absent, in the majority of Dabbahu samples. Available temperature data for peralkaline rhyolites are also very limited due to the difficulties in deriving temperatures from such a limited mineral assemblage. There is no clear correlation in the samples of this study between NK/A and temperature. The narrow temperature range within each sample derived from alkali feldspar thermometry reflects the narrow compositional range of feldspars found in the Dabbahu peralkaline rocks, and reflects the proposal by Thompson and Mackenzie (1967) that pantellerites lie within a 'low temperature zone' which had its origin in the 'thermal valley' of the granite system.

The cpx-liquid thermometry provides temperatures for the basaltic end of the Dabbahu rock-type spectrum which correlate to the sparse olivine-liquid thermometry. A basalt (sample 044) yielded the highest temperatures of any of the samples (1171 - 1205 ^{o}C). This is lower than the 1275 ^{o}C obtained for one Dabbahu basalt by Bizouard et al. (1980), (based on olivine composition and Fe^{2+}/Mg ratio). Some samples have significantly larger temperature ranges than the majority of samples, which can be ascribed to textural evidence of magma mixing in some samples. The cpx-liquid derived temperatures are generally within or closely overlap with temperature ranges derived from Fe-Ti oxide temperatures, or are within the uncertainty limits of both thermometers.

The overall range of temperatures is, like the chemical variation in Dabbahu rocks, consistent with the experiments of Caricchi et al. (2006). In their experiments the liquidus of the basalt starting material at 1000 MPa with 4 wt% H_2O and 700 MPa with 2 wt% H_2O is over 1100 °C. The residual liquid in their experiments is trachytic at 950 °C.

Barometry

An attempt was made to determine the pressure (and therefore the depth) of crystallisation using the CPX-liquid barometer of Putirka (2008). In many of the rhyolites it was not possible to calculate pressures from the cpx; this was either due to the lack of Mg in the liquid, or where the magma chamber is at shallow depth in which case, the cpx barometers can yield a negative pressure (Putirka 2008). Clinopyroxene barometers yield information about deeper magmatic systems more readily than shallow, crustal P-T conditions (Putirka 2008), and therefore these barometers are not ideal for the scenario at

Dabbahu. However, a range of pressures was calculated for some basalts and intermediate rocks (fig. 3.17). Pressures range from 4 – 895 MPa (±0.3 MPa calibration error). It is possible that the higher and lower ends of this range are less than robust as these barometers are not ideal at shallow depths, and the crust is estimated at only ~20 km thick beneath Dabbahu. The deepest calculated pressure relates to ~ 33 km using a crustal density of 2800 kg m^{-3} (e.g. Mahatsente et al. 1999). For each sample a large range of pressures was obtained. Some distinctive clusters can be seen: in TB at ~750 MPa, which is mirrored by the basaltic sample 044, in BTA a cluster is seen at 400-600 MPa. The majority of the more silicic trachyandesites indicate crystallisation pressures <300 MPa. Although the barometer may be indicative of a variety of crystallisation depths, caution should be applied with regards to these pressures providing a robust and accurate reflection of crystallisation depths.

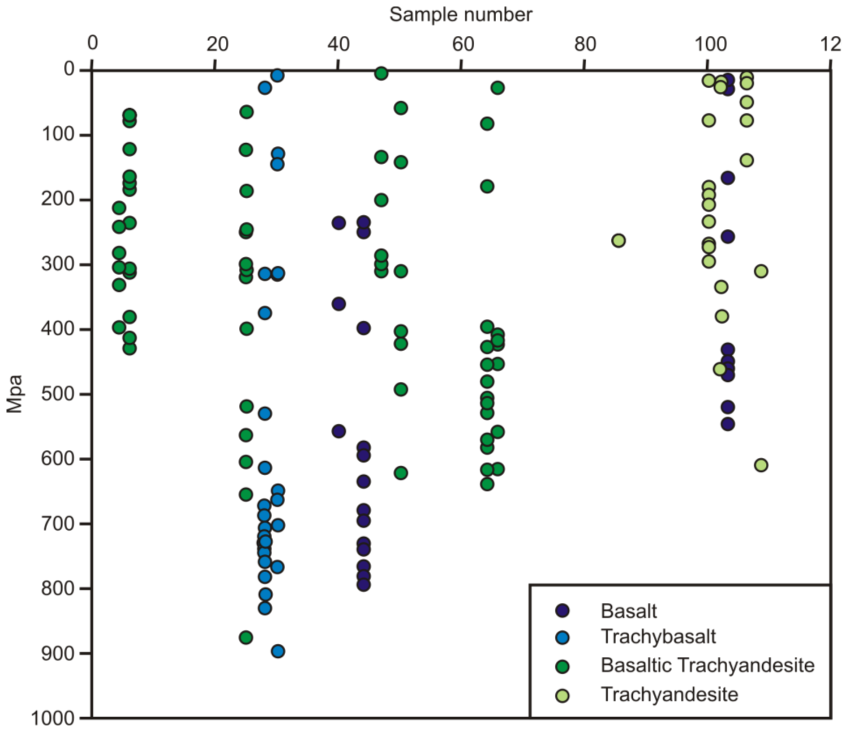

Figure 3.17 *Calculated MPa for basaltic and intermediate samples for cpx-liquid barometry (Putirka 2008), which shows a range of pressures for these samples.*

Oxygen fugacity

Oxygen fugacity was determined using Fe-Ti oxide equilibria following the same procedure as for temperature (table 3.9). Each equilibrium pair was processed using the method of Ghiorso and Evans (2008) and calculated as log units relative to the fayalite-magnetite-quartz (FMQ) buffer (fig. 3.16). QUILF was also used to determine fO_2, using the method of Anderson et al. (1993) outlined above.

When viewed as a whole, the data show a broad range of log fO_2 equilibrium conditions in relation to the FMQ buffer (-3.6 to +0.5) without any significant trends. However, the lowest fO_2 are recorded by the most evolved rocks. The samples from this study broadly correlate with data calculated from the literature using the same methodology e.g. the QUILF data from Pantelleria (White et al. 2005), indicate a similar spread of log fO_2 values, however the temperature range is lower. White et al. (2005) summarised natural peralkaline and cogenetic high-alkali metaluminous rocks which consistently have fO_2 near or below the FMQ buffer for a temperature range of 1025 ^{o}C to 685 ^{o}C.

Magmatic Evolution of Dabbahu

Fractional crystallisation has long been argued as a feasible method of producing peralkaline rocks, both at Dabbahu and elsewhere in the African Rift (e.g. Barberi et al. 1974; Marshall et al. 2009). The evidence from the rock types and Harker diagrams (fig. 3.11 & 3.12) from Dabbahu, certainly supports this hypothesis. Recent experimental work by Caricchi et al. (2006) emphasizes the importance of polybaric fractional crystallization of hydrous, but reduced alkaline basalts for the derivation of peralkaline liquids. Plotted in conjunction with the Dabbahu analyses (fig. 3.11), there is a close correlation, supportive of fractionation at Dabbahu. However, the Caricchi (2006) experiments were carried out with a transitional basalt starting composition under hydrous conditions with an initial 4 wt% H_2O. This is significantly higher than the estimates for alkali basalts (up to 1 wt%) (Andersen 1975) which are generally presumed to be more H_2O rich than comparable tholeiitic basalts (0.2 - 0.4 wt%) (Lowenstern and Mahood 1991). Melt inclusion analysis of the Dabbahu pantellerites (Field et al. 2011) have revealed H_2O contents of up to 5.8 wt%. Assuming between 80 - 90% crystallisation, this can be back calculated to give parent basalt H_2O contents of between ~1.2 - 0.6 wt % respectively. These are lower bounds, because they assume that the pantellerites are at the point of H_2O saturation and have not degassed significantly. Lower water content is a plausible explanation for the observed differences between the Caricchi et al., (2006) experiments and the Dabbahu trends, such as the crystallisation of amphibole in the Carrichi et al., (2006) experiments which is lacking at Dabbahu. The incompatible behaviour of yttrium (fig. 3.12g) also supports the proposal that amphibole did not play a significant role in magma differentiation at Dabbahu.

A plot of Zr/Th v Zr shows a near constant ratio (average 68) across all samples; this is strongly indicative of a fractionating system with a single parent composition (fig. 3.18). The Manda Hararo analyses of Barrat et al. (2003) have a higher and more variable ratio, suggesting a difference in the source for the two localities. The rift eruptions in 2007 and 2009 (Ferguson et al. 2010), approximately 30 km south of Dabbahu, are within the envelope of the Dabbahu samples with ratios of 98. The high Zr and Th concentrations in Dabbahu rocks make the Zr/Th ratio relatively insensitive to minor crustal contamination. However, the consistency of this ratio clearly shows that crustal melting did not play a significant role in generating the evolved rocks. We can assess the viability of fractional crystallisation in generating the Dabbahu suite of rocks, following the approach of Blundy and Wood which was applied to the Main cone series Aden Volcanics. Zr was used as a proxy for melt fraction, while Sr behaves as a compatible element in the feldspar-dominated crystallising assemblage. To perform the calculations we first selected a plausible parent magma.

Based on their chemistry, plausible parent compositions to the Dabbahu suite are basalt sample 045, or the Ferguson 2007 rift basalt (Ferguson et al. 2010). We adopted the former as a parent with 228 Zr and 403 Sr. Zr_{parent} / Zr_{sample} therefore acts as an indicator of the degree of fractionation (F), and Sr_{sample} / $S_{rparent}$ is the parent-normalised concentration of Sr in the liquid (C_L / C_O). The calculations were performed in increments of 10% crystallisation. At each step the An content and temperature was adjusted, using a smoothed fit to the data presented in figures 3.13 and 3.16, starting at 1150 ^{o}C and An_{88}. We assumed that the fraction of plagioclase in the crystallising assemblage was constant at 50%. This is a reasonable match to the modal data presented in figure 3.8. The phenocryst proportions are generally too low to deduce any significant variation with F.

Due to the low modal % of phenocrysts in the natural samples, a constant proportion of plagioclase (0.50) was used. The model was adjusted by changing the temperature and An content until the best fit to the Dabbahu samples was found. A starting temperature of 1150 ^{o}C with an An value of plagioclase set at 0.88 was found to provide the best fit. The modelled starting temperature of 1150 ^{o}C is close to the average calculated temperature for the Dabbahu basalts of 1148 ^{o}C (cpx/liquid and olivine/liquid thermometry), and the An value of 0.88 for the model is slightly higher than the highest An value in sample 045 (An 0.81), but close to the highest An value (0.86) found in a Dabbahu basalt. The curved evolution of the whole rocks is closely matched by the model, supporting generation of the Dabbahu suite by fractional crystallisation. Note that the Sr content of the evolved magmas is so low that they are very susceptible to crustal contamination, yet the data show little evidence for deviation from the modelled trend at low F. Due to the low modal % of phenocrysts in the natural samples, a constant proportion of plagioclase (0.50) was used. The model was adjusted by changing the temperature and An content until the best fit to the Dabbahu samples was found. A starting temperature of 1150 ^{o}C with an An value of plagioclase set at 0.88 was found to provide the best fit. The modelled starting temperature of 1150 ^{o}C is close to the average calculated temperature for the Dabbahu basalts of 1148 ^{o}C (cpx/liquid and olivine/liquid thermometry), and the An value of 0.88 for the model is slightly higher than the highest An value in sample 045 (An 0.81), but close to the highest An value (0.86) found in a Dabbahu basalt. Results of the modelling are shown in figure 3.19. The curved evolution of the whole rocks is closely matched by the model, supporting generation of the Dabbahu suite by fractional crystallisation. Note that the Sr content of the evolved magmas is so low that they are very susceptible to crustal contamination, yet the data show little evidence for deviation from the modelled trend at low F. However, although limited crustal assimilation cannot be discounted, without isotope analysis this cannot be distinguished.

Again we propose that crustal contamination or melting played little part in magma differentiation at Dabbahu. The partitioning equation of Sr between plagioclase feldspar and silicate melt as a function of An and T is taken from Blundy and Wood (1991). Ar-Ar geochronology and field evidence (fig. 3.7) suggests a hiatus in eruptive activity between the youngest comenditic lavas and the more evolved pantellerites. The youngest comendites were dated at 30.1 ±0.4 and 28.6 ±0.7 ka.

The oldest pantellerites, those which are pumice covered to the N and NW of the summit, erupted around 7.8 ±4.3 ka. This may in part be a result of a sampling bias (for example, it is not currently possible to reach the eastern side of Dabbahu). However we also suggest that the gap of ~16 ka may give an indication of the timespan required to fractionate the pantellerite liquids at Dabbahu.

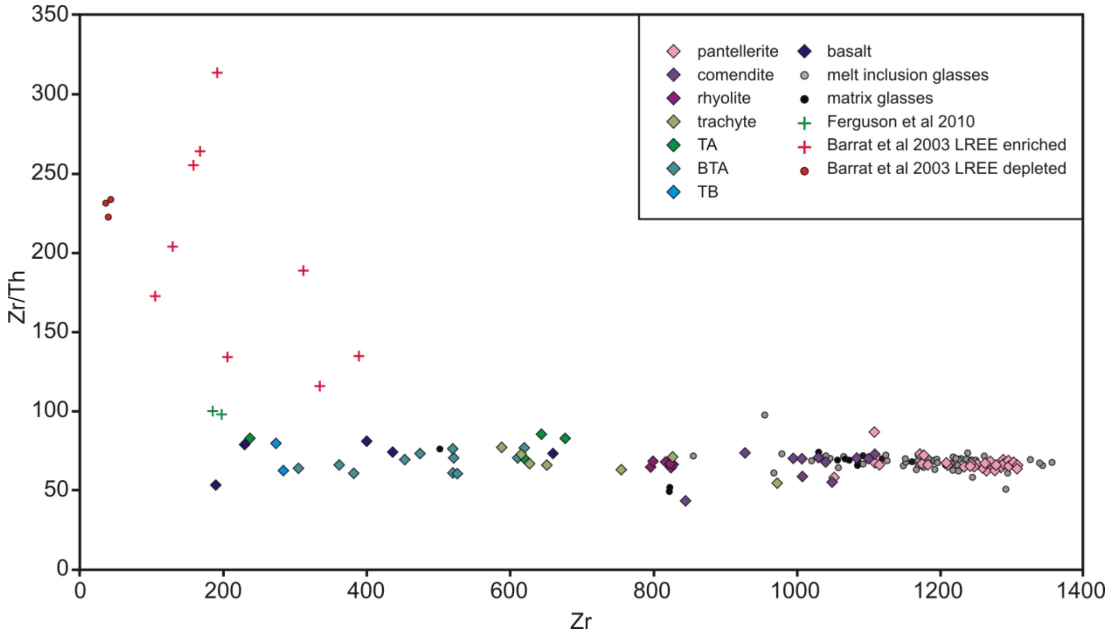

***Figure 3.18** – the Zr/Th ratio remains constant throughout the sequence for Dabbahu rocks, which is indicative of a fractionating system in which these two elements are incompatible. The Manda Hararo basalts (Barrat et al 2003) have a more variable, and higher ratio.*

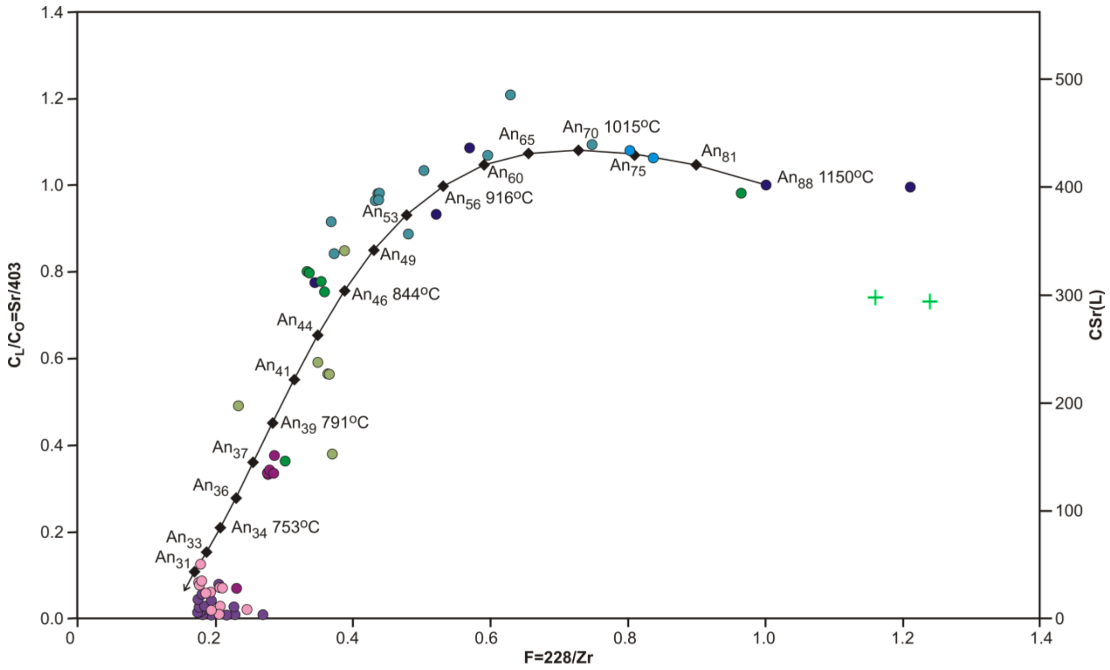

***Figure 3.19**. Variation in Sr content of Dabbahu samples during fractionation. Data are plotted using the same symbols as figure 3.11. The abscissa denote the fraction of liquid remaining (assuming that Zr behaves as a completely incompatible element). The solid line denotes the modelled evolution using compositions of plagioclase in the rocks, the calculated temperatures and the plagioclase-melt partition coefficient for Sr from Blundy & Wood (1991). See text for details of the calculations.*

The bulk of the pantellerite rocks have also been erupted from fissure systems, whereas the comenditic lavas have been erupted as individual flows from a single point, suggesting there may have been changes in eruptive style and/or magma plumbing during this time. Melt inclusion analysis, InSAR and seismicity at Dabbahu have indicated the presence of a shallow magma chamber in the upper 5 km of the crust, formed from multiple sill emplacements (Field et al. 2011).

An important issue is the depth at which magmatic differentiation occurred. Although there is geophysical and petrological evidence for a shallow pre-eruptive magma storage region (Field et al. 2011) we consider it unlikely that this was the site of differentiation for several reasons. First, the volume of cumulates required would be equivalent to ~15 times the total volume of erupted silicic magmas. The erupted volume of peralkaline products alone is >0.55 km^3, which would require a volume of cumulates of ~8.25 km^3; the volume required for rhyolites and intermediates would be substantially greater. Such a large volume of cumulates would be hard to hide geophysically in the shallow crust. For example, there is no evidence from receiver function analysis of seismic data (Hammond et al. 2011) for an appropriate volume of dense cumulates at depths of 5 km or so. Secondly, the eruptive sequence at Dabbahu does not follow a simple temporal relationship (fig. 3.7). A wide variety of magma types has been tapped and erupted over a 60 ka period. This is hard to reconcile with a single large shallow, fractionating magma chamber, as originally envisaged by Barberi et al., (1974), although this may reflect the tapping of a series of variably evolved products stored in individual storage areas e.g. sills. Thirdly, the longevity of eruptive activity at Dabbahu would require a significant input of hot basaltic magma into the shallow crust in order to maintain a viable magma chamber, if one single large chamber is to be maintained for differentiation. Annen (2006) has shown through numerical simulations of shallow magma chamber growth that heat loss through the roof leads to rapid cooling of magma unless the heat input is maintained through continued basalt intrusion.

Fourthly, the evidence for magma mixing in many Dabbahu samples suggests that chemically-related magmas of distinct composition were juxtaposed pre-eruptively. The shallow magma storage region provides a suitable location for such mixing to occur, but cannot then also be the site of differentiation. Finally, the close correspondence between the observed liquid line of descent, and calculated variation in melt fraction (F) with temperature (fig. 3.20) at Dabbahu, and the experimental liquid line of descent for a Main Ethiopian Rift basalt at mid- to lower crustal pressures (500 – 1000 MPa) by Caricchi et al.,

(2006) suggests that fractionation occurred at depth. The experiments of Caricchi et al., (2006) involve basalts with slightly higher H_2O than we think is likely at Dabbahu, leading to the crystallisation of amphibole and suppression of plagioclase. We venture that experiments with initial H_2O contents of 1 wt% or less would provide an even better match, although such experiments remain to be carried out. Experiments from intra-continental basalts to look at the evolution of potassium rhyolites have been performed by Whitaker et al. (1998) at both lower pressure and H_2O content (430 MPa and 0.4 wt% H_2O) and these data have been plotted as a comparison (fig. 3.20). The experimental compositions have a reasonable similarity to the Dabbahu compositions. Although these experiments show a similar slope to the Dabbahu samples and Caricchi experiments, the temperatures are higher. It is likely that the Dabbahu trend is at water contents and pressures between the two sets of experiments. In light of the above arguments we propose that magmatic differentiation beneath Dabbahu occurred in a mid- to deep crustal region, possibly of the type envisaged by Annen et al., (2006), or a series of sills at a range of depths such as suggested by Kelemen et al. (1997) and Maclennan et al. (2001), for oceanic and icelandic senarios, however it should be remembered that the Dabbahu/MHRS area is not yet fully oceanic. The crust is ~ 20 km thick beneath Dabbahu, so it is envisaged that this intermediate magma storage region may be located at ~ 16 -20 km (refer also to Chapter 4). This zone is likely to be fuelled by repeated influxes of rift-related basalts from the mantle. The depth of this region removes the exacting thermal difficulties of maintaining a shallow magma chamber for a sufficient amount of time. Within this zone, evolved melt are produced by a combination of basalt crystallisation and crustal melting. The extent of the latter depends critically on the fertility of the suprajacent crust, which is not well constrained at Dabbahu.

However, there is scant evidence for appreciable crustal melting, and we suggest that the bulk of the silicic melts are the products of basalt crystallisation. The structure of deep crustal hot zones means that they contain melts of varying degrees of crystallisation, hence at any one time there is a variety of magma types that can be extracted and erupted. This is entirely consistent with the absence of any temporal evolution of magma types at Dabbahu. We propose that variously fractionated melts, once extracted from the differentiation region, ascend into the shallow crust, where they are temporarily stored pre-eruptively. This shallow storage region becomes the site of mixing between different magma types, linked co-genetically through fractionation in the deeper differentiation region.

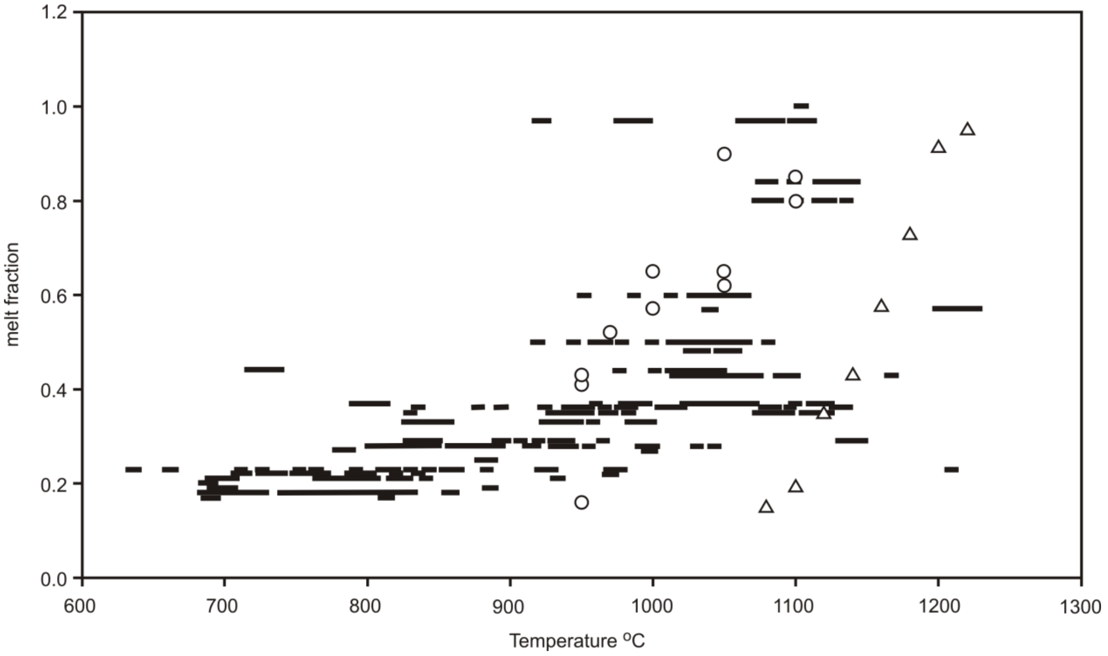

Figure 3.20. *Calculated variation in melt fraction (F) with temperature for Dabbahu samples shown as black lines. Temperatures are taken from figure 3.16; F is calculated from 228/Zr. Despite scatter in the temperatures calculated using different methods, the overall variation shows a sharp drop in F between 1100 and 950°C. The experimental data of Caricchi et al. (2003) show a similar relationship between T and F (open circles), although their experimental basaltic starting materials contained higher H_2O contents than are likely to have been present at Dabbahu. Experimental pressures were at 500 – 1000 MPa. In contrast, the experiments of Whitaker et al. (1998) for basalt to potassic rhyolites, show a similar slope but are displaced at higher temperatures (open triangles). These experiments are at both lower H_2O content and intermediate pressure (430 MPa). It is likely that the Dabbahu basalts contained lower water (<1 wt%) than the Caricchi experiments, but were formed at intermediate to deep crustal pressures.*

The controlled-source seismic experiments of (Makris and Ginzburg 1987) indicate that the crust is approximately 20 km thick beneath Dabbahu. Thus we propose that the region of differentiation is situated at a depth of approximately 14-20 km. The upper bound is supported by the saturation pressure from a single cpx-hosted melt inclusion and the depth distribution of seismicity (Field et al. 2011). A schematic plot of our proposed Dabbahu plumbing system is shown in figure 3.21.

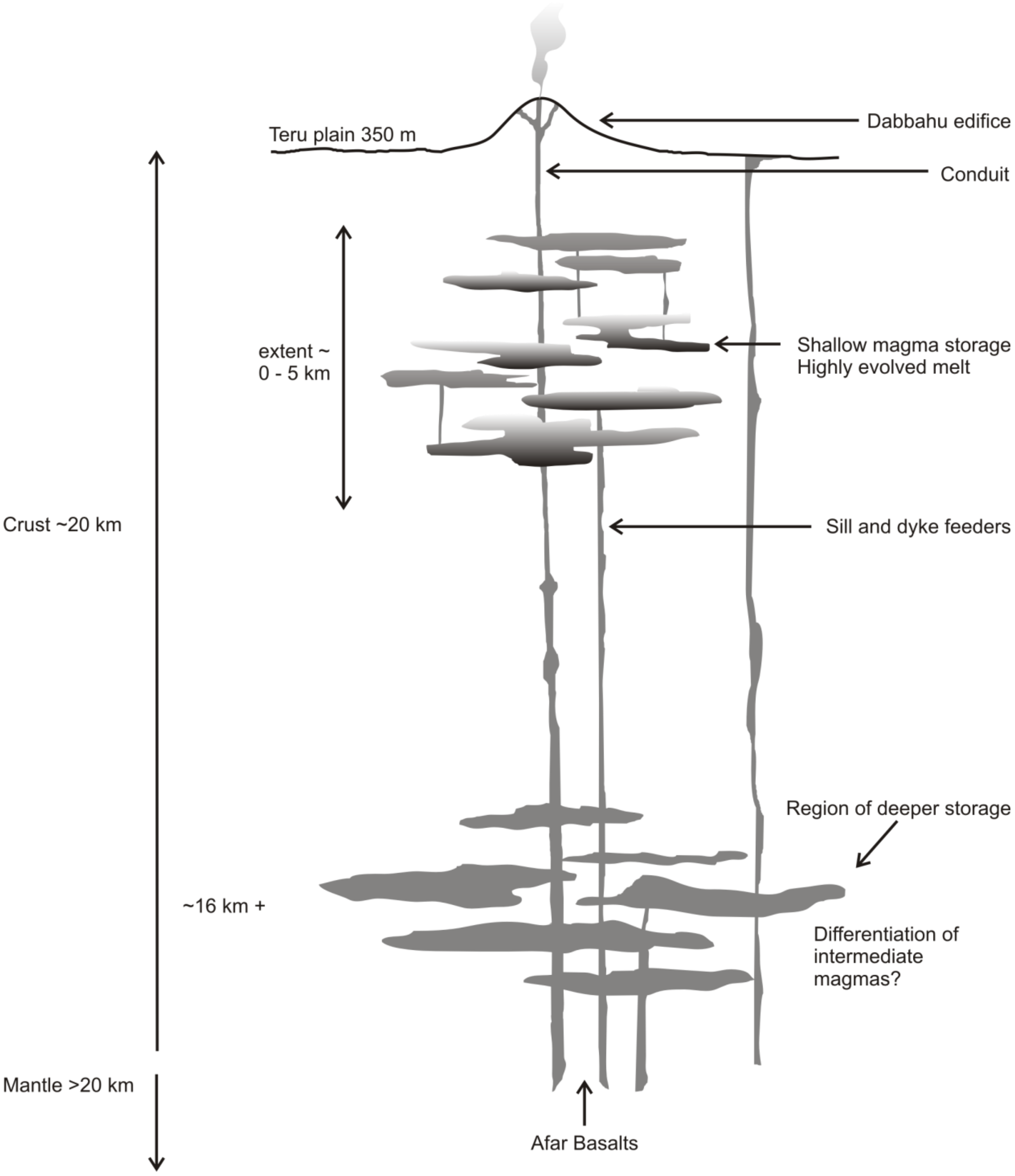

Figure 3.21. *Schematic of the possible magma plumbing system beneath Dabbahu. Not to scale.*

Disruption of the magma storage region, and the subsequent eruption of the pantellerite obsidians from fissure systems may be indicative of processes suggested by Lahitte (2003), whereby silicic central volcanoes are eventually dismantled as rifting continues. He suggests this eventually results in the direct eruption of fissural basalts on the surface of the volcano e.g. Moussa Ali volcano. In this context it is interesting that the metaluminous rhyolites are some of the oldest lavas at Dabbahu; flows have been confirmed both to the SW (>1.58 km^3) and N of the edifice indicating a rhyolitic dome had to exist very close to or adjacent to the original basaltic shield before becoming incorporated in the resulting edifice.

Conclusions

Dabbahu reveals a complex magmatic history. Dabbahu originated as a basaltic shield volcano, but coeval to this, or shortly after its formation, a metaluminous rhyolite complex formed. More evolved silicic domes (comendites) dominate the landscape just north of Dabbahu, with the domes of Aso and Ado Da'Ure, Alcoma and Gab'ho. As time progressed and further eruptions occurred at Dabbahu and, the shield and rhyolite complex became merged. Periodically, influxes of new magma has occurred which have most likely acted as a key eruption trigger throughout Dabbahu's history, most recently in 2005 when a dyke injection is believed to have caused a small ash eruption at the Da'Ure vent. Intermediate lavas are extensive at Dabbahu and may well have erupted explosively from crater forming eruptions. Eventually, as rifting continued, fissures were able to form resulting in the eruption of thin peralkaline rhyolite flows which have covered the northern part of the edifice. The new ^{40}Ar/^{39}Ar dating indicates the formation of Dabbahu began prior to 65 ka, and has continued to the present.

Magma compositions show evolution from mildly alkaline basalt through trachyte to peralkaline rhyolites (pantellerites and rhyolites). Mineral compositions and calculated magma temperatures show continuous and extreme variation across the range in rock types.

The key petrogenic process proposed is fractional crystallisation of rift-related basalts. Modelling shows that to produce the most evolved pantellerite lavas, >80% fractionation is required. Geochemical evolution shows a good match to experimentally determined liquid lines of descent for compositionally similar basalts from the Main Ethiopian Rift, crystallised at mid- to deep crustal pressures. We propose that differentiation occurred in a deeper crustal region, at depths of 14-20 km, fuelled by influx of rift-related basalts from the mantle at temperatures of ~1150°C. Crustal melting/contamination appears to have played a limited role in differentiation. A wide variety of magma types coexisted in the deeper storage region, generated by fractional crystallisation of basalt. Field evidence shows that eruption of the different rock types has not taken place in order of increasing SiO_2 and there is conclusive evidence of mixing between different, cogenetic magmas recorded at Dabbahu on all scales from macro to micro. Mixing is likely to have occurred within a shallow storage region beneath the volcano, and suggests influx of new magmas into this region may have acted as a key eruptive trigger throughout the volcano's history.

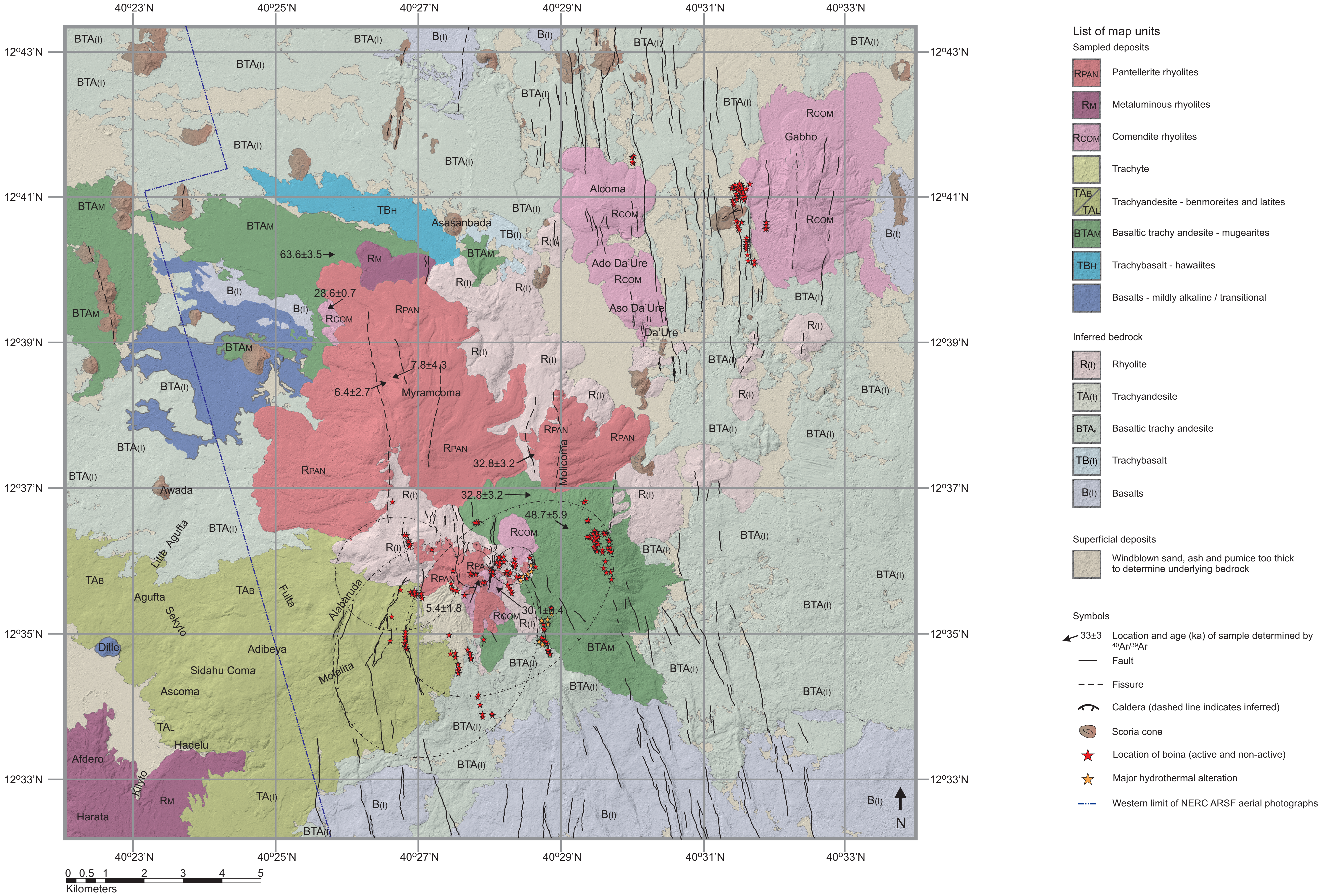

List of map units
Sampled deposits
RPAN Pantellerite rhyolites
RM Metaluminous rhyolites
RCOM Comendite rhyolites
Trachyte
TAB TAL Trachyandesite - benmoreites and latites
BTAM Basaltic trachy andesite - mugearites
TBH Trachybasalt - hawaiites
Basalts - mildly alkaline / transitional
Inferred bedrock
R(I) Rhyolite
TA(I) Trachyandesite
BTA(I) Basaltic trachy andesite
TB(I) Trachybasalt
B(I) Basalts
Superficial deposits
Windblown sand, ash and pumice too thick to determine underlying bedrock
Symbols
33±3 Location and age (ka) of sample determined by ^{40}Ar/^{39}Ar
Fault
Fissure
Caldera (dashed line indicates inferred)
Scoria cone
Location of boina (active and non-active)
Major hydrothermal alteration
Western limit of NERC ARSF aerial photographs
40°23'N
40°25'N
40°27'N
40°29'N
40°31'N
40°33'N
12°43'N
12°41'N
12°39'N
12°37'N
12°35'N
12°33'N
Gabho
Alcoma
Asasanbada
Ado Da'Ure
Aso Da'Ure
Da'Ure
Myramcoma
Molicoma
Awada
Litte Agufta
Agufta
Fulta
Sekyto
Alabaruda
Adibeya
Sidahu Coma
Ascoma
Molalita
Dille
Hadelu
Afdero
Kilyto
Harata
63.6±3.5
28.6±0.7
7.8±4.3
6.4±2.7
32.8±3.2
32.8±3.2
48.7±5.9
5.4±1.8
30.1±8.4
N
0 0.5 1 2 3 4 5
Kilometers

Magma storage conditions beneath Dabbahu

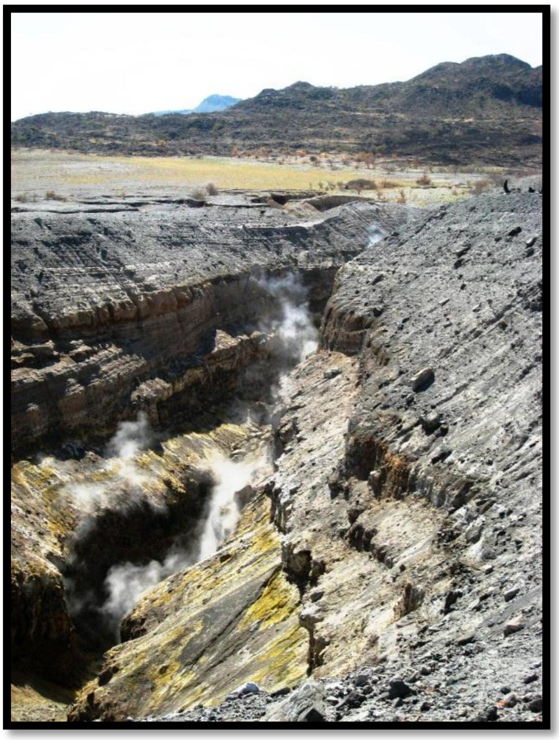

Chapter

4

Author Contribution

This chapter is in review with the Bulletin of Volcanology:

Field, L., Blundy, J., Wright, T., and Yirgu, G., 2011 “Magma storage conditions beneath Dabbahu Volcano (Ethiopia), constrained by petrology, seismicity and satellite geodesy”. Bulletin of Volcanology. *In review*.

Enlightening discussion with J. Blundy provided direction and greatly improved the manuscript. L. Field was the lead author and contributed all work with the exception of all InSAR data and related InSAR paragraphs which were contributed by T. Wright. Seismic longitude, latitude and depth data were kindly provided by C. Ebinger.

Abstract

A variety of methods exist to constrain the sub-volcanic storage conditions of magmas. Here we integrate petrological, seismological and satellite geodetic methods to determine storage conditions of pantelleritic magma beneath Dabbahu Volcano, Afar, Ethiopia. SIMS analysis of volatile contents of melt inclusions trapped within phenocrysts of alkali feldspar, clinopyroxene and olivine from mildly peralkaline obsidian samples representing the youngest eruptive phase (<4 ka) show H_2O contents ≤5.8 wt% and CO_2 contents generally below 500 ppm, although rarely as high as 1500 ppm. Volatile saturation pressures (at 679-835 °C) are in the range 29-249 MPa. This pressure range is consistent with published experimental data for similar pantellerites, which show that the phenocryst assemblage of alkali feldspar + cpx + aenigmatite ± ilmenite is stable at 100 to 150 MPa. The inferred magma storage depths for this historic eruption are 1-5 km below sea-level, consistent with observations from the depths of earthquake, largely to the south of Dabbahu, associated with deflation of the magma chamber following a dyke intrusion in the period Oct 2005 – Apr 2006. InSAR data for the same period reveal a broad area of uplift ~20 km in diameter. Modelling of different magma storage geometries reveals that a series of stacked sills over a 1-5 km depth range best matches the InSAR data. The consistency of depth estimates based on petrological study of ancient eruptions and the ongoing magmatic episode in the vicinity of Dabbahu suggests a stable, and potentially long-lived, vertically extensive, but small magma storage region.

Introduction

Volcanic eruptions are driven by expulsion of magmas. These may contain volatiles and originate from crustal storage regions or magma chambers. Constraining the depth at which magma is stored is critical in evaluating likely eruption styles and mitigating volcanic hazard, and yet is notoriously hard to do remotely. Magma bodies are normally too small to generate sufficient gravity or magnetic anomalies to be measured from the air, while seismic methods cannot yield unequivocal evidence for magma, as opposed to hydrothermal or fault systems. Petrological methods for constraining magma storage depths include measurement of dissolved volatiles (principally H_2O and CO_2) in phenocryst-hosted melt inclusions (Blundy & Cashman, 2008), from which saturation pressures are calculated using solubility models. These methods are, of necessity, a posteriori, in that they require erupted materials. Thus they are useful in determining where magma was stored prior to the last eruption, but this need not be the same as current magma storage depths. Moreover, petrological methods rely on a magma being volatile-saturated, which needs to be independently evaluated, on having reliable pressure-solubility models for the magma of interest (solubility is composition-sensitive), on being amenable to geothermometry (solubility depends also on temperature) and on having a suitable crustal density model with which to convert pressures to depths. Post-entrapment volatile leakage from melt inclusions through cracks or by diffusion through the host mineral further complicates petrological estimates. Finally, there is no guarantee that the magma storage depth has not changed between the previous eruption and the present day.

An alternative means of prospecting for un-erupted magma is to deploy dense arrays of seismometers to record local, teleseismic or marine seismic events and use these date to locate a magma body, either by using precisely located local earthquakes to define the outer margins of a magma body or through full tomographic inversion (e.g. Lees 2007; Shalev et al. 2010). Magneto-telluric methods are also extremely sensitive to the presence of a shallow highly conductive magma layer (e.g. Whaler and Hautot 2006; Hill et al. 2009). But again, data acquisition is time-consuming and expensive and the presence of a shallow, non-magmatic layer, such as an aquifer, can reduce depth resolution. Gravity measurements provide the most robust means of imaging sub-crustal density, but in the absence of other methods, can only identify low-density bodies, rather than magma per se. Repeated gravity surveys have been used successfully to track the migration of density anomalies and hence infer sub-volcanic magma movement (e.g. Williams-Jones et al. 2008).

Interferometric Synthetic Aperture Radar (InSAR) is a tool that enables surface deformation to be mapped with high precision and high spatial resolution, with no requirement for ground-based instrumentation (Bürgmann et al. 2000; Wright 2002). InSAR has recently been used to good effect in the Andes to identify areas of active upwelling, thought to correspond to areas where the shallow magma storage region is being recharged (Pritchard and Simons 2002). Reconstructing magma storage depths from InSAR images is not, however, a straightforward matter because of the uncertainties that accompany the rheological behaviour of crustal rocks surrounding the magma body. Simple models, such as that of Mogi (e.g. Sasai 1991), which treat the crust above a point source magma body as an elastic half-space do not capture the complexity of the natural situation. The shape of the magma body also influences the observed deformation pattern, as does more complex rheological behaviour of the magma chamber roof and walls. Careful matching of the observed and modelled deformation patterns, such as that performed by (Wright et al. 2006), does serve to increase confidence in the estimated magma storage depths, but such solutions are inherently non-unique.

In this paper we combine petrological, seismic and InSAR methods of estimating magma storage conditions beneath an active volcanic area in the Afar region of northern Ethiopia. The petrological estimates are derived from the youngest, peralkaline rhyolites erupted from Dabbahu volcano (< 4ka), whereas seismicity and InSAR data pertain to the ongoing tectono-magmatic activity in the area. Our principal objective is to establish whether current patterns of unrest are consistent with previous, pre-eruptive magma storage conditions. To our knowledge this is the first time that these three approaches have been combined to constrain magma storage depths beneath an active volcano.

Geological Background

Dabbahu is a quaternary volcano situated at the northern end of the Manda Hararo rift segment (MHRS) in the Afar region of Ethiopia (12^{o} 39'39.24" N, 40^{o} 28'45.10" E), (fig. 4.1). The Afar depression at the triple junction between the Red Sea, Gulf of Aden and East African rifts has been produced by rifting between Africa and Arabia over the past ~30 Myr (Wolfenden et al. 2005). The southern Red Sea rift has become punctuated over the past ~3 Ma with ~60 km long magmatic segments as faulting and volcanic activity has become more focused into localised regions (Barberi and Varet 1977). The northern-most magmatic segments of Erta'Ale and Tat'Ale step across to the more western Alayta segment, and then southwards into the MHRS.

The MHRS comprises the currently active Dabbahu magmatic segment (DMS) to the north, and the adjacent Hararo segment to the south (Rowland et al. 2007). The MHRS is characterised by a 35 km wide central depression punctuated by silicic edifices

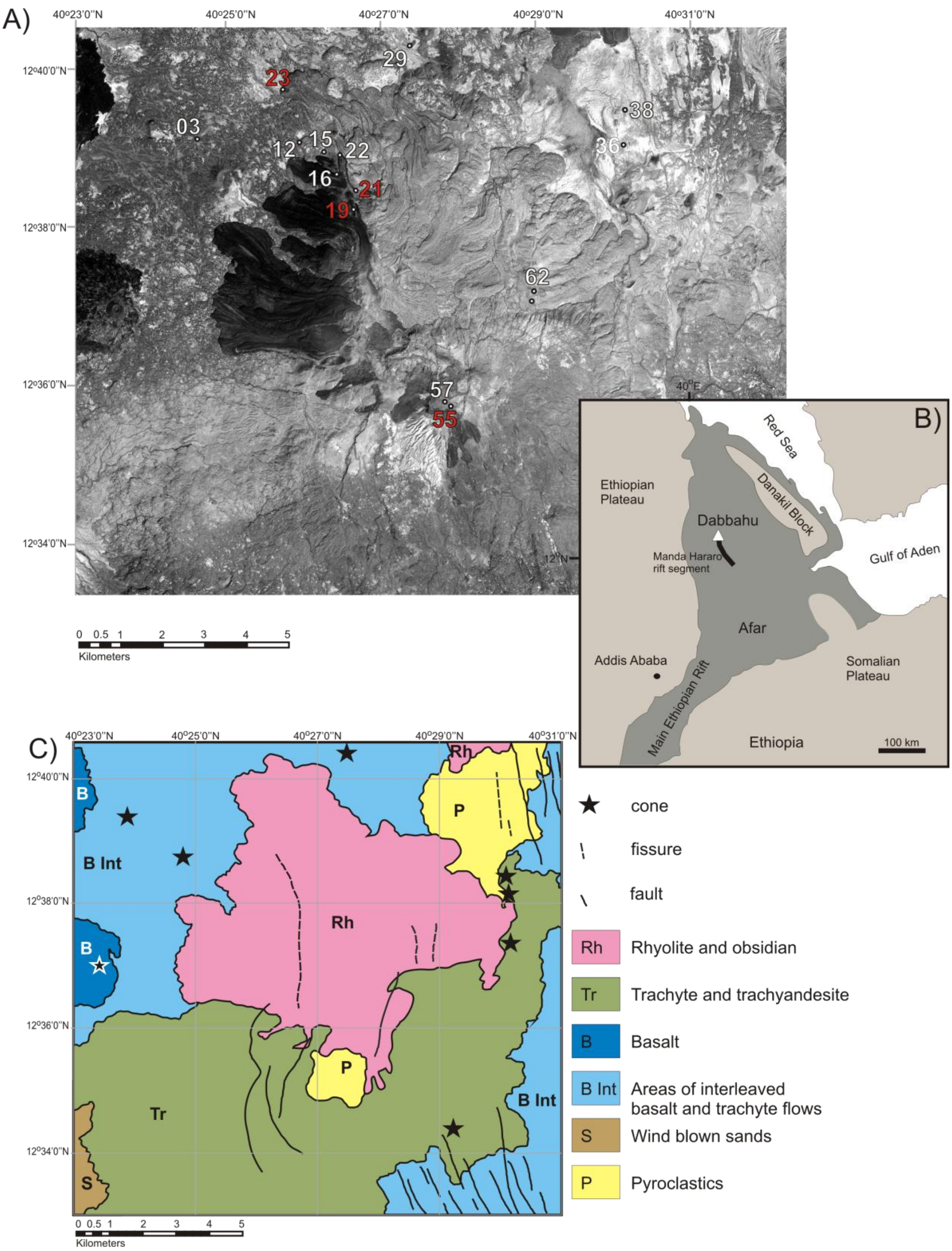

***Figure 4.1** a) Sample localities (Satellite image courtesy of Sophie Hautot). The prominent dark flows in the NW and around the summit are obsidians and represent the youngest volcanic activity in the area. Sample numbers in red denote samples used for melt inclusion analysis, those in white, matrix glass analysis. B) Location map of Dabbahu and the MHRS. C) Simplified geology based on Barberi et al., (1975).*

(Lahitte et al. 2003). The DMS is a ~ 60 km long and ~15 km wide area which trends NW-SE of a dissected central silicic complex known as the Ado'Ale Volcanic Complex (AVC), and then trends SSE-NNW northwards to Dabbahu volcano (Rowland et al. 2007). Known also as Boina, Boyna or Moyna, (Barberi et al. 1974a) describe Dabbahu as ~1400 m high volcanic edifice, rising from a base of fissural basalts. It is cited as an example of a full fractional crystallisation suite from mildly alkaline basalts to mildly peralkaline rhyolites, erupted from a central volcano with a shallow magma chamber (Barberi et al. 1974a; Barberi et al. 1974b; Bizouard et al. 1980). The rhyolites on Dabbahu comprise metaluminous and peralkaline pyroclastic deposits and lava flows. The peralkaline deposits can be further defined into comendites and pantellerites, and these lavas have formed flows on the northern slopes (noteably the distinct NW flows, fig. 4.1a) and around the summit area up to ~8 m high. Individual flow sizes vary from tiny (<0.001 m^3) to ~0.13 km^3. In 2005 there was a small rhyolitic ash eruption and a dome shaped extrusion of vesicular felsic material from the Da'Ure vent on the northern flanks of Dabbahu (12° 39'00.58" N, 40° 31'10.43" E) which coincided with the largest dyke opening event ever measured, and the first such event in the modern age of satellite geodetic methods (Ayele et al. 2007). Modelled as a basaltic dyke injection ~10 km deep, it was shown that up to 8 m of opening along a distance of ~60 km occurred. This event plausibly triggered the Da'Ure eruption by interaction of basaltic magma with a shallow silicic reservoir (Wright et al. 2006). Further analysis has suggested that the sub-horizontal dyke propagation was sourced from three locations: two distinct sources at the Dabbahu-Gab'ho Volcanic Complex, and the third major source at the AVC some 30 km to the south of Dabbahu (Ayele et al. 2007; Ayele et al. 2009). The youngest volcanic rocks at Dabbahu, and many of the surrounding domes, are mildly peralkaline rhyolitic obsidians (Barberi et al. 1974a), characterised by molar $(Na_2O+K_2O)/Al_2O_3$ >1, (NK/A) (Macdonald and Bailey 1973; Macdonald 1975). These overlie trachytes, trachybasalts and basalts dating back to at least 50 ka.

Samples Studied

We analysed matrix glasses from pumices and rhyolite obsidian flows, and glassy melt inclusions from four rhyolite obsidian flows. These were collected from Dabbahu during field campaigns in 2008 and 2009. Samples 019, 021, 023 and 055 are from some of the youngest flows on Dabbahu; sample 055 is from the summit area. No melt inclusions were located in the most recent rhyolitic material erupted from Da'Ure in 2005. Scoria and pumice samples, which due to rapid quenching usually provide superior melt inclusion samples (e.g. Anderson and Brown 1993), were found to be largely aphyric, or with rare crystals too small to be utilised. The obsidian rhyolites are also phenocryst-poor e.g. the most crystal-rich sample used (sample 055) contains just 7 vol% phenocrysts. The obsidian rhyolites are extremely fresh and show no obvious evidence of weathering, rehydration or other secondary alteration in hand sample. The main phenocryst phases are alkali feldspar and Fe-augite. Minor phases vary between samples and are present as phenocrysts or in groundmass: fayalitic olivine, ± ilmenite, ± apatite, ± aenigmatite, ± riebekite, ± quartz, ± zircon. Melt inclusions are scarce within the Dabbahu rocks; sample 055 yielded the greatest number. Alkali feldspar was found to be the most promising host for melt inclusions; a lesser number of melt inclusion were also located in Fe-augite and fayalitic olivine. Melt inclusions in the underlying mafic and intermediate lavas were also inspected, but were unsuitable for analysis (e.g. due to small size, common post entrapment crystallisation etc.). Melt inclusions were screened using SEM for the presence of daughter crystals, cracks, or rims around the inclusion walls which might indicate that the original volatile contents had been compromised by post-entrapment processes.

Analytical Techniques

Detailed analytical techniques are described in Chapter 2, Methodology. The techniques used include whole rock, SEM, EMPA and SIMS. Figure 4.2 depicts typical melt inclusions from the Dabbahu samples.

Results

Whole rocks and matrix and pumice glasses

Major element data (table 4.1), were assessed for post-eruptive alkali loss (e.g. through weathering) using the molar FK/Al (FeO, K_2O, Al_2O_3) criteria of (White et al. 2003).

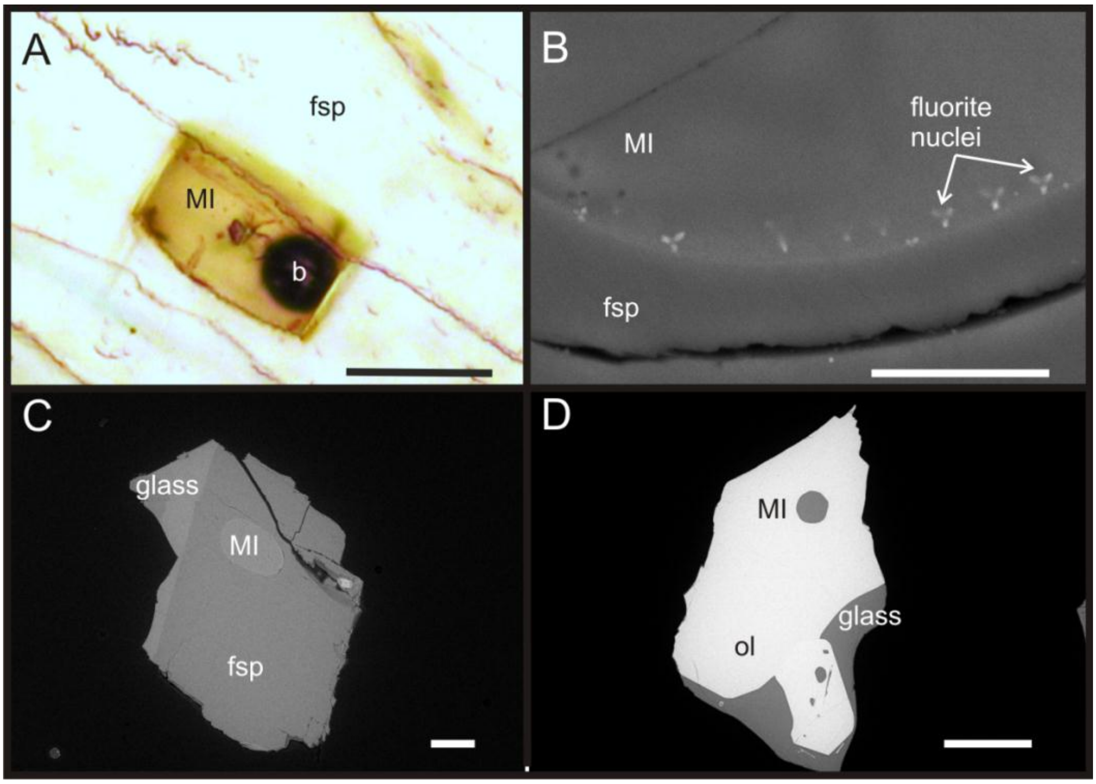

__Figure 4.2.__ Images of typical melt inclusion. A) photomicrograph of a melt inclusion (MI) in feldspar (fsp) with bubble (b). Scale bar 20 µm. B) BSE image of the melt inclusion used for element mapping showing fluorite nuclei around the melt inclusion rim, scale bar 10 µm. C) BSE image of a melt inclusion (MI) in a feldspar (fsp) host (sample 055). Scale bar in C and D 100 µm. D) BSE image of a melt inclusion (MI) in olivine (ol) (sample 021).

All samples used fell inside the 95% confidence lines and therefore the samples used are deemed not to have suffered any significant alkali loss. Samples 019, 021, 023, 055 are rhyolitic obsidians with (hydrous) SiO_2 contents of 72.9 – 73.3 wt%; their matrix glasses have a slightly lower content of 71.4 – 72.4 wt% (tables 4.1 & 4.2). The samples are peralkaline with a molar NK/A range from 1.5 - 1.6. Other obsidian glasses and pumices samples have whole rock SiO_2 contents of 68.6 – 74.0 wt% and the matrix glasses have averages of 70.85 – 74.6 wt% (table 4.2). The H_2O content is low in the matrix glasses ~0.2 wt% in obsidians consistent with extensive syn-eruptive degassing. Pumices have a higher range (0.2 – 1.2 wt%) and it is possible that the pumices with higher water content may have suffered some minor secondary hydration and associated alkali loss. Likewise, CO_2

values range from below detection to a maximum of 26 ppm in the matrix glasses and from below detection level to 349 ppm in the pumice glasses.

Alkali feldspar-hosted melt inclusions

The alkali feldspar hosts are An-poor anorthoclase (Ab_{60-71}) (table 4.3, fig. 4.3), euhedral and <1mm. The hosts typically contain a single melt inclusion up to ~150 µm in length, but occasionally contain up to four. The melt inclusions are mostly rounded or elongate, but one or two are square, and are dispersed throughout the host crystals, showing no preferred location. The melt inclusions are glassy and vary in colour from green (sample 055), to colourless (sample 019). The primary concern when using melt inclusions to infer pre-eruptive volatile contents is whether they truly represent the original melt from which the inclusions were trapped, or whether the inclusions have undergone some post-entrapment modification (Metrich and Wallace 2008). This may be indicated by bubbles, de-vitrification, crystallisation or fracturing which can result in loss of vapour (Nielsen et al. 1998). All alkali feldspar hosted melt inclusions in this study contain 1 or more shrinkage bubbles up to 30 µm diameter, which occupy an average of 2% of the total melt inclusion volume, suggesting they have undergone some post entrapment modification. Tiny cracks around some melt inclusion were also observed on the SEM following carbon coating. Part of a melt inclusion from sample 055 was element mapped by SEM to check for any signs of post-entrapment crystallisation. No crystals or microlites were visible under normal SEM conditions (carbon coated, counts per second <2000), but some crystal nuclei were visible under element mapping conditions at ~40,000 counts per second (fig. 4.2b). These nuclei are too small (<1 µm) to be analysed by EMPA or SIMS, but the element maps show these are CaF_2 and therefore the inclusion was close to, or at, fluorite saturation. The melt inclusions are peralkaline, with values of molar NK/A 1.1 – 1.8 that lie close to their host rocks (tables 4.1 and 4.4). SiO_2 content is very fractionally higher than the whole rock values, ranging from 69.2 – 75.3 wt%. The volatile content within the melt inclusion varies between samples (table 4.4). H_2O content shows a wide range of 2.3 to 5.8 wt %; CO_2 values vary from below detection to 462 ppm.

Whole rock[a]	Melt inclusion host samples				Additional samples									
Sample	019	021	023	055	003	012	015	016	022	029	036	038	057	062
type [b]	*rhyolitic obsidian pantellerite*	*rhyolitic obsidian pantellerite*	*rhyolitic obsidian pantellerite*	*rhyolitic obsidian pantellerite*	*pumice pantellerite*	*pumice pantellerite*	*rhyolitic obsidian pantellerite*	*rhyolitic obsidian pantellerite*	*rhyolitic obsidian pantellerite*	*rhyolitic obsidian comendite*	*pumice comendite*	*pumice comendite*	*rhyolitic obsidian pantellerite*	*pumice pantellerite*
host														
n	*1*	*1*	*1*	*1*	*1*	*1*	*1*	*1*	*1*	*1*	*1*	*1*	*1*	*1*
SiO_2	73.30	72.91	72.58	72.75	71.98	68.57	72.39	72.23	71.24	70.00	73.38	73.98	72.85	71.16
TiO_2	0.36	0.35	0.35	0.36	0.37	0.45	0.36	0.35	0.37	0.40	0.17	0.16	0.36	0.37
Al_2O_3	9.77	9.71	9.63	9.32	9.33	9.50	9.37	9.22	9.27	12.10	11.55	11.63	9.45	9.29
Fe_2O_3t	6.46	6.45	6.41	6.60	6.55	6.43	6.58	6.46	6.53	5.69	2.98	3.01	6.63	6.53
MnO	0.21	0.21	0.20	0.21	0.21	0.19	0.22	0.21	0.21	0.18	0.09	0.09	0.22	0.20
MgO	b.d.	b.d.	b.d.	b.d.	b.d.	b.d.	b.d.	b.d.	b.d.	b.d.	b.d.	b.d.	b.d.	b.d.
CaO	0.29	0.28	0.26	0.27	0.32	0.87	0.27	0.43	0.37	0.67	0.41	0.30	0.26	0.62
Na_2O	5.96	6.01	6.01	5.99	6.01	5.29	6.50	5.69	6.70	6.20	5.44	5.27	5.96	5.64
K_2O	4.17	4.30	4.40	4.25	4.38	4.25	4.44	3.24	4.18	4.48	4.40	4.43	4.18	4.09
P_2O_5	0.01	0.01	0.01	0.01	0.01	0.03	0.01	0.01	0.02	0.02	b.d.	b.d.	0.01	0.01
SO_3	0.02	0.02	0.01	b.d.	0.04	0.04	0.04	0.01	0.04	0.07	b.d.	0.02	b.d.	0.01
LOI	0.30	0.21	0.30	0.16	1.02	3.63	0.28	2.31	1.18	0.60	1.11	1.11	0.18	2.56
Total	100.85	100.46	100.16	99.92	100.21	99.27	100.45	100.09	100.11	100.39	99.94	100.00	100.09	100.46
mol(Na+K)/Al	1.5	1.5	1.5	1.5	1.6	1.4	1.7	1.4	1.7	1.2	1.2	1.2	1.5	1.5

Table 4.1. *Whole rock data for melt inclusion host samples and representative obsidians and pumices. [a]major element analysis – XRF, [b]rock type – definition based on total alkalies vs silica plot (TAS) and the comendite- pantellerite definition of MacDonald (1975), n – denotes number of analysis, b.d. below detection, mol* $(Na_2O+K_2O)/Al_2O_3 > 1$ *is a definition of peralkalinity.*

	Pumice matrix glasses						Obsidian matrix glasses							
Sample	003	012	022	036	038	062	015	016	019	021	023	029	055	057
n	*2*	*8*	*2*	*2*	*2*	*2*	*12*	*12*	*19*	*12*	*12*	*11*	*14*	*12*
$SiO_{2\,(wt\%)}$ [a]	73.07	71.70	73.12	74.05	74.61	72.00	71.91	72.25	72.28	71.42	72.38	70.85	72.19	72.40
TiO_2	0.35	0.09	0.37	0.13	0.13	0.38	0.23	0.21	0.29	0.18	0.25	0.41	0.17	0.24
Al_2O_3	9.51	11.31	9.34	11.79	12.13	9.41	9.12	9.05	9.28	10.20	9.27	10.32	9.58	9.03
FeOt	5.96	3.13	6.19	2.51	2.41	5.96	6.12	6.01	6.03	5.51	5.88	5.65	5.72	5.95
MnO	b.d.	b.d.	b.d.	b.d.	b.d.	b.d.	0.19	0.15	0.22	0.16	0.22	0.13	0.16	0.17
MgO	0.21	0.06	0.25	0.06	b.d.	0.18	b.d.	b.d.	b.d.	b.d.	b.d.	b.d.	b.d.	b.d.
CaO	0.29	0.08	0.19	0.19	0.14	0.30	0.27	0.16	0.27	0.20	0.15	0.32	0.14	0.13
Na_2O	5.84	5.14	5.74	5.06	5.10	5.47	5.74	5.79	5.67	5.73	5.70	5.74	5.97	5.71
K_2O	4.38	4.44	4.42	4.57	4.39	4.39	4.32	4.33	4.32	4.50	4.31	4.48	4.43	4.31
ZrO						b.d.	0.06	0.02	0.10	0.11	0.05	0.06	0.05	0.03
P_2O_5	b.d.	b.d.	b.d.	b.d.	b.d.	b.d.	b.d.	b.d.	b.d.	b.d.	b.d.	b.d.	b.d.	b.d.
SO_2	b.d.	b.d.	b.d.	b.d.	b.d.	b.d.	b.d.	b.d.	b.d.	b.d.	b.d.	b.d.	b.d.	b.d.
F							0.24	0.25	0.24	0.25	0.25	0.26	0.23	0.27
Cl	0.2	0.05	0.21	0.19	0.21	0.19	0.09	0.10	0.13	0.09	0.10	0.10	0.12	0.10
Total	99.81	96.00	99.83	98.55	99.12	98.28	98.30	98.33	98.85	98.35	98.55	98.32	98.76	98.35
mol (Na+K)/Al [b]	1.5	1.2	1.5	1.1	1.1	1.5	1.5	1.6	1.5	1.4	1.5	1.4	1.5	1.6
n	*1*	*1*	*1*	*1*	*1*	*1*	*1*	*1*	*1*			*1*		*1*
H_2O (wt%) [c]	0.19	1.18	0.32	1.19	0.81	0.16	0.16	0.16	0.16			0.16		0.22
error [1]	*0.001*	*0.005*	*0.003*	*0.007*	*0.003*	*0.002*	*0.002*	*0.002*	*0.002*			*0.001*		*0.002*
H2O (wt%) [d]									0.182 (6)		0.177 (6)		0.187 (9)	
error [2]									*0.08*		*0.01*		*0.01*	
CO_2 (ppm) [c]	44	98	35	70	b.d.	349	13	3	13			20	9	9
error [1]	*6*	*11*	*9*	*8*		*16*	*4*	*2*	*3*			*6*	*5*	*5*
T (°C) - ave [e]	*n.c.*	782	*n.c.*	*n.c.*	*n.c.*	*n.c.*	*n.c.*	*n.c.*	*n.c.*	*n.c.*	*n.c.*	*n.c.*	701	*n.c.*
P (Mpa)	*n.c.*	52	*n.c.*	*n.c.*	*n.c.*	*n.c.*	*n.c.*	*n.c.*	*n.c.*	*n.c.*	*n.c.*	*n.c.*	14	*n.c.*
Depth - ave	*n.c.*	1.9	*n.c.*	*n.c.*	*n.c.*	*n.c.*	*n.c.*	*n.c.*	*n.c.*	*n.c.*	*n.c.*	*n.c.*	0.5	*n.c.*

Table 4.2. *Obsidian matrix glasses and pumice glasses analysed for majors and traces. [a]major element analysis EMPA [b]mol (Na_2O+K_2O)/Al_2O_3 > 1 is a definition of peralkalinity, [c]SIMS analysis, [d]Averaged matrix glass measured using FTIR analysis. Number in parenthesis is the number of measurements, [e]temperature in °C using the method of (a) Putirka (2008) and (b) Putirka (2003). Calibration error ±23°C, n – denotes number of analysis, [1]average error as determined by full propagation of counting statistics, instrument background and calibration working curve, [2]standard deviation, b.d. below detection, n.c. not calculated, blank space indicates no analysis.*

	Pumice matrix glasses						Obsidian matrix glasses							
Sample	003	012	022	036	038	062	015	016	019	021	023	029	055	057
Li (ppm)^c	40	37	40	40	41	37	39	38	40			34	39	42
Be	9.2	9.1	9.1	9.3	9.6	9.1	9.1	9.0	9.1			8.3	9.2	9.6
B	11	10	11	12	12	11	11	11	11			10	11	11
Sc	3.6	3.9	3.8	3.4	3.5	3.1	3.6	3.5	3.4			3.5	3.5	3.2
Rb	116	112	128	112	104	114	120	119	118			100	122	118
Sr	1.2	1.2	1.1	1.7	1.8	1.2	1.0	0.9	1.0			16.2	0.9	1.0
Y	102	99	108	97	103	98	102	101	100			86	104	100
Zr	1087	1031	1161	824	823	1057	1093	1088	1070			937	1122	1072
Nb	170	155	182	129	126	166	171	172	165			141	176	165
Ba	14	14	15	85	88	14	14	14	16			302	13	13
La	107	104	114	63	67	103	108	106	103			95	110	105
Ce	213	207	229	134	149	208	216	215	208			192	217	206
Pr	25.3	24.0	26.5	15.7	18.1	25.0	25.3	25.8	24.8			21.9	26.0	24.8
Nd	109	107	117	69	82	101	109	107	106			99	111	103
Sm	21.3	21.9	22.2	14.6	17.6	20.6	21.3	21.7	21.4			17.9	22.1	21.1
Eu	2.8	2.9	2.9	1.9	2.2	2.7	2.6	2.8	2.8			4.9	2.8	2.9
Gd	30.1	28.9	29.9	18.4	19.1	25.8	26.4	28.2	25.3			24.8	28.9	28.1
Tb	4.2	4.1	4.4	3.1	3.7	4.2	4.0	4.3	3.8			3.4	4.2	4.2
Dy	32.6	31.4	35.2	25.2	29.2	31.1	33.8	34.5	31.5			28.1	32.7	31.8
Ho	4.3	4.2	4.7	4.1	4.3	4.2	4.2	4.5	4.2			3.9	4.6	4.1
Er	14.0	12.5	14.0	12.2	13.7	13.0	12.9	13.2	13.2			11.8	13.2	13.3
Yb	12.4	11.8	14.2	12.9	13.4	11.9	12.1	12.0	11.7			9.3	13.6	11.6
Lu	1.9	1.6	1.8	1.7	2.0	1.8	2.0	2.0	1.8			1.5	2.0	1.7
Hf	26	22	26	23	25	24	26	25	26			21	28	24
Ta	13	11	14	10	11	12	13	13	12			10	13	12
Th	11	9	11	11	11	10	10	11	10			9	11	10
U	3	3	3	3	3	3	3	3	3			3	3	3

Table 4.2 cont.

Feldspar

Sample	019 fsp	019 fsp	021 fsp	021 fsp	023 fsp	023 fsp	023 fsp	055 fsp	55 fsp	55 fsp
SiO_2 (wt%)[a]	67.56	67.74	67.48	67.05	67.27	66.88	67.00	67.10	67.50	68.40
TiO_2	b.d.	b.d.	b.d.	b.d.	b.d.	b.d.	b.d.	b.d.	b.d.	b.d.
Al_2O_3	18.28	18.53	18.38	18.85	18.71	18.76	18.26	18.13	18.14	18.77
FeOt	0.66	0.68	0.68	0.36	0.67	0.41	0.58	0.71	0.76	0.71
MnO	b.d.	b.d.	b.d.	b.d.	b.d.	b.d.	b.d.	b.d.	b.d.	b.d.
MgO	b.d.	0.07	b.d.	b.d.	b.d.	b.d.	b.d.	b.d.	b.d.	b.d.
CaO	b.d.	b.d.	b.d.	b.d.	b.d.	b.d.	b.d.	b.d.	b.d.	b.d.
Na_2O	8.04	8.04	7.78	7.92	7.83	8.03	7.94	7.33	7.92	7.63
K_2O	5.41	5.35	5.34	5.65	5.70	5.54	5.53	6.23	5.57	5.58
P_2O_5					b.d.	b.d.	b.d.	b.d.		
SO_2	b.d.	b.d.	b.d.	b.d.	b.d.	b.d.	b.d.	b.d.	b.d.	b.d.
Cl					b.d.	b.d.	b.d.	b.d.		
Total	99.95	100.41	99.66	99.83	100.18	99.62	99.31	99.50	99.89	101.09
An	*0.0*	*0.0*	*0.0*	*0.0*	*0.0*	*0.0*	*0.0*	*0.0*	*0.0*	*0.0*
Ab	*69.3*	*69.5*	*68.9*	*68.1*	*67.60*	*68.8*	*68.60*	*67.8*	*67.0*	*67.1*
Or	*30.7*	*30.5*	*31.1*	*31.9*	*32.40*	*31.2*	*31.40*	*32.2*	*33.0*	*32.9*
Si+Al+Ti+Fe	*4.0*	*4.0*	*4.0*	*4.0*	*4.0*	*4.0*	*4.0*	*4.0*	*4.0*	*4.0*
Ca+Na+K	*1.0*	*1.0*	*1.0*	*1.0*	*1.0*	*1.0*	*1.0*	*1.0*	*1.0*	*1.0*

CPX

Sample	055 cpx	055 cpx	055 cpx
SiO_2	48.32	48.88	48.51
TiO_2	0.42	0.40	0.41
Al_2O_3	0.17	0.15	0.17
FeOt	30.96	31.33	31.02
MnO	1.47	1.49	1.53
MgO	0.11	0.08	0.07
CaO	17.14	16.65	16.81
Na_2O	2.01	2.35	2.06
K_2O	b.d.	b.d.	b.d.
Cr_2O_3	b.d.	b.d.	b.d.
NiO	b.d.	b.d.	b.d.
ZnO	b.d.	b.d.	b.d.
Total	100.60	101.32	100.58
$Fe^{2+ b}$	0.20	0.22	0.18
$Fe^{3+ b}$	0.86	0.84	0.87
(Mg) En	0.4	0.3	0.2
(Fe) Fs	58.3	59.3	58.9
(Ca) Wo	41.3	40.4	40.9
Mg#	0.8	0.6	0.5

Olivine

Sample	021 ol	021 ol
SiO_2	29.54	29.31
TiO_2	b.d.	0.03
Al_2O_3	b.d.	b.d.
FeOt	67.57	67.61
MnO	3.69	3.68
MgO	0.07	0.08
CaO	0.46	0.50
Na_2O	b.d.	b.d.
K_2O	b.d.	b.d.
Cr_2O_3	b.d.	b.d.
NiO	b.d.	b.d.
ZnO	0.12	0.12
Total	101.45	101.33
Fo	*0.2*	*0.2*
Fa	*99.8*	*99.8*
Mg#	*0.2*	*0.2*

***Table 4.3**. Major element analysis of representative host crystals, [a] major element analysis – EMPA. [b]$Fe^{2+}/^{3+}$ in cpx calculated according to the method of Schumacher (1991), b.d. - below detection level, blank space indicates no analysis, Mg# = 100 Mg/(Mg+FeOt+Mn)*

***Table 4.4 (overleaf).** Representative melt inclusion analysis. [a]major element analysis – XRF, [b]SIMS analysis, [c]rock type – definition based on total alkalies vs silica plot (TAS) and the comendite- pantellerite definition of MacDonald (1975), [d]P.I.- mol (Na_2O+K_2O)/Al_2O_3 > 1 is a definition of peralkalinity, [e]temperature in °C using the method of (a) Putirka (2008) and (b) Putirka (2003), calibration error ±23°C, [f] pressure in MPa using the method of Papale et al (2006), [g] depth calculated from P assuming a crustal density of ~2800kgm^{-3}, n – denotes number of analysis, [1] average error as determined by full propagation of counting statistics, instrument background and calibration working curve, b.d. below detection, n.c. not calculated, blank space indicates no analysis.*

Sample	019 a	019 b	021 a	021 b	023 a	023 b	21 J	21 O	055 c	055 d	055 i
host	fsp	fsp	*fsp*	*fsp*	*fsp*	*fsp*	*ol*	*ol*	*cpx*	*cpx*	*cpx*
type ^{c}	*p*	*p*	*p*	*p*	*p*	*p*	*p*	*c*	*p*	*p*	*p*
n	*1*	*1*	*3*	*3*	*2*	*1*	*3*	*2*	*2*	*8*	*2*
SiO_2 (wt%) ^{a}	71.51	72.43	70.45	70.40	75.31	72.85	69.92	69.40	71.82	72.12	72.68
TiO_2	0.29	0.29	0.45	0.47	0.46	0.49	0.54	0.38	0.39	0.38	0.44
Al_2O_3	9.46	9.19	8.23	8.32	6.38	6.28	12.28	12.44	9.54	9.37	9.51
FeO	5.10	5.06	4.91	5.07	4.89	5.25	6.31	5.94	3.95	4.52	4.31
MnO	0.18	0.19	0.19	0.16	0.28	0.26	0.24	0.21	b.d.	0.20	0.19
MgO	b.d.	b.d.	b.d.	b.d.	b.d.	b.d.	b.d.	b.d.	b.d.	b.d.	b.d.
CaO	0.18	0.16	0.12	0.22	b.d.	b.d.	0.43	0.48	0.15	0.15	0.28
Na_2O	5.48	5.42	4.90	5.13	4.49	4.43	6.15	6.10	4.55	5.01	5.27
K_2O	4.23	4.28	4.06	4.06	3.37	3.60	4.87	4.80	4.69	4.53	4.64
P_2O_5	b.d.	b.d.	b.d.	b.d.	b.d.	b.d.	b.d.	b.d.	b.d.	b.d.	b.d.
SO2	b.d.	b.d.	0.04	b.d.	b.d.	b.d.	0.04	0.06	0.06	0.05	b.d.
ZrO			0.25	0.24			0.21	0.25	0.22	0.25	b.d.
Cl	0.23	0.27	b.d.	0.25	0.30	0.30	0.21	0.2	0.19	0.22	0.22
F											
Total	96.67	97.29	93.61	94.32	95.46	93.45	101.20	100.26	95.57	96.79	97.51
mol(Na+K)/Al^d	1.5	1.5	1.5	1.5	1.7	1.8	1.3	1.2	1.3	1.4	1.4
n	*1*	*1*	*1*	*1*	*1*	*1*	*1*	*1*	*1*	*1*	*1*
H_2O (wt%)^b	3.38	2.29	5.79	5.57	3.96	5.25	0.28	0.57	3.56	3.32	3.27
error^1	*0.01*	*0.02*	*0.080*	*0.080*	*0.010*	*0.004*	*0.004*	*0.010*	*0.080*	*0.080*	*0.080*
CO_2 (ppm)^b	52	89	32	71	157	76	279	484	1457	57	44
error^1	*17*	*11*	*11*	*7*	*12*	*7*	*10*	*16*	*34*	*1*	*1*
T (^{o}C)	*746*	*744*	*738*	*764*	*699*	*711*	*n.c.*	*n.c.*	*800* ^{e}	*n.c.*	*n.c.*
P (MPa)	*57*	*55*	*137*	*136*	*100*	*113*	*n.c.*	*n.c.*	*440*	*n.c.*	*n.c.*
Depth	*2.1*	*2.0*	*5.0*	*5.0*	*3.6*	*4.1*	*n.c.*	*n.c.*	*16.0*	*n.c.*	*n.c.*
Li (ppm)^b	39	41	51	35	40	35	20	20	36	40	33
Be	8.8	8.8	9.1	8.0	8.3	8.2	6.8	8.9	7.4	9.4	9.1
B	12	12	13	11	15	15	8	10	10	12	12
Sc	6.4	3.6	4.0	3.8	4.4	3.9	3.8	3.6	6.3	3.8	4.0
Rb	151	161	185	176	203	199	113	108	124	142	140
Sr	0.9	1.0	0.7	0.9	0.8	0.6	5.3	5.4	2.4	0.9	1.0
Y	93	94	104	106	117	88	84	92	137	114	119
Zr	1043	1059	1173	1152	1220	1168	856	980	1221	1220	1170
Nb	157	169	190	198	226	186	128	147	179	206	197
Ba	15	14	16	16	13	12	285	288	16	17	15
La	100	103	115	119	125	92	88	103	135	131	129
Ce	203	212	237	244	259	189	175	201	331	267	274
Pr	23.8	24.6	27.8	28.1	30.4	22.0	20.3	23.4	43.6	31.1	32.4
Nd	103	106	115	121	132	95	87	100	196	130	145
Sm	19.0	20.8	22.1	24.3	23.6	17.9	16.6	17.6	37.4	24.4	28.6
Eu	2.4	2.6	2.7	2.9	3.4	2.2	5.4	5.7	5.0	3.2	3.3
Gd	24.9	24.4	35.3	35.9	30.4	20.7	30.5	34.5	51.7	41.3	45.0
Tb	3.9	4.0	4.9	5.0	4.7	3.1	3.7	4.2	8.1	5.6	5.5
Dy	30.7	30.7	27.5	28.5	36.5	28.8	22.7	23.6	40.1	30.4	29.6
Ho	4.1	3.9	4.3	4.7	5.1	3.7	3.8	4.4	6.5	5.1	5.3
Er	12.5	12.5	b.d.	b.d.	16.2	12.8	b.d.	b.d.	b.d.	b.d.	b.d.
Yb	11.4	10.9	0.4	3.1	14.1	10.7	b.d.	b.d.	4.4	b.d.	0.5
Lu	1.5	1.7	b.d.	b.d.	2.1	1.7	b.d.	b.d.	b.d.	b.d.	b.d.
Hf	23	23	28	28	30	29	21	26	36	32	27
Ta	11	12	12	14	14	14	9	10	14	14	13
Th	10	11	11	11	13	12	8	9	11	11	12
U	3	3	3	3	4	4	2	2	3	4	3

Sample	055 a	055 c	055 h	055 i	055 m	055 n	055 p	055 q	055 aa	055 ae	055 al
host	*fsp*	*fsp*	*fsp*	*fsp*	*fsp*	*fsp*	*fsp*	*fsp*	*fsp*	*fsp*	fsp
type [c]	*p*	*p*	*p*	*p*	*p*	*p*	*p*	*p*	*p*	*p*	*p*
n	*2*	*3*	*3*	*2*	*3*	*2*	*2*	*3*	*3*	*2*	*2*
SiO_2 (wt%) [a]	71.02	70.66	71.35	71.50	70.07	71.07	71.11	70.69	70.12	70.10	72.56
TiO_2	0.45	0.51	0.51	b.d.	0.50	0.55	0.47	0.50	0.26	0.45	0.61
Al_2O_3	8.23	8.84	7.86	8.35	8.06	8.07	8.14	8.16	10.07	8.93	6.79
FeO	5.59	5.49	6.08	5.46	6.18	5.86	4.98	5.76	4.95	5.16	6.42
MnO	0.27	0.21	0.29	0.26	0.23	0.27	0.22	0.23	0.18	0.23	0.35
MgO	b.d.	b.d.	b.d.	b.d.	b.d.	b.d.	b.d.	b.d.	b.d.	b.d.	b.d.
CaO	0.17	0.26	0.26	0.19	0.35	0.23	0.15	0.20	0.42	0.18	0.11
Na_2O	5.26	5.30	5.18	5.19	5.37	5.05	5.12	5.31	6.12	5.77	2.87
K_2O	4.16	4.15	4.06	4.21	4.09	4.14	4.24	4.17	4.46	4.16	3.68
P_2O_5	b.d.	b.d.	b.d.	b.d.	b.d.	b.d.	b.d.	b.d.	b.d.	b.d.	b.d.
SO2	0.05	0.05	b.d.	0.05	0.07	0.04	0.05	0.05	b.d.	b.d.	0.06
ZrO	0.23	0.24	0.34	b.d.	b.d.	0.2	0.35	0.4	b.d.	b.d.	
Cl	0.26	0.22	0.25	0.25	0.27	0.27	0.25	0.24	0.15	0.21	0.31
F				0.30		0.18					
Total	95.69	95.92	96.19	95.45	95.18	95.77	95.07	95.71	96.74	95.20	93.76
mol(Na+K)/Al [d]	1.6	1.5	1.6	1.6	1.6	1.6	1.6	1.6	1.5	1.6	1.3
n	*1*	*1*	*1*	*1*	*1*	*1*	*1*	*1*	*1*	*1*	*1*
H_2O (wt%) [b]	3.91	4.21	4.55	4.03	3.98	3.59	3.38	3.55	3.48	4.50	3.94
error [1]	*0.032*	*0.030*	*0.034*	*0.029*	*0.034*	*0.029*	*0.046*	*0.045*	*0.030*	*0.050*	*0.11*
CO_2 (ppm) [b]	49	138	34	25	8	96	9	9	30	9	317
error [1]	*5*	*8*	*8*	*6*	*6*	*9*	*10*	*10*	*6*	*7*	*19*
T (°C)	*755*	*772*	*781*	*760*	*803*	*776*	*754*	*766*	*807*	*745*	789
P (MPa)	*66*	*114*	*76*	*57*	*49*	*79*	*37*	*39*	*53*	*67*	137
Depth	*2.4*	*4.1*	*2.8*	*2.1*	*1.8*	*2.9*	*1.4*	*1.4*	*1.9*	*2.4*	*5.0*
Li (ppm) [b]	48	45	51	50	46	45	42	46	52	51	71
Be	9.1	9.1	9.7	9.2	8.9	8.9	8.4	9.0	8.8	8.9	12.6
B	12	12	13	12	12	12	12	12	13	13	14
Sc	3.5	3.8	4.2	3.5	4.0	3.8	3.9	4.0	3.9	3.8	1.2
Rb	154	153	154	167	163	166	159	162	175	178	142
Sr	0.8	0.9	0.9	1.1	0.8	1.0	1.7	1.1	0.7	0.6	1.3
Y	111	101	118	109	110	110	109	112	111	113	148
Zr	1226	1124	1239	1205	1193	1245	1228	1219	1326	1250	1728
Nb	199	180	203	205	211	213	210	208	211	213	280
Ba	18	19	17	19	13	15	30	17	19	12	13
La	121	113	130	120	127	123	123	127	126	127	169
Ce	249	235	266	255	264	254	257	265	262	267	352
Pr	30.0	26.5	31.7	30.1	30.7	29.6	29.1	30.4	30.8	30.9	40.3
Nd	125	114	133	121	132	124	127	126	127	133	166
Sm	23.0	22.0	23.7	22.1	22.9	23.9	22.8	23.9	24.5	23.2	32.3
Eu	3.1	2.8	3.4	2.9	3.1	3.1	3.6	3.2	3.3	3.4	5.3
Gd	30.1	37.1	45.0	36.5	41.1	39.7	41.4	38.3	40.7	43.5	21.7
Tb	5.4	5.4	5.5	5.4	5.8	6.1	5.7	5.6	5.1	5.7	5.6
Dy	27.8	26.8	30.6	28.7	32.1	31.2	31.5	32.3	29.5	30.3	45.3
Ho	4.8	4.5	5.3	4.8	5.2	5.3	5.4	5.3	5.3	5.2	6.6
Er	b.d.	b.d.	b.d.	b.d.	b.d.	b.d.	b.d.	b.d.	b.d.	b.d.	21.9
Yb	b.d.	b.d.	b.d.	1.2	b.d.	b.d.	b.d.	2.0	b.d.	b.d.	21.9
Lu	b.d.	b.d.	b.d.	b.d.	b.d.	b.d.	b.d.	b.d.	b.d.	b.d.	3.3
Hf	31	28	30	31	30	31	32	31	35	31	47
Ta	14	13	12	14	15	15	15	15	15	14	22
Th	12	10	11	12	12	12	13	12	13	12	19
U	3	3	3	4	4	4	4	3	4	3	6

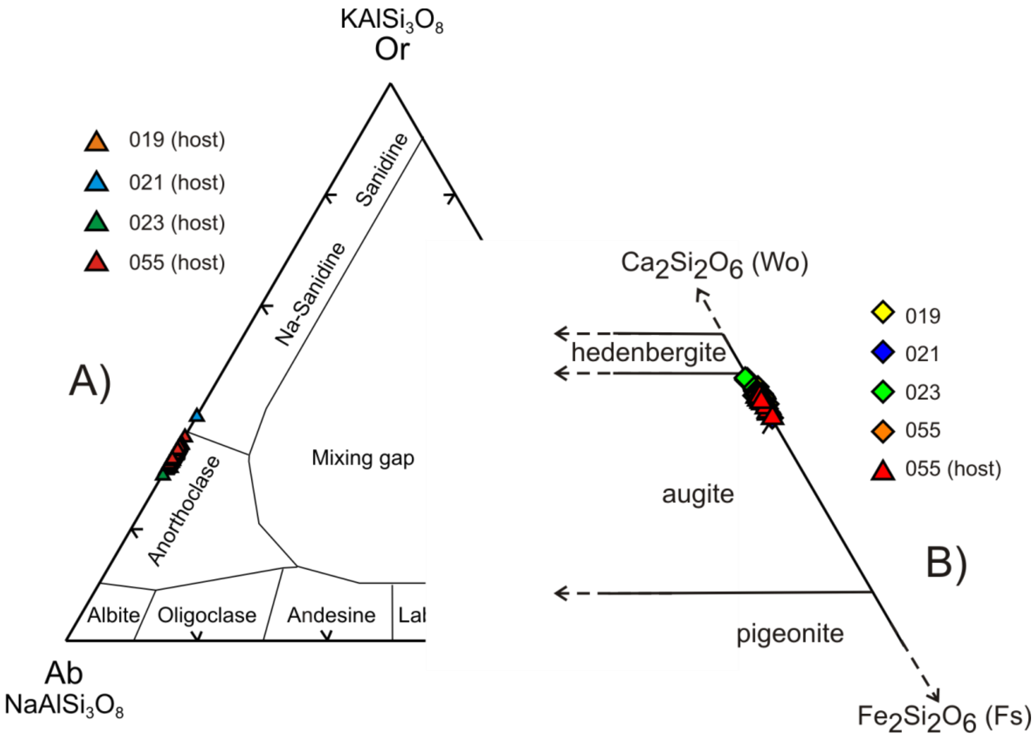

Figure 4.3. *Partial classification diagrams for feldspar melt inclusion host crystals (a,) and (b) pyroxene host and non-host compositions. Both plots show limited range in compositions.*

Cpx- and olivine-hosted melt inclusions

Cpx- hosted melt inclusion were located only in sample 055, which contains euhedral Fe-augite crystals <1 mm in length with average compositions of Wo_{41}, Fs_{58}, En_0, Mg# <1 (table 4.3, fig. 4.3). One to two melt inclusions are contained in each host cpx and these are rounded to elongate. The melt inclusions are up to ~150 µm in length (average ~71 µm). Bubbles when visible are small, up to ~18 µm. The largest bubble occupies 11% of the volume of the total melt inclusions, but the smaller bubbles average 1% volume. The melt inclusions have an SiO_2 range of 71.8 – 74.9 wt%. H_2O contents lie at or below the low end of the alkali feldspar-hosted melt inclusions, 1.1 - 3.6 wt%, whereas CO_2 values of extend the range to higher values, 26 - 1457 ppm (table 4.4).

Three subhedral fayalite olivine hosts (Fa 99.7 - 100) (table 4.3) were located in sample 021 and each found to contain a single melt inclusion <36 µm diameter. No bubbles were visible. Typically olivine-hosted melt inclusions are corrected for post entrapment crystallisation of the host by using the method of (Danyushevsky et al. 2000). However, due to the lack of MgO in both the melt inclusion and the host, this has not been possible. The melt inclusions have an SiO_2 range of 69.2 – 69.9 wt% and low volatile contents: 0.2 - 0.6 wt% H_2O and 279 - 484 ppm CO_2 (table 4.4).

Comparison to volatile contents of other peralkaline rhyolites

Early studies of peralkaline rhyolites proposed that H_2O contents were low (<0.5 wt %) based on low H_2O and high Cl concentrations within matrix glasses (Bailey and Macdonald 1969; Nicholls and Carmichael 1969; Bailey et al. 1974). Melt inclusion studies have now been published from a range of peralkaline rhyolites, but are far from exhaustive. These have consistently shown relatively high H_2O contents, consistent with the present study - e.g. Pantelleria, Italy 1.4 – 4.3 wt% (Lowenstern and Mahood 1991; Gioncada and Landi 2010), Greater Olkaria Province 0.9 – 3.4 wt% (Wilding et al. 1993), Fantale, Ethiopia 0.4 – 8.5 wt% (mean of 4.6 - 4.9 wt%), (Webster et al. 1993), Mayor Island, NZ, 2.6 - 5.0 wt% (Barclay et al. 1996), Baitoushan Volcano, China/North Korea, 1.3 – 6.6 wt% (Horn and Schmincke 2000). Experimental studies such as those from Eburru, Kenya which suggests peralkaline pre-eruptive water contents were > 4 wt%, even as high as 5-6 wt%, support these findings (Scaillet and Macdonald 2006).

Major and trace element systematics

Major element data for Dabbahu as a whole span a wide compositional range from basalt to rhyolite (Barberi et al. 1974a), consistent with protracted fractional crystallisation of a basaltic parent magma. Here we focus only on the intermediate and silicic rock types (>58 wt% SiO_2), in order to provide a framework for interpreting the melt inclusion data. The whole-rock data in table 4.1, for the samples studied here, are augmented by unpublished data for intermediate rocks.

Up to SiO_2 contents of ~69 wt% the whole rocks show a single magmatic lineage, characterised by increasing K_2O, roughly constant Al_2O_3 and falling TiO_2 and FeO, although the latter does show some scatter (fig. 4.4). Above 69 wt% SiO_2 the evolved rocks show two divergent trends, best seen in FeO, but also apparent in Al_2O_3. These two trends correspond to comendites (low FeO, high Al_2O_3) and pantellerites (high FeO, low Al_2O_3). Their divergence can be attributed to differing ratios of alkali-feldspar to mafic minerals (notably Fe-augite) in the fractionating assemblage. The strong negative correlation between FeO and SiO_2 (fig 4.4a) in the comendites requires higher proportions of Fe-augite than for the pantellerites. The modest fall in TiO_2 with SiO_2 for both suites (fig. 4.4d) is consistent with the presence of accessory ilmenite. All of the melt inclusions and obsidian glasses analysed come from the pantelleritic suite, although matrix glasses were analysed from both pantellerite and comendite pumices (sample 036 and 038).

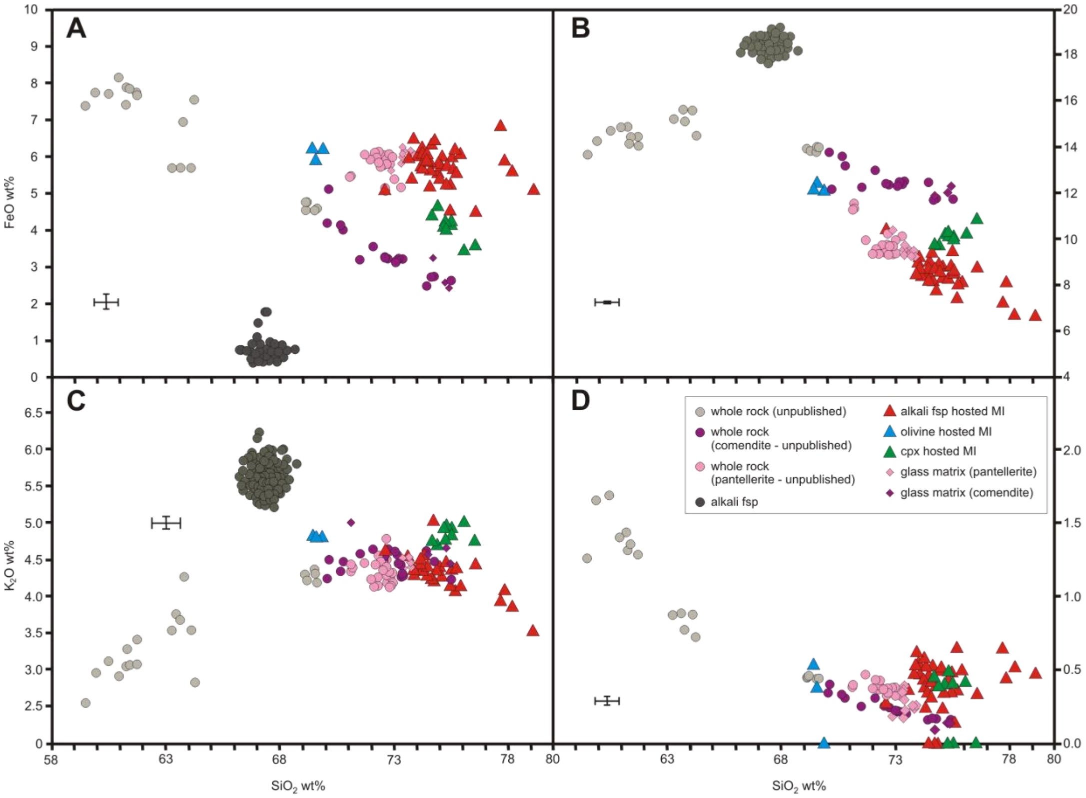

***Figure 4.4**. Selected Harker diagrams for major element oxides (anhydrous wt% basis, normalised to 100%). Data augmented by unpublished whole rock (XRF) data, and where applicable, alkali feldspar data. Typical uncertainties (1σ) indicated by error bars.*

Matrix glasses from pumices and obsidians lie at the high SiO_2 end of the corresponding whole rock trends for comendites and pantellerites, consistent with the nature of the host rock. The very limited enrichment of matrix glass SiO_2 compared to whole rocks is consistent with the very low phenocryst contents. The melt inclusions, which derive exclusively from pantellerites, span a wide range of SiO_2 (69 - 78 wt% SiO_2), that overlaps, but extends, the whole rock range. The olivine-hosted melt inclusions lie at the low SiO_2 end of the range, consistent with trapping at a relatively early stage of magma differentiation. The alkali-feldspar hosted inclusions provide the closest match to the whole rocks, but also extend to the highest SiO_2. Close agreement between the composition of the alkali feldspar-hosted inclusions and the whole rocks testify to limited post-entrapment crystallisation of the melt inclusions around their walls, consistent with our petrographic observations. However, there is scatter evident in the FeO - SiO_2 plot (fig. 4.4a), which is likely caused by crystallisation of alkali feldspar, which is low in FeO. Based simply on mass balance considerations, the amount of post-entrapment crystallisation is modest, about 10 wt% in the case of the most FeO-rich melt inclusion. The majority of the inclusions do not form an array that back-projects to alkali feldspar compositions, best seen in the Al_2O_3 - SiO_2 plot (fig. 4.4b), instead extending the whole-rock trend, which is itself controlled by both alkali feldspar and mafic minerals, such as Fe-augite. Thus post-entrapment crystallisation cannot be considered as the primary driver of melt inclusion compositional variation. The same cannot be said of the Fe-augite-hosted melt inclusions, which do not match the whole rock pantellerites, in having lower FeO and higher K_2O and Al_2O_3.

We attribute these discrepancies to post-entrapment crystallisation of host Fe-augite. Again, using mass balance constraints, the Fe-augite FeO contents are ~31 wt% (table 4.3), but the extent of post entrapment crystallisation is only 7 wt%. The offset is simply more pronounced than for alkali feldspar host melt inclusions because the host mineral in so different in composition to the melt inclusion. In summary, the amount of post-entrapment crystallisation suffered by the melt inclusion suite as a whole is sufficiently small that our measured melt inclusion volatile contents are likely to deviate from their true values at entrapment by no more than 10% relative and, in the vast majority of cases, much less. For that reason we have not attempted to make any post-entrapment crystallisation corrections to volatile contents as measured.

Trace element concentrations in matrix and melt inclusion glasses also overlap with whole rock data, e.g. for Zr (fig. 4.5a). The high Zr contents (>1000 ppm) are a consequence of the high solubility of zircon in peralkaline melts; only the comendites show any evidence for a drop on Zr at high SiO_2, consistent with eventual zircon saturation. Pairs of incompatible trace elements, such as Nb and Zr (fig. 4.5b) are strongly correlated, and lie at the high concentration extrapolation of the trachyandesite and trachyte whole rocks and overlap with the comendites and pantellerites. Some comendites are displaced to slightly lower Nb at a given Zr, perhaps due to a greater role of ilmenite (which can accommodate Nb) in the evolution of these rocks. Again the olivine hosted melt inclusions are the least evolved in terms of their incompatible trace elements. A single Zr-rich (1720 ppm) alkali-feldspar hosted melt inclusion (055-al; table 4.4) may have experienced significant post-entrapment crystallisation, although its FeO content (6.42 wt%) is not remarkably high.

The wide range in Zr contents, and the demonstrable incompatible nature of this element make it a useful monitor of the extent of fractionation (F). Zr is not well correlated with SiO_2 (fig. 4.5a), indicating that the latter component does not adequately reflect F. Thus, the total change in F for melt inclusions, notwithstanding the anomalous high Zr sample, is a factor of 1.75, equivalent to 43% crystallisation, yet the total increase in SiO_2 over the same interval is only 69 to 75 wt%. In large part this reflects the high SiO_2 content of the alkali-feldspar-dominated crystallising assemblage, such that large amounts of crystallisation manifest as only small changes in SiO_2. The onset of alkali feldspar crystallisation is evident on a logarithmic plot of Ba (which is compatible in alkali feldspar) versus Zr (fig. 4.5c). In summary, the chemical variation in the comendites and pantellerites reflects considerable fractionation, despite little variation in SiO_2. The lack of any significant correlation between an incompatible trace element, such as Zr, and SiO_2 (fig. 4.5a) is suggestive of near-eutectic behaviour; the major elements are buffered within the system, and therefore vary little during crystallisation. One explanation is that crystallisation took place close to the ternary minimum. In metaluminous systems it is possible to use the composition of melts within the haplogranite system (orthoclase-albite-quartz) to establish eutectic behaviour and estimate the crystallisation pressure(s). The subaluminous, peralkaline nature of the rocks from Dabbahu removes them from the orthoclase-albite-quartz (Or-Ab-Qz) plane.

Consequently, it is not possible to establish from their major elements alone if these melts are buffered by the minima in the alumina-poor portion of the Qz-Ab-Or system. Thompson and Mackenzie (1967) suggested that pantellerites lie within a ‘low temperature zone’ which had its origin in the ‘thermal valley’ of the granite system. The limited compositional range seen within anorthoclase phenocrysts from pantellerites was proposed by (Thompson and Mackenzie 1967) as further evidence of the presence of a thermal valley, and this constancy of composition can be seen within the phenocrysts from Dabbahu e.g. sample 055 Ar_{64-69} and Or_{30-35} (fig. 4.3).

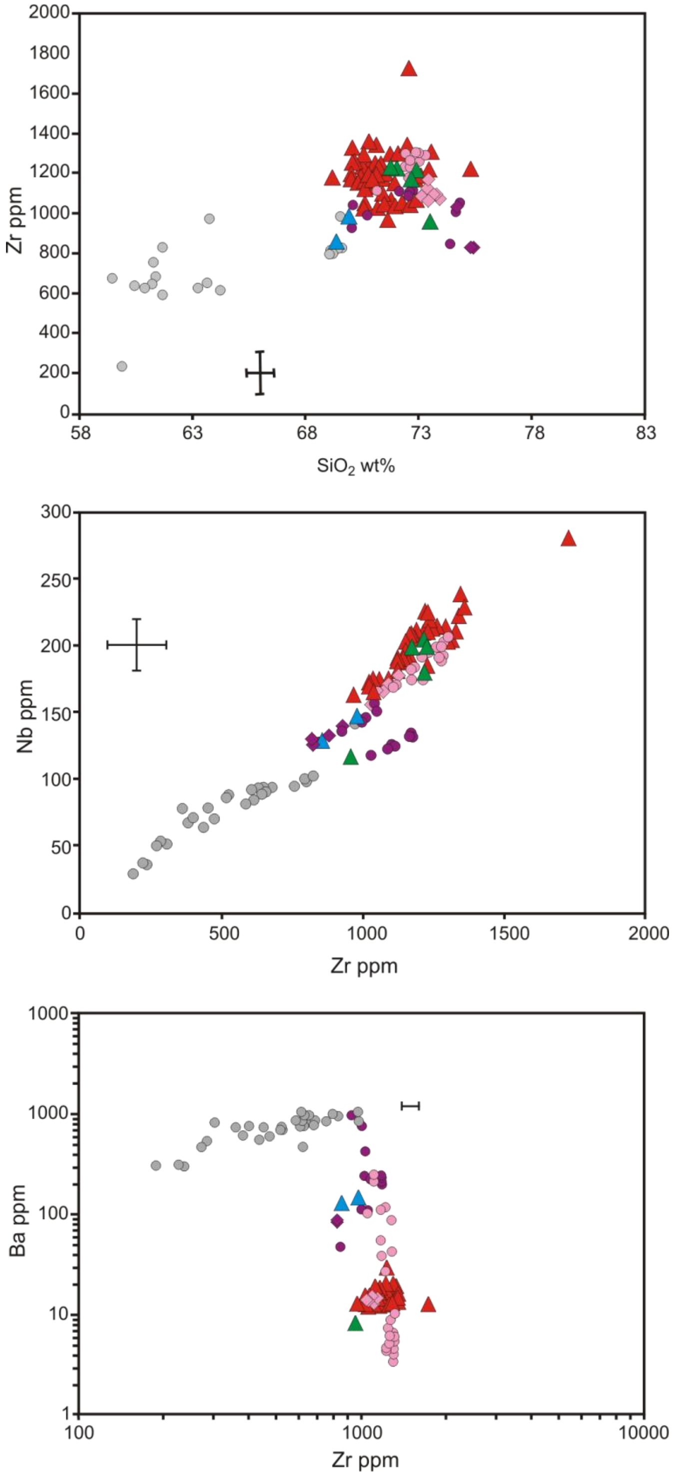

Figure 4.5. *Diagrams of Zr concentration in whole rock, melt inclusion and matrix glasses plotted against a) SiO$_2$, b) Nb, c) Ba - note the logarithmic scale. Key as for fig. 4.4.*

Volatile elements

Figure 4.6 is a conventional plot of CO_2 versus H_2O in the analysed matrix and melt inclusion glasses. As noted above, we have made no attempt to correct volatile contents for post-entrapment crystallisation, which we consider to have been minor.

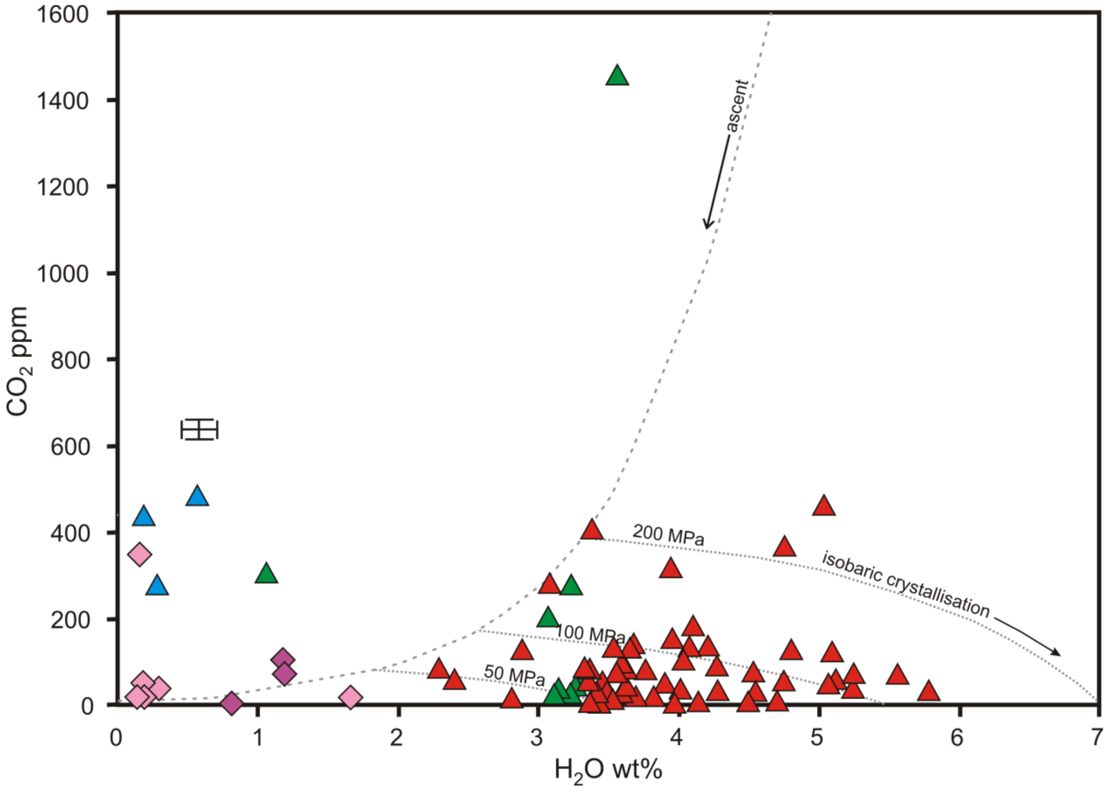

Figure 4.6. *Melt inclusion and matrix glass volatile measurements on a conventional CO_2 versus H_2O plot. Dotted lines are isobars, dashed line denotes vapour isopleth calculated using for 20 mol% H_2O in the vapour. Isobars and isopleths calculated from the average melt inclusion analysis of sample 55 and the method of Papale et al. (2006). The olivine and 1 cpx hosted melt inclusions have lost H_2O. Matrix glasses are degassed; higher values may be analytical artifacts.*

The bulk of the melt inclusions lie between 3 and 6 wt% H_2O with CO_2 contents ≤400 ppm. The matrix glasses have less than 2 wt% H_2O and, with a few exceptions, less than 80 ppm CO_2, consistent with extensive syn-eruptive degassing. All three olivine-hosted and a single cpx-hosted melt inclusion are displaced to very low H_2O (≤1 wt%) from the main body of melt inclusions, but at broadly similar CO_2 levels. The most ready explanation for these melt inclusions is that they have lost H_2O, either by diffusion through the host mineral, or by leakage along cracks. The fact that these same inclusions show no evidence from major or trace elements for significant post-entrapment crystallisation, suggests that diffusion loss was the primary cause of H_2O loss. The groundmass glasses with elevated CO_2 are most likely analytical artefacts, although we cannot discount some interaction with CO_2-rich materials (magmatic vapours, sediments). A single cpx-hosted melt inclusion lies at high CO_2 (1457 ppm) and 3.5 wt% H_2O. This is, by some margin, the most volatile-rich (and hence highest pressure) inclusion analysed.

The field defined by the bulk of the melt inclusions does not match the predicted variation from degassing, under closed or open system. Instead, the field is consistent with vapour-saturated, polybaric crystallisation (Blundy and Cashman 2008). In the presence of a mixed H_2O-CO_2 vapour, crystallisation of anhydrous phases drives the melt composition to high H_2O because of the preferential loss of CO_2 to the vapour. In the simple isobaric case the melt tracks along an isobar (shown as dotted lines in fig. 4.6). Polybaric, vapour-saturated crystallisation, for example in a vertical extensive plumbing system, leads to displacement of the melt inclusions across several isobars, as observed. The greater the extent of crystallisation: the greater the displacement to high H_2O. The data in figure 4.6 are consistent with the large amounts of crystallisation recorded by the melt inclusions, as deduced above from the trace element systematics.

We do not have sufficient data to constrain the volatile content of the melt entering this shallow plumbing system. However, it is noteworthy that the CO_2-rich, cpx-hosted melt inclusion does lie at the high-pressure end of a closed system degassing trend that passes through the left hand extremity of the main melt inclusions data field, as shown by the dashed line labelled “ascent” in figure 4.6. Ascent of a volatile-saturated magma of this composition into a vertically-extensive shallow system, followed by extensive crystallisation across a pressure range of ~50-200 MPa (more detailed pressure estimates are presented below) will produce the observed melt inclusion field. Ascent and degassing of these magmas upon eruption will lead to loss of both H_2O and CO_2, yielding the observed matrix glass compositions. The data suggest that, unlike some silicic systems (e.g. Mount St. Helens; (Blundy and Cashman 2005)) decompression is not the main driving force behind crystallisation. This is apparent from the lack of a negative correlation between incompatible trace elements, such as Zr (fig. 4.7), and H_2O. Instead, we propose that crystallisation is driven primarily by cooling.

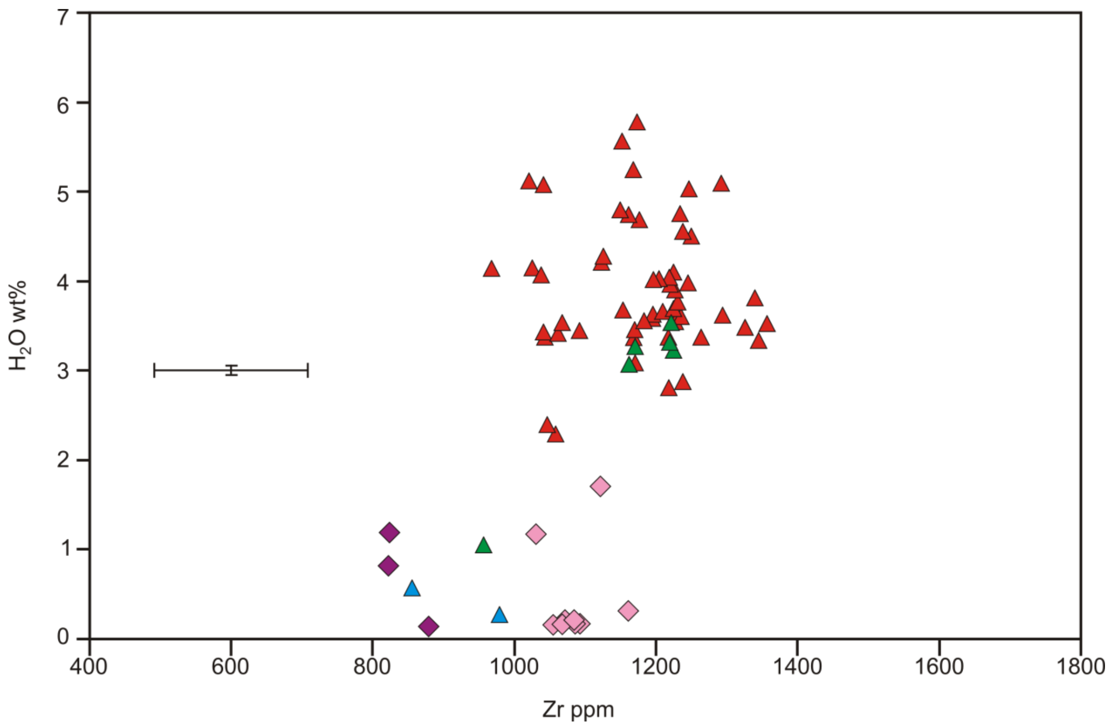

Figure 4.7. *Plot of H_2O vs Zr, for melt inclusion and matrix glass measurements. The lack of correlation strongly suggests decompression crystallisation is not a strong factor in crystallisation at Dabbahu. Key as for fig. 4.4.*

We have also measured Cl and F in a subset of melt inclusion and matrix glasses (tables 4.2 & 4.4). Cl contents are remarkably constant at 0.25 ±0.03 wt%, irrespective of whether glasses are inclusions or matrix. Evidently degassing did not lead to Cl loss from the magma. Constant Cl is not consistent with its behaviour as a truly incompatible element during crystallisation. Buffering of Cl contents will occur if the vapour phase is in equilibrium with a brine, as shown experimentally by (Metrich and Rutherford 1992). In fact, our measured Cl contents are identical to those of (Metrich and Rutherford 1992) for a pantellerite starting material at 100 MPa and 830 °C, conditions close to those estimated for Dabbahu melt inclusions (see below). We have not, however, observed any petrographic evidence for the presence of a coexisting brine phase. F contents, from just six melt inclusions, are similar to Cl.

Magmatic temperatures

Calculating temperatures in peralkaline rocks is notoriously problematic due to the lack of suitable mineral assemblages. Many of the obsidian glasses and pumices are aphyric and therefore temperatures could not be calculated. Where the mineralogy allowed, temperatures were calculated using the alkali feldspar - liquid thermometer of (Putirka 2008). It was not possible to calculate temperatures for cpx- or olivine-hosted inclusions (using the relevant mineral thermometers), due to their very low MgO contents. Entrapment temperatures are within the range 696 to 841 °C (±23 °C calibration uncertainty) for the alkali feldspar-hosted melt inclusion samples (tables 4.2 & 4.4). The maximum temperature range within samples (019 and 055) is 100 °C ±23, (although sample 021 has just a 14 °C range). The majority of the calculated temperatures cluster around 750 ± 50 °C. The large overall variation is likely to reflect temperature variations within the magma storage region, suggesting the temperature was not entirely homogenous, e.g. areas close to the chamber walls may have been cooler. It is also possible that there was some cooling during slow movement of the magma to the surface during eruption, and melt inclusion trapped at this stage would therefore indicate cooler entrapment temperatures. Cooling-induced, polybaric crystallisation is consistent with our interpretation of the melt inclusion data.

Magmatic pressures

In order to reconstruct confidently magma storage pressure, petrological methods require various criteria to be fulfilled. Melt inclusions should be volatile saturated and show no post-entrapment volatile leakage. The magmatic temperature estimate should be reliable and the model used to calculate saturation pressure should account for the peralkaline nature of the melts at Dabbahu.

If the melt was not saturated at the time of melt inclusion entrapment, the pressure calculated provides a minimum only. The pumice and glass matrices have largely degassed prior to quenching (fig. 4.6), and the presence of small volume bubbles in the alkali feldspar hosted melt inclusion suggests some loss of volatile content from the melt into the bubbles during quenching. Blundy and Cashman, (2008) discuss the different evolutionary trends, in terms of dissolved H_2O and CO_2 that a melt can follow for different scenarios, such as isobaric volatile-saturated crystallisation, decompression crystallisation, volatile-undersaturated crystallisation etc. The observed array of CO_2 and H_2O in the melt inclusions (fig. 4.6) closely matches their predictions for vapour-saturated crystallisation over a range of pressure. Vapour-undersaturated crystallisation leads to simultaneous increase in both H_2O and CO_2, which is not observed in our data. Additionally, as shown above, the consistency of Cl contents, across a wide range of H_2O contents, is consistent with the experiments of (Metrich and Rutherford 1992) for pantellerite melts in equilibrium with an aqueous vapour and Cl-rich brine. We conclude that the magmas at Dabbahu were at, or very close to, volatile (+brine) saturation during crystallisation.

Loss of volatiles from a melt inclusion will also lead to pressure underestimates. On the basis of figure 4.6 we have argued that the olivine-hosted melt inclusions, and one cpx-hosted melt inclusion have lost H_2O, probably by diffusion.

The solubility model of (Papale et al. 2006) was used to calculate pressure from the CO_2 and H_2O data. H_2O and CO_2 solubility is known to have a strong compositional dependence in alkali rocks (e.g. Dixon 1997; Tamic et al. 2001), which other models, such as VolatileCalc (Newman and Lowenstern 2002) based primarily on meta-aluminous rhyolite data, do not account for. Papale et al. (2006) applied a regular solution model to a large dataset of experimentally-determined solubilities that contains some peralkaline data. The Papale model requires the input of initial temperature estimates in order to calculate a pressure. Alkali feldspar-melt temperatures calculated from (Putirka 2008) were input to the Papale model, and the pressure output was then re-entered into Putirka's algorithm on an iterative basis until a convergent temperature and pressure value was achieved. These corrections are, however, small, typically < 3 ^{o}C and < 0.5 MPa. The entrapment pressure calculations yield a range of 29 – 249 MPa, at temperatures of 750 – 782 ^{o}C. The single CO_2-rich cpx-hosted melt inclusion gives a pressure of 440 MPa for a nominal temperature of 800 ^{o}C.

<u>Constraints from Experimental Data</u>

Additional constraints on magma storage conditions can be made using experimental studies on magmas with similar major element composition to those from Dabbahu. There have been no experimental studies of Dabbahu sample themselves, although (Di Carlo et al. 2010) have determined the phase relations of a peralkaline pantellerite (sample PAN 01113) from Pantelleria. This sample contains phenocrysts of alkali-feldspar, cpx and aenigmatite and has a bulk composition that is a close match to the Dabbahu peralkaline rhyolites. (Di Carlo et al. 2010) determined phase relations in the presence of a mixed H_2O-CO_2 fluid, over a pressure range of 25 to 150 MPa, 680 - 800 ^{o}C and fO_2 0.3 to 3.9 log units below the NNO buffer. Their results show a strong influence of pressure, temperature and

H_2O content on the equilibrium phase assemblage. It is therefore instructive to compare their experimentally-determined phase relations to the phase assemblages at Dabbahu.

The phenocryst assemblage of 055 is alkali-feldspar + cpx + aenigmatite + apatite. The experiments of (Di Carlo et al. 2010) show that the assemblage alkali-feldspar + cpx + aenigmatite is stable for H_2O-saturated conditions at 680 ^{o}C and 100 MPa (4.1 wt% H_2O in the melt) and for slightly H_2O-undersaturated conditions at 725 ^{o}C and 150 MPa (2.7-3.4 wt% H_2O in the melt). The presence of Ti-magnetite, as opposed to ilmenite, in most of their experiments likely reflects small difference in fO_2, although a single H_2O-undersaturated run at 150 MPa, 750 ^{o}C contains the assemblage alkali-feldspar + cpx + ilmenite + magnetite. Aenigmatite did not form in any experiment above 725 ^{o}C, whereas amphibole (which is almost completely lacking at Dabbahu – just one xenocryst was identified in sample 023) was widespread for water under-saturated conditions at temperatures below 700 ^{o}C. Finally, saturation in quartz (also rare at Dabbahu) occurs when water contents drop below 3.7 wt% H_2O at 680 ^{o}C and below ~1 wt% at higher temperatures. Thus, based on these experiments alone, the field of stability of alkali-feldspar + cpx + aenigmatite ± ilmenite is stable at 100-150 MPa and 680 to 725 ^{o}C for melt H_2O contents between 2.7 and 4.1 wt%. These conditions overlap very well with those that we have deduced from a combination of volatile solubility and alkali-feldspar thermometry, and give us confidence in our petrological methods. Experimental mineral compositions also closely match those at Dabbahu. At 150 MPa and 725 ^{o}C, the experimental alkali feldspar is Ab_{66}, which is identical to that in sample 055 ($Ab_{66\text{-}67}$). The Na content of the experimental cpx is inversely correlated with temperature. The relatively low Na contents of cpx from 055 (~0.2 atoms per formula unit) are indicative of temperatures closer to 800 ^{o}C than 680 ^{o}C.

In summary our calculated pre-eruptive storage conditions for sample 055 are consistent with the experimental data, in terms of pressure, temperature and H_2O content. The 055 magma was stored at or just below H_2O saturation, at temperatures of around 720 - 780 ^{o}C and pressures of over 100 MPa. The experiments offer no higher pressure bound on this assemblage, although our melt inclusion data suggest that pressures can be significantly higher (up to 250 MPa).

Magma Storage Depths

Having established that our pressure estimates are robust, it is necessary to convert pressure into depth. The calculated pressures were used to calculate a depth expressed in km from below the surface. The exact density structure beneath Dabbahu is unknown and therefore it is necessary to assume a crustal density for the region of interest. A crustal density of 2800 kg m^{-3} has been used, based on regional gravity studies in the northern Main Ethiopian rift and in Southern Afar (e.g. Mahatsente et al. 1999; Cornwell et al. 2006; Mickus et al. 2007). Although this may appear high, densities beneath rift volcanoes such as Boset, range from 2770-3000 km in the upper 10 km (Cornwell et al. 2006). The melt inclusion depths are calculated as depth to the surface, i.e. the point of eruption on the volcano edifice, and then corrected relative to sea level. 94% of all melt inclusion show an entrapment depth of between 1 and 5 km (fig. 4.8).

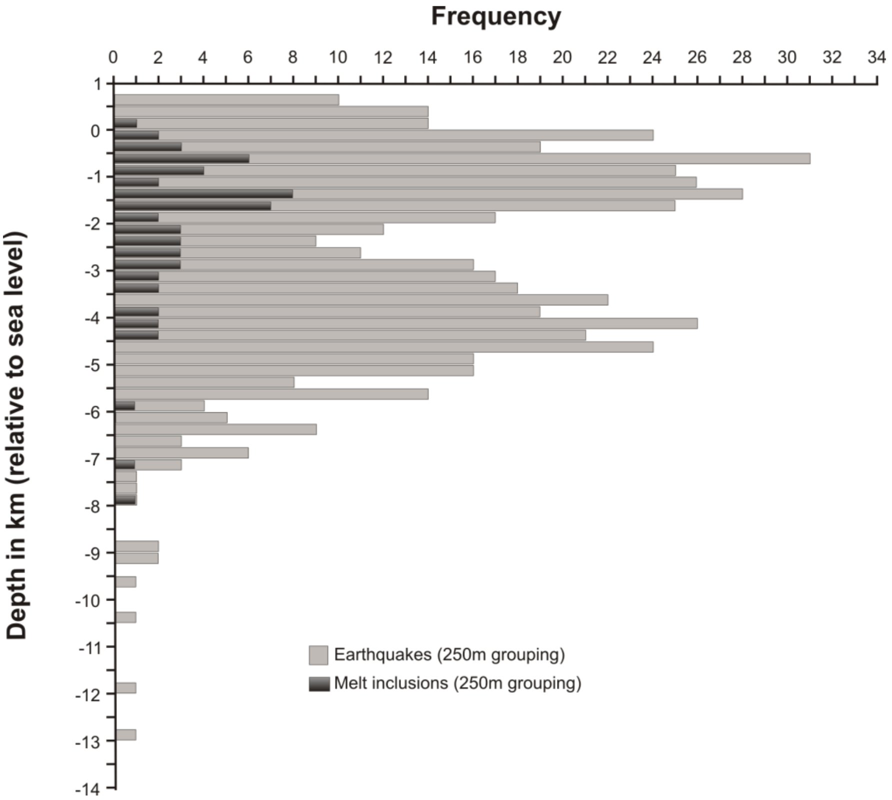

Figure 4.8 *Chart illustrating MI analyses and earthquakes corrected relative to sea level. The plots show a good correlation in that the inferred magma storage region is encompased by earthquakes, despite a time difference of up to 4 ky.*

Just 6% show slightly deeper entrapment depths of up to 7.7 km. The uncertainty on each melt inclusion depth is ~ ±200 m, based on typical accuracy of melt inclusion pressures calculated from H_2O and CO_2 of ±22 MPa (Blundy and Cashman 2008), and an uncertainty of ~10% on the assumed crustal density.

In summary, the melt inclusion data indicate a shallow magma storage area which is vertically extensive over ~4 km (fig. 4.8) with temperatures of ≥700 °C. Crystallisation was driven primarily by cooling under vapour-saturated conditions. The vapour was a mixed H_2O - CO_2 fluid, with H_2O/CO_2 increasing with crystallisation at any given depth. Cl data suggest that a dense brine phase was also present, although not observed petrographically. A single melt inclusion with high CO_2, yields a pressure of 440 MPa, and may represent the melt intruded into the shallow storage region.

Discussion

Having established the conditions under which pantellerite magma was stored prior to the most recent eruptions from Dabbahu it is instructive to compare the storage depths with indirect estimates from seismology and InSAR, to assess whether the current volcanic unrest could involve magmas sourced from a similar system

Comparison to seismic data

Following the September 2005 tectono-magmatic event, a seismic array of six broad-band seismometers was deployed in October 2005 around the Dabbahu and Manda Hararo magmatic segments, including three seismometers around the Da'Ure eruption site (Ebinger et al. 2008). This temporary array recorded a total of 1939 earthquakes throughout the area (163 between 5.5 $>m_b>$3.9), between Oct 2005 and April 2006, 503 of which were associated with the region around Dabbahu (~25 km^2). Focal mechanisms indicate slip along steep normal faults at an orientation of N20°W to N10°E around Dabbahu (Ebinger et al. 2008).

Earthquake locations and S-wave attenuation beneath volcanoes have long been used to suggest the presence of magma (e.g. Einarsson 1978; Feuillet et al. 2004). Earthquakes are typically thought to occur around the margins of magma chambers, which can be triggered by high pore pressures in the aureole. At the Dabbahu edifice it has been interpreted from the persistent and intense swarms of seismicity that pressures remained high, even following the Da'Ure eruption (Ebinger et al. 2008).

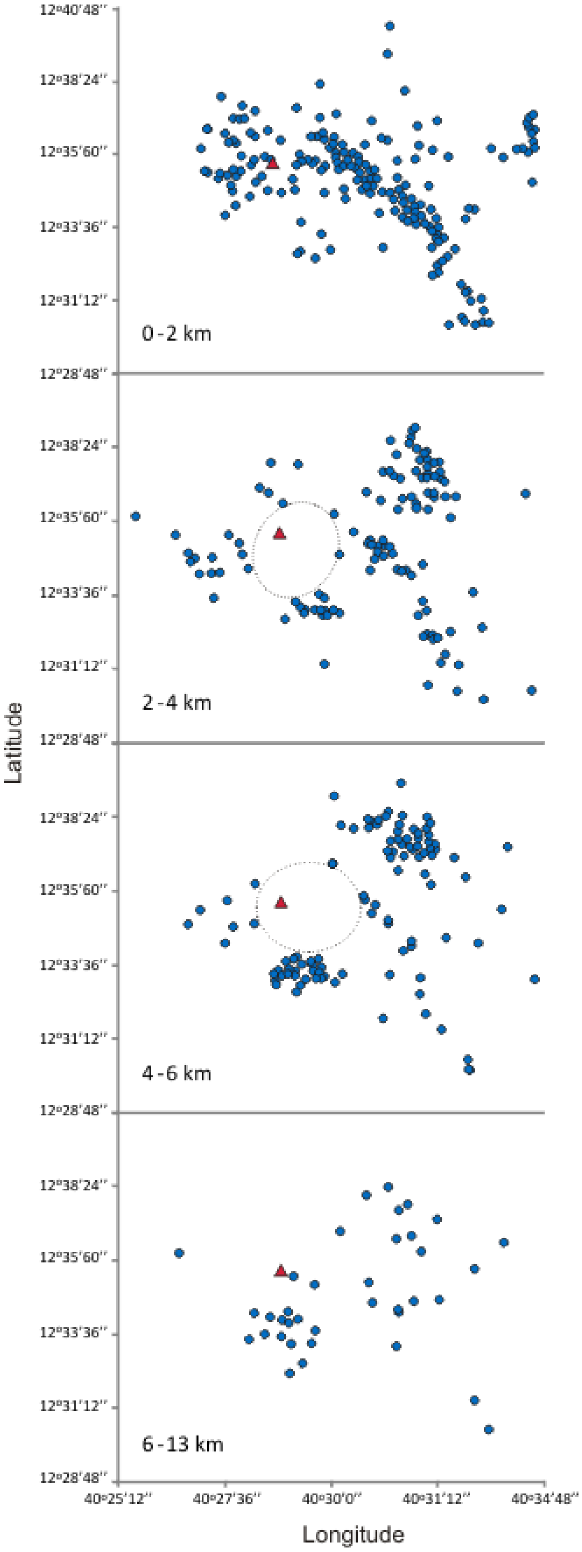

Figure 4.9. *Locations of Dabbahu earthquakes in plan-view for Oct 2005 - Apr 2006 (blue circles): depth relative to sea level. Red triangle (the eruptive vent of sample 055) corresponds to a central earthquake-free area roughly denoted by dotted line ellipse (2-4 km and 4-6 km). Scale and key are the same for all plots.*

The Dabbahu earthquakes were calculated to depth below surface, the surface being defined as a mean datum taken from the elevation of the highest station (745 m a.s.l). The uncertainty on each earthquake depth is ~±500 m and location uncertainty is ~±50 m. In order to compare the melt inclusion depths to the earthquake depths, a correction to sea-level was made to both data sets. Thus the earthquake data (recalculated to the same planar surface) show a good correlation (fig. 4.8) despite the time gap (up to ~ 8 ky), between the eruption of the obsidian samples, and the 2005 - 6 earthquake data. The melt inclusions are contained within the depth span of the earthquakes which should preferentially lie at the margins of the 3-dimensional magma storage region. The recorded earthquakes at Dabbahu are interpreted as deformation following the 2005 dyke injection event (Ebinger et al. 2008). When the data are viewed in plan-view for a specified depth range (fig. 4.9), a central earthquake-free void is clearly indicated at depths between 2 and 6 km. This is interpreted as an area of magma storage; Ebinger et al. (2008) suggested the hypocentral locations from the earthquakes as representing sill-like melt zones at 3 - 5 km depth. Sample 055, for which the eruption source point on Dabbahu is easily located from satellite imagery, plots directly above this area. Abundant earthquakes characterise the region above 2 km suggestive of a fractured roof above the magma chamber. Below 6 km, the earthquakes are less frequent and it is not possible to clearly define the presence of magma storage below this depth. The correlation between the seismic data and the melt inclusion data, suggests that there may have been little change in the magma storage beneath Dabbahu over the last few thousand years. This long-term stability may have contributed to the evolved nature of the most recent eruptive products.

Comparison to InSAR

InSAR observations at Dabbahu following the major dyke intrusion in 2005, would suggest that there is at least one major body of magma storage below Dabbahu controlling the measurable inflation and deflation. The Da'Ure eruption of 2005 is believed to have been triggered as a result of a basaltic dyke intrusion reheating a small amount of rhyolite magma (Ayele et al. 2009). There is no petrological evidence for magma mixing in the Da'Ure eruptive products, although this does not in itself exclude dyke intrusion as a trigger mechanism for previous Dabbahu eruptions.

Modelling of INSAR data is non-unique, as it requires constraints on the shape of the magma body and the rheology of the surrounding rocks. The commonly used Mogi model (e.g. Ayele et al. 2009) assumes a point source, which is inconsistent with any realistic magma chamber geometry. Instead, the depth distribution of the melt inclusions can be used to constrain magma chamber inflation models. The melt inclusion data suggest a vertically extensive magma chamber was tapped during eruptions of the last 4 kyr at Dabbahu and it is instructive to see whether such a configuration can be matched to recent InSAR observations, given the seismic evidence that the current eruptive phase has tapped a body located over a similar depth range.

Data processing

Regular SAR acquisitions from the European Space Agency's Envisat satellite have enabled a large time-series of InSAR data to be built for the Dabbahu area (Grandin et al. 2010; Hamling et al. 2010). In this case, the point of interest is the location and shape of the magmatic source beneath Dabbahu, rather than its temporal behaviour, so interferograms with long time intervals were analysed to maximise the signal to noise ratio. Interferograms on ascending and descending tracks were used, giving two independent observations with different viewing geometries (fig. 4.10). The ascending interferogram is formed from acquisitions on 3rd April 2006 and 1st February 2010; the descending interferogram spans the interval 21st April 2006 to 26th March 2010. It is assumed that they observe the same deformation. Deformation prior to March 2006 is not included since a strong, decaying subsidence signal was observed during this time period, probably associated with faulting under the south flank of Dabbahu (Ebinger et al. 2008). Each interferogram records the motion towards the satellite – vertical motion results in a decrease in distance (range) between the satellite and ground for both viewing geometries, but east-west motion results in a range decrease for the descending interferogram and a range increase for the ascending interferogram. Interferograms were processed using the JPL/Caltech ROI_PAC software (Rosen et al. 2004), a power spectrum filter was applied (Goldstein and Werner 1998) and phase was unwrapped using the branch cut algorithm (Goldstein et al. 1988). Surface deformation in the vicinity of Dabbahu volcano responds to a variety of processes, including ongoing dyke intrusions in the rift to the south (Hamling et al. 2009; Hamling et al. 2010), visco-elastic relaxation (Nooner et al. 2009), and magmatic deformation at the Ado' Ale Volcanic complex, Gabho volcano, and Dabbahu itself (Grandin et al. 2010). The concern here is with relatively shallow processes occurring beneath Dabbahu. Therefore we attempted to isolate the resultant deformation without the requirement for a detailed and accurate model of the other processes which are poorly known.

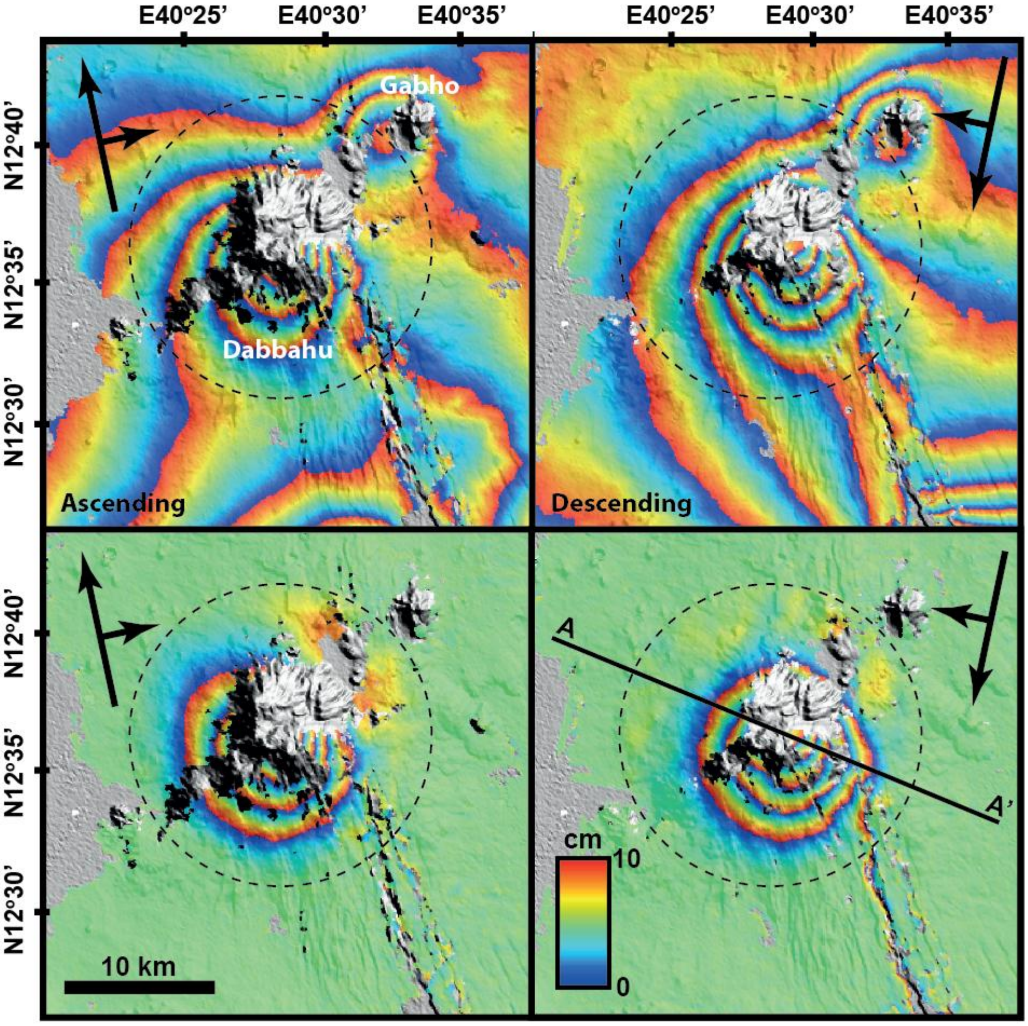

Figure 4.10. *The isolated InSAR signal for Dabbahu. Localised deformation around Dabbahu determined by subtracting the interpolated interferograms from the originals. A-A' is the section used for profile modelling in fig. 4.11.*

To achieve this, we assumed that none of the other processes were capable of producing localised deformation in the vicinity of Dabbahu itself. Interferograms were created in which deformation inside a circle of 10 km radius centred on Dabbahu were masked out, and then interpolated across this gap using continuous curvature splines in tension (Smith and Wessel 1990). Subtracting the interpolated interferograms from the originals leaves the localised deformation around Dabbahu (fig. 4.11). The 10 km radius was the largest possible without including significant deformation associated with nearby Gabho volcano (fig. 4.11). It restricts our sensitivity to deformation sources shallower than ~5 km – deformation from deeper sources will be on longer wavelengths and be removed. The isolated shallow Dabbahu deformation interferograms show concentric range decreases approximately centred on Dabbahu. The maximum observed range decrease is 40 and 50 cm in the ascending and descending interferograms respectively. The concentric range decrease in the ascending interferogram is skewed to the west of that in the descending interferogram. This is consistent with an inflating source, and suggests that the deformation consists of an uplift signal (causing range decrease in both ascending and descending interferograms), and horizontal deformation pointing radially outwards: to the east of Dabbahu, horizontal and vertical motion both result in range decreases for the descending pass, whereas in this location the horizontal motion acts in the opposite direction to the vertical in the case of the ascending pass; the opposite is true west of Dabbahu.

Source Modelling

Prior to modelling, interferograms containing the isolated Dabbahu and Gabho signals were subsampled onto regular 1 km grids, and a variety of simple elastic deformation sources experimented with. As has been shown by previous authors, the differences in deformation resulting from different source geometries can be subtle (e.g. Pritchard and Simons 2004), and therefore it is not attempted to uniquely determine the appropriate geometry. Instead the data were analysed to narrow down the range of possible magma plumbing systems that are compatible with the petrological and seismological analyses. As a baseline, two models were initially tested in which the magma source was at a single depth – (A) a point pressure source (Mogi 1958) and (B) a simple sill (Okada 1985). However, petrological data suggest that the magma from historical eruptions was stored over an extended depth range. Two such models were tested: (C) a vertical ellipsoidal source (Yang et al. 1988), with a variety of aspect ratios, extending from a depth of 1.5 - 4.5 km, and (D) a stacked sills model, in this case consisting of three sills at depths of 1.5, 3.0 and 4.5 km. In all cases the simple analytical solutions that assume an isotropic elastic half-space were used, and Poisson's ratio was fixed at 0.25.

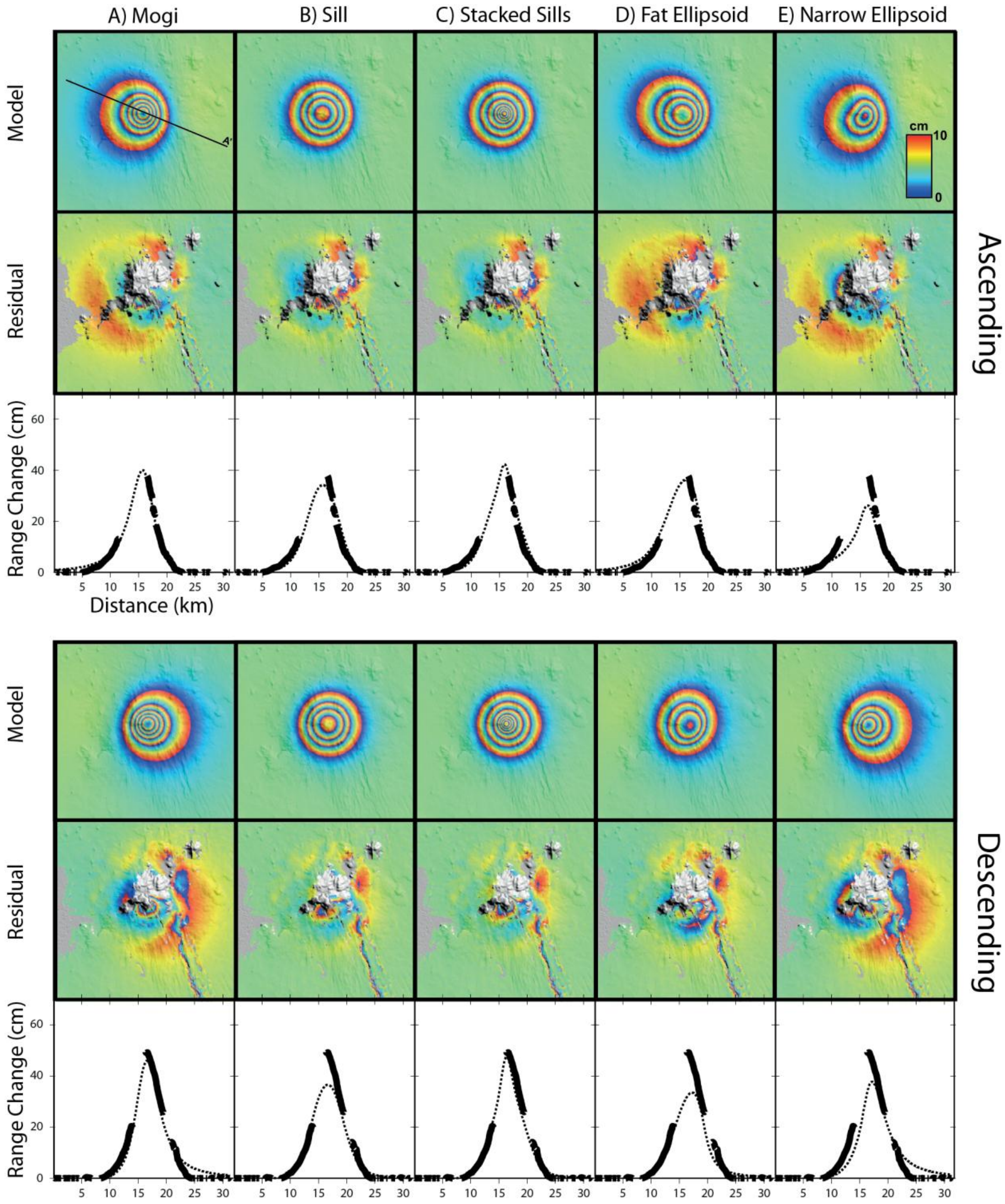

Figure 4.11. *Ascending and descending models and residuals for the Dabbahu InSAR signal. Range-change profiles are modelled from A-A' as shown on the ascending mogi model.*

(1) Point pressure source

The simplest model possible for an inflating magma body is a point pressure source (Mogi 1958; figure 4.11a). The surface deformation is dependent on four free parameters: the location of the source (x,y,z) and the pressure change, which is expressed here as a volume change following (Delaney and McTigue 1994). These four free parameters were solved using a hybrid Monte-Carlo, downhill simple non-linear inversion scheme (Wright et al. 1999). Uncertainties in model parameters were found by inverting 100 data sets perturbed with the addition of correlated noise: the distribution of solutions gives their uncertainties and also samples the trade-offs between model parameters (Wright et al. 2003; Parsons et al. 2006). Correlated noise with a standard deviation of 2 cm and a correlation length scale of 10 km was used. The magnitude of the noise is larger than that observed in the far field of the interferograms but this value was chosen to incorporate some additional uncertainty associated with the process of isolating the Dabbahu deformation signal.

The best-fit depth and volume change are 3.0 ± 0.1 km and 0.022 ± 0.002 km^3 respectively, although the usual trade-off between these two parameters is seen: solutions with larger depths have larger volume changes. However, this volume is within the range of pervious obsidian eruptions at Dabbahu (~0.13 km^3 – 0.006 km^3). The root mean square (rms) misfit between the data and model parameters is 1.67 cm. In general, the model interferograms explain the majority of the observed deformation signal (fig. 4.11), but the models over-predict the deformation at large distances from the source.

(2) Simple Sill

The simple sill model consisted of two superimposed horizontal square sills with uniform opening at the same source depth (figure 4.11b). One sill was oriented east-west, with sides N-S, E-W,and the other rotated by 45° to NW-SE, NE-SW, to simulate a more realistic, penny-shaped crack geometry. Keeping the horizontal location of the sill fixed at the best-fit Mogi location, the same inversion scheme was used to solve for three parameters, the source depth, the length of the edge of the sill, and the amount of opening.

The best fit source has an edge length of 5.6 ± 0.6 km at a depth of 3.5 ± 0.4 km. It opened by 0.7 ± 0.3 m (total from both sills) giving a volume change of 0.023 ± 0.002 km^3. The modelled deformation pattern fits the observed interferograms significantly better than the

Mogi source, with an rms misfit of 1.11 cm. This is mainly because the deformation is more localised, fitting the far field of the deformation source better than the Mogi model (fig. 4.11).

(3) Ellipsoidal source

The petrological evidence suggests that the magma may be distributed over a wide depth range. The petrology by itself does not constrain the shape of that magmatic source. We are interested to assess whether the depth extent found in rocks from previous eruptions at Dabbahu is valid for the present-day shallow magmatic system. Whether the magma could be contained over this depth range in a single magma chamber was first tested by calculating the predicted surface deformation for a vertical ellipsoidal source, centred at the horizontal location of the Mogi source but extending from a depth of 1.5 to 4.5 km beneath the surface (figure 4.11d). The ratio between the vertical axis and horizontal axis was varied, and solved for the best-fitting pressure change for each source-geometry using the formulations of (Yang et al. 1988).

For a narrow, “cigar-shaped” ellipse, with a horizontal axis of half-length 0.1 km, a good fit to the observed data cannot be found (fig. 4.12) – the rms misfit is 2 cm. Furthermore, the best-fit pressure change is unfeasibly large (370 ± 20 MPa, assuming a shear modulus of 1010 Pa). The fit to the data is improved as the length of the horizontal axis increases. A spherical chamber fits the data identically to the point Mogi source, with a more realistic pressure change of 20 ± 1 MPa. The best-fit ellipsoid has a horizontal axis (half length 3.9 km) more than twice the length of the vertical axis with a pressure change of 2 ± 0.1 MPa. The rms misfit for this solution was 1.5 cm: better than the Mogi source, but worse than the simple sill model. The presence of seismicity within this source geometry suggests that a magma chamber of this size and shape is not realistic, and it was therefore ruled out.

(4) Stacked sills

An alternative plumbing system that will allow magma to be distributed over a large vertical extent is a system of stacked sills, connected by a network of narrow conduits or dykes (figure 4.11c). Such a plumbing system has been proposed as a plausible geometry for magma storage and differentiation within the crust (e.g. Zellmer and Annen 2008). To test whether stacked sills can fit the observed deformation pattern, we construct a simple system with three sills superimposed vertically on top of each other, at depths of 1.5, 3.0 and 4.5 km, each constructed using a pair of horizontal, square, tensile dislocations as used for the single sill model (B). For each sill, we solve for the length of the edge of the dislocation, and the amount of opening.

The majority of the volume-change 0.018 ± 0.008 km^3 is found to occur in the sill at 3 km depth, which has an edge length of 7.1 ± 3.5 km and opens by 0.36 ± 0.18 m. The other sills both contributed ~0.0025 ± 0.001 km^3 and have relatively narrow dimensions (1.6 ± 0.6 km length, and 1.6 ± 1.6 m opening for the shallow source at 1.5 km; 1.3 ± 1.3 km length and 1.6 ± 2.7 m opening for the deep source at 4.5 km). Note that the model parameters are strongly co-varying; both for parameters associated with individual sills, and between the different sills. For example, solutions with high volume change in the 3 km sill have low volume change in the 4.5 km sill. The rms misfit to the data of 1.08 cm is marginally better than that of a single sill. Most of this improvement comes from the fact that the shallow source allows the deformation to fit the peak of the deformation pattern significantly better than the single sill model (fig. 4.11).

Although this is the best-fit solution, it would probably not have been selected above the simpler, single-sill model based on the deformation data alone. Given the additional constraint from petrology that the magma has historically been distributed between depths of ~1.5 and 4.5 km, distributing the magma through a series of stacked sills is consistent with the deformation data.

Conclusions

The bulk of the melt inclusions are H_2O rich, up to 5.8 wt %. High H_2O content in melt inclusion is consistent with other findings in peralkaline rocks e.g. Mayor Island, NZ, 2.6 - 5.0 wt% (Barclay et al. 1996). The pumice and glass matrices have largely degassed prior to quenching. The high level of H_2O observed from melt inclusion analysis, together with very low levels of H_2O in pumice and obsidian matrix glasses is consistent with other studies from peralkaline volcanoes. However, H_2O degassing does not appear to govern crystallisation at Dabbahu as is the case at other volcanoes, for example, at Mt St Helens (Blundy et al. 2010). Major elements are buffered within the system suggestive of near-eutectic behaviour and therefore are not reflecting crystallisation processes. Trace element signatures in this system are far more responsive to crystallisation.

Indicated magma storage depths are shallow, which is in line with observations at other peralkaline volcanoes e.g. Pantelleria (Gioncada and Landi 2010), but show a range of depths from <1 to 4 km. This depth range is consistent with seismic data obtained during the current tectonic-magmatic unrest. Using the petrological estimates of magma storage depths we have attempted to fit the InSAR data. We find that a system of thin, stacked sills provides a good match to the deformation data. We conclude that the magma storage system beneath Dabbahu appears to have remained stable over the past few thousand years. Taking a uniformitarian approach by utilising the three disciplines, has enabled us to constrain both the depths of magma storage, but also the geometry. The current magmatic activity at Dabbahu is consistent with storage of magma at similar depths to that involved in historical eruptions, it may currently be being refilled by new batches of magma, or reactivated by injections of basaltic magma, as inferred for the recent (2005) eruption from the Da’ Ure vent to the east of Dabbahu.

The November 2010 eruption of Erta Ale:

ground, satellite and petrological observations

Chapter

5

Author Contribution

This chapter forms the basis for a paper to be submitted to Earth and Planetary Science Letters:

Field, L., Barnie, T., Blundy, J., Brooker, R.A., Keir, D., Lewi, E., and Saunders, K., 2011 "The November 2010 eruption of Erta Ale: ground, satellite and petrological observations." Bulletin of Volcanology. *In review*.

Enlightening discussion with J. Blundy provided direction and greatly improved the manuscript. L. Field was the lead author and contributed all work with the exception of the following: SEVERI data and related SEVERI methodology and initial interpretation were contributed by T. Barnie, phosphorous zoning was modelled by K. Saunders, FTIR was carried out by R.A. Brooker. D. Keir was the field leader, and provided helpful comments on the manuscript. D. Lewi provided information on Ethiopian earthquakes, and assisted in all permissioning required to enter the field. All authors provided helpful reviews and discussion.

Abstract

Erta Ale volcano, Ethiopia, erupted in November 2010, the first such eruption from the southern pit within the main crater since 1973, and the first eruption at this remote volcano in the modern satellite age. Here we combine on the ground observations with multispectral imaging from the SEVIRI satellite to piece together the entire eruptive episode which began on the 11th November, and ending prior to the 14th December. A period of quiescence occurred between the 14 – 20th November. The main eruptive activity developed between the 19th and 22nd November, finally subsiding back to pre-eruptive levels between the 8th and 15th December. The estimated total volume of lava erupted is ~0.6 km^3. Geochemical analysis of three samples reveals that the 2010 lavas are slightly more mafic than previously erupted lava lining the caldera floor, with SiO_2 contents of 49 and 51 wt% and Mg # of 39 and 35 respectively, and a mineralogy of plagioclase + clinopyroxene + olivine. SIMS analysis of olivine hosted melt inclusions show the Erta Ale lavas to be relatively dry, with H_2O contents ≤1300 ppm and CO_2 contents of ≤190 ppm. Volatile saturation pressures are in the range 7 - 40 MPa. Inferred entrapment depths are <1.5 km, indicating shallow crystallisation. Using incompatible trace element analyses of melt inclusions we show that the November 2010 Erta Ale lavas were volatile-saturated, and that crystallisation occurred as a result of repeated decompression and crystallisation. Volatile saturation pressures are in the range 7 - 40 MPa. Inferred entrapment depths are <1.5 km, indicating shallow crystallisation. Calculated pre-eruption and melt inclusion entrapment crystallisation temperatures from mineral / liquid thermometers are ~1170 ^{o}C, consistent with previously published field measurements.

Introduction

The Afar depression lies at the triple junction between the Red Sea, Gulf of Aden and East African rifts, and has been produced by rifting between Africa and Arabia over the past ~30 Myr (Wolfenden et al. 2005). The southern Red Sea rift has become punctuated over the past ~3 Ma with ~60 km long magmatic segments as faulting and volcanic activity have become more focused into localised regions (Barberi and Varet 1977). Erta Ale is a basaltic shield volcano (13^{o}36’11.41”N, 40^{o}39’50.08”E) situated within the Erta Ale magmatic segment (fig. 5.1), comprising six main volcanic centres (Barberi and Varet, 1971). The last eruption in this segment occurred in November 2008 when basaltic lava covered 15 km^2, originating from a fissure between Dalaffilla and Alu volcanoes (Varet et al., 2008). This magmatic segment is the northernmost in Afar and forms the sub-aerial southwards continuation of the Red Sea Rift (Prodehl et al., 1997).

Erta Ale is known for its active lava lakes situated in northern and southern pits within a 0.7 x 1.6 km elliptical summit caldera (fig. 5.1). The Erta Ale lava lake is one of just a handful of long-lived lava lakes existing across the world; others include Erebus (Antarctica) and Nyiragonga (DR Congo). The first systematic study of the lake began in 1967 (Barberi and Varet, 1970), but the lake is likely to have existed from much earlier than this, as reports of a 'smoking mountain' and characteristic red summit glow have been recorded by early visitors to the area (e.g. Barberi and Varet, 1970; Dainelli and Marinelli, 1907; Nesbitt, 1935). The Erta Ale volcano is remote and difficult to access, and the resulting observations have been sporadic: it was not until the CNR-CNRS campaigns of the late 1960s that it began to be studied in detail (e.g. Barberi and Varet, 1970; Tazieff, 1973). At this time a lava lake existed in both the northern and southern pits, however the northern lake solidified between 1988 and 1992 following the emplacement of two lava flows during this period (Vetsch et al., 1992). The southern lake solidified briefly between late 2004 until April 2005 (Bardintzeff, 2004; Yirgu, 2005). The lake was again extremely active in September 2005, possibly in response to the volcano-seismic crisis in Afar (Ayele et al., 2007). The level of the southern lake has fluctuated (Guern et al., 1979), but the majority of recent observations indicate the lake level was generally tens of meters below the floor of the main crater, nestled at the base of the southern pit (e.g. Oppenheimer and Francis, 1997). Overflows and eruptions occur from these lakes from time to time although these are rarely observed. Varet reported the first eruption from the southern pit in March 1972, following the emplacement of two new flows which appeared on the southern side of the south pit, one sometime prior to the 21st and one during the 23rd March (Varet, 1972a). This activity continued with three additional new flows, visible when the volcano was visited in May 1972 (Varet, 1972b). Tazieff (1973) reported overflows which overran the crater rim in March 1973. From this occurrence until November 2010, no further eruptive activity associated with the southern pit has been reported.

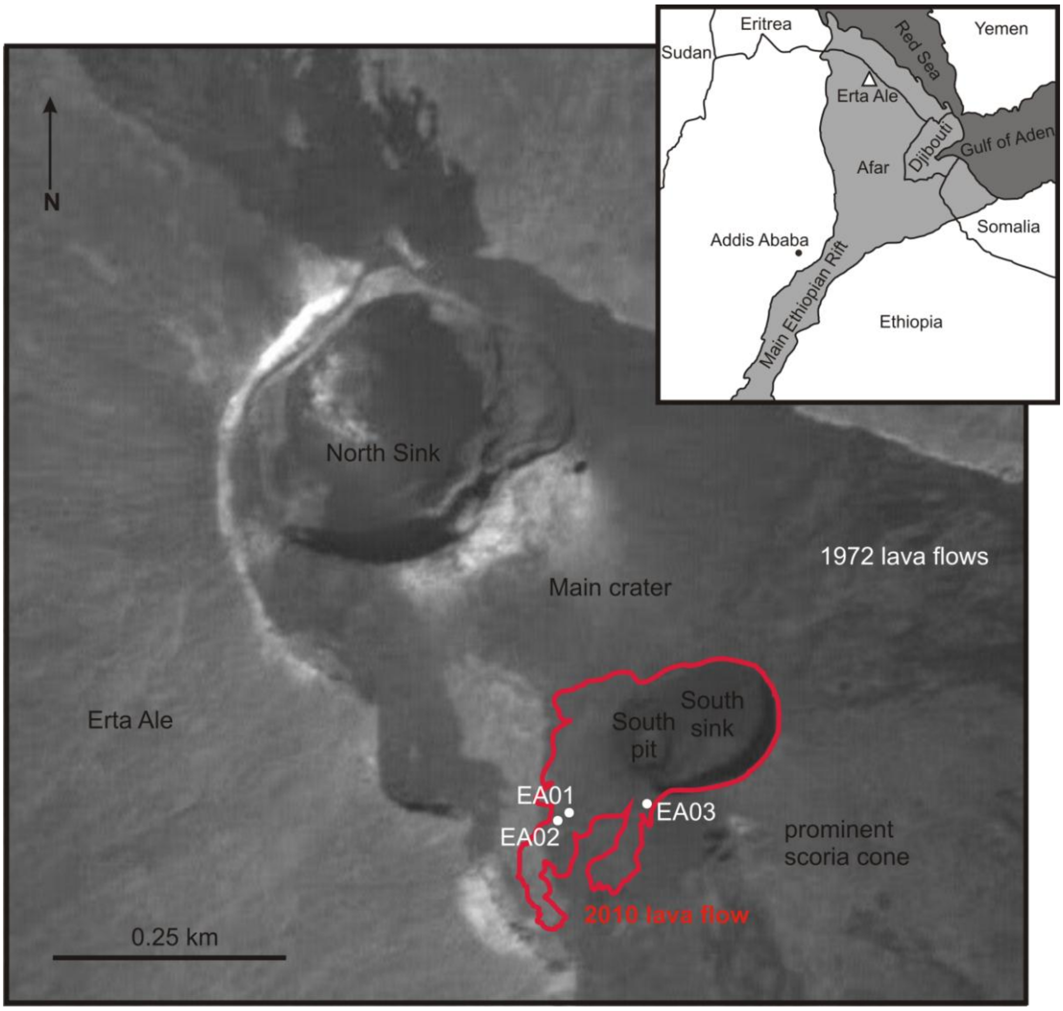

Figure 5.1. *Satellite image of the Erta Ale crater, with the extent of the Nov-Dec 2010 eruption lavas is shown in red (GPS track courtesy of James Hammond (Feb 2011)). Sample locations from the 22nd Nov are shown, which were subsequently covered by further overflows. Insert, sketch map of the region indicating the location of Erta Ale. Image taken by PRISM instrument on ALOS satellite, image resolution 2.5 m, image aquired 19th Nov 2008. Data acquired from ESA.*

Ground observations

Ground observations began on the 21st November 2010 at ~16.00 UTC (Co-ordinated Universal Time). The team were unaware on approaching the volcano of any eruptive activity and no visible signs e.g. plume, could be seen on the 8 km hike up to the crater. However on arrival at the crater, it could be seen that an eruption was underway. Observations from the previous few years have located the lava lake at the base of the pit, ~20 m depth (fig.2c). However, the pit had filled with lava, level with the main crater floor on the western side (fig. 5.2). The first overspill of lava onto the main crater floor occurred at ~16.50 UTC (fig. 5.3a). An embryonic scoria ring cone had built up around the lake (fig.2e), similar to that observed in 1973 (Tazieff).

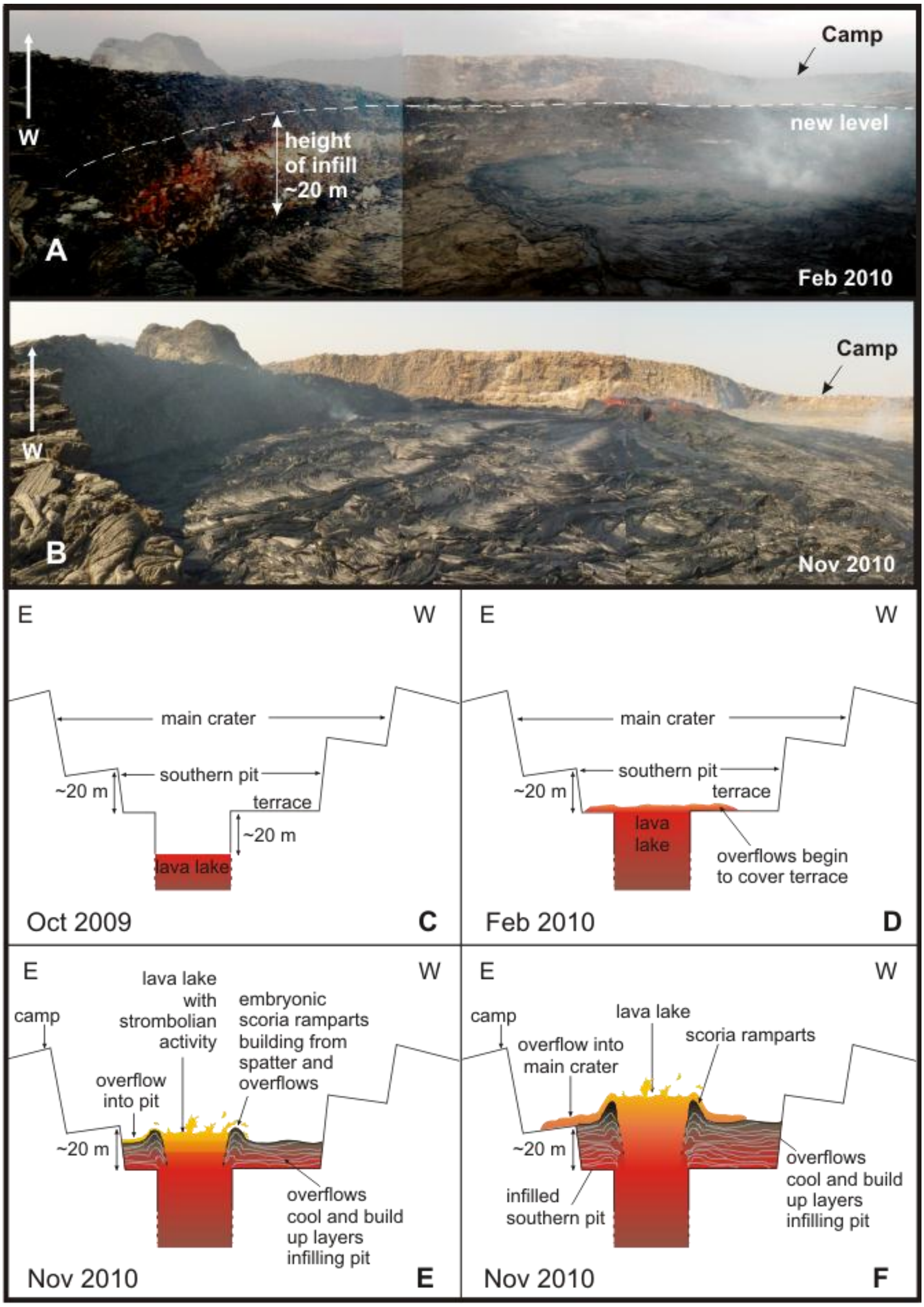

Figure 5.2. *Comparison of the levels in the south sink between a) Feb 2010 and b) 22nd Nov 2010. The lava has filled a depth of ~20 m. The Feb 2010 level is similar to that observed on the 11th and 14th November (J. Wilkinson pers. comm.), c-f) cartoon cross sections of the Erta Ale lava lake from observations from members of the field team, c) Oct 2009, d) Feb 2010 and e and f) stages in the eruption of Nov 2010 indicating the formation of the scoria ramparts and infilling of the southern pit and sink.*

Overspills out of the scoria cone into the pit, and occasionally on to the main crater floor, continued at approximately 2 hr intervals until ~14.30 UTC on the 22nd November. Video footage indicates the lava was of low viscosity (supplemental video 1). For the remainder of the ground observation, the lake was contained within the scoria ring cone, which by 3.00 UTC on the 23rd November had grown to ~4 m high on the southern side. The lava lake level rose and fell by ~4 m on a ~20 minute cycle, with agitated Strombolian activity at the peak of each cycle. On the morning of the 23rd November the northern side of the scoria ring cone suffered partial collapse. Incandescent gas jets could be seen periodically with a blue-green colouration, some burning for several hours. New lava flows were visible within the northern pit, together with some incandescence during the night of the 21st November. Having departed from the summit on the 23rd November, a small but distinct plume was visible above the volcano from the surrounding plain.

Satellite Imaging

Method

The SEVIRI instrument is a multispectral imager aboard the second generation of Meteosat geostationary weather satellites. The Meteosat 9 satellite is positioned over 0°E 0°N and the onboard SEVIRI instrument images the full Earth disc visible from this position every 15 minutes in 12 bands. Four of these bands are useful for monitoring thermal radiation from volcanic products, at wavelengths of 1.6 µm, 3.9 µm, 10.8 µm and 12.0 µm (e.g. Hirn et al., 2009). The resolution of the image at the sub-satellite point is 3 km, but this increases towards the edge of the image due to the constant angular sampling of the instrument and the curvature of the Earth, so that at Erta Ale, the resolution is approximately 4 km in the E-W direction and 5 km in the N-S direction (Müller, 2010). Due to the stable viewing geometry of the instrument, each pixel images the same area of the Earth's surface at the same view angle in successive images, so a sequence of radiance measurements from a given pixel are directly comparable. This is in contrast with instruments on low Earth orbit satellites such as AVHRR and MODIS, where for a given volcanic feature, the observing pixel location, size and view geometry vary substantially with each acquisition, making inter image comparisons difficult.

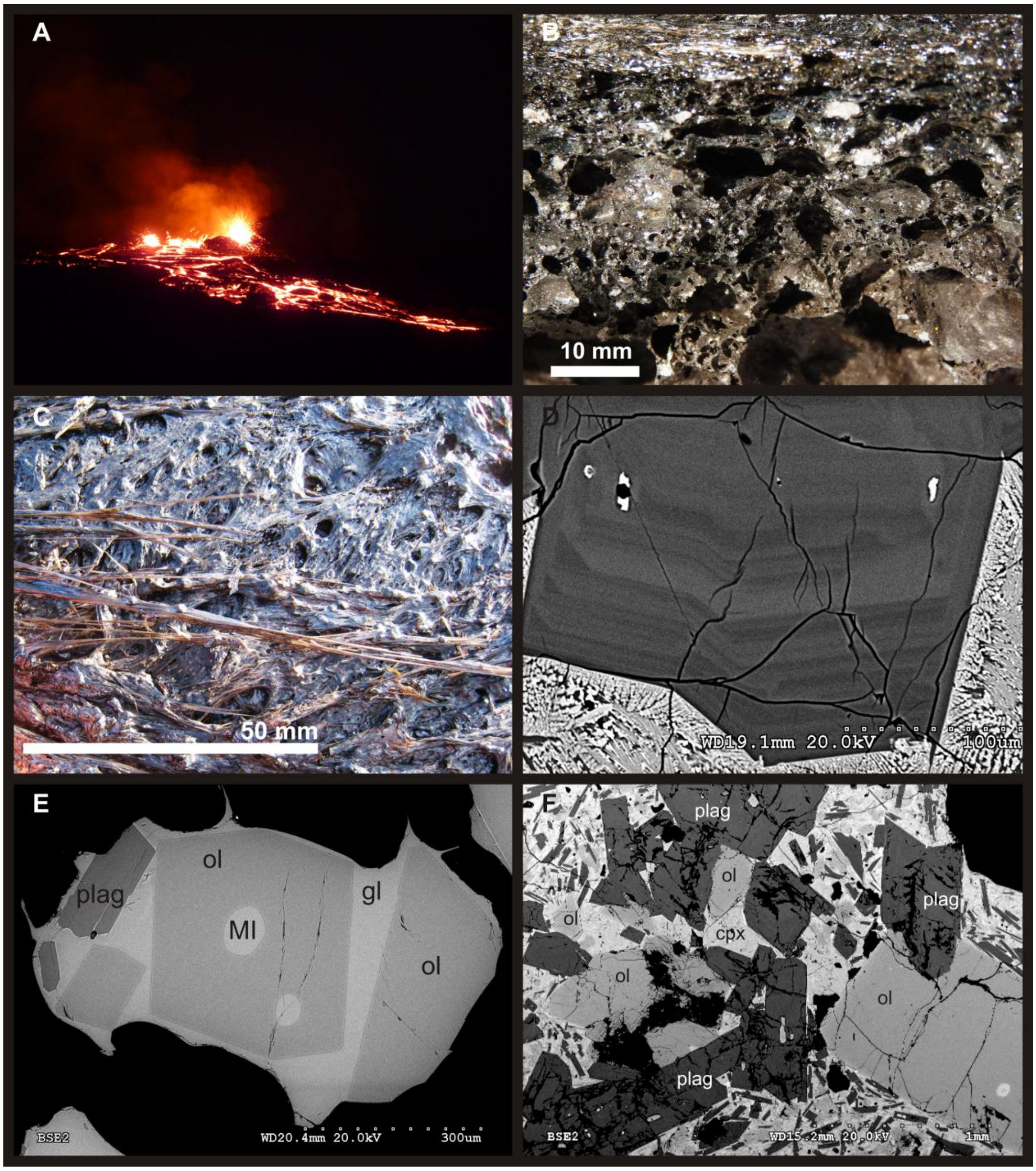

Figure 5.3. *a) emplacement of first observed overspill (sample EA001) ~ 16.50 UTC 21st Nov 2010, b) close up of a section through the fresh lava showing the glassy surface, plagioclase-rich layer and vesicular core, c) close up of the surface of the new lava, d) BSE image of oscillatory-zoned plagioclase rim from sample EA001 with quenched glass matrix, e) euhedral olivine and MI from sample EA003, f) sample EA002, the underlying lava flow, which has a fine-grained groundmass.*

We acquired 9,802 Meteosat 9 SEVIRI images of the Erta Ale region between 1st October 2010 and 10th January 2011. The images were converted to radiance, and the time series of radiance values for the pixel covering the Erta Ale lava lake was extracted, giving a 15 minute time resolution record of the radiant output of the eruption. Thermal anomalies were only observed in the 3.9 µm band, consistent with the presence of a very small

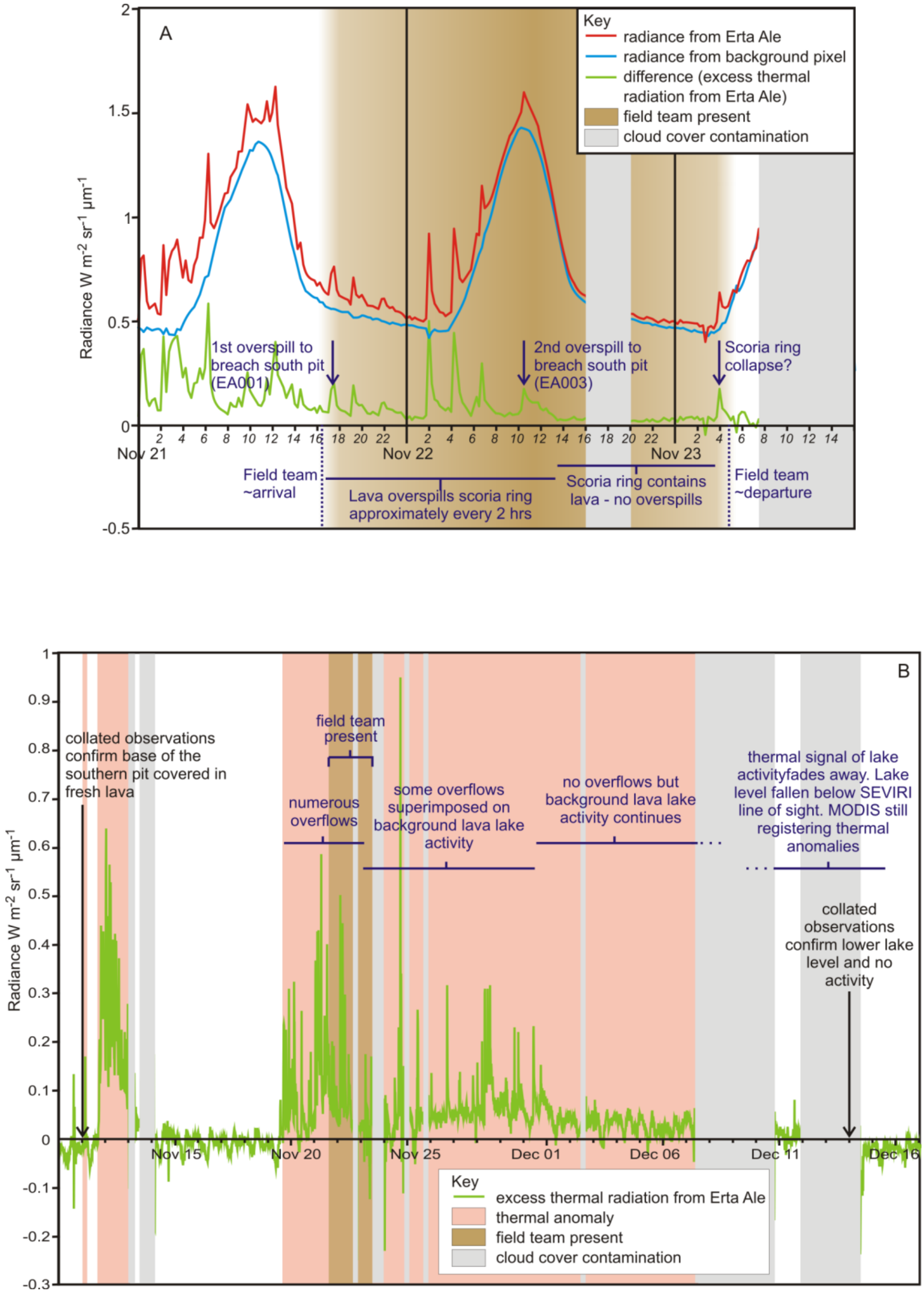

Figure 5.4. *Severi thermal signal of Erta Ale with contemporaneous ground observations. A) detail from when field team were present at Erta Ale showing the radiance from lava and background, and the difference i.e. the excess thermal radiation. Times in UTC. B) overall image of the eruption showing the excess thermal radiation graph only.*

surface area at volcanic temperatures. Larger areas would register at the 10.8 and 12.0 µm bands, saturate the 3.9 µm band and if there was enough incandescent material (e.g. cracks, fire fountains, shear zones), also register at the 1.6 µm band (Davies and Keszthelyi, 2010). We subtracted the radiance from a neighbouring cold pixel to obtain the excess radiance emitted by the hot volcanic material, over and above that radiated and reflected by a region with similar reflective and emissive properties at background temperatures. This gives us a time series of the thermal anomaly associated with the eruption, which we interpret qualitatively. The lava lake and background pixel do have subtle differences in radiance patterns in the absence of hot material in the lava lake pixel, and as a result there is a regular small dip in the thermal anomaly at dawn, however this effect is small and does not invalidate our observations, which are first order and qualitative in nature.

Interpretation

The Erta Ale lava lake does not typically register in any SEVIRI band, despite being frequently observed by MODIS (e.g. Ayele et al., 2007; Wright and Pilger, 2008). The radiance from the lava lake detected by SEVIRI is a function of the area of the lake visible by the sensor and the temperature distribution at the surface of the lake. The area of the lake that is visible by the sensor is a function of the depth of the lake below the rim, since the oblique, low-view angle of the sensor (~42 ^{o}E) ordinarily results in part of the lake being obscured. As the lake level rises towards the main caldera floor, an increasing fraction of the total area of the lake becomes visible to the satellite. The thermal anomaly varies over two time periods; the first is on a timescale of hours that is characterised by sharp increases in radiance over a period of < 15 minutes, followed by an exponential decay over a period of around an hour. From field observations we know the period over which the lake level rose from the former position of ~20 m below the rim to the surface, and this corresponds with a period of steadily increasing background radiance. The final area of the lake at high stand is also similar to the initial area (~500 m^2), so we infer that changes in lake area were secondary to lake height in terms of controlling the thermal radiance received at the sensor. Spikes in radiance have been correlated with overflows observed in the field, so we interpret the spikes as overflows either initially onto the 'terrace' abutting the lake within the pit as the lake level rises, or overflows over the scoria ramparts around the high stand lake onto the new infilled surface of the pit and onto the main caldera floor.

The rapid rise in radiance over 15 to 30 minutes associated with each spike is likely the advance of the overflow; the subsequent exponential decay in radiance over a period of a few hours is the cooling of the surface. Each overflow can be considered a temporary increase in the area of the 'lake'. Between spikes, the background radiance from the lake varies little as the lake level remains relatively constant which we interpret to mean the surface temperature distribution varies little.

The second thermal anomaly variance is on a timescale of days. A thermal anomaly is present during two periods (fig. 5.4). The first starts with an isolated spike in radiance at 02:12 UTC 11th November which decays to the background level after about an hour. The anomaly reappears slightly later at 15:57 UTC, peaks around midnight on the 11th November, and then decays to 06:57 UTC on the 13th November. This overall trend is punctuated by numerous spikes in radiance. The second period begins on 14:42 UTC 19th November and is marked by numerous spikes in radiance.

It continues until ~14:57 UTC 22nd November. The baseline anomaly then slowly increased with markedly fewer radiance spikes to ~midnight 30th November, after which time the background radiance drops to a lower level and remains at roughly this level until early morning 7th December when the lava lake became obscured by cloud. The thermal anomaly decays to background between 8th December and 15th December.

The patterns in the thermal anomaly could be due to increases in lava lake area, temperature, fire fountaining, overflows, or renewal of activity in the solidified northern lake. Comparison with ground observations allow us to discriminate between these possibilities. Radiance spikes during the period of ground observations correlate with overflows and collapses, while a steady low-level radiance anomaly between spikes correlates with background lake activity. The sampling interval of 15 minutes is insufficient to resolve the observed 20 minute variation in lake height. We therefore interpret the radiance spikes as overflows as the lava lake progressively builds itself up by first episodically flooding the pit, and then constructing the scoria ramparts by successive overflows and spatter.

Petrology

Method

Three samples were collected for analysis: EA001 collected from the margin of the first overflow onto the main crater floor (figs. 5.1 and 5.3a) and sampled approximately 12 hrs after emplacement; EA002 collected from the main crater floor i.e. the flow underlying the newly erupted flows; EA003 from the last overflow observed by the field team, collected < 1 hr after emplacement.

Detailed analytical techniques are described in Chapter 2, Methodology. The techniques used include whole rock, SEM, EMPA and SIMS. Figure 5.3e shows olivine crystals hand-picked and mounted in resin for melt inclusion analysis. Thin sections and phenocrysts picked for analysis were taken from the glassy upper 2 cm of the samples.

Results

The lavas are porphyritic (~20% by volume) and vesicle-rich (up to 60% volume in EA003, calculated by point counting (fig.5.3b)). The phenocrysts are largely concentrated in the outer edge of the flow to a depth of ~ 30 mm. The samples lose their glassy appearance towards the centre of the flow and the matrix becomes dull after ~20 mm. The flows were inflated by volatiles and thus hollow inside. The 2010 lavas (EA001 and EA003) are olivine-normative, whereas the older underlying lava (EA002) is quartz-normative, with whole rock silica content varying from 49 – 51 wt% respectively (table 5.1). The matrix in EA001 and EA003 comprises quenched glass (figs. 5.3d and e). EA002 has a fine grained crystalline groundmass (fig. 5.3f). The mineral assemblage is plagioclase + clinopyroxene (cpx) + olivine. No Fe-Ti oxides or other accessory phases are present in any sample. Euhedral plagioclase phenocrysts, up to 4 mm, show normal zoning between core and rim, but within some rims, oscillatory zoning is present (fig. 5.3d). There is evidence of resorption between some of the zones. Plagioclase is the dominant phenocryst with ~90% of all phenocrysts being plagioclase. Plagioclase is also found as small inclusions in both cpx and olivine; anorthite (An) content ranging from An_{83-74}. Anorthite content in plagioclase cores from the 2010 lavas (table 5.2) ranges from An_{85-69}; the range within an individual core is more restricted e.g. An_{85-82}, An_{71-69}. Within the zoned rims, An values show a wide range from An_{80-66} the higher An values, found in those phenocrysts with higher An values in the core. A very similar An content is found in EA002 (An_{82-75} in cores, An_{76-66} in rims). Plagioclase groundmass is only present in EA002 and ranges from An_{71-63}. Cpx crystals are subhedral, small (<1 mm) augites, often forming glomerocrysts with plagioclase (table 5.3). Mg# (molar $Mg/[Mg+Fe_{tot}]$) values range from 84 - 72. One tiny euhedral cpx inclusion was found in an olivine, Mg# 82. Olivines are euhedral with Fo_{84-78} content in phenocrysts and Fo_{80-73} in rims and EA002 groundmass (table 5.4).

The raw analyses of the melt inclusions indicate compositions close to those of the matrix glass, suggesting minor post-entrapment modification (tables 5.5 and 5.6). The compositions were corrected for post entrapment crystallisation (PEC; Danyushevsky et al., 2000), by adding host olivine back into the melt until $Kd_{Fe\text{-}Mg}$ = 0.28, within the bounds defined by Ford and Roeder (1983; 1974). The maximum correction made was only 7 wt.% (table 3). The H_2O content of the five inclusions (after accounting for minor PEC) ranges from 850 to 1276 ppm; CO_2 contents range from 31 – 190 ppm (table 5.6). Multiple analyses of single melt inclusions show them to be homogeneous for H_2O and CO_2. Matrix glass contains ~550 ppm H_2O and <50 ppm CO_2. FTIR values for CO_2 correspond well to those determined by SIMS (<50 ppm in matrix glass and 94-136 ppm in melt inclusions). H_2O is higher than SIMS, with melt inclusion values of 1700-2000 ppm and 1700 ppm in matrix glass). This may be related to the use of compositionally incorrect extinction coefficients for IR. SO_2 content of melt inclusions (MI J and two additional MI – see Table A3.5), measured by electron microprobe (table 5.6) are 163-419 ppm; chlorine, 255-368 ppm. Average SO_2 and Cl values from 25 analyses in matrix glass were determined as 91 and 195 ppm respectively (table 5.4).

Temperatures were calculated using various mineral / liquid thermometers with an average of ~1170 ^{o}C from all methods (table 5.7). Pre-eruptive temperatures derived from plagioclase / liquid (equation 24a, Putirka, 2008) are in the range 1171 – 1180 ^{o}C. Clinopyroxene / liquid (Putirka et al., 1996) derived temperatures are 1148 – 1175 ^{o}C, and olivine / liquid (Putirka, 2008) gives 1151 -1158 ^{o}C, and the method of Beattie (1993) gives 1157 ^{o}C. Melt inclusion entrapment temperatures using post-entrapment corrected data and the method of Putirka (2008) are in the range 1169 – 1182 ^{o}C, with similar temperatures (1169 – 1183 ^{o}C) obtained from the method of Beattie (1993).

Volatile saturation pressures were calculated using the method of VolatileCalc (Newman and Lowenstern, 2002), ranging from 7 to 41 MPa. To convert these pressures to depth, we have assumed a crustal density of ~2850 kg m^{-3} based on gravity studies in the Main Ethiopian Rift (e.g. Mahatsente et al., 1999). The calculated depths are shallow: 0.3 to 1.5 km.

Whole rock data

Sample	**EA001**	**EA002**	**EA003**	***typical error*** [b]
n	**1**	**1**	**1**	
SiO_2[a] **(wt%)**	48.85	51.36	49.12	*0.01369*
TiO_2	1.96	2.13	1.95	*0.00008*
Al_2O_3	16.57	14.88	16.56	*0.00313*
$Fe_2O_{3(T)}$	10.77	11.38	10.77	*0.00043*
MnO	0.17	0.17	0.17	*0.00000*
MgO	6.04	5.61	6.13	*0.00183*
CaO	12.41	10.86	12.40	*0.00111*
Na_2O	2.66	2.62	2.65	*0.00018*
K_2O	0.50	0.70	0.49	*0.00001*
P_2O_5	0.27	0.30	0.27	*0.00000*
SO_3	b.d.	0.42	b.d.	
LOI	-0.37	0.34	-0.39	
Total	99.81	100.77	100.10	
Rb	11	18	12	*0.37*
Sr	310	318	315	*0.11*
Y	28	30	29	*0.24*
Zr	159	198	163	*0.12*
Pb	2	4	2	*0.54*
Th	3	3	2	*0.48*
U	2	1	2	*0.42*
Ga	19	19	19	*0.75*
Zn	76	78	77	*0.40*
Cu	106	96	109	*0.30*
Ni	47	41	52	*0.49*
Co	41	36	42	*0.37*
Cr	128	142	127	*0.38*
V	287	288	292	*0.29*
Sc	37	34	38	*0.83*
Ba	118	190	119	*0.43*
La	18	21	20	*0.44*
Ce	51	48	46	*0.28*
Nd	26	24	26	*0.35*
Cs	b.d.	b.d.	b.d.	*0.42*

[a] *major element analysis - XRF*

[b] *Error is calculated from the counting statistic error ε = value * (cps/100)*

n - denotes number of analyses

b.d. - below detection level

$_T$ *- total iron*

Table 5.1 *– XRF major and trace element analyses*

EMPA analyses of Plagioclase

	Comment	**EA001**	**EA001**	**EA002**	**EA002**	**EA002**	**EA002**	**EA003**	**EA003**	**EA003**	**EA003**	***uncertainty***
	Crystal	1	1	1	3	5	5	2	3	4	4	*1 σ*
	identifier[1]	c	r	g	g	c	r	c	r	c	r	
wt% oxide [a]	**SiO_2**	47.10	47.73	52.11	51.30	48.62	49.67	47.41	47.89	50.23	49.00	*1.70*
	TiO_2	b.d.	b.d.	b.d.	b.d.	b.d.	b.d.	b.d.	b.d.	b.d.	b.d.	
	Al_2O_3	32.96	31.48	29.17	29.76	31.11	30.55	31.80	31.44	30.75	31.48	*1.07*
	FeOt	0.57	0.57	0.60	0.72	0.54	0.53	0.50	0.59	0.41	0.57	*0.08*
	MnO	b.d.	b.d.	b.d.	b.d.	b.d.	b.d.	b.d.	b.d.	b.d.	b.d.	
	MgO	0.15	0.21	0.20	0.17	0.22	0.20	0.16	0.18	0.18	0.21	*0.02*
	CaO	16.60	15.53	12.61	13.34	15.24	14.60	15.77	15.64	14.28	15.27	*1.20*
	Na_2O	1.90	2.54	4.05	3.59	2.67	2.96	2.28	2.35	3.15	2.86	*0.64*
	K_2O	b.d	0.11	0.17	0.17	b.d	b.d	0.10	0.09	0.15	0.12	*0.04*
	ZrO_2	b.d.	b.d.	b.d.	b.d.	b.d.	b.d.	b.d.	b.d.	b.d.	b.d.	
	P_2O_5	b.d.	b.d.	b.d.	b.d.	b.d.	b.d.	b.d.	b.d.	b.d.	b.d.	
	SO_2	b.d.	b.d.	b.d.	b.d.	b.d.	b.d.	b.d.	b.d.	b.d.	b.d.	
	Total	99.27	98.16	98.92	99.05	98.39	98.51	98.03	98.17	99.16	99.52	
	An	82.84	76.64	62.60	66.54	75.96	73.19	78.81	78.20	70.83	74.15	
	Ab	17.16	22.73	36.39	32.43	24.04	26.81	20.62	21.26	28.26	25.14	
	Or	0.00	0.63	1.01	1.03	0.00	0.00	0.57	0.54	0.91	0.71	

[a] EMPA analysis - University of Bristol

[1] identifier - r=rim, c=core, g=groundmass, i=inclusion, p=profile

b.d. - below detection level

blank space indicates no analysis

***Table 5.2** – Representative analyses of Erta Ale plagioclase*

EMPA analyses of Clinopyroxene

	sample	**EA001**	**EA001**	**EA002**	**EA002**	**EA002**	**EA003**	**EA003**	***uncertainty***
	crystal	1	2	1	2	4	1	1	*1 σ*
	identifier[1]	c	r	c	c	g	c	r	
wt% oxide [a]	**SiO_2**	52.01	51.59	49.81	51.25	50.29	53.26	51.30	*1.13*
	TiO_2	0.76	0.89	1.29	0.93	1.36	0.64	0.91	*0.26*
	Al_2O_3	2.62	2.91	3.88	2.99	3.69	1.85	2.52	*0.70*
	FeO_T	5.90	6.45	7.99	6.43	8.14	6.60	7.18	*0.84*
	MnO	0.16	0.17	0.20	0.16	0.21	0.16	0.19	*0.02*
	MgO	16.29	16.16	15.66	16.02	15.65	17.04	16.49	*0.49*
	CaO	21.44	21.09	19.62	20.96	19.84	20.77	20.26	*0.68*
	Na_2O	0.21	0.34	0.37	0.31	0.29	0.28	0.19	*0.07*
	K_2O	b.d.	b.d.	b.d.	b.d.	b.d.	b.d.	b.d.	b.d.
	Cr_2O_3	0.33	0.29	0.23	0.31	0.19	0.18	0.14	*0.07*
	Total	99.72	99.88	99.05	99.35	99.66	100.79	99.17	
Recalculated Fe[2]	**Fe^{3+}**	0.02	0.05	0.07	0.04	0.05	0.02	0.04	
	Fe^{2+}	0.16	0.15	0.18	0.16	0.20	0.18	0.18	
	(Mg) En	47	46	46	46	45	48	47	
	(Fe) Fs	9	10	13	10	13	10	11	
	(Ca) Wo	44	43	41	43	41	42	42	
	Mg number[3]	83	82	78	82	77	82	80	

[a] EMPA analysis - University of Bristol

[1] identifier - r=rim, c=core, g=groundmass, i=inclusion, p=profile

[2] Fe ratio - calculated using the method of Schumacher (1997)

[3] Mg number is MgO/(MgO+FeO_T)

FeO_T is total Fe

b.d. - below detection level

Table 5.3 *– Representative analyses of Erta Ale clinopyroxenes*

EMPA analyses of Olivine

	Sample	**EA001**	**EA001**	**EA002**	**EA002**	**EA002**	**EA003**	**EA003**	***uncertainty***
	crystal	1	1	3	3	6	1	1	*1 σ*
	Identifier[1]	c	r	c	r	g	c	c	
wt% oxide [a]	**SiO_2**	38.77	38.92	40.25	38.94	38.14	38.81	38.85	*0.63*
	TiO_2	b.d.	0.04	b.d.	b.d.	0.05	b.d.	0.02	*0.01*
	Al_2O_3	b.d.	b.d.	0.05	b.d.	b.d.	0.04	0.04	*0.00*
	FeO_T	19.33	20.88	15.62	19.79	24.37	20.42	19.90	*2.57*
	MnO	0.30	0.32	0.23	0.32	0.37	0.32	0.32	*0.04*
	MgO	41.23	40.48	44.41	40.41	36.69	40.27	40.27	*2.25*
	CaO	0.36	0.37	0.30	0.37	0.38	0.37	0.38	*0.03*
	Na_2O	b.d.	b.d.	b.d.	b.d.	b.d.	b.d.	b.d.	
	Total	99.99	101.01	100.86	99.83	100.00	100.23	99.79	
End member	**Forsterite**	78.9	77.3	83.3	78.2	72.6	77.6	78.0	
	Fayalite	20.8	22.4	16.4	21.5	27.0	22.1	21.6	
	Tephroite	0.3	0.3	0.2	0.3	0.4	0.4	0.4	
	Mg#[2]	79	78	84	78	73	78	78	

[a] EMPA analysis - University of Bristol

[1] identifier - r=rim, c=core, g=groundmass, i=inclusion, p=profile

[2] Mg number is MgO/(MgO+FeO_T)

FeO_T is total Fe

b.d. - below detection level

Table 5.4 *– Representative analyses of Erta Ale olivines*

Averaged matrix glass analyses

Sample	**EA003**	
identifier	matrix	*std dev*
n	*5*	
SiO_2 (wt%) [a]	49.26	*0.23*
TiO_2	2.41	*0.09*
Al_2O_3	13.86	*0.19*
FeO	11.36	*0.31*
MnO	0.27	*0.04*
MgO	6.27	*0.19*
CaO	11.33	*0.13*
Na_2O	2.97	*0.10*
K_2O	0.63	*0.01*
P_2O_5	0.37	*0.03*
F	b.d.	
Total	98.86	
n	*25*	
SO_2 (ppm)[a]	91	*27*
Cl (ppm)[a]	195	*35*
SIMS n	*2*	
H_2O (ppm) [b]	559	*20*[d]
CO_2 (ppm) [b]	<50	
FTIR n	*2*	
H_2O (ppm) [c]	1700	*340*[e]
CO_2 (ppm) [c]	<50	

Table 5.5 *–averaged matrix glass analyses. [a] averaged major element analysis - EMPA, [b] SIMS analysis, University of Edinburgh, (volatiles PEC corrected), [c] FTIR analyses, [d]average uncertainty as determined by full propagation of counting statistics, instrument background and calibration working curve, [e]IR propagated uncertainty, n - denotes number of analyses, b.d. - below detection level, blank space indicates no analysis.*

Overleaf. Table 5.6 *– EMPA major element and SIMS volatile and trace element analyses for individual Erta Ale melt inclusions together with major element analysis for the host olivine crystal. [a]averaged major element analysis - EMPA. Values corrected to obtain K_D 28, [b]PEC post entrapment crystallisation, [c]SIMS analysis, University of Edinburgh, (volatiles PEC corrected), [d]average uncertainty as determined by full propagation of counting statistics, instrument background and calibration working curve, [e]average FTIR analyses, University of Bristol (volatiles PEC corrected), [f]IR propagated uncertainty - see text for error source, [g]temperature in °C using the method of Putirka (2007). Calibration error ±45 °C, [h]pressure in Mpa using the method of Newman and Lowenstern, [i]depth calculated from P assuming a crustal density of ~2850kgm$^{-3.}$ Depth is depth below surface, n - denotes number of analyses, b.d.* - below detection level, *blank space indicates no analysis, host - refers to phenocryst hosting the inclusion, identifier - refers to melt inclusion.*

Average melt inclusion and host olivine analysis

	Sample	**EA003**		**EA003**		**EA003**		**EA003**		**EA003**	
	identifier		G		H		I		J		L
	host	olivine		olivine		olivine		olivine		olivine	
Major elements	***n***	*2*	*4*	*2*	*4*	*2*	*4*	*2*	*5*	*2*	*4*
	SiO_2 (wt%)[a]	38.77	48.76	39.11	49.09	39.19	48.43	39.07	49.56	38.32	48.75
	TiO_2	0.01	2.33	0.00	2.33	0.02	2.25	0.00	2.23	0.01	2.38
	Al_2O_3	0.02	13.29	0.02	13.66	0.00	12.90	0.02	13.76	0.04	13.08
	FeO	19.16	11.79	19.36	11.46	19.90	12.25	18.55	11.17	20.15	12.53
	MnO	0.32	0.23	0.31	0.21	0.33	0.22	0.29	0.22	0.31	0.24
	MgO	41.13	7.00	40.75	6.84	40.84	7.04	41.43	7.07	40.29	7.11
	CaO	0.35	11.50	0.33	11.51	0.35	11.61	0.33	11.41	0.35	11.19
	Na_2O	0.00	2.72	0.00	2.66	0.00	2.58	0.00	2.77	0.00	2.79
	K_2O		0.56		0.54		0.51		0.55		0.56
	P_2O_5	0.00	0.49	0.02	0.39	0.02	0.34	0.00	0.37	0.00	0.37
	F		b.d.		b.d.		b.d.		b.d.		b.d.
	Total		98.65		98.72		98.52		99.13		99.01
	Forsterite	79.01		78.69		78.26		79.68		77.83	
	Fayalite	20.64		20.97		21.38		20.00		21.83	
	Tephroite	0.34		0.34		0.36		0.32		0.34	
	Mg# [g]	79.29		78.96		78.54		79.93		78.10	
	% PEC[b]		4		2		7		3		5
Volatiles	***SIMS n***		*2*		*3*		*3*		*2*		*1*
	H_2O (ppm)[c]		1276		850		1040		1004		865
	uncertainty[d]		18		10		15		22		13
	CO_2 (ppm)[c]		31		190		76		120		124
	uncertainty[d]		1		5		2		3		3
	FTIR n						*2*		*2*		*1*
	H_2O (ppm)[e]						2000		1700		865
	uncertainty[f]						400		340		13
	CO_2 (ppm)[e]						94		136		124
	uncertainty[f]						33		50		3
	n								*4*		
	SO_2 (ppm)[a]								419		
	sd (1σ)								67		
	CO_2 (ppm)[a]								368		
	sd (1σ)								148		
	T (°C)[g]		1174		1169		1179		1175		1182
	P (Mpa)[h]		7		40		17		26		27
	Depth (km)[i]		0.2		1.4		0.6		0.9		0.9
Trace elements	***n***		*2*		*3*		*3*		*2*		*1*
	Li (ppm)[c]		5		6		6		5		5
	Be		1		1		1		1		1
	B		4		4		4		4		3
	Sc		45		45		48		45		45
	Sr		330		334		355		327		340
	Y		41		41		43		40		40
	Zr		221		210		218		213		219
	Nb		38		34		36		34		39
	Ba		166		153		164		156		174
	La		33		31		35		33		32
	Ce		65		64		70		64		65
	Pr		8		8		8		8		8
	Nd		26		25		27		26		25
	Sm		8		7		8		8		8
	Gd		7		6		7		5		4
	Tb		1		1		1		1		1
	Dy		6		6		7		5		6
	Ho		1		1		1		1		1
	Er		4		4		4		4		4
	Tm		0		0		0		0		0
	Yb		3		3		3		3		3
	Lu		0		1		0		1		1
	Hf		4		4		4		4		4
	Ta		2		2		2		2		2
	Th		3		4		4		4		3
	U		1		1		1		1		1

Thermometry

Matrix glass thermometry[a] **Melt inclusion thermometry**

Mineral	Plagioclase / liquid	CPX / liquid	Olivine / liquid		Olivine / liquid	
	(Rim / glass)	(Rim / glass)	(Rim / glass)		(corrected olivine / glass)	
Method	Putirka (2008)	Putirka (1996)	Putirka (2007)	Beattie (1993)	Putirka (2007)	Beattie (1993)
calibration error	± 36 °C	± 52 °C	± 45 °C	± 44 °C	± 45 °C	± 44 °C
Temperature °C	1176	1165	1158	1157	1175	1176
	1180	1169	1157	1157	1169	1171
	1176	1151	1158	1157	1180	1178
	1173	1148	1157	1157	1176	1176
	1180	1167	1157	1157	1182	1183
	1171	1175	1157	1157		
	1178	1169	1152	1157		
		1167	1151	1157		
		1157	1155	1157		
		1170	1157	1157		
		1170	1155	1157		
		1162	1155	1157		
			1153	1157		
			1153	1157		
			1156	1157		
			1157	1157		
			1155	1157		
			1155	1157		
Mean	*1176*	*1164*	*1155*	*1157*	*1176*	*1177*
Std Dev (1σ)	*3.1*	*7.9*	*1.9*	*0.0*	*5.8*	*6.0*

[a] *All temperatures calculated from sample EA003*

Table 5.7 *– calculated temperatures for Erta Ale magmas by different methods*

Trace element contents of melt inclusions (table 5.6) are broadly similar to those of the host lavas with slightly elevated incompatible elements and lower compatible elements consistent with ~20% crystallisation. Incompatible elements e.g. Zr, are positively correlated with H_2O and negatively correlated with CO_2, despite a relatively small variation in all parameters.

Kα X-ray mapping of an olivine phenocryst from EA001 indicates homogeneity throughout the crystal for major elements such as Fe and Ca. However, faint concentric, oscillatory zoning is visible in phosphorous (fig. 5.5).

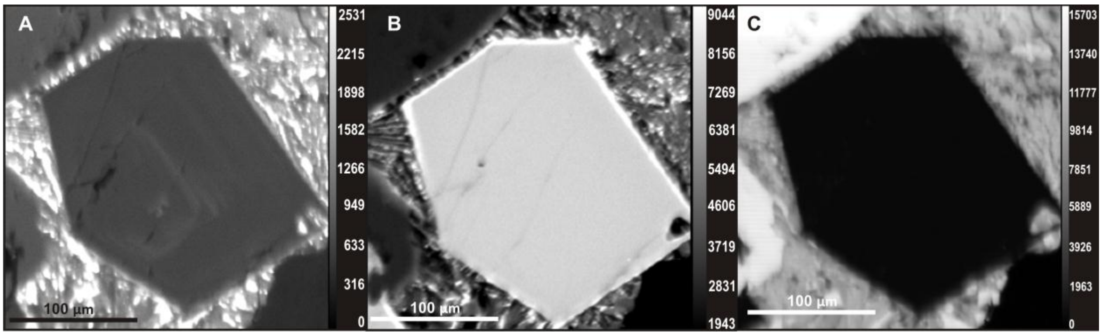

***Figure 5.5**. $K\alpha$ X-ray intensity maps in an olivine from sample EA001. A) Combined phosphorous image from four spectrometers shows faint zoning throughout the crystal. B) Fe, and C) Ca maps show no visible zoning.*

Integration of ground observations, satellite imagery and petrology

In a location as remote as Erta Ale, eruptions can occur unnoticed and unrecorded. The November 2010 eruption was short lived, which is typical of recent eruptions in Afar (e.g. Ferguson et al., 2010; Wright et al., 2006), and ordinarily the brevity would not allow scientists sufficient time to travel to the eruption site to make observations. However, from the interpretation of the SEVERI features of the radiance time-series, together with serendipitous ground observations, we can construct a story of how the eruption proceeded. The SEVIRI data suggest the first thermal anomaly period occurred between the 11th November and the 14th November, UTC (fig. 5.4), and records overflows onto the southern pit floor only. By the end of the first period the pit floor had been covered with fresh lava flows, but the lake level was still low enough that the rim of the pit obscured it from view by SEVIRI. Ground observations from the 11th November confirm that the southern pit was still > 20 m deep, comparable to its state six months earlier in Feb. 2010 (fig. 5.2). However, by the 14th November the base of the pit was covered in fresh lava (J. Wilkinson pers. com. December 2010). There then followed a hiatus of overflows, up until the start of the second thermal anomaly period, as seen by the lack of excess radiation (fig. 5.4). It was during this period of quiescence that seismic activity occurred in the Gulf of Aden (14th – 17th November – (European-Mediterranean Seismological Centre (EMSC)) and around the settlement of Chiro (formerly Asebe Terferi) in the main Ethiopian rift. Disturbance was also reported in the Danakil region with the opening of large sink-holes and unusually high groundwater levels.

The field team arrived at ~16.00 UTC on the 21st November when the second phase of the eruption was well underway, and the southern pit had filled. SEVERI imaging suggests this second phase of activity began during the 19th November, which indicates a rapid infilling of the southern pit between the 19th and 21st (figs. 5.2 and 5.4). Assuming little or no activity between the 15th and 19th November, a flow rate of approximately 2 $m^3 s^{-1}$ would be required to fill the area of the pit between 19th - 21st November (53 hours). Oppenheimer and Francis (1997) estimated an average magma discharge rate (MDR) of ~400 kg s^{-1} for Feb 1972 – Mar 1973. Assuming the same density for comparison, (2700 kg m^{-3}), the calculated MDR for 19-21st November is ~5600 kg s^{-1}. The first overspill outside of the southern pit onto the main crater floor occurred at ~17.50 UTC (fig. 5.3a). Throughout the eruption, the lake was surrounded by a scoria ring cone which continued to build, similar to that observed in 1973 (Tazieff). Overspills continued at approximately 2 hr intervals until ~14.30 UTC on the 22nd November (refer to Appendix 5 – Erta Ale video). For the remainder of the ground observation, the lake was contained within the scoria ring, which by 3.00 UTC on the 23rd November had grown to ~4 m high on the southern side. A 20 minute cycle followed, with lava lake levels rising and falling by ~4. Peak levels were marked by agitated Strombolian activity indicating volatile rich magma. The northern part of the ring suffered a partial collapse on the morning of the 23rd November, which corresponds to a sharp peak at 4.00 UTC in the SEVERI imaging (fig. 5.4). Periodically incandescent gas jets burning with a blue-green colouration were observed, similar to the description of gas flames reported in January 2003 assumed to be SO_2 (Vetsch et al., 2003). The northern pit also showed signs of activity with fresh lava flows and incandescence was visible through cracks in the lava during the night of the 21st November.

After the field team departed on the 23rd November, the eruption continued, with new overflows covering over the sampled flows, and nearly reaching the western rim of the caldera (fig. 5.1). The spacing between successive overflows became long enough such that periods of sustained radiance can be identified, indicating that the lava lake had gained sufficient height to come into view of the sensor. SEVERI indicates lake activity persisted with sparse superimposed overflows for seven days, followed by a period of sustained lake activity with no overflows for six days, and within a further four days, after the 30th November, the lake signal disappeared, indicating a drop in lake level and occultation of the lake by the rim once again. Cloud cover prevents us determining the exact end of the eruption, but activity was confirmed to have ceased prior to the 15th December (J. Wilkinson pers.com. December 2010). In summary, the pattern appears to be 1) first period of lake level rise, 2) hiatus/drop in lake level, 3) lake level rise including lava overspills into the southern pit, 4) lake level stabilisation at high stand including lava overspills into the main crater, 5) lake level drop. The estimated total volume of erupted lava is ~0.6 km^3, based on an estimated pit depth of 20 m.

Thermometry

There is good agreement between temperatures determined in February 2001 by Burgi et al. (2002) using thermocouples and pyrometers (1145 – 1187 ^{o}C), and the petrological estimates reported here (1148 – 1183 ^{o}C). The temperatures are within error indicating a temperature for the system of ~1170, although there are likely to be some fluctuations within the conduit caused by magma circulation between magma storage, the conduit and the lake itself (Harris et al., 2005). Temperatures determined by Le Guern et al. (1979) in December 1971, January 1973 and 1974 provided a range of 1100 ^{o}C through to 1210 ^{o}C. This field team directly inserted thermocouples into active hornitos which may account for differences between this and the study of Burgi et al. (2002).

Volatiles

The petrology indicates that crystallisation is taking place in the upper ~1 km of the conduit. H_2O content in the melt inclusions is low, >0.1 wt%, lower than the water content proposed for a typical alkali basalt (~0.5 wt%), (e.g. Lowenstern and Mahood, 1991). The low water values in the melt inclusions are very similar in content to basaltic melt inclusions from Hawaii (fig. 5.6a, Hauri, 2002), but significantly lower than MORB (e.g. Pineau and Javoy, 1994), Piton de la Fournaise, Réunion (Bureau et al., 1998), and Iceland samples (Nichols et al., 2002; Nichols and Wysoczanski, 2007), which yield H_2O contents up > 0.9 wt%. Low H_2O and CO_2 content can result from leakage e.g. through cracks, and diffusive loss can occur through the host olivine. However, no cracks or bubbles were present in any of the inclusions studied. There are several lines of evidence that the Erta Ale magma was volatile-saturated prior to eruption. Our CO_2-H_2O data define an array which is oblique to the isobars, consistent with decompression-driven degassing (fig. 5.6).

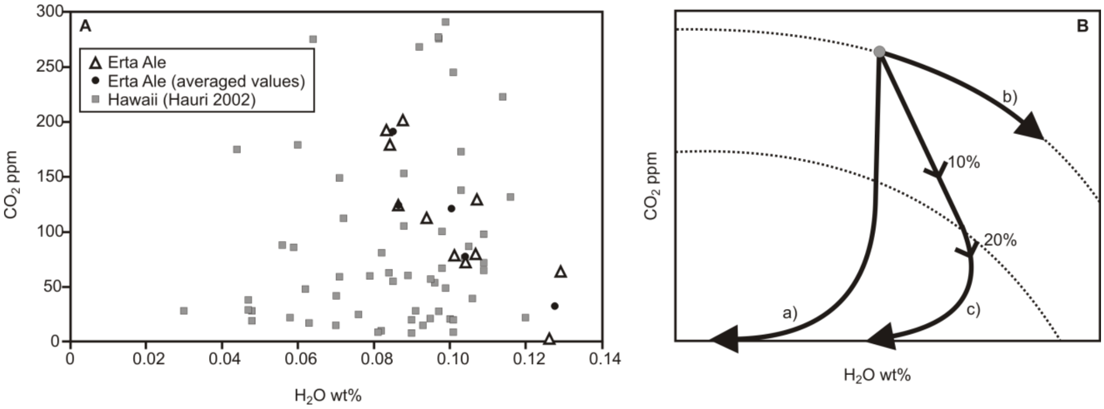

Figure 5.6. *A) Plot of CO_2 v H_2O indicating broad agreement between Erta Ale and Hawaii (Hauri 2002). B) Schematic indicating possible volatile evolution paths in melt inclusions (solid lines), based on Blundy and Cashman (2008). Dotted lines indicate isobars. Path a) indicates decompression without crystallisation, path b) isobaric vapour saturated crystallisation, and path c) vapour saturated decompression with crystallisation, percentages indicate crystallisation. Path c) best describes the Erta Ale data.*

However the negative slope of the array cannot be ascribed to degassing alone, which would produce a steep positive (sub-vertical) array, due to the much lower solubility of CO_2 compared to H_2O. The positive correlation of an incompatible element, such as Zr, with H_2O (fig. 5.7), and negative correlation with CO_2 are consistent with vapour-saturated crystallisation (Blundy and Cashman, 2008). Thus it is apparent that crystallisation occurred concomitantly with decompression in Erta Ale magmas. Point counting for EA003 indicates a low modal volume (~18 vol %) of phenocrysts.

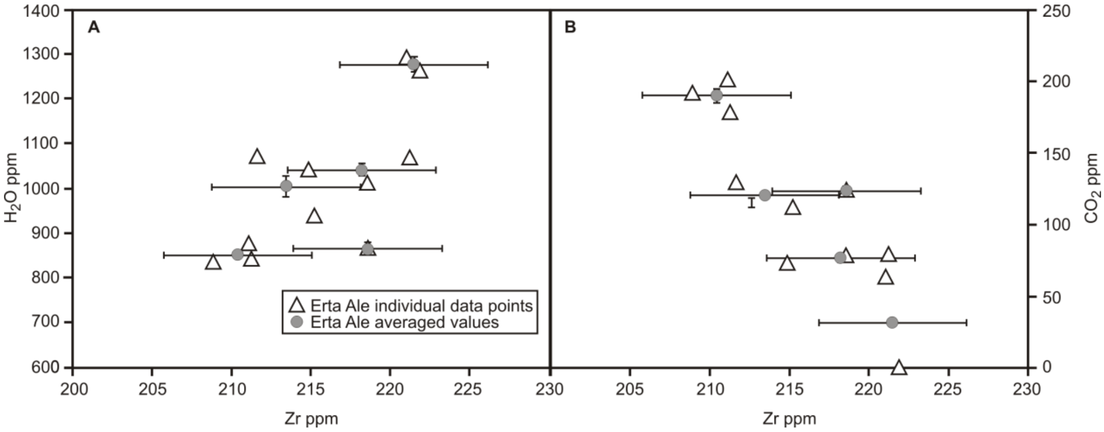

Figure 5.7*. Melt inclusion analyses of A) H_2O and B) CO_2 versus Zr. These plots indicate the November 2010 lavas experienced vapour-saturated crystallisation as Zr is positively correlated with H_2O and negatively correlated with CO_2. Triangles show individual SIMS analyses, grey circles indicate the averaged analysis (and 1 s.d. error bar) for each melt inclusion studied.*

There is currently little evidence to constrain the deeper sub-magmatic plumbing system. However, there is no evidence in the petrology of any mixing or crustal assimilation. The phenocrysts are in equilibrium with the glass matrix, and there is no evidence for xenocrysts or antecrysts, suggesting the magma is undergoing little contamination. This is also the conclusion of isotopic studies which rule out the participation of continental crust at Erta Ale (Barrat et al. 1998). Oppenheimer and Francis (1997) speculate that denser, cooler and partially degassed magma from the lake surface may descend (balanced by influx of fresh magma) and contribute to endogenous growth of the volcano through emplacement of dykes and sills, indicating that the basement at Erta Ale may be gabbroic in nature (Barrat et al. 1998).

Note that if the inclusions had lost water by diffusion, the H_2O (which diffuses more rapidly than CO_2) would be displaced to low values at a given CO_2 content, which is not observed (fig. 5.6a). An additional line of evidence that these samples have not lost H_2O, is the close agreement between an average-calculated dry-liquidus temperature of ~1178 ^{o}C (range of 1173 - 1183 ^{o}C), calculated using MELTS (Ghiorso and Sack, 1995), and those derived for petrological temperatures using thermometry. If the magma had lost significant H_2O the calculated liquidus would be far higher than temperatures estimated from petrology or field thermometry.

The conclusion that Erta Ale magmas were volatile-saturated at shallow levels allows us to estimate using VolatileCalc (Newman and Lowenstern, 2002), the composition of the exsolved gas to be 0.2 – 2.9 mol% H_2O and 97.1 – 99.8 mol% CO_2 i.e. molar H_2O/CO_2 ratios of 0.002 to 0.03. There is some uncertainty in this estimate due to the paucity of experimental data on basalts at low pressures. Nonetheless these estimated volatile compositions are much more H_2O poor than those determined by Gelach (1980) and Sawyer et al. (2008) at Erta Ale, who give molar H_2O/CO_2 ratios of 4 – 7 and 25 respectively (table 5.8). Such values are more consistent with the measured ratios in our melt inclusions (molar H_2O/CO_2 4-56) which would imply that the observed gas fluxes are the product of almost complete degassing at or close to the surface. The degassed H_2O content indicated by the matrix glass is 559 ppm, which indicates ~450 ppm H2O has been lost through degassing (melt inclusion minus matrix). The calculated values for the H_2O/CO_2 ratios fall within the range determined by Sawyer et al (2008) and Gerlach (1980). Gas exsolution deeper within the conduit, rather than at the surface, will further reduce H_2O/CO_2 ratios and may account for the lower ratios measured in the 1970s by Gerlach (1980).

Molar gas ratios

	This study				Sawyer et al (2005)		Gerlach (1980)			
	average[a]	**sd**	**EA003L**[b]	**sd**	**2005**	**sd**	**1974**[c]	**1973**[d]	**1973**[d]	**1971**[e]
H_2O/CO_2 (mol)	10.1	7.0	9.0	1.6	24.8	0.8	6.6	3.8	3.7	3.9
CO_2/SO_2	0.7	0.5	0.5	0.1	1.5	0.1	1.6	2.7	4	2
SO_2/Cl	2.0	3.6	1.0	0.9	12.4	0.2	18.6			
H_2O/SO_2	6.8	3.7	4.8	1.1	38	3	10.4	10.4	14.5	7.9

[a] average from this study, calculated using melt-inclusion minus matrix analysis for each species.

[b] example of an individual melt inclusion, calculated using melt inclusion minus matrix analysis for each species.

[c] ratios from restored gas analysis Gerlach 1980 (gases originally collected in 1974 from hornitos by Giggenbach and Le Guern).

[d] ratios from restored gas analysis Gerlach 1980 (1973 gases originially collected from a hornito by Le Guern).

[e] ratios from restored gas analysis Gerlach 1980 (1971 samples originally collected by Tazieff).

***Table 5.8**. Calculated gas ratios*

The calculated Cl release is much higher than previously noted as indicated by the low SO_2/Cl ratio of 1.0 – 2.0 (table 5.8) compared to 12-19 in the previous studies (Gerlach, 1980, Sawyer et al., 2008). Chlorine is the last gas to be exsolved from magma, and the higher release is indicative of full degassing (Burton et al., 2007). We suggest that in November 2010 the lava erupted and was able to fully de-gas as opposed to circulating within the conduit where it would retain Cl. This implies that the gas at Erta Ale is only being supplied from magma degassing within the shallow conduit, rather than fluxing from a deep-seated reservoir, and the magma is in fact fully degassed. A schematic illustration of the Erta Ale shallow plumbing system is shown in figure 5.8.

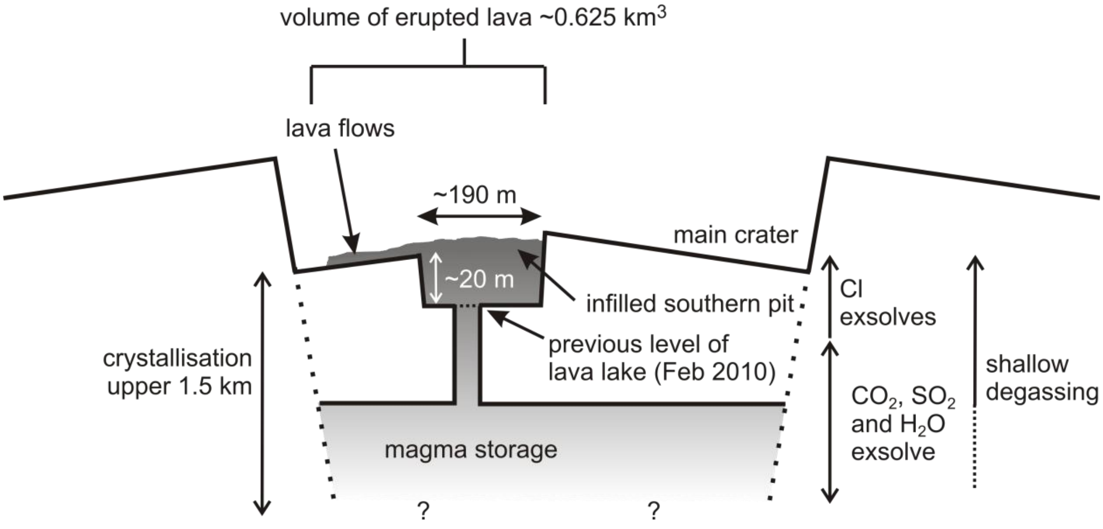

***Figure 5.8.** Schematic of the Erta Ale shallow plumbing system in November 2010 based on integrated ground and satellite observations and petrology (not to scale).*

The sulphur budget required to sustain the flux observed in 2005 (Sawyer et al., 2008), (0.69 kg s^{-1}), requires a magma flux of 0.75 m^3 s^{-1} through the conduit. The overall volatile flux from the Erta Ale lava lake is very small when compared to other lava lakes; Sawyer et al., (2008) calculated a combined flux from gas and FTIR measurements of 7.3 kg s^{-1} (H_2O) and 0.7 (CO_2). The H_2O flux for Erta Ale has been determined to be 19 and 55 times lower when compared to Nyiragonga and Masaya respectively, and for CO_2, 154 and 49 times. The H_2O/CO_2 ratios for Erta Ale determined from the gas plume are similar to Surtsey and Ardoukoba (Sawyer et al., 2008).

However, compared to Nyiragongo, also a divergent plate volcano with a lava lake, but with an alkali-rich composition (melilite nephelinite) these ratios show Erta Ale to be markedly water-rich. Sawyer et al., (2008) noted that the H_2O in the volcanic plume had significantly increased in the 30 years since Gerlach's (1980) work, and suggested this may be related to volatile depletion of the source magma and / or to fractional magma degassing. Alternatively, variation in the H_2O content of Erta Ale gases may reflect small changes in the depth within the conduit at which gases are extracted.

The Erta Ale lavas show a high vesicularity (up to ~60%), which is initially surprising given the low volatile contents indicated by the melt inclusions. Using the ideal gas law (PV=nRT), the averaged value for lost H_2O of 448 ppm, a temperature of 1170 ^{o}C, standard atmospheric pressure and assuming a density for basalt of 2700 kg m^{-3} (e.g. Oppenheimer and Francis, 1997; Sparks and Huppert, 1984), a gas volume of 2.96 x 10^{-3} m^3 is obtained; 8 times more gas than melt. This indicates that if 10% degassing were to take place, ~40% vesicularity would result, and 20% degassing would result in ~60% vesicularity. Thus releasing <448 ppm gas at, or close to the surface at the eruption temperature is sufficient to generate the observed high vesicularities. During eruption, the viscosity of the lava appeared to be very low, (supplementary video 1). The calculated viscosity of the melt at eruption temperature using the model of Giordano et al., (2008) is 70 Pa s. The low crystal fraction (~18 vol% in EA003) is unlikely to have any major impact on the viscosity (Caricchi et al., 2007). However, the vesicularity will have a greater effect. The vesicles observed in the Erta Ale samples are largely elongated, which result in a lowering of viscosity, whilst spherical vesicles act like phenocrysts raising the viscosity (Llewellin and Manga, 2005). Consequently, the calculated viscosity of the vesicular magma is reduced to 5 Pa s (Pal, 2003), or 15 Pa s (Llewellin and Manga, 2005),

Diffusion

Kα X-ray mapping revealed phosphorous zoning in the olivines, not apparent in other elements e.g. Fe, Ca (fig. 5.5). Phosphorous diffuses extremely slowly compared to Fe-Mg and Ca in olivine (Milman-Barris et al., 2008; Spandler and O'Neill, 2010). Hence, the P zoning is preserved whilst Fe-Mg and Ca zoning are homogenised during residence in hot magma. An estimate of the minimum time it would take to homogenise the crystal with respect to Fe-Mg and Ca whilst it resided in the magma, can be obtained from the characteristic diffusion length ($x=(Dt)^{1/2}$; where x = distance, D=Diffusivity, t=time) of each element of interest. Diffusion coefficients for Ca and Fe-Mg, parallel to the c-axis, were calculated using the methods of Coogan et al., (2005), Dohmen et al., (2007) and Dohmen and Chakraborty (2007), at a magmatic temperature of 1170 °C and an oxygen fugacity equating to the QFM buffer. For a typical 200 µm olivine crystal, this indicates Fe-Mg would have homogenised in approximately 0.2 years, and Ca in 10 years, providing a minimum estimate for the residence time of a crystal within this magma. Phosphorous diffusion rates have not been constrained, but are at least two orders of magnitude slower than other major cations (Spandler and O'Neill, 2010). Studies of experimental and some natural olivines have shown P and Cr to be correlated (Milman-Barris et al., 2008). Irrespective of whether Cr (not measured) and P behave similarly in these samples, P has one of the slowest measured diffusion coefficients in olivine. Thus, Cr diffusion coefficients (Ito and Ganguly, 2006) were used to give an indication of the minimum timescales required to eradicate the P zoning. This gives a minimum timescale of ~94 years for homogenisation of P within a typical 200 µm olivine crystal. As P is not homogenous in the studied olivines, this provides a maximum residence time for this crystal. Although crystals can be retained during an eruptive episode it is considered unlikely in this case as the appearance of the crystals from the last overspill (EA002) are very different (see fig. 3 e and f). As the last eruptive episode at Erta Ale was in 1973, it is possible that the period between the eruptions acts as a maximum. We therefore suggest that the crystal residence time is between 10 and 23 years.

Conclusions

We present an integrated field, satellite and petrological study of the November 2010 eruption of the Erta Ale volcano. The timeline of this small, but rare, eruption has been reconstructed from a combination of ground observations and SEVERI imaging. Two phases occurred, beginning on the 11th and 19th November 2010. Pristine melt inclusions have shown the Erta Ale magma to be relatively dry (≤ 1280 ppm water), although several petrological lines of evidence suggest the magma was volatile saturated prior to eruption. The low volatile contents within the melt inclusions are sufficient at eruption temperature and low pressure, to account for the vesicularity seen within the erupted lava. The high vesicularity also affects the viscosity of the erupted magma which is low. We suggest this gas is sourced exclusively from the shallow conduit as indicated by the gas ratios which show higher calculated Cl release than previously recorded. The eruption and overflow of magma from the lava lake in November 2010 facilitated full degassing. This is in contrast to previous studies which recorded gas flux from hornitos, or the confined lava lake, and which have recorded partial degassing. Crystallisation also took place at shallow levels, in the top ~1.5 km of the conduit, with typical crystals being resident in the shallow, convecting magma storage region between ~10 and 23 years.

The November 2010 eruption was coincident with a seismic swarm in the Gulf of Aden; increased activity in 2005 was noted coincident with the 2005 volcano-seismic crisis in the Manda-Hararo magmatic rift segment. It is possible that Erta Ale is particularly sensitive to tectonic activity in the region, but future monitoring will be required to confirm this.

Summary and further work

Chapter

6

Introduction

This thesis explores volcanism in the Afar region of Ethiopia through a study of two very different volcanoes. The main focus of the thesis is Dabbahu volcano at the northern end of the active Manda Hararo rift segment. The magmatic history and evolution of this volcano was investigated, together with the sub-magmatic system. In addition, the fortuitous eruption of the Erta Ale lava lake in November 2010, provided an opportunity to investigate zero-age lava samples to determine what information could be revealed regarding the plumbing system of this unique volcano, and what relationship, if any, can be inferred to Dabbahu. In this chapter the key findings are summarised and possible future directions are also highlighted.

Dabbahu

Dabbahu is a complex volcano, with a range of products from basalt through to both metaluminous and peralkaline rhyolite (SiO_2 46 – 74 wt%). The mineralogy reflects this diversity, with nearly complete suites of minerals in terms of composition (e.g. olivines range from Fo_{83} through to nearly pure end member fayalite). This is unusual since African Rift volcanoes are predominately bimodal or monogenetic for example, Ma’alalta (Wiart and Oppenheimer 2005), Gedemsa (Peccerillo et al. 2003) and Fantale in Ethiopia (Webster et al. 1993) and the Central Kenyan Peralkaline Province (CKPP) (Macdonald and Baginski 2009), which also contains the Greater Olkaria Volcanic Province (GOVP) (Marshall et al. 2009). Occasionally a complete suite of rock types is reported, but across an entire volcanic range such as the Erta Ale magmatic segment (Bizouard et al. 1980), rather than from just one volcanic centre.

Early work on Dabbahu proposed that the rock series could be entirely explained in terms of fractional crystallisation (Barberi et al. 1974). Although fractional crystallisation has also been proposed for peralkaline rocks found elsewhere in the African Rift (e.g., the Greater Olkaria Volcanic Province (Marshall et al. 2009)), the magmatic histories of these volcanoes differ from that determined for Dabbahu. Macdonald and Baginski (2009) argue that the geochemical evolution of the Kenyan complexes have been dominated by the interplay of, amongst other processes, fractional crystallisation, magma mixing and crustal assimilation. A combination of fractional crystallisation and crustal assimilation has also been proposed for Gedemsa (Peccerillo et al. 2003). This study of Dabbahu supports fractional crystallisation of rift-related basalts as the single key petrogenic process; modelling has determined that >80% fractionation is required across the suite to obtain the most evolved pantellerites. This is consistent with work carried out further south in the African Rift at the Kenyan peralkaline centres where Macdonald et al., (2008) determined ~92% fractionation was required. At Dabbahu, there appears to be little in the way of evidence for crustal contamination. The ratio of incompatible elements, Zr/Th, remains constant throughout the entire rock sequence (fig.3.17), which is strongly indicative of a fractionating system with a single parent composition. The modelling in this study also supports generation by fractional crystallisation without crustal contamination. Evolved magmas have low Sr content, and are therefore susceptible to crustal contamination, yet the data show little deviation from the modelled fractionation trend (fig. 3.18) at low melt fraction, suggesting crustal contamination played little part in the evolution of Dabbahu.

Barberi et al., (1974) suggested that fractionation took place at shallow depth. However, although petrological and geophysical evidence indicates the existence of shallow magma storage region within the upper 5 km beneath Dabbahu (refer to Chapter 4), differentiation of the Dabbahu products is unlikely to occur here, but in a deeper crustal area in the lower crusst at ~14-20 km. No evidence has yet been found for the presence of a large volume of cumulates in the shallow crust. However, evidence of significant volumes of cumulates in the lower crust has been found elsewhere in Afar (e.g. Teklay et al. 2010). The eruptive sequence at Dabbahu has not occurred in the order of increasing SiO_2; close correlation between the observed liquid line of descent, and a Main Ethiopian Rift basalt experimental liquid line of descent at mid to lower crustal pressures (Caricchi et al. 2006), suggests fractionation occurred at depth. Evidence for magma mixing at Dabbahu also suggests the co-existence of compositionally distinct, but chemically related magmas, which is difficult to reconcile with fractionation within a large shallow magma chamber.

The location of silicic central volcanoes at the end of rift segments is not yet fully understood and two hypothesis have so far been proposed; that the volcano (e.g. Dabbahu) is substantially older than the rift segment and existed prior to the localisation of strain and magmatism being ‘captured’ by the current rift zone configuration (van Wyk de Vries and Merle 1996; Lahitte et al. 2003; Ebinger et al. 2008); or alternatively, the en-echelon offset of the segments places the tips of the rift segments against colder, older lithosphere (e.g. the Dabbahu segment in relation to the Alayta segment) which may inhibit dyke propagation causing magma to pond in crustal reservoirs (Ebinger et al. 2008). New geochronology indicates Dabbahu has been active for at least 65 ka. Although the age of the basalts underlying the Dabbahu edifice are yet to be fully constrained, it is plausible that Dabbahu post-dates the initiation of the rift (>193 kyrs, D. Ferguson et al. 2011). Dabbahu is likely to have evolved initially as a basaltic shield, alongside a coeval or slightly younger rhyolite centre. The first eruptions probably occurred from fissures linked to the evolution of the rift segment. In contrast, the silicic centres of Ado Ale, ~30 kms south of Dabbahu in the rift segment, and Badi which is slightly off axis to the main rift, are both substantially older than Dabbahu. Ado Ale has been dismantled by the widening of the rift over time (Lahitte et al. 2003), and Badi has been active for more than 445 kyrs (D. Ferguson pers. comm.). It is possible that Ado Ale existed as the original silicic centre at the northern end of the rift, and the rift propagated further northwards over time as Ado Ale was gradually dismantled. The location of other silicic volcanoes in Afar cannot be explained by the ideas proposed above e.g. Nabro (Wiart and Oppenheimer 2005), and it is more plausible that a number of factors in combination may influence the localisation of silicic volcanism in Afar.

Erta Ale

The eruption of Erta Ale in November 2010 is the first recorded eruption and overflow of the southern pit lava lake since 1973 (Tazieff 1973). A combination of field observations and SEVERI multispectral imagery data indicates that the eruption began on the 11th November and continued until sometime between the 8th and 15th December 2010. Although the magmas are dry, with low H_2O contents of up to 0.1 wt%, and CO_2 up to 182 ppm, several lines of evidence indicate that despite this, the Erta Ale magma was volatile saturated. However, this is sufficient to account for the high (~60%) vesicularity observed within the lava samples. Crystallisation is shallow and comprises a limited suite of minerals (plagioclase, cpx and olivine), with a proposed crystal residence time of between 10 and 23 years within the magma storage system. The eruption produced vesicular lavas are (up to ~60 vol%) through degassing of the primary volatiles in the shallow system. This study has shown that 8% degassing of the low volatile content found within the melt inclusions is sufficient to account for this high vesicularity. The calculated lava viscosity is low (between 5 and 15 Pa s) due to the presence of the elongated vesicles, and the behaviour of the lava as recorded in video footage of the eruption reflects this low viscosity.

The dry nature of the magma indicate that Erta Ale basalts would be unsuitable as a parent for the Dabbahu lavas as this would require H_2O contents of ~0.5 wt%. This variability in H_2O content is indicative of the heterogeneity in the ‘plume’ signature beneath Africa, which has been well illustrated, particularly by isotopic studies, including Pik et al. (2006) and Furman et al. (2007).

Future work

Key issues for fieldwork in Afar include accessibility, security, food and water supplies and isolation from medical facilities. As a result there is limited systematic petrological study of the numerous volcanoes which punctuate the Afar depression. Erta Ale, Dabbahu, Tat Ali and Ma’alalta (Woolley 2001) have been studied to variable degrees, but few other volcanoes have been sampled or investigated in any depth. Most studies on Ethiopian rift magmatism have been carried out on a regional scale (Peccerillo et al. 2003).

One of the key problems encountered at Dabbahu is access: the volcano is remote, requiring full expedition planning, including camels, in order to reach it. On reaching the volcano, there is no guarantee that the security situation is, or will remain, stable enough for the planned fieldwork to be carried out. It has never yet been possible to access the eastern side of the volcano, and the security situation is unlikely to change in the immediate future. However, at some point the situation may improve. When, and if this occurs, sampling of the lava flows on the NE and E side may be possible, and will greatly add to the overall understanding of this volcano. Determination of the peralkaline or metaluminous nature of the rhyolites will provide further understanding to the dimensions of the early rhyolitic dome. If additional metaluminous samples are located they may also prove suitable for geochronology. More detailed fieldwork is required around some of the structures on Dabbahu, to address the hypothesis that these structures exist due to earlier infilled calderas: mainly the curved faulting on and around the summit area, and the curved plateau structure to the SE.

There is little isotope data for Dabbahu; some limited data exists from the CNR-CNRS campaigns (Barberi et al. 1974), but no modern analysis has been carried out. A systematic analysis of isotope contents across the Dabbahu suite, together with a complete set of trace elements (ICP-MS) would be beneficial, and should support the lack of crustal assimilation seen in the whole rock and trace element geochemistry. There is a paucity of well constrained isotope data from volcanoes in the Afar region, and such data would be useful for comparison to other areas in the African rift, and other rift systems in general.

Very limited experimental work on peralkaline samples has been carried out in recent years (Scaillet and Macdonald 2003; Caricchi et al. 2006). The Caricchi (2006) experiments are a reasonable fit to the Dabbahu samples, but involve basalts with higher H_2O than is plausible for Dabbahu parent basalts. This leads to crystallisation of amphibole in the Caricchi (2006) experiments which is extremely rare at Dabbahu. Experiments starting with a basalt of lower initial H_2O content (1 wt% or less), to determine a fractionation path from basalts through to peralkaline samples would be useful to confirm any evolution path that has been proposed for Dabbahu, and may well apply to other peralkaline centres.

At Erta Ale there is a poor understanding of the deeper magmatic system, and the geometry of the plumbing system as a whole. The lava lake has potentially been in existence for over 100 years, but the constraints on the dynamics which maintain this magmatic system are still incomplete. This is the most northerly and the oldest magmatic segment in the Afar region. We still do not understand the point at which the transition from continental crust to oceanic crust is finally completed, and further study of Erta Ale may provide additional insight. With the growth of satellite monitoring, and increasingly dense seismic networks in the region, it is now possible to monitor this volcano more closely. Due to its lava lake, Erta Ale may act as a regional ‘barometer’; eruptions or periods of increased agitation may be a sensitive response to tectonic activity within the region, as suggested by the activity in 2005 and 2010. Improved seismic monitoring in the region, together with modern satellite geodetic techniques, may in the future enable the means to provide an answer to this question.

Bibliography

References

*Acocella, V. (2010). "Coupling volcanism and tectonics along divergent plate boundaries: Collapsed rifts from central Afar, Ethiopia." Geological Society of America Bulletin **122**(9-10): 1717-1728.*

*Acocella, V., B. Abebe, et al. (2008). "Structure of Tendaho Graben and Manda Hararo Rift: Implications for the evolution of the southern Red Sea propagator in Central Afar." Tectonics **27**(4): 17.*

*Andersen, A. T. (1975). "Some basaltic and andesitic gases." Reviews of Geophysics **13**(1): 37-55.*

*Andersen, D. J., D. H. Lindsley, et al. (1993). "QUILF - a PASCAL program to assess equilibria among Fe-Mg-Mn-Ti oxides, pyroxenes, olivine and quartz " Computers & Geosciences **19**(9): 1333-1350.*

*Ando, A. (1984). "New silicate rock reference materials issued from the Geological Survey of Japan, 1984." Journal of Geochemisty **18**: 215-216.*

*Annen, C., J. D. Blundy, et al. (2006). "The genesis of intermediate and silicic magmas in deep crustal hot zones." Journal of Petrology **47**(3): 505-539.*

*Ayalew, D., C. Ebinger, et al. (2006). Temporal compositional variation of syn-rift rhyolites along the western margin of the southern Red Sea and northern Main Ethiopian Rift. Afar Volcanic Province within the East African Rift System. G. Yirgu, C. J. Ebinger and P. K. H. Maguire. **259:** 121-130.*

*Ayele, A., E. Jacques, et al. (2007). "The volcano-seismic crisis in Afar, Ethiopia starting September 2005." Earth and Planetary Science Letters **255**(1-2): 177-187.*

*Ayele, A., D. Keir, et al. (2009). "September 2005 mega-dike emplacement in the Manda-Harraro nascent oceanic rift (Afar depression)." Geophysical Research Letters **36**.*

*Bacon, C. R. and M. M. Hirschmann (1988). "Mg/Mn partitioning as a test for equilibrium between co-existing Fe-Ti oxides." American Mineralogist **73**(1-2): 57-61.*

*Barberi, F., E. Bonatti, et al. (1974). "Transverse tectonics during the split of a continent: Data from the afar rift." Tectonophysics **23**(1-2): 17-29.*

*Barberi, F., J. L. Cheminee, et al. (1973). "Long-lived lava lakes of Erta-Ale volcano." Revue De Geographie Physique Et De Geologie Dynamique **15**(4): 347-351.*

*Barberi, F., R. Ferrara, et al. (1974). "A transitional basalt - pantellerite sequence of fractional crystallisation, the Boina centre, (Afar Rift, Ethiopia)." Journal of Petrology **16**(1): 22-56.*

*Barberi, F., R. Santacroce, et al. (1974). "Silicic peralkaline volcanic rocks of the Afar Depression (Ethiopia)." Bulletin Volcanologique **38**(2): 755-790.*

Barberi, F., H. Tazieff, et al. (1972). "Volcanism in the Afar depression: Its tectonic and magmatic significance." Tectonophysics ***15****(1-2): 19-29.*
Barberi, F. and J. Varet (1970). "The Erta Ale Volcanic Range." Bulletin of Volcanology ***34****(4): 848-917.*

Barberi, F. and J. Varet (1971). "The Erta Ale volcanic range (Danakil depression, northern Afar, Ethiopia)." Bulletin Volcanologique ***34****(4): 848-917.*

Barberi, F. and J. Varet (1977). "Volcanism of Afar - small-scale plate tectonic implications." Geological Society of America Bulletin ***88****(9): 1251-1266.*

Bardintzeff, J. (2004). Bulletin of the Global Volcanism Network. BGVN, Smithsonian Institute. ***29:11****.*

Barrat, J.A., S. Fourcade, et al. (1998). "Isotope (Sr, Nd, Pb, O) and trace-element geochemistry of volcanics from the Erta Ale range, Ethiopia." Journal of Volcanology and Geothermal Research ***80****(1-2):85-100*

Barrat, J. A., J. L. Joron, et al. (2003). "Geochemistry of basalts from Manda Hararo, Ethiopia: LREE-depleted basalts in Central Afar." Lithos ***69****(1-2): 1-13.*

Beattie, P. (1993). "Olivine-melt and orthopyroxene-melt equilibria." Contributions to Mineralogy and Petrology ***115****(1): 103-111.*

Beutel, E., J. van Wijk, et al. (2010). "Formation and stability of magmatic segments in the Main Ethiopian and Afar rifts." Earth and Planetary Science Letters ***293****(3-4): 225-235.*

Bizouard, H., F. Barberi, et al. (1980). "Mineralogy and petrology of Erta Ale and Boina volcanic series, Afar Rift, Ethiopia." Journal of Petrology ***21****(2): 401-436.*

Blundy, J. and K. Cashman (2008). Petrologic Reconstruction of Magmatic System Variables and Processes. Minerals, inclusions and volcanic processes. P. K. T. FJ, Mineralogical Soc Amer, 3635 Concorde Pkwy STE 500, Chantilly, VA 20151-1125 USA ***69:*** *179-239.*

Blundy, J. D. and B. J. Wood (1991). "Crystal-chemical controls on the partitioning of Sr and Ba between plagioclase feldspar, silicate melts, and hydrothermal solutions." Geochimica Et Cosmochimica Acta ***55****(1): 193-209.*

Brinckmann, J. and M. Kuersten (1970). Geologische Uebersichtskarte der Danakil-Senke; geological sketch map of the Danakil depression, scale 1:250 000, Federal Republic of Germany.

Bureau, H., F. Pineau, et al. (1998). "A melt and fluid inclusion study of the gas phase at Piton de la Fournaise volcano (Réunion Island)." Chemical Geology ***147****(1-2): 115-130.*

Burgi, P.-Y., M. Caillet, et al. (2002). "Field temperature measurements at Erta'Ale Lava Lake, Ethiopia." Bulletin of Volcanology ***64****(7): 472-485.*

Calvert, A. T. and M. A. Lanphere (2006). "Argon geochronology of Kilauea's early submarine history." Journal of Volcanology and Geothermal Research ***151****(1-3): 1-18.*

Caricchi, L., A. Pommier, et al. (2011). "Strain-induced magma degassing: insights from simple-shear experiments on bubble bearing melts." Bulletin of Volcanology ***online*** *1-13.*

Caricchi, L., L. Burlini, et al. (2007). "Non-Newtonian rheology of crystal-bearing magmas and implications for magma ascent dynamics." Earth and Planetary Science Letters ***264****(3-4): 402-419.*

Caricchi, L., P. Ulmer, et al. (2006). "A high-pressure experimental study on the evolution of the silicic magmatism of the Main Ethiopian Rift." Lithos (Science Direct) ***91****(1-4): 46-58.*

Carmichael, I. S. E. (1967). "The iron-titanium oxides of salic volcanic rocks and their associated ferromagnesian silicates." Contributions to Mineralogy and Petrology ***14****: 36-64.*

Chu, D. and R. G. Gordon (1999). "Evidence for motion between Nubia and Somalia along the Southwest Indian ridge." Nature ***398****(6722): 64-67.*

Chu, D. Z. and R. G. Gordon (1998). "Current plate motions across the Red Sea." Geophysical Journal International ***135****(2): 313-328.*

Coogan, L. A., A. Hain, et al. (2005). "Experimental determination of the diffusion coefficient for calcium in olivine between 900°C and 1500°C." Geochimica Et Cosmochimica Acta ***69****(14): 3683-3694.*

Cornwell, D. G., P. K. H. Maguire, et al. (2010). "Imaging detailed crustal structure and magmatic intrusion across the Ethiopian Rift using a dense linear broadband array." Geochemistry Geophysics Geosystems ***11****.*

d'Acremont, E., S. Leroy, et al. (2005). "Structure and evolution of the eastern Gulf of Aden conjugate margins from seismic reflection data." Geophysical Journal International ***160****(3): 869-890.*

Dainelli, G. and O. Marinelli (1907). "Vulcani attivi della Dancalia." Rivista Geografica Italiana ***13****: 261-270.*

Dalrymple, G. B., ., E. C. Alexander Jr., et al. (1989). "Irradiation of samples for 40Ar/39Ar dating using the Geological Survey TRIGA reactor." U.S. Geol. Surv. Prof. Paper ***1176****: 1-55.*

Danyushevsky, L. V., F. N. Della Pasqua, et al. (2000). "Re-equilibration of melt inclusions trapped by magnesian olivine phenocrysts from subduction-related magmas; petrological implications." Contributions to Mineralogy and Petrology ***138****(1): 68-83.*

Davies, A. G. and L. P. Keszthelyi (2010). "The thermal signature of volcanic eruptions on Io and Earth." Journal of Volcanology and Geothermal Research ***194****(4).*

Davies, G. (1998). "A channelled plume under Africa." Nature ***395****: 743-744.*

Deer, W. A., R. A. Howie, et al. (1992). An introduction to the rock-forming minerals. Harlow, Longman.

Di Carlo, I., S. G. Rotolo, et al. (2010). "Phase Equilibrium Constraints on Pre-eruptive Conditions of Recent Felsic Explosive Volcanism at Pantelleria Island, Italy." Journal of Petrology ***51****: 2245-2276.*

Dixon, J.E., E. Stolper, et al. (1988). "Infrared spectroscopic measurements of CO2 and H2O glasses in the Juan de Fuca Ridge basaltic glasses." EPSL ***90****:87-104*

Dohmen, R., H. W. Becker, et al. (2007). "Fe-Mg diffusion in olivine I: experimental determination between 700 and 1,200 degrees C as a function of composition, crystal orientation and oxygen fugacity." Physics and Chemistry of Minerals ***34****(6): 389-407.*

Dohmen, R. and S. Chakraborty (2007). "Fe-Mg diffusion in olivine II: point defect chemistry, change of diffusion mechanisms and a model for calculation of diffusion coefficients in natural olivine." Physics and Chemistry of Minerals ***34****(6): 409-430.*

Duffield, W. A. and G. B. Dalrymple (1990). "The Taylor Creek Rhyolite of New-Mexico - A rapidly emplaced field of lava domes and flows " Bulletin of Volcanology ***52****(6): 475-487.*

Ebinger, C., A. Ayele, et al. (2010). Length and Timescales of Rift Faulting and Magma Intrusion: The Afar Rifting Cycle from 2005 to Present. Annual Review of Earth and Planetary Sciences, Vol 38. Palo Alto, Annual Reviews. ***38:*** *439-466.*

Ebinger, C., D. Keir, et al. (2008). "Capturing magma intrusion and faulting processes during continental rupture: seismicity of the Dabbahu (Afar) rift." Geophysical Journal International ***174****: 1138-1152.*

Ebinger, C. J. and N. J. Hayward (1996). "Soft plates and hot spots: Views from Afar." Journal of Geophysical Research-Solid Earth ***101****(B10): 21859-21876.*

Ebinger, C. J. and N. H. Sleep (1998). "Cenozoic magmatism throughout east Africa resulting from impact of a single plume." Nature ***395****: 788-791.*

Ernst, W. G. (1962). "Synthesis, Stability Relations, and Occurrence of Riebeckite and Riebeckite-Arfvedsonite Solid Solutions." The Journal of Geology ***70****(6): 689-736.*

Esser, R. P., P. R. Kyle, et al. (2004). "^{40}Ar /^{39}Ar dating of the eruptive history of Mount Erebus, Antarctica: volcano evolution." Bulletin of Volcanology ***66****(8): 671-686.*

Ferguson, D. J., T. D. Barnie, et al. (2010). "Recent rift-related volcanism in Afar, Ethiopia." Earth and Planetary Science Letters ***292****(3-4): 409-418.*

Ferguson, D. J., A., Calvert, et al. (2011). “Asymmetric magmatic rifting in southern Afar,Ethiopia. (submitted).” Nature.

Field, L., J. Blundy, et al. (2011). "Magma storage conditions beneath Dabbahu Volcano (Ethiopia) constrained by petrology, seismicity and satellite geodesy. (In review)." Bulletin of Volcanology.

*Fine, G., E. Stolper (1986). “Dissolved carbon dioxide in basaltic glasses: concentrations and speciation.” EPSL **76**:263-278*

Ford, C. E., D. G. Russell, et al. (1983). "Olivine liquid equilibria - temperature, pressure and composition dependence of the crystal liquid cation partition-coefficients for Mg, Fe^{2+}*, Ca and Mn." Journal of Petrology **24**(3): 256-265.*

Frost, B. R., Ed. (1991). Introduction to oxygen fugacity and its petrologic importance. In Oxide Minerals: Petrologic and magnetic significance. Reviews in Mineralogy, Mineralogical Society of America.

*Frost, B. R. and D. H. Lindsley (1992). "Equilibria among Fe-Ti oxides, pyroxenes, olivine and quartz. 2 Application " American Mineralogist **77**(9-10): 1004-1020.*

*Furman, T. (2007). "Geochemistry of East African Rift basalts: An overview." Journal of African Earth Sciences **48**(2-3): 147-160.*

*George, R., N. Rogers, et al. (1998). "Earliest magmatism in Ethiopia: Evidence for two mantle plumes in one flood basalt province." Geology **26**: 923-926.*

*Gerlach, T. M. (1980). "Investigation of volcanic gas analyses and magma outgassing from Erta' Ale lava lake, Afar, Ethiopia." Journal of Volcanology and Geothermal Research **7**(3-4): 415-441.*

*Ghiorso, M. S. and B. W. Evans (2008). "Thermodynamics of Rhombohedral Oxide Solid Solutions and a Revision of the FE-TI Two-Oxide Geothermometer and Oxygen-Barometer." Am J Sci **308**(9): 957-1039.*

*Ghiorso, M. S. and R. O. Sack (1995). "Chemical mass-transfer in magmatic processes 4. A revised and internally consistent thermodynamic model for the interpolation and extrapolation of liquid-solid equilibria in magmatic systems at elevated-temperatures and pressures. ." Contributions to Mineralogy and Petrology **119**(2-3): 197-212.*

*Gibson, I. L. (1970). "A Pantelleritic Welded Ash-Flow Tuff from the Ethiopian Rift Valley." Contributions to Mineralogy and Petrology **28**: 89-111.*

*Giordano, D., J. K. Russell, et al. (2008). "Viscosity of magmatic liquids: A model." Earth and Planetary Science Letters **271**: 123-134.*

*Grew, E. S., U. Halenius, et al. (2008). "Recommended nomenclature for the sapphirine and surinamite groups (sapphirine supergroup)." Mineral Mag **72**(4): 839-876.*

Grove, A. T. (1986). "Geomorphology of the African Rift System." Geological Society, London, Special Publications ***25****(1): 9-16.*

Guern, F. L., J. Carbonnelle, et al. (1979). "Erta'ale lava lake: heat and gas transfer to the atmosphere." Journal of Volcanology and Geothermal Research ***6****(1-2): 27-48.*

Hamling, I. J., A. Ayele, et al. (2009). "Geodetic observations of the ongoing Dabbahu rifting episode: new dyke intrusions in 2006 and 2007." Geophysical Journal International ***178****(2): 989-1003.*

Hamling, I. J., T. J. Wright, et al. (2010). "Stress transfer between thirteen successive dyke intrusions in Ethiopia." Nature Geosci ***3****(10): 713-717.*

Hammond, J. O. S., J. M. Kendall, et al. (2011). "The nature of the crust beneath the Afar Triple Junction: evidence from receiver functions (in review)." Geochem. Geophys. Geosyst.

Harris, A. J. L., R. Carniel, et al. (2005). "Identification of variable convective regimes at Erta Ale Lava Lake." Journal of Volcanology and Geothermal Research ***142****(3-4): 207-223.*

Hart, W. K., G. WoldeGabriel, et al. (1989). "Basaltic Volcanism in Ethiopia: Constraints on Continental Rifting and Mantle Interactions." Journal of Geophysical Research ***94****(B6): 7731-7748.*

Hauri, E. (2002). "SIMS analysis of volatiles in silicate glasses, 2: isotopes and abundances in Hawaiian melt inclusions." Chemical Geology ***183****(1-4): 115-141.*

Hayward, N. J. and C. J. Ebinger (1996). "Variations in the along-axis segmentation of the Afar Rift system." Tectonics ***15****(2): 244-257.*

Hirn, B., C. Di Bartola, et al. (2009). "Combined Use of SEVIRI and MODIS for Detecting, Measuring, and Monitoring Active Lava Flows at Erupting Volcanoes." IEEE Transactions on Geoscience and Remote Sensing ***47****(2): 2923-2930.*

Hofmann, C., V. Courtillot, et al. (1997). "Timing of the Ethiopian flood basalt event and implications for plume birth and global change." Nature ***389****(6653): 838-841.*

Howarth, R.J. (1998). "Improved estimators of uncertainty in proportions, point-counting, and pass-fail test results." American Journal of Science ***7****: 594-607.*

Humphreys, M. C. S., S. L. Kearns, et al. (2006). "SIMS investigation of electron-beam damage to hydrous, rhyolitic glasses: Implications for melt inclusion analysis." American Mineralogist ***91****(4): 667-679.*

Irvine, T. N. and W. R. A. Baragar (1971). "A guide to the chemical classification of the common volcanic rocks." Canadian Journal of Earth Sciences ***8****: 523-548.*

Ito, M. and J. Ganguly (2006). "Diffusion kinetics of Cr in olivine and 53Mn-53Cr thermochronology of early solar system objects." Geochimica Et Cosmochimica Acta ***70****(3): 799-809.*

Kelemen, P.B., K. Koga, et al. (1997). "Geochemistry of gabbro sills in the crust-mantle transition zone of the Oman ophiolite: implications for the origin of the oceanic lower crust." Earth and Planetary Science Letters ***146****: 475-488.*

Kunzmann, T. (1999). "The aenigmatite-rhonite mineral group." European Journal of Mineralogy ***11****(4): 743-756.*

Lahitte, P., P. Gillot, et al. (2003). "Silicic central volcanoes as precursors to rift propagation; the Afar case." Earth and Planetary Science Letters ***207****(1-4): 103-116.*

Lahitte, P., P. Y. Gillot, et al. (2003). "New age constraints on the timing of volcanism in central Afar, in the presence of propagating rifts." Journal of Geophysical Research-Solid Earth ***108****(B2).*

Le Maitre, R. W., Ed. (2002). Igneous Rocks: A classification and glossary of terms. Recommendations of the International Union of Geological Sciences Subcommission on the systematics of igneous rocks. Cambridge, Cambridge University Press.

Leake, B. E., G. L. Hendry, et al. (1969). "The chemical analysis of rock powders by automatic X-ray fluorescence." Chemical Geology ***5****(1): 7-86.*

Leake, B. E., A. R. Woolley, et al. (1997). "Nomenclature of amphiboles; Report of the Subcommittee on Amphiboles of the International Mineralogical Association, Commission on New Minerals and Mineral Names." American Mineralogist ***82****(9-10): 1019-1037.*

Lepage, L. D. (2003). "ILMAT: an Excel worksheet for ilmenite-magnetite geothermometry and geobarometry." Computers & Geosciences ***29****(5): 673-678.*

Lifshin, E. and R. Gauvin (2001). "Minimizing Errors in Electron Microprobe Analysis." Microscopy and Microanalysis ***7****(02): 168-177.*

Llewellin, E. W. and M. Manga (2005). "Bubble suspension rheology and implications for conduit flow." Journal of Volcanology and Geothermal Research ***143****(1-3): 205-217.*

Lowenstern, J. B. and G. A. Mahood (1991). "New data on magmatic H2O contents of pantellerites with implications for petrogenesis and eruptive dynamics at Pantelleria." Bulletin of Volcanology ***54****(1): 78-83.*

Maclennan, J., D. McKenzie, et al. (2001). "Crustal accretion under northern Iceland." Earth and Planetary Science Letters ***191****(3-4): 295-310.*

Macdonald, R. (1975). "Nomenclature and petrochemistry of the peralkaline oversaturated extrusive rocks." Bulletin Volcanologique ***38****(2): 498-516.*

Macdonald, R. and B. Baginski (2009). "The central Kenya peralkaline province: a unique assemblage of magmatic systems." Mineralogical Magazine ***73****(1): 1-16.*

Macdonald, R. and D. K. Bailey, Eds. (1973). Chemistry of Igneous Rocks. Part 1. The chemistry of the peralkaline oversaturated obsidians. Data of Geochemistry, Geological Survey Professional Paper.

*MacDonald, R., H. E. Belkin, et al. (2008). "The roles of fractional crystallization, magma mixing, crystal mush remobilization and volatile-melt interactions in the genesis of a young basalt-peralkaline rhyolite suite, the Greater Olkaria Volcanic Complex, Kenya rift valley." Journal of Petrology **49**(8): 1515-1547.*

*Maguire, P. K. H., G. R. Keller, et al. (2006). Crustal structure of the northern Main Ethiopian Rift from the EAGLE controlled-source survey; a snapshot of incipient lithospheric break-up. Afar Volcanic Province within the East African Rift System. G. Yirgu, C. J. Ebinger and P. K. H. Maguire. Bath, Geological Soc Publishing House. **259:** 269-292.*

*Mahatsente, R., G. Jentzsch, et al. (1999). "Crustal structure of the Main Ethiopian Rift from gravity data: 3-dimensional modeling." Tectonophysics **313**(4): 363-382.*

*Makris, J. and A. Ginzburg (1987). "The Afar Depression: transition between continental rifting and sea-floor spreading." Tectonophysics **141**(1-3): 199-214.*

*Manighetti, I., P. Tapponnier, et al. (1997). "Propagation of rifting along the Arabia-Somalia plate boundary: The Gulfs of Aden and Tadjoura." Journal of Geophysical Research-Solid Earth **102**(B2): 2681-2710.*

*Marshall, A. S., R. MacDonald, et al. (2009). "Fractionation of Peralkaline Silicic Magmas: the Greater Olkaria Volcanic Complex, Kenya Rift Valley." Journal of Petrology **50**(2): 323-359.*

*Marshall, L. A. and R. S. J. Sparks (1984). "Origin of some mixed-magma and net-veined ring intrusions." Journal of the Geological Society **141**(1): 171-182.*

*McKenzie, D. P., D. Davies, et al. (1970). "Plate tectonics of the Red Sea and East Africa." Nature **226**(5242): 243-&.*

*Milman-Barris, M. S., J. R. Beckett, et al. (2008). "Zoning of phosphorus in igneous olivine." Contributions to Mineralogy and Petrology **155**(6): 739-765.*

*Mohr, P. A. (1972). "Surface structure and plate tectonics of Afar." Tectonophysics **15**(1-2): 3-9.*

*Morimoto, N. (1989). "Nomenclature of pyroxenes." Can Mineral **27**(1): 143-156.*

Müller, J. (2010). MSG Level 1.5 Image Data Format Description, EUM/MSG/ICD/105.

*Mutter, J. C. and J. A. Karson (1992). "Structural Processes at Slow-Spreading Ridges." Science **257**(5070): 627-634.*

Nesbitt, L. M. (1935). Hell-hole of creation: the exploration of Abyssinian Danakil. New York, Alfred. A. Knopf.

*Newman, S. and J. B. Lowenstern (2002). "VolatileCalc: a silicate melt-H2O-CO2 solution model written in Visual Basic for excel." Computers & Geosciences **28**(5): 597-604.*

*Nichols, A. R. L., M. R. Carroll, et al. (2002). "Is the Iceland hot spot also wet? Evidence from the water contents of undegassed submarine and subglacial pillow basalts." Earth and Planetary Science Letters **202**(1): 77-87.*

*Nichols, A. R. L. and R. J. Wysoczanski (2007). "Using micro-FTIR spectroscopy to measure volatile contents in small and unexposed inclusions hosted in olivine crystals." Chemical Geology **242**: 371-384.*

*Nielsen, C. H. and H. Sigurdsson (1981). "Quantitative methods for electron micro-probe analysis of sodium in natural and synthetic glasses " American Mineralogist **66**(5-6): 547-552.*

*Noble, D. C. (1968). "Systematic variation of major elements in comendite and pantellerite glasses." Earth and Planetary Science Letters **4**(2): 167-172.*

*Oppenheimer, C. and P. Francis (1997). "Remote sensing of heat, lava and fumarole emissions from Erta 'Ale volcano, Ethiopia." International Journal of Remote Sensing **18**(8): 1661 - 1692.*

*Pal, R. (2003). "Rheological behaviour of bubble-bearing magmas." Earth and Planetary Science Letters **207**: 165-179.*

*Peccerillo, A., M. R. Barberio, et al. (2003). "Relationships between Mafic and Peralkaline Silicic Magmatism in Continental Rift Settings: a Petrological, Geochemical and Isotopic Study of the Gedemsa Volcano, Central Ethiopian Rift." J. Petrology **44**(11): 2003-2032.*

*Pik, R., C. Deniel, et al. (1998). "The northwestern Ethiopian Plateau flood basalts: Classification and spatial distribution of magma types." Journal of Volcanology and Geothermal Research **81**(1-2): 91-111.*

*Pik, R., C. Deniel, et al. (1999). "Isotopic and trace element signatures of Ethiopian flood basalts: evidence for plume-lithosphere interactions." Geochimica Et Cosmochimica Acta **63**(15): 2263-2279.*

*Pik, R., B. Marty, et al. (2006). "How many mantle plumes in Africa? The geochemical point of view." Chemical Geology **226**(3-4): 100-114.*

*Pineau, F. and M. Javoy (1994). "Strong degassing at ridge crests: The behaviour of dissolved carbon and water in basalt glasses at 14°N, Mid-Atlantic Ridge." Earth and Planetary Science Letters **123**(1-3): 179-198.*

*Plas, L. v. d. and A. C. Tobi (1965). "A chart for judging the reliability of point counting results." Am J Sci **263**(1): 87-90.*

Pouchou, I. and F. Pichoir, Eds. (1991). Quantitative analysis of homogeneous or stratified microvolumes applying the model "PAP". In: Electron Microprobe Quantification. New York, Plenum Press.

Pouchou, J. L. and F. Pichoir, Eds. (1984). "PAP" (φ-ρ-z) correction procedure for improved quantitative microanalysis. . Microbeam Analysis, San Francisco Press, California.

*Prodehl, C., K. Fuchs, et al. (1997). "Seismic-refraction studies of the Afro-Arabian rift system - a brief review." Tectonophysics **278**(1-4): 1-13.*

*Putirka, K., M. Johnson, et al. (1996). "Thermobarometry of mafic igneous rocks based on clinopyroxene-liquid equilibria, 0-30 kbar." Contributions to Mineralogy and Petrology **123**(1): 92-108.*

*Putirka, K. D. (2008). "Thermometers and barometers for volcanic systems." Minerals, inclusions and volcanic processes: Reviews in Mineralogy and Geochemistry **69**: 61-120.*

*Reay, A., R. D. Johnstone, et al. (1989). "Kaersutite, a possible international microprobe standard " Geostandards Newsletter **13**(1): 187-190.*

*Ren, M., P. A. Omenda, et al. (2006). "Application of the QUILF thermobarometer to the peralkaline trachytes and pantellerites of the Eburru volcanic complex, East African Rift, Kenya " Lithos (Science Direct) **91**(1-4): 109-124.*

*Roeder, P. L. (1974). "Activity of iron and olivine solubility in basaltic liquids." Earth and Planetary Science Letters **23**(3): 397-410.*

*Rogers, N. W. (2006). "Basaltic magmatism and the geodynamics of the East African Rift System." Geological Society, London, Special Publications **259**(1): 77-93.*

*Rowland, J., E. Baker, et al. (2007). "Fault growth at a nascent slow-spreading ridge: 2005 Dabbahu rifting episode, Afar." Geophysical Journal International (Geophys. J. Int) **171**(3): 1226-1246.*

*Sawyer, G. M., C. Oppenheimer, et al. (2008). "Magmatic degassing at Erta 'Ale volcano, Ethiopia." Journal of Volcanology and Geothermal Research **178**(4): 837-846.*

*Scaillet, B. and R. MacDonald (2001). "Phase relations of peralkaline silicic magmas and petrogenetic implications." Journal of Petrology **42**(4): 825-845.*

*Scaillet, B. and R. Macdonald (2006). "Experimental constraints on pre-eruption conditions of pantelleritic magmas: Evidence from the Eburru complex, Kenya Rift." Lithos **91**(1-4): 95-108.*

*Scaillet, B. and R. A. Y. Macdonald (2003). "Experimental Constraints on the Relationships between Peralkaline Rhyolites of the Kenya Rift Valley." J. Petrology **44**(10): 1867-1894.*

*Schumacher, J. C. (1991). "Empirical Ferric Iron Correction - necessity, assumptions, and effects on selected geothermobarometers " Mineralogical Magazine **55**(378): 3-18.*

*Shishkina, T. A., R. E. Botcharnikov, et al. (2010). "Solubility of H_2O and CO_2 bearing fluids in tholeiitic basalts at pressures up to 500 MPa." Chemical Geology **277**(1-2): 115-125.*

*Spandler, C. and H. O'Neill (2010). "Diffusion and partition coefficients of minor and trace elements in San Carlos olivine at 1,300°C with some geochemical implications." Contributions to Mineralogy and Petrology **159**(6): 791-818.*

Sparks, R. S. J. and H. E. Huppert (1984). "Density changes during the fractional crystallization of basaltic magmas: fluid dynamic implications." Contributions to Mineralogy and Petrology ***85****: 300-309.*

Tamic, N., H. Behrens, et al. (2001). "The solubility of H_2O and CO_2 in rhyolitic melts in equilibrium with a mixed CO_2-H_2O fluid phase." Chemical Geology ***174****(1-3): 333-347*

Tazieff, H. (1973). "Erta Ale Volcano." Revue De Geographie Physique Et De Geologie Dynamique ***15****(4): 437-441.*

Teklay, M., E. E. Scherer, et al. (2010). "Geochemical characteristics and Sr-Nd-Hf isotope compositions of mantle xenoliths and host basalts from Assab, Eritrea: implications for the composition and thermal structure of the lithosphere beneath the Afar Depression." Contributions to Mineralogy and Petrology ***159****(5): 731-751.*

Tesfaye, S., D. J. Harding, et al. (2003). "Early continental breakup boundary and migration of the Afar triple junction, Ethiopia." Geological Society of America Bulletin ***115****(9): 1053-1067.*

Thompson, R. N. and W. S. Mackenzie (1967). "Feldspar-liquid equilibria in peralkaline acid liquids - an experimental study." American Journal of Science ***265****(8): 714-734.*

Toplis, M. J. and M. R. Carroll (1995). "An experimental study of the influence of oxygen fugacity on Fe-Ti oxide stability, phase relations and mineral melt equilibria in ferro-basaltic systems. ." Journal of Petrology ***36****(5): 1137-1170.*

Trua, T., C. Deniel, et al. (1999). "Crustal control in the genesis of Plio-Quaternary bimodal magmatism of the Main Ethiopian Rift (MER): geochemical and isotopic (Sr, Nd, Pb) evidence." Chemical Geology ***155****(3-4): 201-231.*

van Wyk de Vries, B. and O. Merle (1996). "The effect of volcanic constructs on rift fault patterns." Geology ***24****(7): 643-646.*

Varet, J. (1972). Card 1363, Center for Short-Lived Phenomena Event Report. CSLP, Smithsonian Institute. ***16:72****.*

Varet, J. (1972). Card 1390, Center for Short-Lived Phenomena Event Report. CSLP, Smithsonian Institute. ***16:72****.*

Varet, J., C. Holliday, et al. (2008). Smithsonian Institute. Bulletin of the Global Volcanism Network. ***BGVN****.*

Venezky, D. Y. and M. J. Rutherford (1999). "Petrology and Fe-Ti oxide reequilibration of the 1991 Mount Unzen mixed magma." Journal of Volcanology and Geothermal Research ***89****(1-4): 213-230.*

Vetsch, P., G. Assefa, et al. (1992). Bulletin of the Global Volcanism Network. BGVN, Smithsonian Institution. ***17:09****.*

Vetsch, P., M. Caillet, et al. (2003). Bulletin of the Global Volcanism Network. BGVN, Smithsonian Institute. ***29:02****.*

Villa, I.M. (1997). "Direct determination of 39Ar recoil distance." Geochimica et Cosmochimica Acta ***61****: 689-691*

Waldbaum, D. R. (1966). "Calorimetric investigation of the alkali feldspars" Ph.D. Thesis. Cambridge, Massachusetts, Harvard University. ***Ph.D.***

Webster, J., R. P. Taylor, et al. (1993). "Pre-eruptive melt composition and constraints on degassing of a water-rich pantellerite magma, Fantale volcano, Ethiopia." Contributions to Mineralogy and Petrology ***114****(1).*

Whitaker, M., H. Nekvasil, et al. (2008). "Can crystallization of olivine tholeiite give rise to potassic rhyolites?—an experimental investigation." Bulletin of Volcanology ***70****(3): 417-434.*

White, J. C. (2003). "Trace-element partitioning between alkali feldspar and peralkalic quartz trachyte to rhyolite magma. Part II: Empirical equations for calculating trace-element partition coefficients of large-ion lithophile, high field-strength, and rare-earth elements." American Mineralogist ***88****(2-3): 330-337.*

White, J. C., D. F. Parker, et al. (2009). "The origin of trachyte and pantellerite from Pantelleria, Italy: Insights from major element, trace element, and thermodynamic modelling." Journal of Volcanology and Geothermal Research ***179****(1-2): 33-55.*

White, J. C., M. Ren, et al. (2005). "Variation in mineralogy, temperature and oxygen fugacity in a suite of strongly peralkaline lavas and tuffs, Pantelleria, Italy." Canadian Mineralogist ***43****: 1331-1347.*

Wiart, P. and C. Oppenheimer (2005). "Large magnitude silicic volcanism in north Afar; the Nabro volcanic range and Ma'alalta Volcano." Bulletin of Volcanology ***67****(2): 99-115.*

Wilson, S. A. (1997). "The collection, preparation and testing of USGS reference material BCR-2, Columbia River, Basalt." USGS openfile report ***98****.*

Wolfenden, E., C. Ebinger, et al. (2004). "Evolution of the northern Main Ethiopian rift: birth of a triple junction." Earth and Planetary Science Letters ***224****(1-2): 213-228.*

Wolfenden, E., C. Ebinger, et al. (2005). "Evolution of a volcanic rifted margin: Southern Red Sea, Ethiopia." Geological Society of America Bulletin ***117****(7-8): 846-864.*

Woolley, A. R. (2001). Alkaline rocks and carbonatites of the world. Pt. 3, Africa. Bath, Geological Society.

Wright, R. and E. Pilger (2008). "Satellite observations reveal little inter-annual variability in the radiant flux from the Mount Erebus lava lake." Journal of Volcanology and Geothermal Research ***177****(3): 687-694.*

Wright, T. J., C. J. Ebinger, et al. (2006). "Magma maintained rift segmentation at continental rupture in the 2005 Afar dyking episode." Nature ***442****: 291-294.*

Yirgu, G. (2005). Bulletin of the Global Volcanism Network. BGVN, Smithsonian Institute. ***30:09****.*

Yirgu, G., A. Ayele, et al. (2006). "Recent seismovolcanic crisis in northern Afar, Ethiopia." EOS ***87****(33): 325-336.*

Yirgu, G., C. Ebinger, et al. (2006). The Afar volcanic province within the East African Rift System. London, Geological Society.